Condensats de Bose-Einstein, champs évanescents et champs radio-fréquences

Hélène Perrin

UNIVERSITÉ PARIS XIII
INSTITUT GALILÉE

LABORATOIRE DE PHYSIQUE DES LASERS

Habilitation à diriger des recherches

Spécialité : Sciences

présentée par

Hélène Perrin

Sujet de la thèse d'habilitation :

Condensats de Bose-Einstein, champs évanescents et champs radio-fréquences

Soutenue le 4 décembre 2008 devant le jury composé de :

Mme	Michèle Leduc	Présidente du jury
M.	Christoph Foot	Rapporteur
M.	Rudolf Grimm	Rapporteur
M.	Christoph Westbrook	Rapporteur
M.	Christian Chardonnet	Examinateur
M.	Vincent Lorent	Examinateur

Table des matières

Remerciements

Après 9 années passées au Laboratoire des lasers, je voudrais remercier tous ceux qui ont contribué, directement ou indirectement, aux travaux présentés dans ce mémoire.

Avant tout, je remercie Vincent Lorent, à la fois pour son rôle moteur à la tête de l'équipe mais aussi pour ses qualités humaines, essentielles dans les moments difficiles où les résultats ne viennent pas aussi vite qu'espérés. Je remercie également Christian Chardonnet, qui non seulement m'a fait découvrir le laboratoire mais a tenu ensuite auprès de moi un rôle de tuteur, dans les deux sens de conseil et soutien. Je le remercie en tant que directeur du laboratoire, ainsi que Charles Desfrançois, pour m'avoir permis de mener à bien nos expériences dans un laboratoire connu pour la bonne ambiance qui y règne.

Je suis très reconnaissante à Chris Foot, Rudi Grimm et Chris Westbrook d'avoir accepté la charge de rapporteur de cette habilitation. Je remercie également Michèle Leduc d'avoir présidé le jury de soutenance. Je profite de cette occasion pour lui exprimer ma reconnaissance pour son soutien tout au long de ces années, que ce soit comme directrice du LKB, de l'IFRAF ou comme membre actif de l'association Femmes et Sciences.

Brigitte Mercier faisait partie de la toute première équipe qui a monté l'expérience. Sa fiabilité est exemplaire. J'ai beaucoup appris avec elle, sur l'expérience comme sur le plan humain, et je lui en suis très reconnaissante.

Paul-Eric Pottie a remplacé Brigitte dans l'équipe en 2005. Merci à Polo pour sa bonne humeur et sa faculté extraordinaire de faire avancer cinq projets en même temps ! Merci aussi à Laurent Longchambon pour son implication dans l'expérience depuis qu'il a rejoint l'équipe, et pour son sang-froid en toutes circonstances.

Tout le monde sait que ce sont les thésards qui font avancer les manips... Merci à Yves Colombe, Olivier Morizot, Elena Knyazchyan et Raghavan Kollengode Easwaran pour leur contribution essentielle aux résultats de cette habilitation. Merci à Yves aussi pour avoir créé pour sa thèse les fichiers LaTeX que nous utilisons toujours dans l'équipe. J'ai eu la chance, à deux reprises, de travailler pendant un an avec un post-doc. Cela a été à chaque fois très stimulant, et je remercie pour cela Demascoth Kadio et Carlos Garrido Alzar. Merci enfin aux nombreux stagiaires qui ont apporté leur savoir-faire et leur bonne humeur.

Pour aborder la partie théorique de mes sujets de recherche, j'ai eu la chance de pouvoir travailler avec Maxim Olshanii, Carsten Henkel et Barry Garraway. Ces échanges ont été très enrichissants, et fructueux sur le plan des publications. Beaucoup de résultats présentés dans ce mémoire ont bénéficié de cette collaboration. Merci aussi à Ludovic Pricoupenko, pour l'école aux Houches passionnante que nous avons organisée ensemble. Sa bonne humeur et son optimisme sont de grands stimulants.

Étant donné la complexité de l'expérience, le soutien compétent des ateliers du laboratoire nous a été absolument nécessaire. Je voudrais en particulier remercier ceux qui ont contribué de façon essentielle au montage initial de l'expérience : Olivier Lopez, Jean-Yves Chauvet et Germaine Simon à l'atelier d'électronique, Gérard Baquet et Michel Fosse à l'atelier de mécanique, Thierry Billeton à l'atelier d'optique. Pour leur soutien constant par la suite, dans la phase où l'expérience donnait des résultats et où les ateliers étaient sommés de répondre le plus vite possible à nos demandes, j'associe à ces pionniers tous les membres des ateliers : Stéphane Callier, Fabrice Wiotte, Julien de Lapeyre, Albert Kaladjian, Marc Barbier et Dejan Kocic.

Je suis particulièrement reconnaissante aux administratives du laboratoire pour leur disponibilité et l'efficacité de leur travail, dans un domaine dans lequel les chercheurs sont souvent démunis. Elles ont su être à l'écoute de nos demandes, et faire tout ce qui était possible pour arrondir les angles quand il le fallait. Merci à Solange Dousset, Sabine Barbut, Martine Alsters, Antonia Wilk et Nathalie Froger.

Je remercie l'ensemble de mes collègues au laboratoire, avec lesquels les contacts sont faciles et agréables, que ce soit pour l'emprunt de matériel, les discussions scientifiques ou l'enseignement. Merci notamment aux collègues de l'équipe atomes froids pour les échanges stimulants lors des séminaires communs. Je remercie spécialement Anne Amy-Klein pour sa disponibilité auprès de moi, malgré un emploi du temps surchargé, et la pertinence de ses conseils.

Merci à Pierre-Yvan et aux Clairacais de me changer les idées en musique.

Enfin, je remercie ma famille, toujours là pour me soutenir quand les atomes sont partis faire la fête ailleurs et que le moral est au plus bas : la famille *stricto sensu* et les autres, d'Antony, de Bonn, de Paris, de Bretagne, de l'Est et du Nord, et avant tout Ronan, Solal, Lou-Anne et Simon.

Curriculum vitae

Hélène PERRIN
Tél : 01 49 40 33 93 ou 33 71
Fax : 01 49 40 32 00
helene.perrin@univ-paris13.fr

née le 13 juin 1972
trois enfants
nés en 1998, 2000 et 2004

Formation et parcours professionnel

2002- : Chargée de Recherche de 1re classe au CNRS affectée au Laboratoire de physique des lasers (UMR 7538, Université Paris 13) dans l'équipe COMETA (Condensat, Mesures Et Applications) dirigée par Vincent Lorent.

Mots-clés : physique atomique, atomes ultra froids, atomes de rubidium, condensation de Bose-Einstein, dimensions restreintes, champs radio-fréquences, champs évanescents, contrôle des atomes par laser, rugosité de surface, bruit radiofréquence. Notre équipe est membre de l'Institut Francilien de Recherche sur les Atomes Froids (IFRAF).

1999-2002 : Chargée de Recherche de 2e classe, dans la même équipe.

août 1999 : Participation à l'école des Houches *Ondes de matière cohérentes.*

1998-1999 : Stage post-doctoral au Service de Physique de l'Etat Condensé du CEA (Saclay), dans l'équipe de Christian Glattli. *Mesures de bruit dans les gaz d'électrons bidimensionnels.*

Ce séjour post-doctoral a été consacré à une thématique différente de la thèse et de la recherche au LPL. Mots-clés : physique du solide, physique mésoscopique, très basses températures (20 mK), réfrigérateur à dilution, effet Hall quantique fractionnaire, anyons, charges fractionnaires, mesure de bruit.

1995-1998 : Thèse de doctorat de l'Université Paris VI intitulée *Refroidissement d'atomes de césium dans un piège dipolaire très désaccordé*, soutenue le 26 juin 1998 avec la mention Très Honorable et les félicitations du jury. Travail effectué sous la direction de Christophe Salomon, au sein du groupe de Claude Cohen-Tannoudji, laboratoire Kastler Brossel, École normale supérieure, Paris. Rapporteurs : Jacques Baudon et Andrew M. Steane.

Mots-clés : atomes froids, piège magnéto-optique, piège dipolaire, atomes de césium polarisés, transitions Raman, passage adiabatique, refroidissement par bandes latérales, refroidissement Raman, refroidissement par évaporation tout optique.

Allocataire monitrice polytechnicienne à l'Université Pierre et Marie Curie, sous la direction de Jacques Treiner et Benoît Mosser.

1994-1995 : DEA de Physique Quantique (mention Bien). Stage de DEA : *Observation d'atomes de césium confinés dans un piège opto-électrique* (Christophe Salomon). Bourse de l'École polytechnique.

Mots-clés : atomes froids de césium, champ électrique, piégeage optique, pince optique.

1991-1994 : Scolarité à l'École polytechnique (Palaiseau). Stage de fin d'étude : *Étude théorique d'un miroir à atomes et étude expérimentale des grandes densités dans un piège magnéto-optique*, sous la direction de Jean Dalibard.

Mots-clés : atomes froids de césium, piège magnéto-optique, densité dans l'espace des phases, champ évanescent, optique atomique.

1989-1991 : Mathématiques supérieures et spéciales (option M') au lycée Louis-le-Grand, Paris.

1989 : Baccalauréat série C, mention Très Bien.

Responsabilités

Activités d'encadrement, d'animation et d'administration de la recherche

Encadrement :

1. Codirection de la thèse de Thomas Liennard, étudiant dans l'équipe depuis septembre 2007.
2. Encadrement (à 80%) de la thèse de Raghavan Kollengode Easwaran, étudiant indien en thèse au laboratoire depuis février 2006.
3. Encadrement (à 90%) de la thèse d'Olivier Morizot (septembre 2003 – janvier 2007) : *Pièges radiofréquence très anisotropes pour un condensat de Bose-Einstein.*
4. Encadrement (80%) d'un post-doc en 2005-2006 (travail expérimental et théorique), Carlos Garrido Alzar.
5. Intégration à l'équipe et encadrement (80%) d'un ingénieur de recherche CNRS recruté en février 2005, Paul-Éric Pottie.
6. Participation (20%) à l'encadrement de la thèse d'Elena Knyazchyan. Sujet : *Optique atomique cohérente.* Elena Knyazchyan a contribué à l'expérience d'Olivier Morizot en début de thèse.
7. Participation (50%) à l'encadrement de la thèse d'Yves Colombe (septembre 2000 – juillet 2004) : *Condensat de Bose-Einstein, champs évanescents et piégeage bidimensionnel.*
8. Encadrement (80%) d'un post-doc en 2002-2003 (travail théorique), Demascoth Kadio.
9. Encadrement de nombreux stagiaires depuis 1996.

Autres activités d'animation :

1. Organisation des séminaires généraux du laboratoire de 2001 à fin 2003.
2. Mise en place des réunions « bibliographie » dans l'équipe COMETA en 2002, étendues aux deux équipes COMETA et Atomes Froids à partir de fin 2003. Organisation de ces réunions en 2002-2003, puis à partir de la rentrée 2006.
3. Correspondante communication du laboratoire depuis janvier 2003.
4. Participation au jury de recrutement d'un ingénieur de recherche, en tant que représentante du laboratoire (décembre 2004). Cet ingénieur, Paul-Éric Pottie, a rejoint notre équipe en février 2005.
5. Membre titulaire de la commission de spécialiste 30e section de l'université Paris 13. Participation aux campagnes de recrutement de 2004 à 2008.
6. Membre titulaire de la commission de spécialiste 30e section de l'université Paris 7. Participation à la campagne de recrutement de 2005.

7. Membre élue du Conseil de laboratoire.
8. Membre élue du Conseil de l'Institut Galilée (faculté des sciences de l'Université Paris 13).
9. Membre élue du Comité National du CNRS de 2006 à 2008, section 4.
10. Rapportrice pour European Physical Journal D, Physical Review A et Physical Review Letters.
11. Membre du jury de quatre thèses dont deux en tant que rapportrice et une à l'étranger.

Activités de formation, d'enseignement et de diffusion

Diffusion scientifique :

1. Membre du comité scientifique des Ateliers de Cargèse *Sexe et genre dans le travail scientifique*, 12 au 15 novembre 2002 ; modération d'un atelier sur le thème *Preuve, imaginaire et genre* ; compte-rendu publié dans les actes.
2. Organisation avec Cécile Robilliard des premières rencontres du GDR *Optique Atomique Intégrée et Nanostructures* à Villetaneuse, janvier 2003.
3. Organisation et édition des actes (cours et séminaires) d'une école de physique de printemps aux Houches du 15 au 25 avril 2003 avec Ludovic Pricoupenko et Maxim Olshanii. L'école a été financée par l'Union Européenne (HLSC), le CNRS, la DGA, la NSF, le ministère des affaires étrangères et les Universités Paris 13 et Paris 6. Ont participé 59 étudiants en thèse ou post-doctorants, 6 enseignants théoriciens, 13 intervenants expérimentateurs pour un séminaire, tous de très haut niveau. Je me suis occupée de l'édition des articles des expérimentateurs, Ludovic Pricoupenko se chargeant de l'édition des cours théoriques. Les actes sont publiés chez EDP-Sciences (voir le paragraphe « Livres et ouvrages »).
4. Organisation du séminaire de l'IFRAF à Villetaneuse le 7 mars 2006, 70 participants.
5. Réalisation de la fiche concernant l'équipe dans la plaquette du laboratoire (2003, 2005 et 2007). Validation de la version anglaise de l'ensemble de la plaquette.
6. Élaboration et mise à jour de la page de l'équipe sur le site internet du laboratoire : http://www-lpl.univ-paris13.fr:8083 .

Séminaires en France :

1. Séminaire général au CNAM à Paris (LNE-CNAM), décembre 2001.
2. Séminaire au LUTH (Observatoire de Paris-Meudon), mars 2002.
3. Séminaire lors des journées du GDR *Optique Atomique Intégrée et Nanostructures*, Villetaneuse, janvier 2003.
4. Séminaire au Laboratoire Aimé Cotton (Orsay), mai 2003.
5. Séminaire interne au LPL, mai 2003.

6. Séminaire dans le cadre de la formation des étudiants à l'ENS Cachan, janvier 2005.
7. Séminaire de l'IFRAF, mars 2006.
8. Séminaire à l'Institut Non Linéaire de Nice, juin 2007.
9. Séminaire au Laboratoire Kastler Brossel, avril 2008.

Vulgarisation :

1. Organisation et animation d'un stand sur le refroidissement laser et la condensation de Bose-Einstein à la fête de la science les 18 et 19 octobre 2001 à Paris 13 lors de la manifestation *Savante Banlieue*, organisée par Paris 13 et les collectivités locales. 5000 visiteurs typiquement. Reprise de ce stand pour l'édition 2002 de *Savante Banlieue*, du 17 au 19 octobre. Depuis 2006 j'anime le stand *Femmes et Sciences* avec quelques collègues.
2. Elaboration d'un stand pour l'exposition grand public *Et voilà le travail !* à Montreuil du 15 au 30 mars 2003. 19 000 visiteurs.
3. Intervention à la table ronde *Le goût de la physique* lors de la journée *Physique en fête* au Ministère de la Recherche le 19 octobre 2001.
4. Depuis 2003 : mise au point et présentation d'une « mini-conférence » intitulée *Qu'est-ce que la température ?* à destination de collégiens et de lycéens dans le cadre de *Savante Banlieue*. Trois à huit présentations selon les années, en impliquant d'autres membres de l'équipe.
5. Intervention en lycée à Saint-Denis pour présenter cette conférence (février 2005).
6. Rédaction d'un article dans le numéro 2003 de la revue SupOptique Avenir des étudiants de l'École supérieure d'optique (*Atomes ultra froids : la spécificité des basses dimensions*). 5000 exemplaires.
7. Rédaction d'un article dans le numéro 1 de la gazette de l'Institut Galilée, *Le LPL, point le plus froid de la Seine-St-Denis*, Université Paris 13 (2005).
8. Une à deux fois par an, journée porte ouverte dans le cadre de l'opération *Et voilà le travail !*, organisée par le Conseil Général.
9. En 2006 et 2007, participation au concours Eurêka de la Fondation 93 (2-3 jours) : rencontre avec des collégiens qui doivent concevoir et réaliser une machine roulante fonctionnant avec l'énergie de pesanteur comme énergie initiale, conférence de physique à leur portée, visite d'expériences et participation au jury du concours.
10. Présentation, en juillet 2006, au Festival des Petits Débrouillards à la Cité des sciences, puis à *Paris-Montagne* à l'ENS du montage d'holographie que j'avais construit pour *Savante Banlieue* : une journée à chaque fois.
11. Participation ponctuelle en 2005 à l'année mondiale de la physique (radio + document de synthèse).

12. Intervention dans le film *La jeunesse des atomes froids*, commande de l'IFRAF diffusée sur France 5. Le film est disponible sur le site du CNRS : http://videotheque.cnrs.fr/index.php?urlaction=doc&id_doc=1769 .
13. Rédaction en collaboration avec Christophe Daussy d'une brève pour le département MPPU, en tant que correspondante communication, sur les résultats de l'équipe HOTES sur la mesure de la constante de Boltzmann. Cela a donné lieu à un article dans le journal du CNRS en juillet 2007, consultable ici : http://www2.cnrs.fr/presse/journal/3478.htm .

Enseignement :

1. DEUG SM 1re année, matière et énergie, 64 heures de TD et colles par an à Paris 6 dans le cadre du monitorat de 1995 à 1998.
2. Licence de Sciences Physique, optique ondulatoire, 40 heures de TD et TP à Paris 7 en tant que vacataire en 1999.
3. DEUG STPI 1re année, mécanique du point, 20 heures de TD à Paris 13 au premier semestre 2002-2003.
4. DEUG SM 2e année, électromagnétisme, 26 heures de TD à Paris 13 au premier semestre 2002-2003).
5. Séminaire-cours donné au magistère inter-universitaire de physique dans le cadre de l'enseignement prévu, décembre 2003 : *Au cœur de la matière quantique : la condensation de Bose-Einstein.*
6. Examinatrice au concours d'entrée à l'École normale supérieure, concours PC Ulm, épreuve de Physique 2 (concours d'entrée 2004 et 2005) : 2×45 heures.
7. Depuis 2005 : Travaux Dirigés en master de physique deuxième année, parcours de Physique quantique, option Atomes froids (12 heures par an). Depuis 2007, je fais aussi des cours, et je suis responsable de cette option depuis 2008.
8. Accueil de polytechniciens pour des Travaux Pratiques au sein du laboratoire, en partenariat avec leur enseignant à l'École polytechnique (2 séances de 6 heures), en 2005 et 2006.
9. Série de 4 cours à l'école prédoctorale des Houches sur le refroidissement laser (septembre 2006). Reprise de ces cours en 2008.
10. Série de 2 cours à l'école des Houches *Quantum metrology* (octobre 2007). Les actes seront publiés prochainement.
11. IUT Mesures physiques, 2e année, optique ondulatoire et lasers, 70 heures de cours et TD à l'IUT de Saint-Denis au premier semestre 2008-2009.

Publications

Pour les séminaires et communications, ne sont indiquées que les interventions que j'ai présentées moi-même.

Articles parus dans des revues à comité de lecture

1. O. Morizot, L. Longchambon, R. Kollengode Easwaran, R. Dubessy, E. Knyazchyan, P.-E. Pottie, V. Lorent et H. Perrin, *Influence of the Radio-Frequency source properties on RF-based atom traps*, Eur. Phys. Jour. D **47**, 209 (2008).
2. O. Morizot, C. L. Garrido Alzar, P.-E. Pottie, V. Lorent et H. Perrin, *Trapping and cooling of rf-dressed atoms in a quadrupole magnetic field*, J. Phys. B : At. Mol. Opt. Phys. **40**, 4013 (2007).
3. E. Dimova, O. Morizot, C.L. Garrido Alzar, A. Fioretti, V. Lorent, D. Comparat, H. Perrin et P. Pillet, *Continuous transfer and laser guiding between two cold atom traps*, Eur. Phys. Jour. D **42**, 299 (2007).
4. H. Perrin, Y. Colombe, B. Mercier, V. Lorent et C. Henkel, *Diffuse reflection of a Bose-Einstein condensate from a rough evanescent wave mirror*, J. Phys. B : At. Mol. Opt. Phys. **39**, 4649-4658 (2006).
5. C. L. Garrido Alzar, H. Perrin, B. M. Garraway et V. Lorent, *Evaporative cooling in a radio-frequency trap*, Phys. Rev. A **74**, 053413 (2006).
6. O. Morizot, Y. Colombe, V. Lorent et H. Perrin, et B. M. Garraway, *Ring trap for ultracold atoms*, Phys. Rev. A **74**, 023617 (2006).
7. Y. Colombe, B. Mercier, H. Perrin et V. Lorent, *Diffraction of a Bose-Einstein Condensate in the Time Domain*, Phys. Rev. A **72**, 061601 (2005).
8. Y. Colombe, E. Knyazchyan, O. Morizot, B. Mercier, V. Lorent et H. Perrin, *Ultracold atoms confined in rf-induced two-dimensional trapping potentials*, Europhys. Lett. **67**, 593 (2004).
9. Y. Colombe, D. Kadio, M. Olshanii, B. Mercier, V. Lorent et H. Perrin, *Schemes for loading a Bose-Einstein condensate into a two-dimensional dipole trap*, Journal of Optics B : Quantum and Semiclassical Optical **5**, S155 (2003).
10. D. C. Glattli, V. Rodriguez, H. Perrin, P. Roche, Y. Jin et B. Etienne, *Shot noise and the Luttinger liquid-like properties of the FQHE*, Physica E **6**, 22 (2000).
11. H. Perrin, A. Kuhn, I. Bouchoule, T. Pfau et C. Salomon, *Raman cooling of spin polarized atoms in a crossed dipole trap*, Europhys. Lett. **46**, 141 (1999).
12. I. Bouchoule, H. Perrin, A. Kuhn, M. Morinaga et C. Salomon, *Neutral atoms prepared in Fock states of a one-dimensional harmonic potential*, Phys. Rev. A **59**, R8 (1999).
13. H. Perrin, A. Kuhn, I. Bouchoule et C. Salomon, *Sideband cooling of neutral atoms in a far-detuned optical lattice*, Europhys. Lett. **42**, 395 (1998).
14. A. Kuhn, H. Perrin, W. Hänsel et C. Salomon, *Three Dimensional Raman Cooling using Velocity Selective Rapid Adiabatic Passage*, OSA TOPS on Ultracold Atoms and BEC 1996, **7**, édité par Keith Burnett (1997).
15. P. Lemonde, O. Morice, E. Peik, J. Reichel, H. Perrin, W. Hänsel et C. Salomon, *An opto-electric trap for cold atoms*, Europhys. Lett. **32**, 555 (1995).

16. C.G. Townsend, N.H. Edwards, C.J. Cooper, K.P. Zetie et C.J. Foot, A.M. Steane, P. Szriftgiser, H. Perrin et J. Dalibard, *Phase-space density in the magneto-optical trap*, Phys. Rev. A **52**, 1423 (1995).

Actes de colloques à comité de lecture

1. H. Perrin, O. Morizot, C. Garrido Alzar, P.-E. Pottie et V. Lorent, *Condensation de Bose-Einstein et basse dimensionnalité*, COLOQ9, Dijon (septembre 2005), poster ; Journal de Physique IV **135**, 255 (2006).
2. H. Perrin, Y. Colombe, B. Mercier, V. Lorent et C. Henkel, *A Bose-Einstein condensate bouncing off a rough mirror*, Conference on Atoms and Molecules near Surfaces, Heidelberg, Allemagne (avril 2005), papier invité ; Journal of Physics : Conference Series **19**, 151 (2005).
3. E. Knyazchyan, B. Mercier, H. Perrin, P.-E. Pottie and V. Lorent, *Focusing at the nanoscale by atomic holography ?*, Conference on Atoms and Molecules near Surfaces, Heidelberg, Allemagne (avril 2005), poster ; Journal of Physics : Conference Series **19**, 44 (2005).
4. Y. Colombe, H. Perrin, D. Kadio, M. Olshanii, B. Mercier et V. Lorent, *Transport et chargement d'un condensat de Bose-Einstein dans un piège dipolaire bidimensionnel*, COLOQ8, Toulouse (septembre 2003), poster ; publié sous le titre *Adiabatic transportation of a Bose-Einstein condensate to a dielectric surface* dans Journal de Physique IV (Proceedings) **119**, 159 (2004).

Publications dans des revues sans comité - Vulgarisation

1. O. Morizot, J. de Lapeyre de Bellair, F. Wiotte, O. Lopez, P.-E. Pottie et H. Perrin, *Agile low phase noise radio-frequency sine wave generator applied to experiments on ultracold atoms*, Preprint arXiv:0704.1974v1 (2007).
2. Hélène Perrin, *Atomes ultra froids : la spécificité des basses dimensions*, revue SupOptique Avenir des étudiants de l'Ecole supérieure d'optique (2003).
3. Hélène Perrin, *Le LPL, point le plus froid de la Seine-St-Denis*, la gazette de l'Institut Galilée, Université Paris 13 (2005).

Conférences invitées dans des congrès

1. H. Perrin, Y. Colombe, O. Morizot, E. Knyazchyan, B. Mercier et V. Lorent, *A Bose-Einstein condensate bouncing off a rough mirror*, 4th Russian-French Laser Symposium, Nice, France (septembre 2005).
2. H. Perrin, Y. Colombe, B. Mercier, V. Lorent et C. Henkel, *A Bose-Einstein condensate bouncing off a rough mirror*, Conference on Atoms and Molecules near Surfaces, Heidelberg, Allemagne (avril 2005).

Communications à des congrès

1. H. Perrin, L. Longchambon, R. Kollengode Easwaran, O. Morizot, C. L. Garrido Alzar, P.-E. Pottie, V. Lorent and B. M. Garraway, *Trapping and cooling of rf-dressed atoms*, INTERF08, Levico Terme, Italie (avril 2008), poster.
2. L. Longchambon, O. Morizot, C. L. Garrido Alzar, P.-E. Pottie, R. K. Easwaran, V. Lorent et H. Perrin, *RF-dressed ultracold atoms : adiabatic potentials, 2D trapping and evaporation*, Bose-EInstein Condensation Conference, Sant Feliu de Guixols, Espagne (septembre 2007), poster.
3. H. Perrin, Y. Colombe, B. Mercier, V. Lorent et C. Henkel, *Diffuse reflection of a Bose-Einstein condensate from a rough evanescent wave mirror*, International Conference on Atomic Physics, Innsbruck, Autriche (juillet 2006), poster.
4. H. Perrin, Y. Colombe, B. Mercier, V. Lorent et C Henkel, *Diffuse reflection of a Bose-Einstein condensate from a rough evanescent wave mirror*, International Conference on Atomic Physics, Innsbruck, Austria (juillet 2006), poster.
5. H. Perrin, Y. Colombe, E. Knyazchyan, B. Mercier et V. Lorent, *Bose-Einstein condensates confined in 2D traps*, Bose-Einstein Condensation, San Feliu de Guixols, Espagne (septembre 2003), poster.
6. Y. Colombe, H. Perrin, B. Mercier et V. Lorent, *Condensat de Bose-Einstein confiné à deux dimensions*, congrès général de la Société Française de Physique, Lyon (juillet 2003), poster.
7. H. Perrin, Y. Colombe, D. Kadio, M. Olshanii, B. Mercier et V. Lorent, *Loading a 2D evanescent light trap with a degenerate Bose gas*, Quantum Optics, San Feliu de Guixols, Espagne (septembre 2002), poster.
8. H. Perrin, Y. Colombe, B. Mercier et V. Lorent, *Towards a 2DAG (a two-dimensional atomic gas)*, International Workshop Quantum Gases, Konstanz, Allemagne (juillet 2001), poster.
9. H. Perrin, I. Bouchoule, A. Kuhn et C. Salomon, *Neutral atoms prepared in Fock states of a one-dimensional harmonic potential*, Quantum Optics, Castelvecchio, Italie (septembre 1998), poster.
10. H. Perrin, A. Kuhn, I. Bouchoule et C. Salomon, *Raman and evaporative cooling in a crossed dipole trap*, 3rd Young Atom Optics physicists conference, Pisa, Italie (avril 1997), communication orale.
11. H. Perrin, A. Kuhn, W. Hänsel et C. Salomon, *Three-dimensional Raman cooling of cesium atoms in a crossed dipole trap*, Quantum Optics, Castelvecchio, Italie (septembre 1996), poster.

Séminaires à l'étranger, workshops

1. H. Perrin, Y. Colombe, B. Mercier, V. Lorent et C Henkel, *Diffuse reflection of a Bose-Einstein condensate from a rough evanescent wave mirror*, conférence invitée donnée lors du workshop *Bose-Einstein Condensation* à Leuven (Belgique), 28 juin 2006.

2. H. Perrin, Y. Colombe, D. Kadio, E. Knyazchyan, O. Morizot, B. Mercier et V. Lorent, *Bose-Einstein condensates and 2D traps*, conférence donnée au LENS, Florence, Italie (novembre 2003).
3. H. Perrin, Y. Colombe, D. Kadio, E. Knyazchyan, O. Morizot, B. Mercier et V. Lorent, *Bose-Einstein condensates and 2D traps*, workshop du réseau européen FASTNet, Sienne, Italie (novembre 2003).
4. H. Perrin, Y. Colombe, D. Kadio, B. Mercier, V. Lorent et M. Olshanii, *Bose-Einstein condensates confined in 2D traps*, conférence donnée à l'université de Tübingen, Allemagne (juin 2003).
5. H. Perrin, Y. Colombe, D. Kadio, M. Olshanii, B. Mercier et V. Lorent, *How to load a Bose-Einstein condensate into a 2D trap ?*, workshop du réseau européen FASTNet, Villetaneuse, France, 27 et 28 janvier 2003.
6. H. Perrin, Y. Colombe, B. Mercier, et V. Lorent, *Towards a 2DAG (a two-dimensional atomic gas)*, conférence donnée à Munich dans le groupe de Gerhard Rempe, Allemagne (juillet 2000).

Livres et ouvrages

1. Edition des actes (cours et séminaires) d'une école de physique de printemps aux Houches du 15 au 25 avril 2003 avec Ludovic Pricoupenko et Maxim Olshanii. L'école a été financée par l'Union Européenne (HLSC), le CNRS, la DGA, la NSF, le ministère des affaires étrangères et les Universités Paris 13 et Paris 6. Ont participé 59 étudiants en thèse ou post-doctorants, 6 enseignants théoriciens, 13 intervenants expérimentateurs pour un séminaire, tous de très haut niveau. Je me suis occupée de l'édition des articles des expérimentateurs, Ludovic Pricoupenko se chargeant de l'édition des cours théoriques. Les actes sont publiés chez EDP-Sciences, Journal de Physique IV **116** (2004).

Chapitres d'ouvrages

1. H. Perrin, *Ultracold atoms and Bose-Einstein condensation*, à paraître dans *Quantum Metrology and Fundamental Constants*, Proceedings de l'école des Houches Quantum Metrology 2007, édité par F. Piquemal, B. Jeckelmann et V. Cappronnier, EPJ - Special Topics (2008).
2. Y. Colombe, B. Mercier, H. Perrin et V. Lorent, *Loading a dressed Zeeman trap with cold atoms*, Euroschool on Quantum Gases in Low Dimensions, *in Quantum gases in low dimensions*, Proceedings de l'école des Houches QGLD 2003, édité par L. Pricoupenko, H. Perrin et M. Ol'shanii, Journal de Physique IV **116**, 247 (2004).
3. M. Arndt, J. Dalibard, P. Desbiolles, P. Lemonde, O. Morice, E. Peik, H. Perrin, J. Reichel, C. Salomon, A.M. Steane, W. Hänsel et P. Szriftgiser, *Atomic cavities and traps*, Proc. of the 5th Symposium on Frequency Standards and Metrology, édité par J. Bergquist, p. 499, Woodshole, USA (1996).

Chapitre 1

Introduction

J'ai commencé ma thèse de doctorat en 1995, l'année où les condensats de Bose-Einstein ont été observés pour la première fois [1, 2]. Dans les années qui ont suivi, les quelques groupes qui maîtrisaient la production des condensats ont étudié leurs propriétés statiques et dynamiques, leur degré de cohérence, ont mis en évidence l'importance des interactions, la superfluidité de ce gaz quantique [3, 4, 5, 6]. Ces premières expériences ont été menées dans des pièges anisotropes, mais le condensat conservait un caractère tridimensionnel. Qu'en est-il de toutes ces propriétés lorsque l'on contraint le gaz en dimension restreinte, à 1D ou 2D ? *Stricto sensu*, la condensation de Bose-Einstein n'apparaît pas en dimension 1 ou 2, dans un système homogène et à la limite thermodynamique. En revanche, V. Bagnato et D. Kleppner ont montré en 1991 [7] que l'on retrouve le phénomène de condensation si les atomes sont confinés dans un piège harmonique — cela modifie en effet la densité d'états. Cependant, on peut s'attendre à ce que la physique soit notablement différente en dimensions restreintes, comme c'est le cas aussi en physique du solide par exemple avec l'effet Hall quantique [8, 9]. En effet, de nouveaux phénomènes physiques sont attendus dans les gaz quantiques en dimensions restreintes [10], comme par exemple la renormalisation des interactions [11, 12, 13].

Dans le régime de Thomas-Fermi où l'énergie d'interaction domine par rapport à l'énergie de point zéro, la taille du condensat dans la direction i est liée au nombre d'atomes et aux fréquences d'oscillations du piège $\omega_{x,y,z}$ par [14]

$$R_i = \frac{1}{\omega_i}\sqrt{\frac{2\mu}{M}} \propto \omega_i^{-4/5}(\omega_j\omega_k)^{1/5}(Ng)^{1/5} \tag{1.1}$$

où M est la masse de l'atome, μ le potentiel chimique, g est le paramètre d'interaction et N le nombre d'atomes condensés. R_i doit donc décroître lorsque le nombre d'atomes diminue. Cependant, cela n'a de sens que si R_i est supérieur à $\ell_i = \sqrt{\hbar/M\omega_i}$, la taille de l'oscillateur harmonique dans la direction i. Si le nombre d'atomes est réduit, ou si le piège est fortement comprimé dans une ou plusieurs directions (i, j...), les degrés de liberté i (et j) sont gelés et la fonction d'onde du condensat est le produit de l'état fondamental selon la direction i (et j) par une fonction d'onde Thomas-Fermi dans la

ou les autres directions, avec un paramètre d'interaction g renormalisé :

$$\text{si } \mu/\hbar \gg \omega_x,\omega_y,\omega_z : \qquad g_{3D} = \frac{4\pi\hbar^2 a}{M} \tag{1.2}$$

$$\text{si } \omega_i \gg \mu/\hbar : \qquad g_{2D} = \frac{g_{3D}}{\sqrt{2\pi}\ell_i} = \frac{2\sqrt{2\pi}\hbar^2 a}{M\ell_i} \tag{1.3}$$

$$\text{si } \omega_i,\omega_j \gg \mu/\hbar : \qquad g_{1D} = \frac{g_{3D}}{2\pi\ell_i\ell_j} = \frac{2\hbar^2 a}{M\ell_i\ell_j}. \tag{1.4}$$

La nouvelle expression de g, qui est valable en première approximation seulement [11, 12], revient à moyenner sur la ou les directions gelées. La toute première observation, en 2001, de l'effet du confinement d'un condensat à 1D ou 2D est la saturation de sa taille, mesurée après temps de vol, à celle de l'oscillateur harmonique, lorsque le nombre d'atomes est réduit [15].

La même année, le groupe de Wolfgang Ertmer à Hannovre a mis en évidence les fluctuations de phase d'un condensat très allongé, qui se traduisent en fluctuations de densité après expansion balistique [16]. La réduction de la longueur de cohérence dans le régime quasi-unidimensionnel a été étudiée en détail dans le groupe d'Orsay [17, 18]. Les corrélations entre particules sont modifiées par la réduction de la dimension [19], et dans la situation extrême où les interactions sont très fortes, on atteint le régime de Tonks-Girardeau [20, 21, 22, 10] pour lequel la fonction d'onde à N corps s'annule lorsque deux particules sont au même endroit, comme s'il s'agissait de fermions. Le régime de Tonks a été mis en évidence récemment dans deux expériences [23, 24].

En dimension 2, le confinement peut modifier la constante d'interaction [11, 13], qui dépend alors de la densité et peut présenter une résonance dans le cas d'interactions attractives en dimension 3 ($a < 0$). De plus, dans un condensat en rotation, un effet analogue à l'effet Hall quantique fractionnaire devrait apparaître [25, 10]. Enfin, en l'absence de rotation, la transition de phase est modifiée et un régime intermédiaire apparaît, où l'on a un superfluide avec des paires de vortex et d'anti-vortex. Le changement de phase est décrit par la transition de Berezinskii-Kosterlitz-Thouless [26, 27, 28, 10]. Il a été observé récemment dans l'équipe de Jean Dalibard [29].

Notre équipe a démarré en 1999 le montage d'une expérience de condensation de Bose-Einstein, avec l'objectif initial d'étudier les gaz de bosons en dimension 2. Pour mieux comprendre les enjeux et les effets attendus, j'ai organisé avec Ludovic Pricoupenko et Maxim Olshanii une école sur le sujet aux Houches en 2003 [10]. Outre les points fondamentaux évoqués plus haut, il est apparu que les expériences faites sur des puces à atomes, qui se sont fortement développées depuis 1999 [30, 31] et qui paraissent le mieux à même de donner aux condensats de Bose-Eintein des applications technologiques, sont sensibles à ces questions de dimensionnalité. Les expériences que nous avons menées au Laboratoire de physique des lasers, bien qu'étant effectuées avec un piège macroscopique, ont développé une proximité importante avec les expériences sur puce et ont eu un impact important et inattendu dans ce domaine.

Ce mémoire relate une série d'expériences faites avec comme leitmotiv la condensation en dimension restreinte. Pour confiner très fortement les atomes dans une direction, nous avons utilisé deux approches différentes. Dans un premier temps, nous avons pro-

jeté d'utiliser deux champs évanescents [32], ce qui permet de réaliser des gradients de champ très importants. Avec cet objectif, nous avons produit un condensat et mis au point une méthode de transfert vers le piège à ondes évanescentes [33]. Nous avons réalisé une série d'expériences impliquant une seule onde évanescente, qui ont montré que la surface du diélectrique présentait une rugosité trop importante pour confiner efficacement les atomes en dimension 2. Cette étude nous a permis en revanche de caractériser très précisément l'interaction entre les atomes et le champ diffusé par les défauts de surface [34]. Dans un second temps, sur la proposition d'Oliver Zobay et Barry Garraway [35], nous avons mis au point une nouvelle approche pour confiner les atomes dans des potentiels très anisotropes [36]. La combinaison d'un champ radiofréquence (RF) et d'un champ magnétique statique résulte en un potentiel adiabatique dont la géométrie peut être largement contrôlée, y compris dynamiquement [37]. Ces potentiels RF permettent de réaliser une « bulle » à atomes, un double puits [38], un anneau [39]... Nous nous sommes intéressés principalement à produire un piège quasi bidimensionnel dans l'épaisseur de la bulle. Ces pièges sont compatibles avec les condensats de Bose-Einstein, et les atomes peuvent être refroidis par évaporation *in situ* [40]. A la suite de nos travaux, de nombreuses équipes ont utilisé cette technique avec succès, notamment dans des expériences sur puce [38, 41, 42, 43].

Cette habilitation est le résultat d'un travail d'équipe. Au démarrage de l'expérience en 1999, l'équipe était composée de Vincent Lorent, Brigitte Mercier et moi-même. Yves Colombe nous a rejoint presque aussitôt pour une thèse de 2000 à 2004. Les autres étudiants en thèse ayant contribué aux expériences présentées ici sont Olivier Morizot et Elena Knyazchyan — de fin 2003 à 2006 — et Raghavan Kollengode Easwaran — de 2006 à 2008. Demascoth Kadio, ATER pendant l'année universitaire 2002–2003, a contribué aux simulations du chargement du piège à ondes évanescentes. Carlos Garrido Alzar a travaillé pendant un an et demi avec nous en tant que post-doc, notamment sur le refroidissement par évaporation dans le piège adiabatique. À partir de 2005, Paul-Eric Pottie a remplacé Brigitte Mercier, partie fin 2003 au Laboratoire d'optique appliquée à Palaiseau. Laurent Longchambon a rejoint l'équipe comme maître de conférence en 2006. Enfin, j'ai eu la chance de travailler en collaboration pour les aspects théoriques avec Maxim Olshanii, Carsten Henkel et Barry Garraway.

Dans ce mémoire, je commencerai par présenter brièvement l'expérience de condensation que nous avons construite. Au chapitre 3, je décrirai les expériences et les analyses théoriques relatives aux champs évanescents. Le chapitre 4 est consacré aux potentiels adiabatiques obtenus en habillant les atomes avec un champ RF. Une conclusion générale clôture le mémoire. Les principaux articles relatifs à chaque thème sont regroupés à la fin du chapitre concerné.

Chapitre 2

Présentation de l'expérience

Ce court chapitre donne un aperçu du montage expérimental avec lequel les résultats présentés dans ce mémoire ont été obtenus. On trouvera plus de détails sur le montage dans les thèses d'Yves Colombe [44] et d'Olivier Morizot [45]. L'expérience a démarré pour l'essentiel à mon arrivée au laboratoire en 1999, et nous avons observé le premier condensat en janvier 2001.

Lorsque nous avons débuté la construction du montage en 1999, seules deux autres expériences en région parisienne, à Paris et à Orsay, avaient permis un an auparavant l'observation d'un condensat. Le Laboratoire de physique des lasers possédait une culture récente dans le domaine des atomes froids, mais il s'agissait à présent de construire la première expérience de condensation de Bose-Einstein au laboratoire. Nous nous sommes largement inspirés de ce qui avait été fait dans les autres équipes, et plus particulièrement du montage de l'équipe de Jean Dalibard [46]. Le piège magnétique s'inspire quant à lui du piège mis au point en 1998 à Munich [47]. L'originalité importante de notre montage réside dans la cellule de quartz, décentrée, qui offre la possibilité d'accéder à la face d'entrée d'un prisme diélectrique posé au fond (voir figure 2.1). Ce prisme est au cœur des expériences décrites dans le troisième chapitre de ce mémoire. Dans la suite de ce chapitre, je décrirai les différents éléments constitutifs de l'expérience, en insistant sur les points importants pour la compréhension des chapitres suivants.

Le condensat est obtenu après un refroidissement par évaporation d'une trentaine de secondes dans un piège magnétique statique. Pour concilier la longue durée de vie que cela impose, et donc la très basse pression requise, avec un chargement efficace du piège magnétique, l'expérience comporte deux enceintes de pression différente. Ces enceintes sont reliées par un petit tube de diamètre 6 mm qui permet d'instaurer une différence de pression de deux ordres de grandeur entre la chambre supérieure, dans laquelle est chargé en 1 s environ un piège magnéto-optique à partir d'une vapeur de rubidium, et la cellule en *Vycor* (une sorte de quartz) dans laquelle on réalise le condensat. Cela permet d'atteindre une durée de vie de plusieurs minutes dans la cellule. L'ensemble du dispositif est représenté sur la figure 2.1 empruntée à la thèse d'Yves Colombe [44].

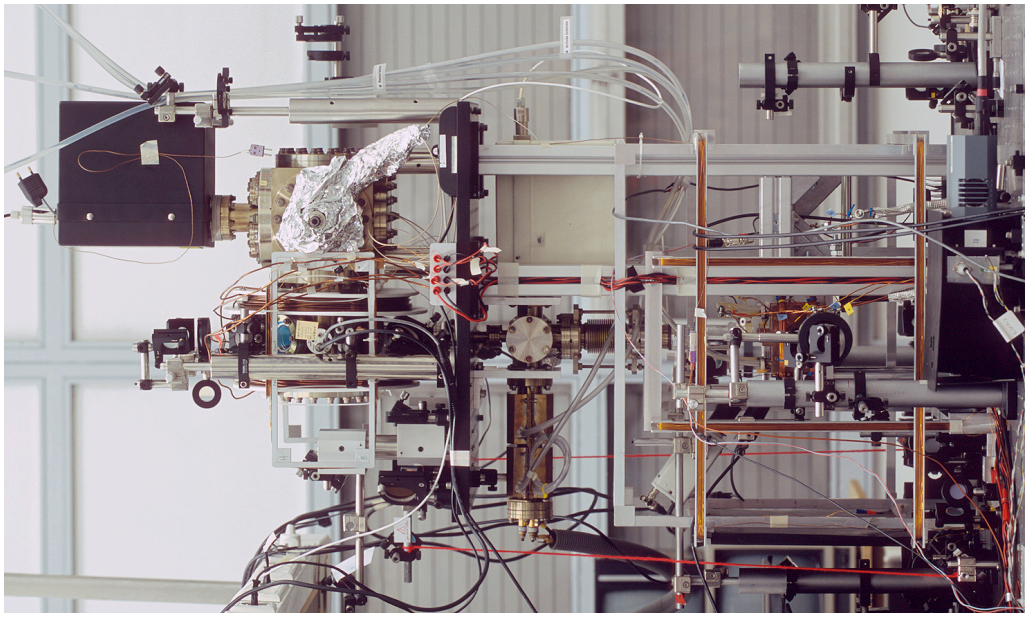

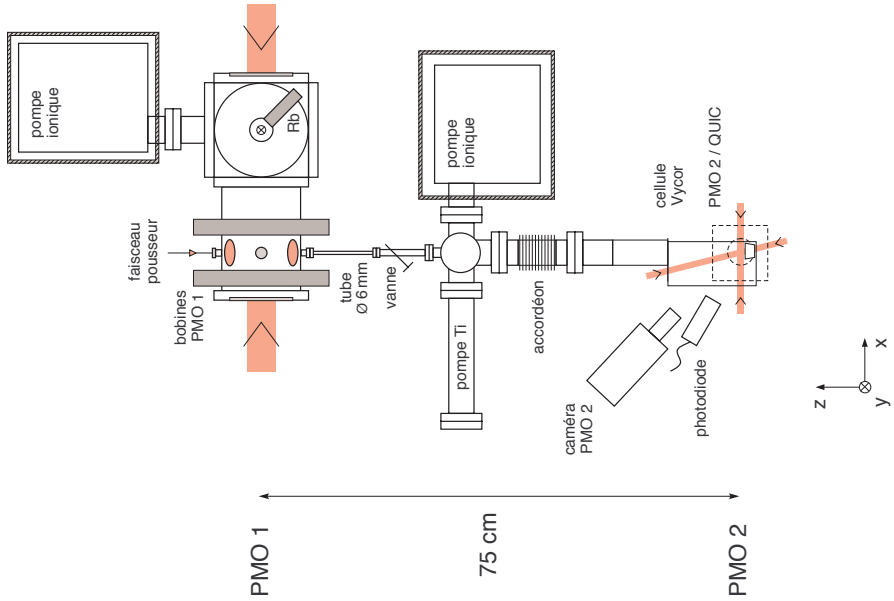

Figure 2.1 — Dispositif expérimental : l'enceinte à ultra-vide. Figure tirée de la thèse d'Yves Colombe [44].

Experimental setup : the vacuum chamber. Figure reprinted from [44].

Le transfert d'une enceinte à l'autre est assuré par un faisceau « pousseur ». Les atomes sont ensuite capturés par un second piège magnéto-optique situé au niveau de la cellule. Ce dispositif s'inspire de celui construit par Pascal Szriftgiser au cours de sa thèse [46, 48]. Le faisceau pousseur a été utilisé successivement à faible intensité en mode pulsé à résonance, en mode continu à quelques Γ vers le rouge de la résonance, puis à plus forte intensité en mode continu loin de résonance. C'est cette configuration qui a donné les meilleurs résultats en termes d'efficacité de transfert et surtout de stabilité du montage. En effet, les atomes sont à la fois poussés par la pression de radiation, qui reste importante pour un désaccord de -1 GHz environ, et guidés par la force dipolaire du moins au début du trajet, partie la plus critique où ils doivent passer dans le tube différentiel. Nous utilisons pour cela un laser à diode dédié, d'une cinquantaine de mW, dont la fréquence est contrôlée à l'aide d'un battement avec le laser refroidisseur du piège magnéto-optique. L'équipe de Daniel Comparat et de Pierre Pillet, au laboratoire Aimé Cotton, a fait un choix analogue et nous avons étudié l'efficacité de transfert d'un piège magnétique à l'autre en collaboration avec eux [49].

Après une phase de mélasse et un pompage optique vers le niveau $F = 2, m_F = 2$, les atomes sont transférés dans un piège magnétique conservatif obtenu à l'aide de trois bobines parcourues par un courant de 45 A environ. Ce piège est du même type que celui réalisé par Tilman Esslinger et ses collègues à Munich, le QUIC pour « QUadrupole-Ioffe Configuration trap » [47]. Il a l'avantage d'être très compact et de dissiper peu de puissance électrique. Les bobines quadrupolaires produisent un gradient de 300 G/cm selon leur axe[1] y et 150 G/cm selon les axes x et z, et la petite bobine Ioffe crée une courbure de 275 G/cm^2 selon son axe x. Le champ magnétique statique obtenu est dirigé essentiellement selon l'axe x lorsque les atomes sont refroidis au fond du piège. Le refroidissement jusqu'au seuil de condensation est réalisé à l'aide d'une antenne radiofréquence d'axe vertical (z) située sous la cellule. Comme la géométrie du champ magnétique statique a une grande importance pour les expériences faites avec les champs RF, je donne dans la figure 2.2 l'allure des équipotentielles et de la direction du champ. Pour les expériences faites dans le piège quadrupolaire seul, la petite bobine Ioffe est éteinte. À la fin de chaque expérience, on prend une image en enregistrant le profil d'absorption par le nuage d'une sonde résonnante, obtenue sur une caméra Andor DV437 à CCD E2V 57-10.

Pour les expériences présentées dans ce mémoire, nous n'avons utilisé que des lasers à diode. Dans la première version de l'expérience, nous avions trois diodes sur réseau, deux lasers maîtres pilotant la fréquence des faisceaux refroidisseurs des deux piège magnéto-optiques, et un laser repompeur. Le laser sonde permettant d'imager les atomes était issu de l'un des maîtres. Dans un second temps, nous avons utilisé une diode DBR de largeur inférieure au MHz comme unique laser maître. Ce laser injecte la diode *Sanyo* du refroidisseur du piège supérieur, de laquelle dérivent tous les faisceaux nécessaires, et qui injecte une seconde diode *Sanyo* pour le second piège. Ces diodes sont suffisamment étroites pour être utilisées sans injection pour réaliser un piège magnéto-optique [50], et le repompeur est d'ailleurs obtenu directement à partir

1. Les axes x, y et z sont indiqués sur la figure 2.1. Je garderai ces notations tout au long de ce mémoire.

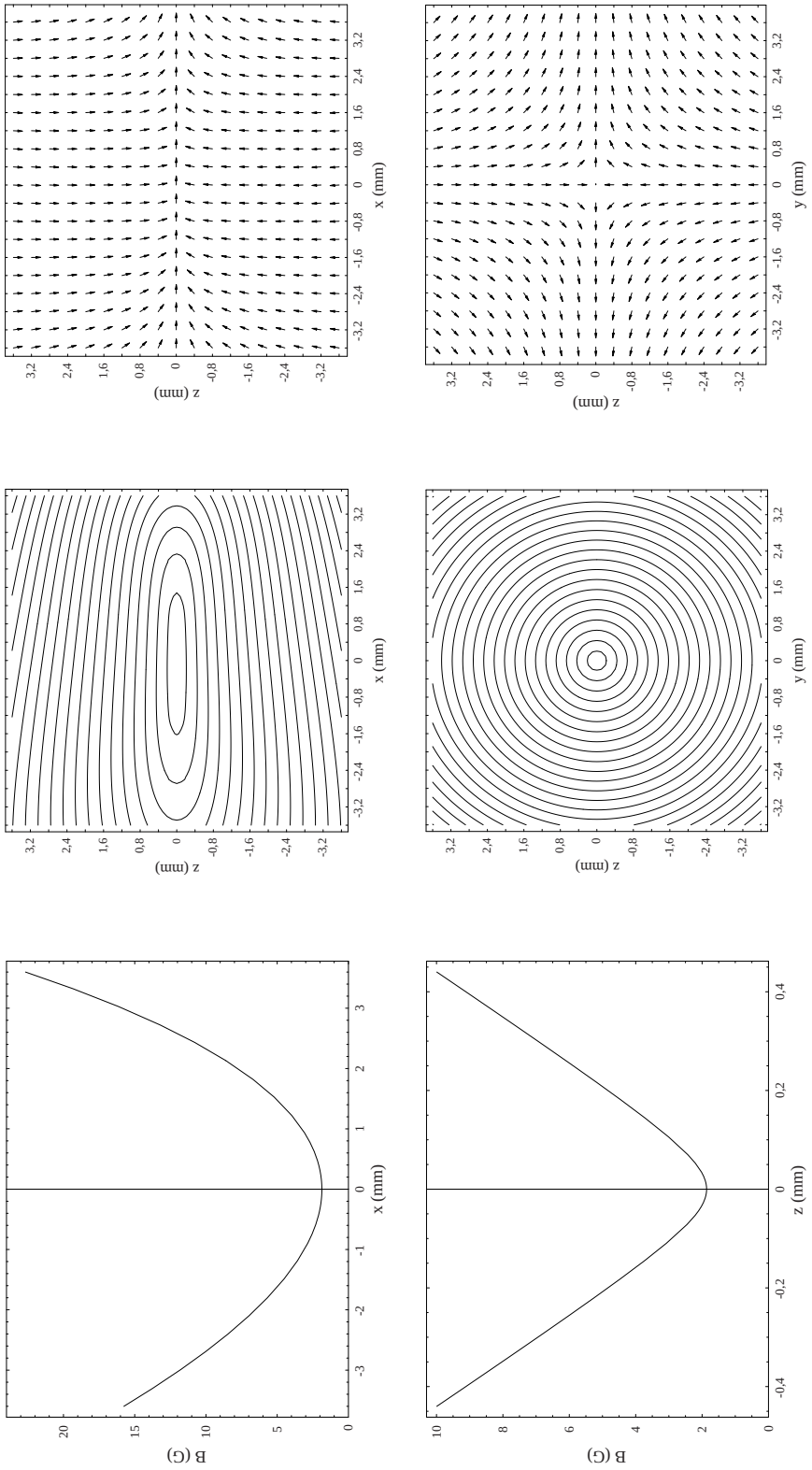

Figure 2.2 — Champ magnétique du piège QUIC (calcul). À gauche : champ selon les axes Ox (en haut) et Oz (en bas). Au centre : lignes iso-B dans les plans Oxz (en haut) et Oyz (en bas), tracées tous les 5 G. À droite : direction du champ magnétique dans ces plans. Le prisme est situé à $z = -3{,}6$ mm et la paroi verticale la plus proche à $x = 3{,}4$ mm, vers la bobine Ioffe. Figure tirée de la thèse d'Yves Colombe [44].

Computed magnetic field in the QUIC trap. Left : field along the Ox (top) and Oz (bottom) axes. The points on the lower curve are measurements taken with a Hall field probe. Center : iso-B lines in the Oxz (top) and Oyz (bottom) vertical planes. Subsequent lines are spaced by 5 G. Right : direction of the B field in these respective planes. The upper surface of the dielectric prism lies at $z = -3.6$ mm and the nearest cell wall is at $x = 3.4$ mm, next to the Ioffe coil. Figure reprinted from [44].

d'une telle diode non injectée. Le faisceau pousseur et le faisceau produisant l'onde évanescente sont chacun issus d'une autre diode *Sanyo*, à 1 ou 2 GHz de la résonance, et la grande stabilité de ces diodes permet de ne pas les asservir . Leur puissance relativement faible (40 à 50 mW typiquement disponibles pour l'expérience) limite cependant le nombre d'atomes que l'on peut capturer dans un piège magnéto-optique.

Outre le laser pousseur très désaccordé, les deux éléments originaux de notre montage sont d'une part le prisme diélectrique, d'autre part les champs radiofréquences supplémentaires.

Le prisme est réalisé dans un verre *Schott* LaSFN15 à haut indice ($n = 1{,}86$). Ses caractéristiques principales sont rappelées au paragraphe 3.3. Il est directement posé au fond de la cellule en quartz, comme le montre la figure 2.3, de sorte que nous l'avons déplacé — sous vide — pour les expériences pour lesquelles il n'était pas nécessaire. En effet, le nombre d'atomes dans le condensat est légèrement inférieur en présence du prisme, qui rend plus délicat l'équilibre des faisceaux du piège magnéto-optique qui le traversent.

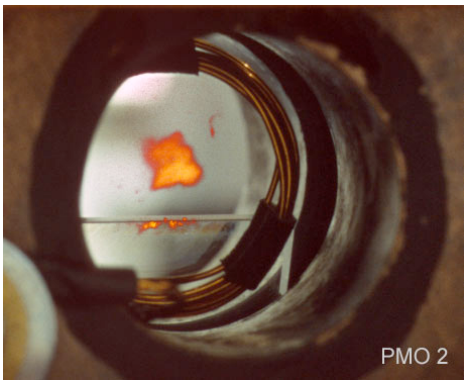

Figure 2.3 — Vue du second piège magnéto-optique. En dessous, on distingue clairement le prisme posé au fond de la cellule en quartz. L'antenne RF pour les potentiels adiabatiques est également visible. Les bobines au-dessus et en dessous permettent le déplacement vertical du condensat.

View of the second MOT. The prism is visible below the atomic cloud, and lies on the bottom of the Vycor cell. Also visible is the RF antenna used in the adiabatic potential experiments. The BEC can be displaced using the two coils above and below the MOT.

L'altitude du prisme par rapport au piège magnéto-optique peut être ajustée à l'aide d'un soufflet réglable connecté à la cellule, voir la figure 2.1. Une paire de bobines d'axe vertical permet également de déplacer le condensat de quelques millimètres, jusqu'à la surface du prisme. Cette surface est traitée avec des couches diélectriques déposées sur le substrat qui permettent d'amplifier le champ évanescent [51, 52, 53, 54]. Le champ est ainsi supporté par un guide d'onde en TiO_2 d'indice $n = 2{,}3$ déposé sur un *gap* d'indice faible en SiO_2. En raison de ce guide, l'angle d'incidence à l'interface entre le prisme et le *gap* est imposé et l'amplitude du champ évanescent présente un caractère résonnant.

Pour les expériences sur les potentiels adiabatiques, nous avons utilisé plusieurs antennes RF et plusieurs synthétiseurs. J'ai déjà mentionné l'antenne qui permet de refroidir les atomes jusqu'à la condensation, d'axe z. Elle est rectangulaire, ajustée pour se glisser entre les bobines quadrupolaires, et est constituée de huit tours de fil de cuivre. Le champ est créé par un synthétiseur Stanford DS-345. Au démarrage de l'expérience, nous utilisions en aval un amplificateur de puissance 5 W. Cependant, nous avons eu besoin de cet amplificateur pour les expériences sur les potentiels adiabatiques, et nous avons constaté que le refroidissement RF fonctionnait très bien sans amplificateur, avec une amplitude affichée au synthétiseur comprise entre 8 et 10 V pic-pic.

Les expériences avec la RF ont pour l'essentiel été réalisées avec une seule antenne supplémentaire, d'axe y, placée juste devant l'une des bobines quadrupolaires, à 2 cm environ du nuage atomique. L'antenne fait 3 cm de diamètre et comporte 8 spires de fil de cuivre, on peut la voir sur la figure 2.3. La chaîne RF est composée d'un synthétiseur, un atténuateur piloté en tension, un commutateur, un amplificateur et l'antenne. Selon les expériences, nous avons utilisé soit un amplificateur 5 W, soit un amplificateur 10 W. Les amplificateurs sont de classe A pour supporter les ondes retour, inévitables lorsque l'on doit faire varier la fréquence entre 0,8 et 11 MHz comme c'est le cas ici. Pour des expériences de spectroscopie menées récemment au laboratoire, nous avons utilisé une seconde antenne RF identique à la première, et placée en face, toujours selon l'axe y. Celle-ci n'était pas connectée à un amplificateur, mais directement, via un commutateur, à un synthétiseur Stanford DS-345 analogue à celui employé pour le refroidissement dans le piège QUIC.

Nous avons testé différents synthétiseurs comme source RF pour la réalisation de potentiels adiabatiques. Leurs performances sont diverses pour cet usage, et discutées au paragraphe 4.3. J'en donnerai simplement ici la liste :

Dans son ensemble, le montage s'est avéré efficace pour produire des condensats de Bose-Einstein. Le chargement prend de 10 à 30 s et le refroidissement par évaporation 25 à 40 s, si bien que la durée d'un cycle reste de l'ordre de la minute, ce qui est raisonnable pour une expérience « macroscopique ». La qualité du vide, excellente au début avec jusqu'à trois minutes de durée de vie dans le piège QUIC, s'est détériorée lentement pour atteindre plutôt 60 s de durée de vie en 2008. La limitation majeure du montage est son accès optique réduit par les blocs de cuivre enserrant les bobines (figure 2.3), qui n'a pas permis par exemple d'imager le nuage diffusé selon toutes les directions intéressantes, voir paragraphe 3.3, ou de faire passer une onde stationnaire pour réaliser un anneau à atomes (cf. paragraphe 4.6). Notre équipe a démarré cette année la construction d'un nouveau montage qui devrait remédier à ces limitations.

Article en relation avec ce chapitre

Je reproduis ici l'article [49] sur le faisceau « pousseur ».

Synthétiseur	Plage	$N_{\max}$	Commentaire
Stanford DS-345	DC – 30 MHz	1500	Revient toujours à la fréquence initiale après une rampe.
Rohde & Schwarz SML-01	9 kHz – 1,1 GHz	analogique	Modulation externe (VCO) possible sur une faible plage (2,6 MHz max), mais pas de balayage.
Agilent 33250A	DC – 80 MHz	VCO	Souple d'utilisation, avec une commande externe de la fréquence par une tension, mais bruité [36, 55].
Tabor WW1071 ou 1072	DC – 50 MHz	20 000	Une ou deux sorties face avant avec un déphasage variable, une sortie sinus face arrière.
DDS « maison »	DC – 10 MHz	260 000	DDS réalisé à l'atelier d'électronique [56]. Plusieurs plages mémoires distinctes avec des vitesses de rampe différentes.

Tableau 2.1 — Les différents synthétiseurs utilisés dans l'expérience. $N_{\max}$ indique le nombre maximal de points de fréquences pour un balayage arbitraire de la fréquence de la porteuse.

List of the synthesizers used in the experiments. $N_{\max}$ labels the maximum number of frequency points in an arbitrary frequency sweep.

Eur. Phys. J. D **42**, 299–308 (2007)
DOI: 10.1140/epjd/e2007-00022-0

THE EUROPEAN PHYSICAL JOURNAL D

Continuous transfer and laser guiding between two cold atom traps

E. Dimova[1,a], O. Morizot[2,b], G. Stern[1], C.L. Garrido Alzar[2], A. Fioretti[1], V. Lorent[2], D. Comparat[1], H. Perrin[2], and P. Pillet[1]

[1] Laboratoire Aimé Cotton, CNRS, bâtiment 505, Université Paris-Sud, 91405 Orsay, France
[2] Laboratoire de physique des lasers, CNRS-Université Paris 13, 99 av. Jean-Baptiste Clément, 93430 Villetaneuse, France

Received 27 September 2006 / Received in final form 8 December 2006
Published online 2nd February 2007 –

Abstract. We have demonstrated and modeled a simple and efficient method to transfer atoms from a first Magneto-Optical Trap (MOT) to a second one. Two independent setups, with cesium and rubidium atoms respectively, have shown that a high power and slightly diverging laser beam optimizes the transfer between the two traps when its frequency is red-detuned from the atomic transition. This pushing laser extracts a continuous beam of slow and cold atoms out of the first MOT and also provides a guiding to the second one through the dipolar force. In order to optimize the transfer efficiency, the dependence of the atomic flux on the pushing laser parameters (power, detuning, divergence and waist) is investigated. The atomic flux is found to be proportional to the first MOT loading rate. Experimentally, the transfer efficiency reaches 70%, corresponding to a transfer rate up to 2.7×10^8 atoms/s with a final velocity of 5.5 m/s. We present a simple analysis of the atomic motion inside the pushing–guiding laser, in good agreement with the experimental data.

PACS. 07.77.Gx Atomic and molecular beam sources and detectors – 32.80.Lg Mechanical effects of light on atoms, molecules, and ions – 32.80.Pj Optical cooling of atoms; trapping

1 Introduction

The realization of degenerate quantum gases requires the production of an initial dense and cold trapped atomic sample. The lifetime of the trapped atoms must be long enough to allow for appropriate evaporative cooling ramps, lasting up to several tens of seconds. A standard vapour Magneto-Optical Trap (MOT) setup cannot always satisfy this last condition because of the relatively high background pressure of the atomic vapour in the cell. The use of a dispenser [1] or of a desorption source [2,3] to load the MOT does not usually provide a trap lifetime longer than a few seconds. To obtain the required lifetime, the MOT has to be placed in an ultra-high vacuum chamber and loaded from a cold atom source, in general a slow and cold atomic beam. One of the demonstrated and widely used methods to create a cold atomic beam is the Zeeman slower technique. However, this solution requires an important technical development of different experimental techniques than the one implied in a MOT setup. In this paper, we will then concentrate on the transfer of atoms from a first cold source to a trap situated in a second high vacuum chamber.

There are several ways to transfer atoms from a cold atomic source to the high vacuum chamber. Mechanical devices [4] or magnetic guides [5] are used to implement an efficient transfer of atoms initially in a MOT directly to either magnetic, electrostatic or atom chip traps. Other techniques, based on quasi-resonant light forces, allow a faster transfer to a recapture MOT. Beam velocities low enough to allow the capture in a MOT in an ultra-high vacuum chamber can be obtained by the pyramidal MOT [6,7], the conical mirror funnel [8] or the two-dimensional MOT [9–12]. Even simpler devices exist such as the low velocity intense atomic source (LVIS) [13–15]. Very high flux, up to 3×10^{12} atoms/s, have been reported with a transversely cooled candlestick Zeeman slower type of setup [16]. However, the counterpart of this large flux is a higher atomic velocity, 116 m/s in this last experiment, which is by far too high to load a second MOT. A pulsed multiple loading, starting from a three-dimensional MOT, has been performed in reference [17]. The atoms are pushed by a near resonant laser beam resulting in a high number of atoms 1.5×10^{10} in second MOT, loading rate 2×10^8 atoms/s and allow lower velocity 16 m/s. However, the transfer is based on using an hexapole magnetic field, produced by a current above 60 A, which complicates the experiment. Simpler devices, without magnetic guiding, have achieved similar result by using continuous

[a] e-mail: Emiliya.Dimova@lac.u-psud.fr
[b] e-mail: morizot@lpl.univ-paris13.fr

transfer [18–20]. In these experiments, a thin extraction column is created in the centre of a MOT and, due to a radiation pressure imbalance, a continuous beam of cold atoms is produced. It is possible to couple these simple devices with a distinct dipolar atomic guide [21]. We propose here to use the same laser beam for pushing and guiding the atoms, resulting in an even simpler setup.

This paper reports on a double MOT setup combining the ability of a pushing laser to extract the atoms from a first trap (MOT1) and to guide them to a second trap (MOT2). The idea is to merge the leaking MOT technique [13,18,19] with the red-detuned far off–resonance optical dipole guide technique [22–24]. Two experiments have been simultaneously performed in two different laboratories, with different atoms: ^{133}Cs at Laboratoire Aimé Cotton and ^{87}Rb at Laboratoire de physique des lasers. Our setups are as simple as the one used in the leaking MOT techniques, but provide a higher flux and a lower atomic beam velocity. We can achieve a transfer efficiency up to 70% with a mean atomic velocity 4 to 12 m/s depending on the pushing beam parameters. Our setups are very robust against misalignments of the pushing and guiding laser beam, and small variations of its detuning or power. The only requirement is a sufficiently high laser power (tens of mW) to produce a significant dipolar force to guide the atoms during their flight.

This paper is organized as follows: in Section 2 we give details on the experimental realization of the beam and discuss the role of MOT1 parameters. In Section 3 we describe theoretically the pushing and guiding processes during the atom transfer. Section 4 discusses the experimental parameter dependences of the setup as compared with the theory. Finally we present a comparison with other available techniques.

2 Experimental realization

2.1 Experimental setup

The vacuum system is similar in both experiments, except for a slight difference in the design of the differential vacuum tubes and the MOT2 cells.

For the cesium (resp. rubidium) experiment the setup consists of two cells vertically separated (see Fig. 1). The distance between the two traps is $D = 57$ cm (resp. $D = 72$ cm). A reservoir connected to the upper source cell supplies the atomic vapour. The recapture chamber is a glass cell with $1 \times 1 \times 10$ cm^3 (resp. $1.25 \times 7.5 \times 12$ cm^3) volume. A differential pumping tube located 3 cm (resp. 10 cm) below MOT1 provides a vacuum within the 10^{-11} mbar range in the bottom MOT2 cell while in the MOT1 cell it is in the 10^{-8}–10^{-9} mbar range. For the cesium experiment, the tube is 18 cm long and has a conical shape (3 mm diameter at its top and 6 mm at its bottom part) whereas it is cylindrical, 12 cm long and 6 mm diameter in the rubidium experiment.

In both cases, MOT1 runs in a standard magneto-optical trap configuration with a magnetic field gradient around 15 G/cm along the horizontal axis of the MOT1 coils. All the laser beams have a 2.5 cm diameter (clipped by the mounts of the quarter-wave plates) and are provided by laser diodes. In the rubidium experiment, the laser is divided into 3 retroreflected beams carrying 10 mW laser power. They are 10 MHz red-detuned from the ^{87}Rb $5s(F = 2) \rightarrow 5p_{3/2}(F' = 3)$ transition. In the cesium experiment, two 5 mW radial beams are retroreflected and make an angle $\pm 45°$ with the vertical axis. Each of the two (non reflected) axial beams carries 10 mW laser power. They are 15 MHz red-detuned from the Cs $6s(F = 4) \rightarrow 6p_{3/2}(F' = 5)$ transition. The 5 mW repumping light, with a frequency on resonance respectively with the Cs transition $6s(F = 3) \rightarrow 6p_{3/2}(F' = 4)$ and the ^{87}Rb transition $5s(F = 1) \rightarrow 5p_{3/2}(F' = 2)$, is mixed with all the trapping beams. In MOT2, the trapping beams are limited to about $2R = 8$ mm in diameter in both experiments due to the cell dimensions and in order to reduce the scattered light.

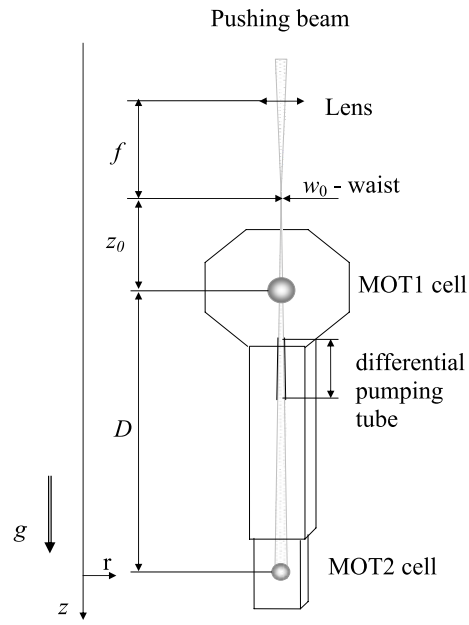

Fig. 1. Scheme of the experimental setups. The parameters used in the discussion (f, D, z_0, w_0) are labeled on the picture. The vertical z-axis is oriented downwards.

In addition to these trapping lasers, the linearly polarized pushing–guiding beam, red-detuned from the MOT ($F \longrightarrow F + 1$) transition ($F = 4$ for Cs, $F = 2$ for ^{87}Rb) with maximum power of $P_0 = 63$ mW for Cs (resp. $P_0 = 21$ mW for Rb), is aligned vertically into the trap. The parameters used in both experiments are summarized in Table 1. In contrast with the similar setups reported in [18,19], the pushing lasers are not frequency-locked in our experiments. The detuning is chosen to optimize the transfer efficiency and is found to be such that the number of atoms in MOT1 is roughly reduced by a factor ten when the "pushing–guiding beam" is present. The beam is focused at position $z_0 = -34$ cm (resp. $z_0 = -13$ cm) before MOT1 by a lens $f = 2$ m (resp. $f = 1$ m). It is not perfectly Gaussian, however the waist at position z is still given by $w(z) = w_0\sqrt{1 + (z - z_0)^2/z_R^2}$,

Table 1. Pushing beam parameters used in cesium and rubidium experiments (see text and Fig. 1). All distances are given in mm, the laser power P is in mW. w_0, w_1 and w_2 are the pushing beam radius at $1/e^2$ at focus, MOT1 and MOT2 positions, respectively.

exp.	D	f	$\|z_0\|$	w_0	w_1	w_2	z_R	P
Cs	570	2000	340	0.2	0.65	1.7	110	< 63
Rb	720	1000	130	0.3	0.33	1.0	260	< 21

where $w_0 = 200$ μm (resp. 300 μm) is the measured minimum waist and $z_R = 110$ mm is the estimated Rayleigh length (resp. $z_R = 260$ mm, measured value for Rb). It diverges to a $1/e^2$-radius of $w_1 = 0.65$ mm (resp. 0.33 mm) in MOT1 and about 1.7 mm (resp. 1.0 mm) in MOT2. The larger size of the beam at the position of MOT2 limits the perturbation of the trapping and cooling mechanisms.

2.2 Flux from MOT1

Experimentally, the main features of the atomic beam are deduced from the loading characteristics of MOT1 and MOT2, where the number of atoms is determined using a calibrated photodiode monitoring the scattered MOT light. The main goal is to have the highest possible recapture rate of atoms in the MOT2 region. This ingoing flux is obviously related to the characteristics of MOT1.

The extraction process can be summarized as follows [18,19]. In MOT1 hot atoms are first decelerated by the MOT radiation pressure, then slowly moved to the centre of the trap where they are extracted by the pushing laser. In addition to its pushing effect, the laser beam shifts the atomic levels by a few natural linewidths so that a transverse cooling of the atomic beam takes place during extraction, limiting the initial atomic temperature to about 25 μK for Cs (40 μK for Rb). Moreover, the trapping forces are reduced and the pushing beam becomes dominant. Hence, atoms are extracted from the trap and accelerated in the direction of MOT2. After the transfer to the second chamber, the atoms are finally recaptured in MOT2 by radiation pressure.

In a first set of experiments, we study the flux of atoms extracted from the upper chamber. This outgoing flux depends on the number of captured atoms in MOT1, which is related to the background pressure of the alkali vapour. As there is no direct access to the background pressure value, we have measured the loading time of MOT1, which, in a large regime of operating parameters, is inversely proportional to the atomic pressure in the source cell. The number of atoms in a MOT in the stationary regime is [25]

$$N = \frac{L}{\gamma + \gamma_p + \beta n}, \tag{1}$$

where L represents the loading rate of the MOT, γ is the loss rate due to background collisions, γ_p gives the loss rate induced by the pushing laser, β is the rate of the cold two-body collisions between the trapped atoms, and n is the average atomic density in the MOT. The density in MOT1 is limited to about 10^{10} atoms/cm^3, so that the term βn is negligible in both setups.

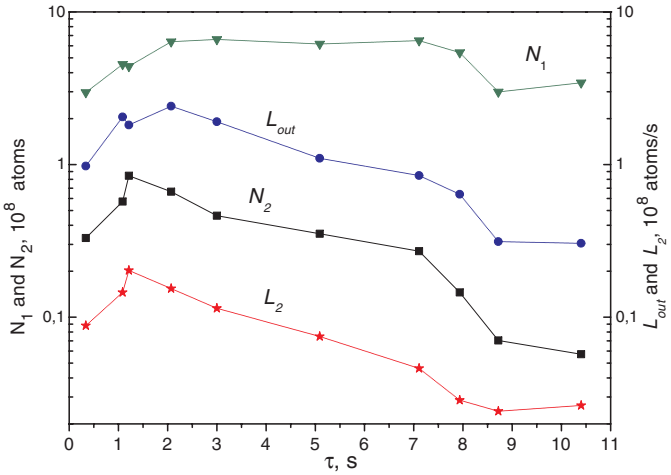

Fig. 2. (Color online) Dependence of the MOT2 parameters on the MOT1 loading time τ in the Cs experiment. N_1 is the number of atoms in MOT1 without pushing beam, $L_{\rm out}$ is the atomic flux, L_2 the loading rate of MOT2 and N_2 the number of recaptured atoms in MOT2.

Loading rates in both MOTs are given by the measured initial slope of the number of trapped atoms in the MOT versus time. In MOT2, this measure is performed after suddenly switching on the pushing laser and waiting for the arrival of the first atoms. In MOT1, the loss rate γ is inferred by measuring the $1/e$-loading time τ ($\gamma = 1/\tau$ in a wide range of vapour pressure [25]) or by dividing the loading rate L_1 by the number of atoms N_1 measured when the pushing beam is off. When the pushing laser is switched on, the loss processes in MOT1 increase drastically. If N_1^p is the number of atoms in MOT1 in the presence of the pushing beam, then $L_{\rm out} = \gamma_p N_1^p$ is the flux of atoms leaking out of MOT1 through the optical guide. We deduce it from parameters we already measured via the formula:

$$L_{\rm out} = L_1 - \gamma N_1^p. \tag{2}$$

To get the data plotted in Figure 2, τ is tuned by varying the background pressure. Whatever the background pressure, the number N_1 of atoms is approximately constant. At high background pressure (i.e. low values of τ), the outgoing atomic flux $L_{\rm out}$ increases with the loading time τ because the number of atoms without pushing beam N_1 slightly does. Then at relatively low pressure $L_{\rm out}$ decreases, following the behaviour of the MOT1 loading rate L_1 (inversely proportional to τ). The loading rate of MOT2 L_2 and the number of atoms N_2 in MOT2 are presented as a function of τ in Figure 2. Their dependence with the MOT1 loading time is similar to that of the atomic flux $L_{\rm out}$. The overall efficiency of the transfer process is defined by the incoming flux in MOT2 divided by the outgoing flux from MOT1, that is $L_2/L_{\rm out}$.

We conclude that for higher MOT2 loading rate we need a relatively high background pressure in MOT1 and a large laser power in the trapping beams (to have higher N_1 value). For our experimental conditions the optimum

is at a MOT1 loading time of about 1−2 s. The data presented here were not taken with optimized pushing–guiding beam parameters, the efficiency being here limited to typically 10%. Once these parameters are well set we are able to achieve maximum transfer efficiency of about 70% for Cs (resp. 50% for ^{87}Rb), without affecting the overall dependence of the different quantities on the MOT1 loading time.

3 Pushing and guiding processes

After leaving the MOT1 region, the atomic beam is no longer affected by the MOT1 lasers and is guided due to the attractive dipolar force created by the red-detuned pushing–guiding beam. In this section, we describe the guiding process using an analytical model similar to that given in references [22,24]. The total force applied on the atoms is the sum of a radiation pressure "pushing force" $\boldsymbol{F}_{\text{push}}$ and of a dipolar "guiding force" $\boldsymbol{F} = -\boldsymbol{\nabla} U$, where U is the guiding potential. The gravitational force plays a minor role in the loading process.

A two-level model function of the laser parameters (power, detuning and waist) describes qualitatively the experimental dependence of the transfer efficiency between the two MOTs. A more detailed quantitative analysis of the processes is proposed in the rest of this section.

3.1 Two-level model

In this first simple model we neglect gravity, the initial velocity and temperature of the atoms and beam divergence. We consider the atoms as a two-level system with a transition energy $\hbar\omega_0$, a natural linewidth Γ ($\Gamma/2\pi = 5.2$ MHz for Cs, 5.9 MHz for Rb) and a saturation intensity $I_s = \frac{1}{6}\hbar c k^3 \frac{\Gamma}{2\pi}$ (1.1 mW/cm^2 for Cs, 1.6 mW/cm^2 for Rb). We use here z as the vertical coordinate along the laser beam propagation with origin in the centre of MOT1 and r for the radial cylindrical coordinate (see Fig. 1). For this two-level model, the waist w of the pushing–guiding laser is assumed to be constant and equal to its experimental value at MOT1 position $z = 0$. The laser beam has a power P_0, a wave vector $k = 2\pi/\lambda$, and an angular frequency ω detuned by $\delta = \omega - \omega_0$ with respect to the atomic transition.

The on-axis light shift is given by $U_0 = \frac{\hbar\delta}{2}\ln(1+s)$ where $s = (I/I_s)/(1+4\delta^2/\Gamma^2)$ is the saturation parameter and $I = 2P_0/(\pi w^2)$ is the peak laser intensity. As the laser is far detuned, saturation is always very low and one can simply replace $\ln(1+s)$ by s in this expression. In this limit, the guiding potential is

$$U_0\, e^{-\frac{2r^2}{w^2}}. \tag{3}$$

As the waist is considered constant, the guide does not affect the longitudinal motion. On the contrary, it is crucial for confining the transverse motion.

The atoms absorb and emit spontaneously photons at a rate

$$\Gamma' = \frac{\Gamma}{2}\frac{s}{1+s} = \frac{\Gamma}{2}\frac{I/I_s}{1+4\frac{\delta^2}{\Gamma^2}+I/I_s}, \tag{4}$$

which gives a pushing force

$$F_{\text{push}} = \Gamma'\hbar k = \Gamma' M v_{\text{rec}}, \tag{5}$$

where $v_{\text{rec}} = \hbar k/M$ is the recoil velocity and M the atomic mass. The velocity increases due to photon absorption, and the number of scattered photons to reach the position z is approximately $v(z)/v_{\text{rec}} = \sqrt{2\Gamma' z/v_{\text{rec}}}$. The pushing process is also responsible for a heating due to random spontaneous emission in all directions. The mean horizontal kinetic plus potential energy per atom $2k_BT$ in the 2D confining potential is increased by two third of the recoil energy $E_{\text{rec}} = Mv_{\text{rec}}^2/2 = k_BT_{\text{rec}}/2$ at each scattering event [24,26]. This gives rise to a horizontal kinetic temperature

$$T_h(z) = \frac{v(z)}{v_{\text{rec}}}\frac{T_{\text{rec}}}{6}. \tag{6}$$

To have an efficient pushing–guiding beam we require in this simple two–level approach that the atoms remain trapped in two dimensions inside the guide during the whole transfer. This condition is

$$2k_{\text{B}}T_h(z) < |U_0| \text{ for all } z. \tag{7}$$

As the horizontal velocity spread increases with z, this is equivalent to $2k_{\text{B}}T_h(D) < |U_0|$. A second constraint is that the beam velocity at the MOT2 position (v_{beam}) should be lower than the capture velocity (v_{capture}) of the MOT

$$v_{\text{beam}} < v_{\text{capture}}. \tag{8}$$

The value of v_{capture} is on the order of the maximal velocity for an atom to be stopped on the MOT beam diameter distance $2R$, that is $v_{\text{capture}} = \sqrt{\Gamma R v_{\text{rec}}}$ [25]. As a result, we evaluate v_{capture} to be about 21 m/s for cesium and 30 m/s for rubidium.

The efficiency of the pushing–guiding process is determined by how deep the conditions (7) and (8) are verified. To describe qualitatively the guiding efficiency in relation with these conditions, we propose to describe each condition by a function f, equal to zero when the inequality is strongly violated and to 1 when it is fully verified, with a continuous transition between these two extremes. The guiding efficiency is then described by the product $f(\frac{2k_BT_h(D)}{|U_0|}) \times f(\frac{v_{\text{beam}}}{v_{\text{capture}}})$ of the two conditional functions. The result is given for Cs in Figure 3 as function of the laser detuning, with $v_{\text{capture}} = 21$ m/s and the function f chosen arbitrarily to be $f(x) = \frac{1}{1+x^{10}}$.

A comparison of the two-level model with experimental results (see Fig. 7, left) presents a good qualitative agreement, reproducing the presence of an optimal red detuning at given laser power. The maximum transfer efficiency increases with the power of the pushing beam while the position of the peak is shifted to larger absolute values of the detuning. This simple model is sufficient to

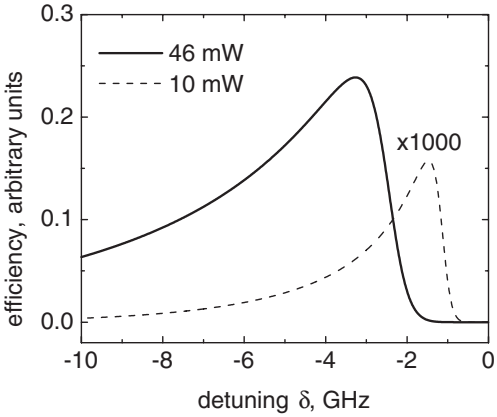

Fig. 3. Efficiency (see text) of the pushing–guiding processes versus laser detuning δ for a $650\,\mu$m waist laser beam with different laser power 10 mW (dashed line $\times 1000$) and 46 mW (solid line). The other parameters are: initial temperature $T_0 = 25\,\mu$K, $I_{\rm sat} = 1.1\,{\rm mW/cm^2}$, $\Gamma = 2\pi \times 5.2\,$MHz, $v_{\rm rec} = 3.5\,$mm/s, $T_{\rm rec} = 0.2\,\mu$K and the two MOT cells are separated by 57 cm (the values used are those of the Cs experiment).

derive the main conclusion: the transfer is more efficient with a far red-detuned and intense laser beam. However, the theory predicts a peak further from resonance than observed experimentally. Moreover, the sensitivity to the laser power is much more pronounced than observed in the experiment. This motivates a more detailed analysis of the processes operating during the travel of the atoms from MOT1 to MOT2. In particular, the effect of optical pumping to the lower hyperfine state has to be considered.

3.2 Optical pumping

The absorbed photons can lead to optical pumping between the two hyperfine levels of the ground state which have different laser detuning with respect to the pushing laser. Indeed, very quickly after leaving the MOT1 region, the atoms are pumped essentially in the lower ground state $F = 3$ for cesium (resp. $F = 1$ for rubidium) as there is no repumping laser light superimposed with the pushing laser beam. This optical pumping is essential for a good transfer efficiency, as it greatly reduces the final velocity of the atomic beam (see Sects. 3.6 and 4.2). However, a small population in the other ground state is still present, typically 1 to 3 percent for a linearly polarized beam, as we shall see [27]. As the radiation pressure is much larger for atoms in the upper ground state (about 100 times larger for detuning values discussed here), even this small fraction plays a role and both ground state populations have to be taken into account for the estimation of the pushing force. On the contrary, the dipolar force may be estimated by assuming that the atoms are only in the lower ground state, as this force is only about 10 times smaller than in the upper ground state, which is 100 times less populated.

An estimate of the populations in the ground states is obtained by assuming an equal detuning for the transitions from the upper hyperfine ground state to all the hyperfine excited states. We define an "effective" detuning $\bar{\delta} \approx \delta + \Delta'_{\rm HFS}/2$, where $\Delta'_{\rm HFS}$ is the total width of the hyperfine structure in the excited state ($\Delta'_{\rm HFS} \simeq 600$ MHz for Cs and $\Delta'_{\rm HFS} \simeq 500$ MHz for ^{87}Rb respectively). Using this mean detuning $\bar{\delta}$ we calculate the pumping rates between the two hyperfine ground states. This is fairly good for large detunings (above 1 GHz from the cycling transition). To illustrate our results we will choose the following typical values: $\delta/2\pi = -2$ GHz from the ($F = 4 \rightarrow F' = 5$) transition of the Cs (i.e. $\bar{\delta}/2\pi = -1.70$ GHz) and $\delta/2\pi = -1$ GHz (i.e. $\bar{\delta}/2\pi = -750$ MHz) from the ($F = 2 \rightarrow F' = 3$) transition of the ^{87}Rb. We also define $\Delta_{\rm HFS}$ as the hyperfine structure interval in the ground state ($2\pi \times 9.2$ GHz for Cs, $2\pi \times 6.8$ GHz for ^{87}Rb) (see [28]).

The ratio of populations in the upper hyperfine ground state N_{F+1} and in the lower one N_F may then be estimated as:

$$\eta = \frac{N_{F+1}}{N_F + N_{F+1}} \approx \frac{N_{F+1}}{N_F} = \alpha \left(\frac{\bar{\delta}}{\bar{\delta} - \Delta_{\rm HFS}} \right)^2$$

$$\text{with} \quad \alpha = \frac{2F+3}{2F+1} = \begin{cases} 9/7 & \text{for Cs}(F=3) \\ 5/3 & \text{for } ^{87}\text{Rb}(F=1) \end{cases} . \qquad (9)$$

The factor α is simply the ratio between the number of substates in the $F + 1$ and F ground states, to which N_{F+1}/N_F should be equal at a detuning large as compared to the hyperfine structure $\Delta_{\rm HFS}$; the term involving the detuning is related to the ratio of excitation rates from the two hyperfine ground states. The formula leads to $\eta = 3.2\%$ of the atoms in the Cs($6s, F = 4$) state and $\eta = 1.6\%$ in the Rb($5s, F = 2$). This value is in excellent agreement with a full calculation taking into account all the different detunings with the hyperfine excited states.

3.3 Pushing force

Another factor should be considered: the laser mode shape. Indeed, a relatively strong divergence is needed in order to both efficiently push and guide atoms in the MOT1 region and not affect the MOT2 operation. The guiding beam waist varies with position, according to

$$w(z) = w_0 \sqrt{1 + (z - z_0)^2/z_R^2}. \qquad (10)$$

The depth U_0 is then modified along the atomic trajectory due to the change in the laser intensity and, taking into account the results of the previous section, the pushing force in the centre of the beam may be estimated as follows:

$$F_{\rm push}(z) = \frac{\Gamma}{2}\hbar k \bar{s}(z) \left((1-\eta) + \eta \left(\frac{\bar{\delta} - \Delta_{\rm HFS}}{\bar{\delta}} \right)^2 \right)$$
$$\simeq \frac{\Gamma}{2}\hbar k \bar{s}(z)(1+\alpha), \qquad (11)$$

where $\bar{s}(z)$ is the saturation parameter calculated for the lower ground state, at detuning $\bar{\delta} - \Delta_{\mathrm{HFS}}$. We take into account the linear polarization of the pushing beam by multiplying $\bar{s}$ by a factor 2/3 in all calculations. We neglect however the small change in $\bar{\delta}$ due to the light shift, which is even reduced when the waist $w(z)$ becomes larger.

The mean pushing force is reduced due to the Gaussian transverse profile of the pushing beam and the finite size of the atomic cloud. This may be taken into account approximately by dividing the force by a factor 2 [24]. Note that this underestimates the initial pushing force, when the atoms are still well guided (rms radius less than $w(z)/2$), and overestimates it when the cloud size becomes larger than half the waist. As the mean pushing force now depends only on z, it may be written as the derivative of a "pushing potential" U_{push}:

$$U_{\mathrm{push}}(z) = \frac{\Gamma}{2}\hbar k s_0 z_R (1+\alpha) \arctan \frac{z - z_0}{z_R} \tag{12}$$

where $s_0 = \bar{s}(z_0)$. The velocity at each point is then easily calculated by energy conservation (z-axis is oriented downwards):

$$v(z) = \left[v_0^2 + 2gz + \Gamma v_{\mathrm{rec}} s_0 z_R (1+\alpha) \times \left(\arctan \frac{z - z_0}{z_R} + \arctan \frac{z_0}{z_R} \right) \right]^{1/2}, \tag{13}$$

where v_0 is the input velocity in the guide. The effect of gravity is not dominant, but was taken into account by the $2gz$ term. v_0 can be estimated as the output velocity of the MOT1 region. We have calculated it using formula (13) assuming that the atoms in the MOT1 region have a zero initial velocity and are in the upper hyperfine ground state due to the presence of the repumping light ($\eta = 1$). For instance, using a travel distance z roughly equals to the MOT1 region radius (10 mm) and a laser power of 21 mW, we find that atoms enter the guide with a velocity $v_0 \approx 9$ m/s for Rb; for the Cs parameters, we obtain in the same way $v_0 \approx 3.1$ m/s. From equation (13), we also infer the traveling time as $\Delta t = \int_0^D dz/v(z)$.

3.4 Guiding condition

As previously discussed, the light shift of the lower ground state is dominant in our case. The atoms leaving MOT1 are thus guided by the on-axis light shift potential given by

$$U_0(z) = \frac{\hbar(\bar{\delta} - \Delta_{\mathrm{HFS}})}{2}\, \bar{s}(z). \tag{14}$$

Equation (7) is still the strongest constraint for the choice of the parameters and becomes more and more difficult to fulfil as z increases, because $|U_0|$ is reduced due to the beam divergence. The horizontal kinetic temperature $T_h(z)$ is evolving due to two opposite effects: photon scattering [29] is responsible for an increase of T_h while adiabatic cooling tends to lower it as the waist increases. The adiabaticity condition $|d\omega_p/dt| \ll \omega_p^2$, where ω_p is the transverse oscillation frequency of the guide, is well fulfilled in both experiments except when the atoms move in the non harmonic part of the potential. This breakdown of the adiabaticity occurs only when the atoms are close to leave the guide. This only marginally affects the guiding condition and will not be taken into account here. ω_p varies with the inverse squared waist, and one has $\omega_p(z) = \omega_p(0) w^2(0)/w^2(z) = \omega_p(0) \frac{z_0^2 + z_R^2}{(z-z_0)^2 + z_R^2}$. To obtain an expression for $T_h(z)$, valid while the atoms remain guided, we write the change in T_h for a small change δz in z. As the phase space density is conserved during this adiabatic cooling, the cooling contribution is proportional to the inverse squared waist. Spontaneous scattering is responsible for a supplementary heating term, proportional to the number of photons scattered during $\delta t = \delta z/v$:

$$T_h(z + \delta z) = T_h(z) \frac{w^2(z)}{w^2(z+\delta z)} + \frac{\Gamma}{2} \bar{s}(z) \frac{T_{\mathrm{rec}}}{6} \frac{\delta z}{v(z)}. \tag{15}$$

The temperature increase is $T_{\mathrm{rec}}/6$ for each spontaneous scattering event. $\bar{s}(z)$ is proportional to $1/w(z)^2$, just like the oscillation frequency. Using the dependence in $w(z)$, we obtain the following differential equation for T_h:

$$\frac{dT_h}{dz} = -T_h(z) \frac{2}{w(z)} \frac{dw}{dz} + \frac{T_{\mathrm{rec}}}{6} \frac{w^2(0)}{w^2(z)} \frac{\Gamma}{2} \bar{s}(0) \frac{1}{v(z)}. \tag{16}$$

Using the expression of $w(z)$, the solution of this equation reads:

$$T_h(z) = \frac{z_0^2 + z_R^2}{(z-z_0)^2 + z_R^2} \left[T_0 + \frac{T_{\mathrm{rec}}}{6} \frac{\Gamma}{2} \bar{s}(0) \int_0^z \frac{dz'}{v(z')} \right] \tag{17}$$

where T_0 is the initial temperature at the guide entrance. The integral in the last term is the time necessary for an atom to travel to position z. In the range of parameters explored in our experiments, the sum of these two terms decreases with z, but slower than the trap depth. As can be seen in Figure 4 (left), the mean horizontal energy $2k_B T_h$ becomes larger than the trap depth at some position z_{out} before reaching MOT2. However, as will be discussed below, this partial guiding is sufficient for limiting the size of the atom cloud to below the MOT2 beam diameter.

3.5 Recaptured atoms

For a good transfer efficiency, two main criteria have to be fulfilled. First, the atomic beam should stay roughly collimated on a distance long enough to pass through the differential tube, and then the transverse cloud radius at the end should be comparable to the capture radius of MOT2. This means that even if they leave the guide before reaching MOT2, the atoms can still be recaptured. Second, the final longitudinal velocity of the atomic beam must not exceed the capture velocity of MOT2. As the atomic beam velocity is in any case lower than the capture velocity of MOT2, the recapturing mechanism is mostly

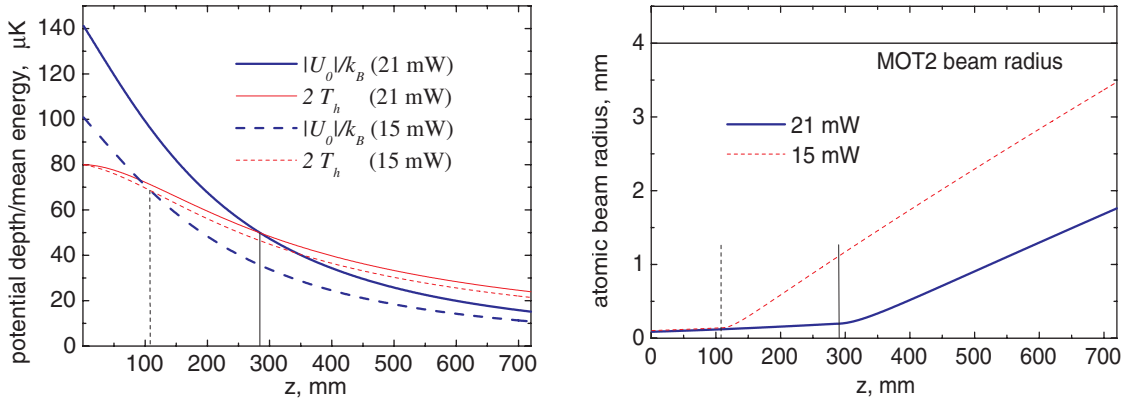

Fig. 4. (Color online) Evolution for the ^{87}Rb experiment of different parameters with the traveling distance z between the two MOTs, at different powers: 15 mW (dashed lines) and 21 mW (solid lines); the initial temperature at the guide entrance was set to $T_0 = 40$ μK. The point z_{out} where the atoms leave the guide is marked by a vertical line. Left: mean horizontal energy $2k_BT_h$ (thin lines, Eq. (17)) and trap depth $|U_0|$ (bold lines, Eq. (14)). Right: rms radius of the guided atomic beam. The radius of the MOT2 beams is marked by a horizontal line.

limited by the matching between the atomic beam size and the size of the capturing region of MOT2.

The capture size of MOT2 is limited by the radius $R = 4$ mm of the collimated trapping laser beams. According to the former considerations about heating of the guided atoms (see Sect. 3.4), the mean horizontal energy of the cloud is lower than the guiding trap depth over a distance $z_{\text{out}} = 38$ cm for a laser power of 63 mW and an initial temperature $T_0 = 25$ μK in the case of Cs (resp. $z_{\text{out}} = 28.5$ cm with $T_0 = 40$ μK and a laser power of 21 mW in the case Rb) (see Fig. 4). For simplicity we consider hereafter that all the atoms remain pushed and guided up to that point and then undergo a free ballistic expansion as they keep falling. Including this assumption in our model, we can evaluate the size of the atomic cloud Δr_f as it reaches MOT2. While the atoms remain trapped, the cloud size is of the order of $\omega_p^{-1}(z)\sqrt{k_BT_h/m}$. The guiding step ends when k_BT_h reaches $|U_0(z)|/2$, such that the rms size at the guide output is $\Delta r_{\text{out}} = \omega_p^{-1}(z)\sqrt{|U_0(z)|/2m} = w(z)/\sqrt{8}$, that is $\Delta r_{\text{out}} = 470$ μm for Cs (resp. $\Delta r_{\text{out}} = 200$ μm for Rb). We assume a fixed temperature for the falling atoms, as the adiabatic cooling is not efficient for a non trapped cloud and the heating rate is also very low after z_{out}. T_h is about 10 μK for Cs and 25 μK Rb. After the remaining falling time of 36 ms (resp. 36 ms for Rb) the atomic beam has a typical standard deviation for the transverse Gaussian atomic density distribution of $\Delta r_f \approx 1$ mm for Cs and $\Delta r_f \approx 1.75$ mm for Rb, smaller than MOT2 radius, meaning that almost all the atoms are recaptured in MOT2 for both experiments. Note that this model allows to predict $\Delta r(z)$ at any position z, as shown in Figure 4, right.

3.6 Transfer efficiency

We come back now to an estimation of the transfer efficiency as discussed in Section 3.1 and presented in Figure 3. Within the frame of the refined model presented now, we are able to compute a transfer efficiency in the same spirit. As we have seen in the previous section, the guiding is not required until the end for the whole cloud to be recaptured. We thus retained the two following conditions: (i) the arrival velocity has to be smaller than v_{capture} and (ii) the cloud size must be less than the MOT2 beam waist. We then calculate the efficiency $f[\Delta r(D)/R] \times f[v(D)/v_{\text{capture}}]$, with the function f previously used in Section 3.1, and plot it in Figure 5. The model predicts a good efficiency in a detuning range between -0.5 GHz and -1.6 GHz, the width of the large efficiency region being reduced with a smaller laser power. These predictions have to be compared with the rubidium experimental data of Figure 7, right. The agreement is qualitatively good, and reproduces the main features. The two limits of the large efficiency region have different

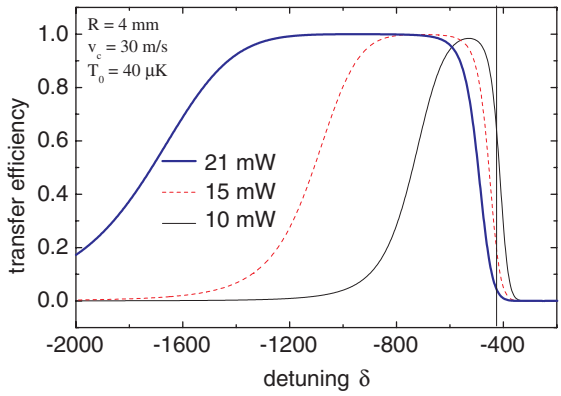

Fig. 5. (Color online) Efficiency (see text) of the pushing–guiding processes versus laser detuning δ, calculated for ^{87}Rb for the parameter of the pushing beam given in text, with different laser power 10 mW (thin solid line, black), 15 mW (dashed line, red) and 21 mW (thick solid line, blue). The maximal capture velocity in MOT2 has been fixed to $v_{\text{capture}} = 30$ m/s, the initial temperature to $T_0 = 40$ μK and the MOT2 beam radius R to 4 mm. The corresponding experimental values are shown in Figure 7, right.

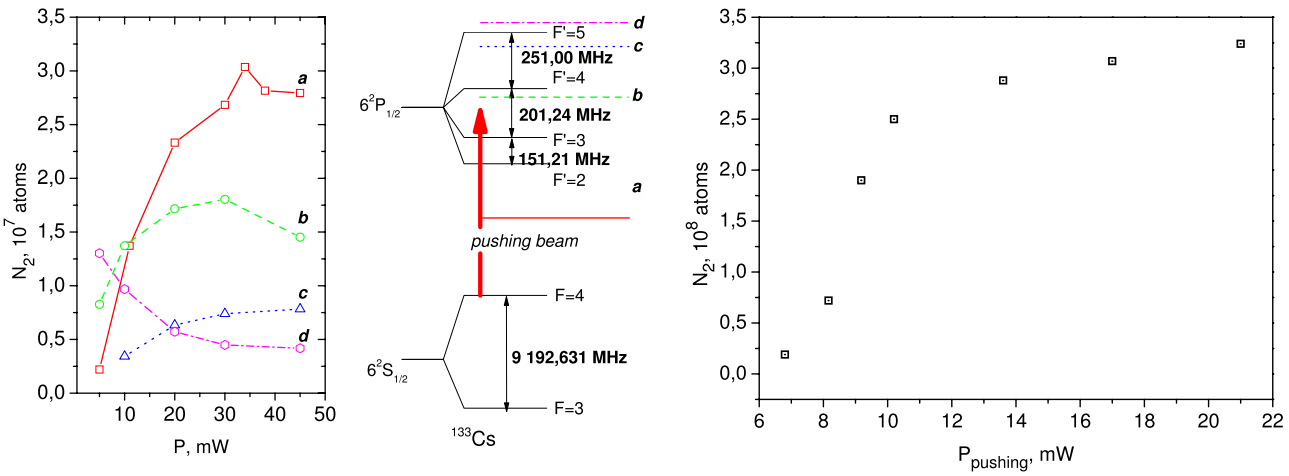

Fig. 6. (Color online) Dependence of the number of recaptured atoms N_2 in MOT2 on the pushing beam power. Left: Cs data. The experiment is done at four different frequencies (see the diagram in the centre). Right: ^{87}Rb data, recorded at -1 GHz detuning from the $5S_{1/2}(F=2) \rightarrow 5P_{3/2}(F^{'}=3)$ transition.

origins: on the large detuning side, the efficiency drops due to an increase in the atomic cloud size, as the guiding potential is weaker. On the lower detuning side, close to resonance, the efficiency becomes limited by the final velocity, which is larger than the capture velocity of MOT2. On this side, theory fails to predict the less measured efficiency at lower laser power, as the mean detuning $\bar{\delta}$ approach (Sect. 3.2) is not valid any more. In particular, the efficiency should drop to zero at the resonance with the rubidium $5S_{1/2}(F=2) \rightarrow 5P_{3/2}(F^{'}=1)$ line, situated at $\delta/2\pi = -424$ MHz and marked with a vertical line in Figure 5.

4 Experimental results

In this section, we present the experimental study of the guiding process and compare it with the above theoretical model. The dependence of the recaptured atom number on the pushing beam parameters are first investigated. We then measure the mean atomic velocity and the traveling time. During the experimental investigation the atom vapour pressure in MOT1 is kept constant.

4.1 Pushing beam parameters

The parameters of the pushing beam that we have experimentally optimized are its divergence, waist, power and detuning.

Divergence and waist

In order to optimize the atomic beam characteristics we have first investigated the role of the laser beam waist, related to the divergence of the pushing beam and to the pushing force. It is clear that the pushing–guiding beam should diverge, to have a significant effect on MOT1 without disturbing MOT2. Moreover, this divergence provides an horizontal adiabatic cooling of the guided atoms. We have used three different lenses ($f = 0.75$ m ; 1 m ; 2 m) to focus the pushing beam. For each lens the transfer efficiency is studied as a function of the focus distance from MOT1. The position of the lens is more critical than its focal length. The optimum is obtained with a lens $f = 2$ m for the Cs experiment (resp. $f = 1$ m for ^{87}Rb) and distance from MOT1 34 cm (resp. ≈ 13 cm), where the beam diameter on the MOT1 region is ≈ 1.3 mm (resp. ≈ 0.6 mm). The measured waist at the focal point is 200 μm (resp. 300 μm). It leads to a divergence w_0/z_R of about 2 mrad (resp. 1 mrad).

In conclusion we found that the best transfer efficiency occurs when the pushing beam, focused before MOT1, has a diameter smaller than 1 mm in MOT1 and a divergence such that the beam diameter at MOT2 position is less than 3 mm. In this sense our results are similar to the one found in references [18,19].

Power and detuning

The recaptured number of atoms into MOT2 at different laser powers of the pushing beam and at different detunings for the two elements Cs and ^{87}Rb is shown resp. on left and right of Figure 6.

It is first obvious that the best experimental conditions are achieved with a laser frequency red-detuned with respect to all atomic transitions (curve (a) in Fig. 6, left). The transfer efficiency is larger for a red-detuned laser frequency than for the other laser frequencies due to the fact that after leaving the MOT1 area the atoms feel the pushing light also as a guide. For such detunings, the atomic flux as well as the number of recaptured atoms N_2 in MOT2 increase when the power of the pushing light increases, and saturates at large power when all the atoms are efficiently guided to MOT2 (see also Fig. 6, right). At a given detuning, an increase of the laser power leads to a decrease of the transfer efficiency, due to an excessive

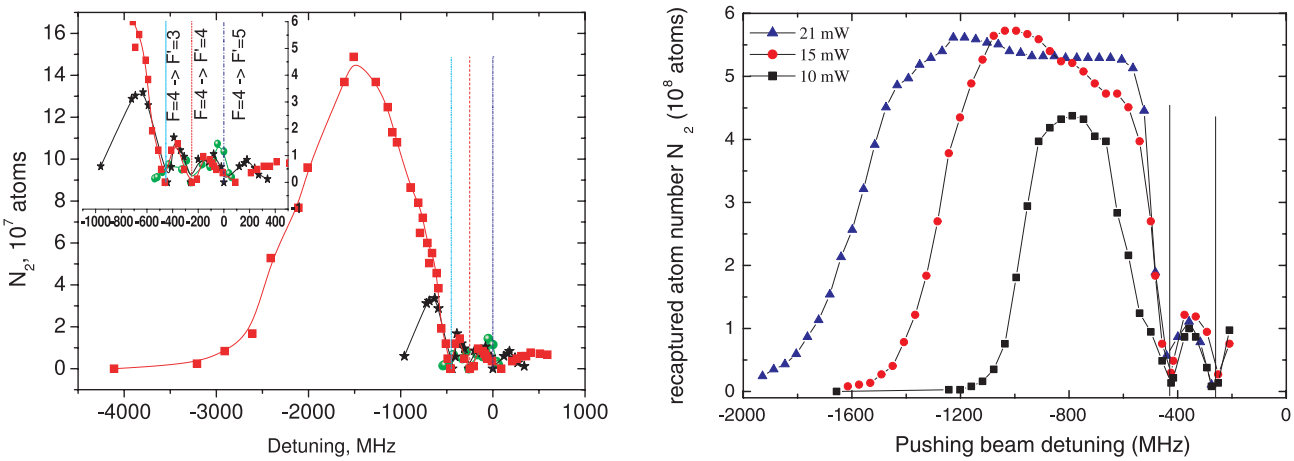

Fig. 7. (Color online) Number of atoms recaptured in MOT2 N_2 vs. pushing beam detuning for different optical powers. The vertical lines indicate the position of hyperfine resonance frequencies. Left: Cs data. The detuning is given with respect to the $6S_{1/2}(F=4) \rightarrow 6P_{3/2}(F'=5)$ transition. The pushing beam power is 46 mW (squares), 10 mW (stars) or 2 mW (circles). Right: ^{87}Rb data. The frequency is measured relatively to the $5S_{1/2}(F=2) \rightarrow 5P_{3/2}(F'=3)$ cycling transition. Pushing beam power: 10 mW (squares), 15 mW (circles), and 21 mW (triangles).

final velocity, a strong perturbation of both MOTs, and a large heating of the atoms.

In order to optimize the conditions for the atomic beam, the influence of the detuning of the pushing light was investigated in more details (see Fig. 7 left and right resp. for Cs and ^{87}Rb). For a frequency close to resonance (corresponding to the best conditions found in Refs. [18,19]) the number of recaptured atoms into MOT2 is much smaller than the one we could achieve with a much more red-detuned light and a higher power. In conclusion we find that the best loading of MOT2 is at highest possible power of the pushing laser beam and, given this power, at the value of red detuning optimizing the flux.

4.2 Atomic beam velocity

For a high recapture efficiency, a relatively slow and collimated atomic beam is required (see Sect. 3.5). After the pushing and guiding process, the atoms reach MOT2 within a time delay Δt. This time has been measured in two different ways. First, one can record the MOT2 fluorescence after having suddenly removed the atoms in MOT1 (the MOT1 laser beams are stopped by a mechanical shutter). In this case, one observes the delay after which the number of atoms in MOT2 starts to drop. The second method consists in pulsing the pushing beam through a permanently loaded MOT1. Both methods lead to the same result $\Delta t \approx 130$ ms for the Cs experiment at 63 mW power. In the Rb experiment presented in Figure 8, the measured time delay as a function of the pushing beam power is obtained by using the second method. A similar dependence on the pushing beam power is observed in the cesium experiment. The two–level model is not sufficient to describe accurately the atomic beam velocity, the predicted transfer time Δt being by far too short (see Fig. 8, lower curve). On the contrary, the theoretical model presented in Section 3.3, equation (13) describes well the experimental results as demonstrated in Figure 8. From the model, we also deduce the final longitudinal velocity of the atomic beam $v \approx 5.5$ m/s (resp. 12.6 m/s for Rb). Note that this final velocity is not very different from the mean velocity $D/\Delta t$, as the acceleration stage takes place essentially in the MOT1 zone, where the atoms remain in the $F+1$ state thanks to the repumping MOT beams.

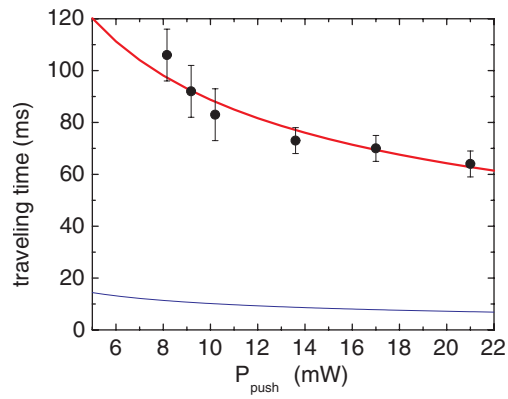

Fig. 8. (Color online) Experimental (points) and theoretical results (solid lines) for the traveling time Δt between MOT1 and MOT2 for different pushing beam powers. The beam is red-detuned by 1 GHz from the cycling transition of ^{87}Rb, $5S_{1/2}(F=2) \rightarrow 5P_{3/2}(F'=3)$. The theoretical calculations are done for both the two-level model approximation (blue lower curve) and for the more detailed model described above (red upper curve). In the calculations the radius of MOT1 trapping region is 10 mm.

5 Conclusion

In our work we have studied a very efficient setup to transfer cold atoms from a first MOT to a second one. Our

setups have a similar geometry to the ones described in references [18,19], but due to the higher laser power (tens of mW) we could achieve a partial dipolar guide for the atoms at a larger detuning (1 GHz typically). As a result, the mean longitudinal velocity of the atomic beam is lower (4.3−12 m/s) than in these previous experiments (15 m/s). Moreover, thanks to the lower sensibility of the method to the frequency of the pushing laser, its frequency does not need to be locked (see for instance the detuning dependence in Fig. 7, right) and the setup is much more robust to small misalignments of the pushing beam. The atomic flux is limited only by the number of atoms loaded into MOT1. We estimated the transfer efficiency to MOT2 which is about 70% for the ^{133}Cs experiment and about 50% for the ^{87}Rb experiment.

We used a two-level system model to describe the processes during the atomic transfer. A good qualitative agreement between theory and experiment was found. The transfer efficiency is maximum for a large red detuning, and this maximum efficiency increases with the laser power. A more detailed discussion of the pushing, guiding and recapture processes is presented for a better understanding of the atomic transfer between the two traps. Our theoretical description, which takes into account the optical pumping, the pushing force and the guiding potential nicely reproduces the experimentally observed traveling time.

In conclusion, we experimentally described and theoretically modelled a method to transfer cold atoms between two traps. Two different setups lead qualitatively to the same optimized parameters – a large laser power (tens of mW), ≈ 1 GHz detuning, 300 μm waist. The implementation of this technique in our setups brought in both cases a much better stability and improved loading efficiency, with respect to the use of a near resonant laser beam.

This work was partially supported by European RTN networks COMOL, QUACS, FASTNet and Atom Chips. LAC and LPL are members of IFRAF. LAC is UPR 3321 of CNRS associée à l'Université Paris-Sud and member of LUMAT FR 2764, and LPL is UMR 7538 of CNRS and Université Paris 13. We are very grateful to Brigitte Mercier for giving us the seminal idea of this pushing–guiding scheme. The authors also thank Laurent Vernac for helpful discussions on optical pumping and for providing us a computing code on the calculation of the populations in the magnetic sublevels.

References

1. U.D. Rapol, A. Wasan, V. Natarajan, Phys. Rev. A **64**, 023402 (2001)
2. B.P. Anderson, M.A. Kasevich, Phys. Rev. A **63**, 023404 (2001)
3. S.N. Atutov, R. Calabrese, V. Guidi, B. Mai, A.G. Rudavets, E. Scansani, L. Tomassetti, V. Biancalana, A. Burchianti, C. Marinelli, E. Mariotti, L. Moi, S. Veronesi, Phys. Rev. A **67**, 053401 (2003)
4. H.J. Lewandowski, D.M. Harber, D.L. Whitaker, E.A. Cornell, J. Low Temp. Phys. **132**, 309 (2003)
5. M. Greiner, I. Bloch, T.W. Hänsch, T. Esslinger, Phys. Rev. A **63**, 031401(R) (2001)
6. J.J. Arlt, O. Maragò, S. Webster, S. Hopkins, C.J. Foot, Opt. Commun. **157**, 303 (1998)
7. J.M. Kohel, J. Ramirez-Serrano, R.J. Thompson, L. Maleki, J.L. Bliss, K.G. Libbrecht, J. Opt. Soc. Am. B **20**, 1161 (2003)
8. K.H. Kim, K.I. Lee, H.R. Noh, W. Jhe, N. Kwon, M. Ohtsu, Phys. Rev. A **64**, 013402 (2001)
9. K. Dieckmann, R.J. Spreeuw, M. Weidemüller, J.T. Walraven, Phys. Rev. A **58**, 3891 (1998)
10. J. Schoser, A. Batär, R. Löw, V. Schweikhard, A. Grabowski, Y.B. Ovchinnikov, T. Pfau, Phys. Rev. A **66**, 023410 (2002)
11. R.S. Conroy, Y. Xiao, M. Vengalattore, W. Rooijakkers, M. Prentiss, Opt. Commun. **226**, 259 (2003)
12. T. Lahaye, J.M. Vogel, J.M. Günter, Z. Wang, J. Dalibard, D. Guéry-Odelin, Phys. Rev. Lett. **93**, 093003 (2004)
13. Z.T. Lu, K.L. Corwin, M.J. Renn, M.H. Anderson, E.A. Cornell, C.E. Wieman, Phys. Rev. Lett. **77**, 3331 (1996)
14. P. Cren, C.F. Roos, A. Aclan, J. Dalibard, D. Guéry-Odelin, Eur. Phys. J. D **20**, 107 (2002)
15. B.K. Teo, T. Cubel, G. Raithel, Opt. Commun. **212**, 307 (2002)
16. C. Slowe, L. Vernac, L. Vestergaard Hau, Rev. Sci. Instrum. **76**, 103101 (2005)
17. C.J. Myatt, N.R. Newbury, R.W. Ghrist, S. Loutzenhiser, C.E. Wieman, Opt. Lett. **21**, 290 (1996)
18. W. Wohlleben, F. Chevy, K. Madison, J. Dalibard, Eur. Phys. J. D **15**, 237 (2001)
19. L. Cacciapuoti, A. Castrillo, M. de Angelis, G.M. Tino, Eur. Phys. J. D **15**, 245 (2001)
20. Yan Shu-Bin, Geng Tao, Zhang Tian-Cai, Wang Jun-Min, Chin. Phys. **15**, 1746 (2006)
21. D. Müller, E.A. Cornell, D.Z. Anderson, E.R. Abraham, Phys. Rev. A **61**, 033411 (2000)
22. L. Pruvost, D. Marescaux, O. Houde, H.T. Duong, Opt. Commun. **166**, 199 (1999)
23. K. Szymaniec, H.J. Davies, C.S. Adams, Europhys. Lett. **45**, 450 (1999)
24. B.T. Wolschrijn, R.A. Cornelussen, R.J.C. Spreeuw, H.B. van Linden van den Heuvell, New J. Phys. **4**, 69 (2002)
25. A.M. Steane, M. Chowdhury, C.J. Foot, Phys. Rev. A **9**, 2142 (1992)
26. R. Grimm, M.s Weidemüller, Y.B. Ovchinnikov, Adv. At. Mol. Opt. Phys. **42**, 95 (2000)
27. This population ratio may be adjusted by using an elliptically polarized laser beam. It may be a way to optimize experimentally the final atomic beam velocity. In the model, we restrict ourselves to a linear polarization for sake of simplicity
28. Daniel A. Steck, Alkali D Line Data, October 2003, `http://steck.us/alkalidata/`
29. In this model, we have neglected the heating term related to the fluctuations of the guiding force when the atom jumps between the two hyperfine states. However, this contribution is smaller by about a factor $[\lambda\delta/(2\pi w\Gamma)]^2$ than the spontaneous scattering term, that is more than two orders of magnitude everywhere along the guide

Chapitre 3

Condensat de Bose-Einstein et ondes évanescentes

Les ondes évanescentes à la surface de diélectriques ont été utilisées dans des expériences de physique atomique bien avant l'avènement des condensats de Bose-Einstein. En effet, la décroissance très rapide du champ évanescent à l'interface d'un diélectrique d'indice n et du vide permet d'atteindre des forces dipolaires élevées, proportionnelles au gradient d'intensité lumineuse dans l'onde évanescente. R. Cook et R. Hill ont proposé dès 1982 de les utiliser comme miroir pour une onde atomique [57], et la démonstration expérimentale de leur efficacité a été faite quelques années plus tard par Balykin *et al.* [58] avec un jet d'atomes à incidence rasante. Kasevich *et al.* [59] ont ensuite montré que ces miroirs pouvait réfléchir des atomes froids, même à incidence normale, et l'équipe de Jean Dalibard a montré que les atomes lâchés verticalement au-dessus du miroirs subissaient plusieurs réflexions, la gravité repliant les trajectoires [60]. Enfin, l'équipe d'Alain Aspect a utilisé un tel miroir pour sonder l'interaction atome-surface [61].

L'utilisation de champs évanescents est naturelle pour la réalisation de pièges à atomes très anisotropes et permet d'envisager un piège de très grande raideur transverse. Par rapport à l'option d'utiliser une onde stationnaire, également très confinante, que j'avais étudié en partie au cours de ma thèse [62, 63], les pièges de surface présentent l'avantage de pouvoir réaliser un seul piège, et non une collection de pièges analogues [1]. Le premier piège de surface réalisé avec des atomes froids, le GOST pour « Gravito-optical surface trap », était constitué d'une seule onde évanescente faisant office de miroir orienté vers le haut, la gravité ramenant les atomes vers ce miroir [65, 66]. Dans la phase de chargement du piège, le désaccord est choisi proche de la résonance atomique de sorte que les atomes dissipent leur énergie par échange de photons spontanés avec l'onde évanescente [67, 66]. Le désaccord est ensuite fortement augmenté pour rendre le piège conservatif. Les atomes sont confinés transversalement soit par

1. Cette difficulté a été contournée récemment par l'équipe de Jean Dalibard, en utilisant l'interférence de deux lasers sous incidence faible [64, 29].

une onde laser creuse (un mode Gaussien $TEM_{0,1}$) décalée vers le bleu, soit par un laser décalé vers le rouge. C'est avec ce dispositif que Rudi Grimm et ses collègues ont pu condenser un gaz en dimension 2 pour la première fois [68]. Une autre tactique, mise au point dans l'équipe de Tilman Pfau avec de l'argon métastable, consiste à faire se réfléchir une onde à la surface d'un miroir, et à confiner les atomes aux nœuds de l'onde stationnaire ainsi obtenue [69]. Le confinement est meilleur qu'avec une seule onde évanescente. Ovchinnikov *et al.* [32] ont proposé dès 1991 d'utiliser la combinaison de deux ondes évanescentes pour confiner des atomes à trois dimensions dans un piège très anisotrope. L'équipe de Grimm a démontré en 2002 que le piège fonctionnait [70] et a refroidi des atomes *in situ*, sans toutefois atteindre le seuil de condensation [71].

C'est ce piège que nous avions initialement prévu d'utiliser pour confiner les atomes en dimension 2, et pour lequel nous avons imaginé deux méthodes de chargement possibles. Je présenterai dans ce chapitre le piège à ondes évanescentes ou POE, baptisé DEW pour « Double Evanescent Wave trap » par Rudi Grimm et ses collègues [71]. J'indiquerai les deux méthodes de chargement que nous avons imaginées pour transférer un condensat de Bose-Einstein dans ce piège (paragraphe 3.2). Nous n'avons pas réalisé expérimentalement ce transfert, en raison de contraintes techniques liées à la surface diélectrique utilisée. Nous avons mené en revanche les premières expériences de réflexion d'un condensat sur une onde évanescente qui ont montré l'impact de la rugosité de surface sur la diffusion des atomes. L'analyse quantitative de cette diffusion est présentée au paragraphe 3.3. Cette diffusion importante n'a pas empêché l'observation de la diffraction de l'onde de matière incidente sur le miroir lorsque celui-ci vibre, comme le montrent les résultats présentés au paragraphe 3.4.

3.1 Description du piège à ondes évanescentes

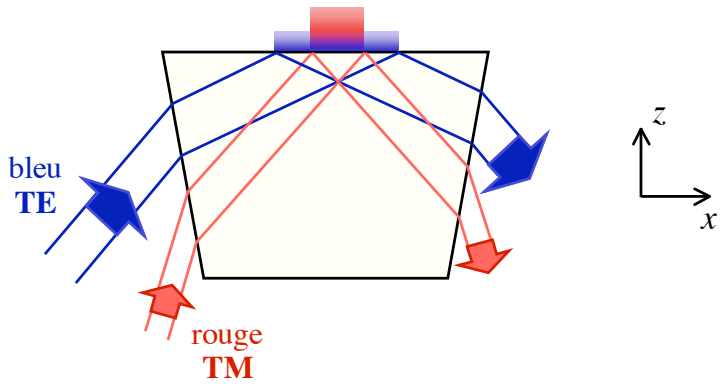

Figure 3.1 — Principe du piège à ondes évanescentes.

Principle of the double evanescent waave trap.

Le principe du piège est illustré sur la figure 3.1. Un diélectrique d'indice n supporte deux ondes évanescentes, désaccordées de part et d'autre de la résonance atomique et

qui seront donc désignées par les indices b pour « bleu » et r pour « rouge ». Les angles d'incidence $\theta_{b,r}$ sur le dioptre sont choisis de telle sorte que la portée κ_r^{-1} de l'onde rouge est supérieure à celle de l'onde bleue κ_b^{-1}. Le potentiel auquel sont soumis les atomes selon la direction z transverse à la surface du diélectrique est alors analogue au potentiel de Morse :

$$U(x,y,z) = -|U_r(x,y)|\, e^{-2\kappa_r z} + U_b(x,y)\, e^{-2\kappa_b z}. \tag{3.1}$$

La partie attractive à longue portée confine les atomes à la surface, alors que l'onde bleue à courte portée empêche les atomes de s'approcher trop près et de coller à la surface. Le confinement dans le plan horizontal Oxy est assuré par le choix d'un rayon à $1/e^2$ du faisceau rouge w_r inférieur à celui du faisceau bleu w_b.

Au minimum du potentiel, le déplacement lumineux de l'onde rouge est plus grand que celui de l'onde bleue par un facteur κ_b/κ_r environ. Pour éviter la diffusion de photons spontanés, on a intérêt à choisir un laser rouge très désaccordé. L'utilisation d'un laser de quelques watts à la longueur d'onde du Nd :YAG à 1064 nm pour le rouge, associé à un laser saphir-titane décalé de quelques nanomètres pour le bleu est un bon compromis. C'est aussi le choix qu'a effectué l'équipe d'Innsbruck [71]. A 1064 nm, le désaccord à la résonance est beaucoup plus grand que la structure fine de l'état excité, la raie $D1$ ayant pour longueur d'onde 795 nm. Par conséquent, le déplacement lumineux de l'onde rouge est scalaire et ne dépend pas de la polarisation de l'onde évanescente. Il est alors préférable de choisir une polarisation transverse magnétique (TM), dans le plan d'incidence xz, car le champ évanescent est alors plus intense [44]. En revanche, la polarisation de l'onde bleue doit être prise en compte dans le calcul du déplacement lumineux. Nous avons choisi d'utiliser une polarisation transverse électrique (TE), de sorte que la polarisation de l'onde évanescente est elle-même linéaire, selon y. Ce choix garantit un potentiel indépendant du sous-niveau magnétique $|F,m_F\rangle$ considéré.

Je ne détaillerai pas ici le calcul du potentiel de piégeage, dont on trouvera une description très complète dans la thèse d'Yves Colombe [44], mais simplement le résultat. On note Δ_b et Δ_r le désaccord respectif des deux ondes par rapport à la raie D_2 du rubidium à $\lambda_0 = 780$ nm, $\lambda_{b,r}$ leur longueur d'onde et $k_{b,r} = 2\pi/\lambda_{b,r}$ leur nombre d'onde dans le vide ; de même $k_0 = 2\pi/\lambda_0$. Pour une incidence supérieure à l'angle critique, le champ décroît transversalement exponentiellement avec $\kappa_{b,r} = k_{b,r}\sqrt{n^2 \sin^2\theta_{b,r} - 1}$. Dans le plan horizontal, le champ se propage selon x avec un vecteur d'onde $K_{b,r} = k_{b,r} n \sin\theta_{b,r}$ supérieur à $k_{b,r}$. Le potentiel dipolaire auquel les atomes sont soumis est de la forme :

$$\begin{aligned} U_{\mathrm{dip}}(\mathbf{r}) \;=\; & \frac{I_{0,r}}{2\,I_{\mathrm{sat}}}\,\frac{\Gamma}{4\,\Delta_r}\,\hbar\Gamma e^{-2\left(\frac{x^2}{w_r'^2}+\frac{y^2}{w_r^2}+\kappa_r z\right)} \\ & + \frac{I_{0,b}}{2\,I_{\mathrm{sat}}}\left(\frac{1}{3}\,\frac{\Gamma}{4(\Delta_b+\Delta_{\mathrm{SF}})}+\frac{2}{3}\,\frac{\Gamma}{4\,\Delta_b}\right)\hbar\Gamma e^{-2\left(\frac{x^2}{w_b'^2}+\frac{y^2}{w_b^2}+\kappa_b z\right)}. \end{aligned} \tag{3.2}$$

Les intensités effectives à la surface $I_{0,r}$ et $I_{0,b}$ dépendent, outre de la puissance et du rayon des faisceaux, de la polarisation et de l'angle d'incidence [44]. Les rayons des faisceaux $w'_{b,r}$ selon l'axe x sont modifiés par rapport à leur valeur incidente sur la face

d'entrée du prisme en raison de la réfraction puis de la coupe par la face supérieure. Enfin, les deux termes intervenant dans l'expression du déplacement lumineux de l'onde bleue correspondent aux contributions respectives des raies $D1$ et $D2$, séparées de la structure fine Δ_{SF}. Cette distinction est négligeable pour le déplacement dû au faisceau rouge puisque $|\Delta_r| \gg \Delta_{\mathrm{SF}}$.

Au déplacement lumineux des ondes évanescentes, il faut ajouter l'effet de la gravité Mgz ainsi que l'interaction de surface avec la paroi du prisme d'indice n. Nous avons utilisé pour modéliser cette dernière la formule empirique pour $U_{\mathrm{vdW}}(z)$ proposée par Arnaud Landragin et ses collègues [61, 72], valable à 0,6% près entre 0 et $10\,k_0^{-1}$, soit jusqu'à 1,24 μm de la surface. Le potentiel total s'écrit donc de façon approchée

$$U(\mathbf{r}) = U_{\mathrm{dip}}(\mathbf{r}) + U_{\mathrm{vdW}}(z) + Mgz \tag{3.3}$$

et il ne dépend par de l'état interne avec le choix de polarisation effectué. La forme exacte de U dépend du choix des paramètres des lasers. Nous avons proposé un jeu de paramètres permettant d'obtenir un rapport d'anisotropie élevé, compatible avec la puissance des lasers disponibles au laboratoire et limitant le taux d'émission spontanée. Ces paramètres sont présentés dans le tableau 3.1 [2]. Le facteur le plus contraignant est la puissance laser disponible avec un laser saphir-titane (1 W maximum dans notre cas), qui contraint le désaccord du laser bleu à rester assez faible. La puissance nécessaire à 1064 nm est en revanche toujours nettement inférieure à la puissance disponible avec notre laser Nd :YVO_4 de 7 W.

	$P_{b,r}$ (W)	$\lambda_{b,r}$ (nm)	$\theta_{b,r}$	$w_{b,r}$ (μm)	$w'_{b,r}$ (μm)
bleu	0,5	777,5	52°	165	268
rouge	1,7	1064	43°	150	207

Tableau 3.1 — Paramètres retenus pour le piège à ondes évanescentes. L'angle critique vaut 41,5° pour un prisme d'indice $n = 1{,}51$.

Typical parameters for the realisation of a DEW trap. For a prism of index $n = 1.51$, the critical angle is 41,5°.

La figure 3.2 présente une coupe le long de l'axe vertical z du potentiel U ainsi obtenu, ainsi qu'une représentation des équipotentielles dans le plan yz. On remarquera la différence des échelles de la figure 3.2(b). Les calculs ont été faits pour un prisme en BK7 d'indice $n = 1{,}51$, identique pour les deux longueurs d'ondes, avec un angle de 50° entre la face d'entrée des lasers et la face horizontale supportant les ondes évanescentes.

Les fréquences d'oscillations calculées dans l'approximation harmonique au voisinage du minimum à $z_0 = 370$ nm sont $\nu_x = 45$ Hz, $\nu_y = 60$ Hz et $\nu_z = 24$ kHz, confirmant la nature très anisotrope du potentiel. Dans ce piège, un condensat présentera un caractère quasi 2D dès lors que le nombre d'atomes est inférieur à 10^6. Pour

2. Les valeurs ne correspondent pas exactement à celles que nous avons publiées dans la référence [33].

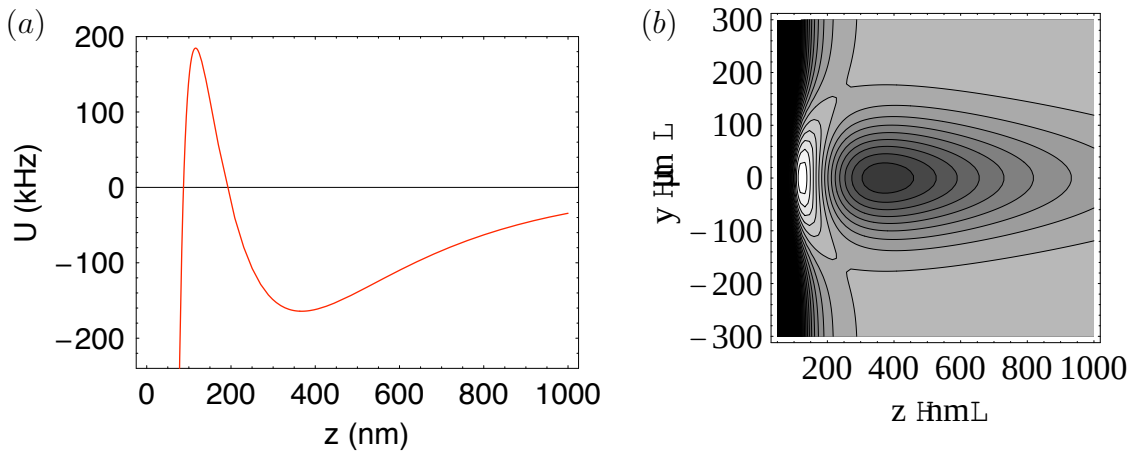

Figure 3.2 — Allure du potentiel U/h du piège à ondes évanescentes. Les paramètres sont ceux de la table 3.1. On a pris en compte la gravité et l'attraction de surface avec le prisme. (a) U/h en kHz en fonction de z, pour $x = y = 0$. (b) Équipotentielles dans le plan yz. On remarquera la différence d'échelle des deux axes, ainsi que les deux points col.

Sketch of the DEW trap potential U/h, with the parameters of Table 3.1. Gravity and the interaction with the surface are taken into account. (a) U/h as a function of z for $x = y = 0$. (b) Isopotential lines in the yz plane for $x = 0$. Note the different y and z scaling, as well as the two saddle points.

100 000 atomes par exemple, le potentiel chimique calculé naïvement avec l'expression valable à trois dimensions dans la limite Thomas-Fermi serait de 10 kHz, inférieur à la fréquence d'oscillation transverse. En réalité, les atomes occupent alors l'état fondamental à un atome du potentiel transverse et le gaz est quasi 2D.

La profondeur du puits de potentiel est de 150 kHz ou 7,2 μK, et elle est limitée par l'existence de points cols très bien visibles sur la figure 3.2(b). Le piège doit donc être chargé avec des atomes déjà très froids, et nous décrirons à la section 3.2 deux méthodes pour y parvenir.

Le taux de diffusion de photons est évalué à 2 photons par seconde et par atome, ce qui conduit à un taux de chauffage linéaire d'environ 5 kHz/s (ou 240 nK/s) [73]. Ceci limite à quelques centaines de millisecondes la durée d'une expérience dans ce piège avec des atomes ultra froids.

3.2 Chargement

Comme nous l'avons vu plus haut, le piège à ondes évanescentes présente (POE) un caractère fortement anisotrope. Cela pose une difficulté pour le chargement du piège à partir d'un condensat ou d'un gaz ultra froid confiné dans un piège magnétique. L'équipe d'Innsbruck a résolu ce problème en refroidissant les atomes directement au voisinage de la surface, dans un piège intermédiaire constitué de l'onde évanescente bleue répulsive et d'un faisceau rouge traversant la surface du prisme à incidence nor-

male [70]. Les atomes sont alors déjà très proches de la surface, et le transfert dans le piège à deux ondes évanescentes s'effectue en remplaçant progressivement l'onde rouge progressive par l'onde évanescente.

Dans notre cas, nous partons au contraire d'atomes condensés ou très froids, confinés dans un piège magnétique à environ 3 mm de la surface. Nous avons proposé deux méthodes pour charger les atomes de ce piège magnétique vers le POE, que nous détaillons ci-dessous.

3.2.1 Transport magnétique

L'idée la plus naturelle est de transporter magnétiquement les atomes jusqu'au voisinage immédiat de la surface. Cela est possible en ajoutant au champ magnétique du QUIC un champ vertical homogène, produit par une paire de bobines supplémentaires d'axe vertical, dites « bobines de translation ». En augmentant graduellement le courant dans ces bobines, nous pouvons déplacer adiabatiquement le condensat jusqu'au contact avec la surface, 3,6 mm plus bas, comme le montre la figure 3.3. Pour vérifier le caractère adiabatique de ce déplacement, nous avons effectué un aller-retour et vérifié que les atomes étaient toujours condensés à la suite de ce déplacement [74]. Nous avons également produit le condensat directement dans le piège translaté, en déplaçant le nuage à la fin de la rampe d'évaporation.

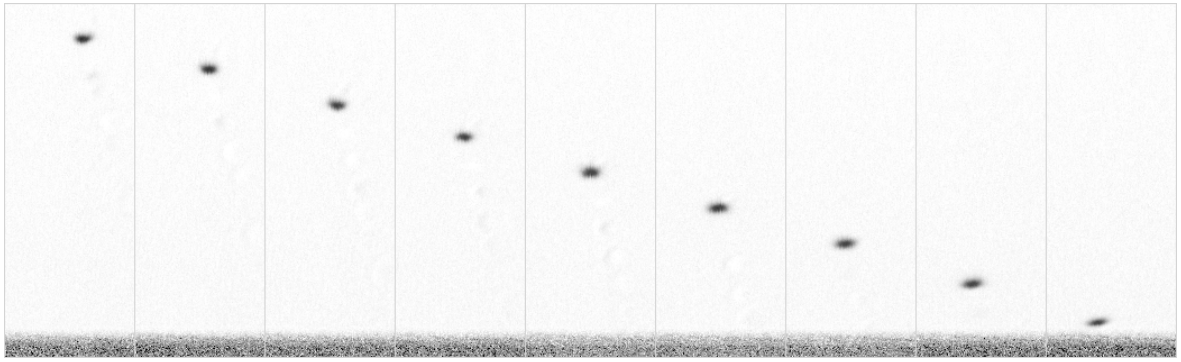

Figure 3.3 — Translation contrôlée du condensat jusqu'à la surface du prisme. Les images sont prises après un temps de vol de 5 ms. Entre la première et la dernière image, le courant dans les bobines de translation augmente de 0 à 20 A.

Absorption images showing the magnetic transportation of a condensate to the prism surface. Each image is taken after a 5 ms time-of-flight. The current in the translation coils in increased from 0 to 20 A between the first and the last picture.

Si l'onde évanescente bleue est présente lorsque les atomes sont approchés de la surface, elle empêchera ceux-ci de coller. On réalise alors un piège hybride opto-magnétique, qui a l'allure d'une moitié supérieure de piège magnétique. Il suffit ensuite d'allumer adiabatiquement le second laser, l'onde évanescente rouge, pour que les atomes soient transférés dans le POE. L'extinction du champ magnétique termine le processus.

En collaboration avec Maxim Olshanii, nous avons testé l'adiabaticité du transfert en simulant l'étape de branchement du faisceau rouge [33]. Pour cela nous partons de l'état fondamental du système dans le piège hybride, calculé par la méthode de l'évolution en temps imaginaire de l'équation de Gross-Pitaevskii. Puis, nous simulons l'équation de Gross-Pitaevskii pendant le branchement du laser rouge. Nous pouvons alors estimer l'efficacité du transfert en analysant la proportion finale d'atomes piégés dans le POE.

Résultats de la simulation Pour réduire le temps de calcul nécessaire à cette simulation 3D, nous sommes partis d'un piège magnétique isotrope de fréquence d'oscillation 300 Hz. Dans la simulation, le piège à ondes évanescentes seul a pour fréquences d'oscillation (30 Hz, 64 Hz, 30 kHz) dans les directions (x,y,z). La simulation montre que le transfert est d'autant plus efficace que la durée de branchement τ de l'onde rouge est longue. Une durée supérieure à 10 ms serait convenable, comme le suggère la figure 3.4. Cette valeur est liée à la condition d'adiabaticité lors de la déformation des fréquences d'oscillations [75]. Autant la variation de fréquence est très faible dans les directions horizontales, autant elle est importante dans la verticale où elle passe de 300 Hz à 30 kHz en un temps τ, et l'on doit assurer que $\dot{\omega} \ll \omega^2(t)$ au cours du temps. Pour un branchement optimal $\omega^{-1} = \omega_0^{-1} + \varepsilon t$ avec $|\varepsilon| \ll 1$, le temps de branchement τ doit être grand devant $|\omega_{\text{final}}^{-1} - \omega_0^{-1}|$. Dans la direction z la fréquence augmente de deux ordres de grandeur et l'on doit avoir $\tau \gg 1/\omega_z(0)$ soit un temps très long devant 0,5 ms.

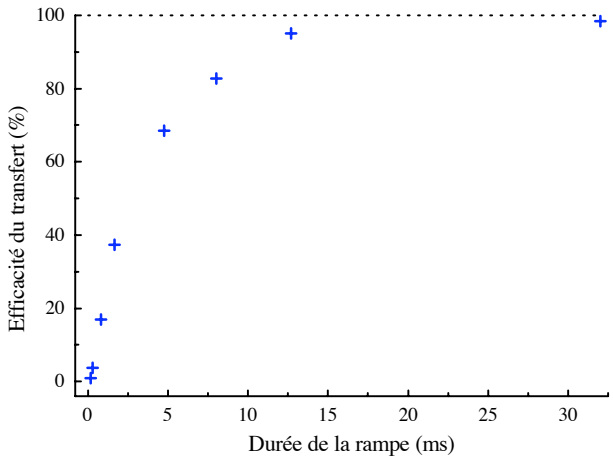

Figure 3.4 — Efficacité du transfert d'atomes depuis le piège hybride opto-magnétique lors du branchement de l'onde évanescente rouge. Le graphique représente le pourcentage d'atomes transférés en fonction de la durée du transfert.

Efficiency of the atom transfer resulting from the red laser power increase. The plots show the percentage of transferred atoms as a function of the transfer duration.

Ces résultats permettent d'évaluer le temps de branchement à partir des fréquences d'oscillation. Notons que dans le cas réel du piège QUIC translaté à proximité de la

surface, le jeu des fréquences d'oscillation est différent. La direction la plus contraignante est en fait y, où la fréquence d'oscillation passe de 220 à 62 Hz, ce qui donne $\tau \gg 1{,}8$ ms, soit typiquement 40 ms. Un compromis entre l'adiabaticité du transfert et la limitation de la diffusion de photons sera sans doute nécessaire.

3.2.2 Ascenseur à atomes

Nous avons proposé une alternative originale à cette méthode de chargement. Les atomes pourraient être transférés du piège magnétique dans une onde stationnaire optique d'axe vertical et de désaccord négatif. Ils seraient ainsi piégés dans une série de galettes séparées de la demi-longueur d'onde. En faisant alors varier la phase de l'un des faisceaux, on peut déplacer ces galettes jusqu'à l'onde évanescente bleue et faire se déverser les plans les uns après les autres au voisinage de la surface, comme le suggère la figure 3.5.

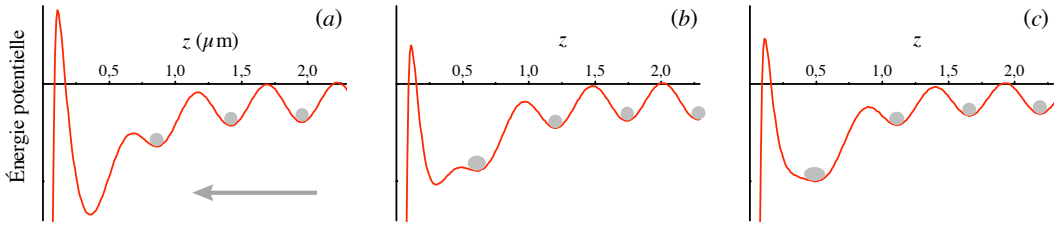

Figure 3.5 — Principe du transfert des plans atomiques dans le piège de surface. La différence de phase à la surface entre les deux ondes vaut (a) : $0{,}6\,\pi$; (b) : $1{,}5\,\pi$; (c) : $1{,}8\,\pi$.

Principle of the atom transfer from the standing wave planes into the surface trap. The phase difference at the surface between the two counterpropagating waves is respectively (a) *:* $0{,}6\pi$ *;* (b) *:* $1{,}5\pi$ *;* (c) *:* $1{,}8\pi$.

Le principe du glissement de la phase a été utilisé dans l'équipe de Dieter Meschede pour transporter un atome unique dans une onde stationnaire [76]. Notre proposition s'inspire surtout du transport magnétique d'un condensat sur une puce, dans des potentiels périodiques qui sont déplacés pour permettre aux atomes de parcourir quelques centimètres [77]. L'équipe de Jakob Reichel a en effet montré que ce transport pouvait préserver le condensat.

L'avantage de cette technique est que le nuage est mis en forme avant d'être chargé dans le POE. Cependant, le temps de chargement est allongé car il faut déverser successivement une quinzaine de puits, chacun en un temps de quelques dizaines de millisecondes. Les limites imposées par le taux de diffusion de photons rendent difficilement acceptable une telle durée de chargement. De plus, la simulation de ce transfert par une méthode analogue à celle décrite plus haut montre la difficulté d'éviter de peupler des états excités du piège de surface, en raison du couplage tunnel entre le dernier puits de l'onde stationnaire et le POE [33]. Pour ces différentes raisons, le chargement du POE par la méthode du transport magnétique paraît plus prometteur. Notons en revanche

que la technique de l'ascenseur, utilisée en sens inverse, peut être un moyen d'extraire les atomes du POE et de peupler un puits unique d'une onde stationnaire.

3.3 Rebond diffusif

Avant de mettre en œuvre expérimentalement le piège à ondes évanescentes, nous avons mené une série d'expériences impliquant une seule onde évanescente, l'onde bleue, dans une configuration de miroir à atomes [57, 58, 59]. Ces expériences nous ont permis de tester les propriétés de surface du prisme, qui se sont avérées très médiocres. Nous avons observé que le condensat lâché au-dessus de la surface était réfléchi par l'onde évanescente, et que cette réflexion s'accompagnait d'une forte diffusion [34], beaucoup plus prononcée que celle observée par le groupe d'Orsay [78]. La partie spéculaire de la réflexion n'est en effet plus détectable, l'ensemble de la population atomique se retrouvant dans l'onde diffusée. En collaboration avec Carsten Henkel, nous avons étudié en détail cette diffusion et nous l'avons reliée aux propriétés de surface mesurées indépendamment avec un microscope à force atomique (AFM).

Les expériences de rebond ont été faites avec un prisme diélectrique posé au fond de l'enceinte en quartz. Ce prisme a un indice relativement élevé $n_p = 1{,}86$ et est recouvert d'un traitement de surface devant amplifier l'onde évanescente [51, 52, 53, 54]. Ce traitement consiste en une couche de SiO_2, d'indice 1,46 et d'épaisseur 400 nm et une couche de TiO_2 d'indice 2,3 et d'épaisseur 360 nm. Cette dernière couche constitue un guide d'onde, couplé à l'onde réfléchie dans le prisme par l'onde évanescente présente dans le *gap* d'indice faible. Ce couplage est résonnant pour le mode TE, et pour une longueur d'onde proche de 780 nm, à un angle $\theta = 63{,}4°$ imposé par l'épaisseur des couches.

3.3.1 Résultats expérimentaux

Les expériences de rebond ont été menées selon le protocole suivant : on produit tout d'abord un condensat de Bose-Einstein par la méthode décrite au chapitre 2, à 3,6 mm au-dessus du prisme. Le condensat peut être rapproché si besoin à l'aide des bobines de translation. On coupe ensuite les champs magnétiques, et le condensat tombe dans le champ de pesanteur, atteignant la surface après un temps de vol de 27 ms à incidence quasi normale, avec une vitesse verticale $v_z = 266$ mm/s et une faible vitesse horizontale $v_x = -30$ mm/s. L'onde évanescente bleue est produite par une diode laser Sanyo 70 mW désaccordée de 1,5 GHz par rapport à la raie $D2$. Le faisceau est focalisé à la surface du diélectrique, avec un rayon à $1/e^2$ à l'extérieur du prisme $w_i = 100$ μm dans le plan d'incidence et $w_y = 85$ μm selon l'axe y, suffisants pour que le condensat soit entièrement réfléchi. Le laser est allumé pendant 2 ms seulement pour éviter la diffusion spontanée de photons pendant la chute et après le rebond, qui ne dure que 0,7 ms. L'intensité pic à la surface vaut 210 W/cm^2, elle a été calibrée en relevant l'intensité seuil en deçà de laquelle les atomes ne sont plus réfléchis, et en comparant cette valeur avec un modèle prenant en compte l'énergie incidente et le potentiel total créé par l'onde laser, la gravité et l'interaction avec la paroi [44]. À partir de ces données,

on peut estimer le nombre moyen de photons diffusés spontanément par chaque atome lors du rebond, qui vaut 0,13 pour le désaccord choisi. Cette faible valeur permet de décrire la réflexion comme un processus élastique.

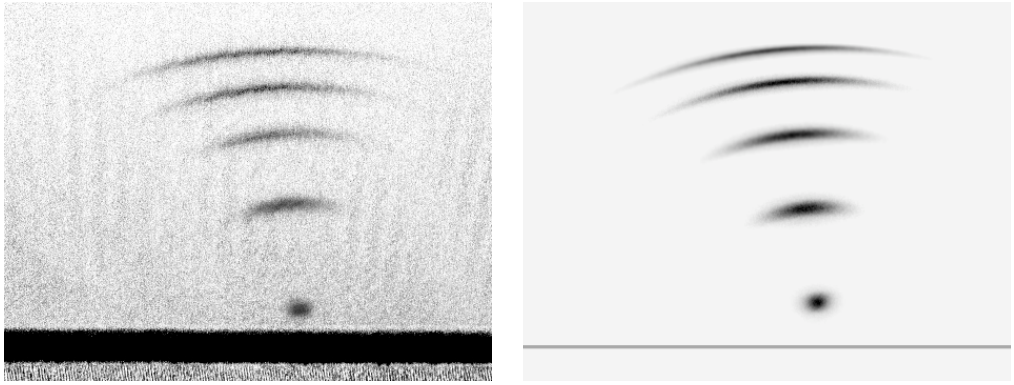

Figure 3.6 — (a) Réflexion diffuse d'un condensat sur une onde évanescente supportée par une surface rugueuse. On a superposé sur cette image les données correspondant aux temps de vol après rebond suivants : 2, 7, 12, 17 et 22 ms. (b) Simulation avec les mêmes paramètres que l'expérience, en imposant une diffusion selon y deux fois plus faible que selon x : $\Delta v_x/\Delta v_y = 2$.

(a) *Diffuse reflection of a BEC off an evanescent wave above a rough dielectric surface. Images from different time-of-flights are superimposed : 2, 7, 12, 17 and 22 ms.* (b) *Numerical simulation in the same conditions, with a scattering amplitude along x twice as large as along y :* $\Delta v_x/\Delta v_y = 2$.

Après la réflexion, le nuage est fortement diffusé dans les directions horizontales. La diffusion étant élastique, la vitesse initiale $v_0 = \sqrt{v_z^2 + v_x^2}$ est conservée en norme mais sa direction change. Les atomes après réflexion se répartissent alors au voisinage d'une portion de sphère, de centre $-gt^2/2$ et de rayon $v_0 t$ où t est le temps écoulé à partir du rebond. Notre objectif était de relier l'amplitude de la diffusion, c'est-à-dire les largeurs en vitesse Δv_x et Δv_y après le rebond, aux caractéristiques microscopiques de la surface. La valeur de $\Delta v_x = 6{,}6 \pm 0{,}2\ v_{\mathrm{rec}}$ est directement lisible sur les images d'absorption (figure 3.6a), puisqu'elle est reliée à la largeur σ_x du nuage (à $1/e^2$) après un temps de vol t_{vol} après le rebond, selon $\Delta v_x = \sigma_x t_{\mathrm{vol}}$. Pour extraire Δv_y en l'absence d'imagerie selon un deuxième axe, nous avons analysé finement le profil de densité selon la verticale, notamment l'aile s'étendant vers le centre de la projection dans le plan xz de la sphère de diffusion. Plus la diffusion selon y est importante et plus cette aile doit être marquée. Nous avons alors comparé les coupes verticales des images expérimentales à celles produites par une simulation Monte-Carlo du rebond dans laquelle tous les paramètres (température, distribution de vitesse initiale...) sont connus, hormis Δv_y que l'on fait varier d'un calcul à l'autre. La simulation calcule classiquement [3]

3. Après environ 1 ms d'expansion, les interactions entre atomes deviennent négligeables et la distribution des vitesses reste figée. Les trajectoires atomiques sont alors celles de particules classiques dans le champ de pesanteur.

la trajectoire des atomes et modifie aléatoirement la vitesse lors du rebond selon une loi gaussienne de largeur $\Delta v_x = 6{,}6\ v_{\mathrm{rec}}$ et Δv_y. La figure 3.6*b* montre un exemple de résultat du calcul. Le choix d'un rapport $\Delta v_x/\Delta v_y = 2 \pm 0{,}5$ permet de s'approcher le plus des données expérimentales [34]. Nous avons ainsi mis en évidence le caractère anisotrope de la diffusion, qui est dû à l'existence d'une direction préférentielle imposée par la partie réelle du vecteur d'onde de l'onde évanescente, orientée selon x.

3.3.2 Analyse quantitative

Carsten Henkel a modélisé pendant sa thèse [79, 80] la réflexion diffuse d'atomes par une onde évanescente. Ce modèle permet de relier l'amplitude de la diffusion à la puissance spectrale de rugosité de la surface par convolution avec une fonction de transfert atomique. Je reprendrai dans cette partie ses notations, et désignerai par des lettres capitales les coordonnées dans le plan horizontal xy, dans l'espace réel (par exemple $\mathbf{R}$) ou réciproque ($\mathbf{Q}$). En collaboration avec lui, j'ai relié les résultats expérimentaux décrits ci-dessus avec les caractéristiques de la surface mesurées par Yves Colombe avec un AFM. Le dépôt d'une couche de TiO_2 permettant d'exalter l'onde évanescente a produit une structure en colonnes de diamètre 90 nm typiquement, bien visible sur la figure 3.7. La rugosité obtenue en calculant l'écart type de la distribution des altitudes est de $\sigma_{\mathrm{AFM}} = 3{,}34$ nm.

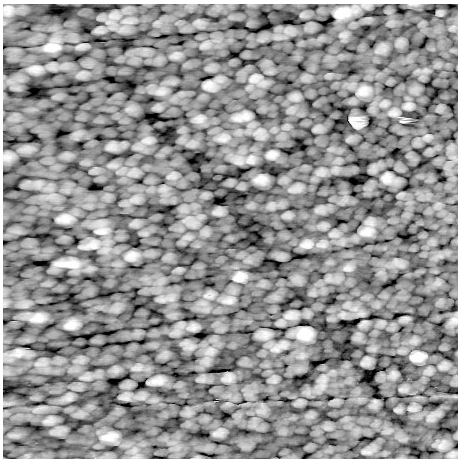

Figure 3.7 — Image de la surface du prisme obtenue par un microscope à force atomique. Le champ analysé a pour dimensions 4 μm $\times$4 μm. La structure en colonnes du dépôt de TiO_2 est bien visible.

Atomic force microscop (AFM) image of the prism surface, in a 4 μm $\times$4 μm frame. The dots are due to the column strucutre of the TiO_2 layer.

À partir de cette image, on obtient par transformée de Fourier de l'altitude de la surface $s(\mathbf{R})$ la puissance spectrale de rugosité $P_S(\mathbf{Q})$. Celle-ci est isotrope et bien

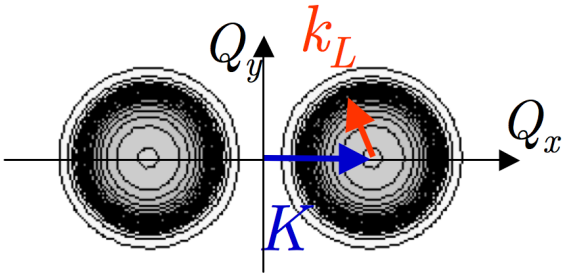

Figure 3.8 – Fonction de réponse atomique $B_{\rm at}(Q_x,Q_y)$ représentée par ses contours dans le plan (Q_x,Q_y). La fonction de réponse est piquée autour de deux cercles correspondant à la diffusion de Bragg de deux photons d'implulsions différentes.

Contour plot of the atomic response function $B_{\rm at}(Q_x,Q_y)$. The function is peaked around two cirles, corresponding to the Bragg scattering of two photons of different momentum.

ajustée par une loi de puissance tronquée du type

$$P_S(Q) = \frac{P_0}{(1+Q^2/Q_0^2)^{\alpha/2}} \tag{3.4}$$

avec $Q_0 = 4{,}94\ k_L$, $P_0 = 5{,}3\times 10^{-4}\ k_L^{-4}$ et $\alpha = 4{,}8$. On a exprimé ces valeurs en unités déduites de k_L, le vecteur d'onde dans le vide du laser incident sur le prisme. On peut vérifier la validité de ce modèle en calculant la rugosité correspondante

$$\sigma = \frac{1}{(2\pi)^2}\int P_S(Q)\,2\pi Q\,dQ\,. \tag{3.5}$$

On trouve une valeur de 3,36 nm, en excellent accord avec $\sigma_{\rm AFM}$.

Une fois que $P_S(Q)$ est déterminé, on en déduit les largeurs en vitesse après rebond. Dans le régime de forte diffusion, où les atomes effectuent successivement plusieurs processus élémentaires de diffusion lors du rebond [4], on peut montrer que la distribution de vitesse attendue est gaussienne [80], de largeur

$$\frac{\Delta v_x^2}{v_{\rm rec}^2} = \frac{1}{k_L^2}\int \frac{d\mathbf{Q}}{(2\pi)^2}\,Q_x^2\,P_S(Q)|B_{\rm at}(\mathbf{Q})|^2\,. \tag{3.6}$$

La fonction de réponse atomique $B_{\rm at}(\mathbf{Q})$, représentée sur la figure 3.8, dépend de la vitesse incidente et présente un caractère anisotrope à l'origine de l'anisotropie observée dans l'expérience [80]. Physiquement, la fonction de réponse décrit la probabilité des processus Bragg en fonction du moment $\hbar\mathbf{Q}$ transféré à l'atome. Elle est fortement piquée au voisinage de deux cercles centrés en $Q_x = \pm K$ et de rayon k_L, correspondant à l'absorption d'un photon de l'onde évanescente [5] suivie par l'émission stimulée dans un mode diffusé d'un photon en incidence rasante – ou le processus inverse.

4. C'est bien notre cas, puisque la largeur de la distribution de vitesse après rebond est nettement supérieure à $v_{\rm rec}$.

5. On rappelle que le vecteur d'onde réel de l'onde évanescente vaut $K\mathbf{e_x}$ où $K = k_L n \sin\theta$.

Avec les paramètres de l'expérience mesurés indépendamment et la fonction $P_S(Q)$ déterminée avec l'AFM, on obtient par l'équation (3.6) une largeur en vitesse après rebond $\Delta v_x = 6{,}60 \pm 0{,}36\ v_{\mathrm{rec}}$ en excellent accord[6] avec la valeur mesurée [34]. L'anisotropie prédite vaut quant à elle $\Delta v_x/\Delta v_y = 2{,}6$, en bon accord là aussi avec l'expérience compte tenu de l'incertitude expérimentale.

expérience	a	b	c
désaccord à résonance $\Delta/2\pi$ (GHz)	+1,5	+2,1	+2,1
hauteur de chute z_0 (mm)	3,6	3,6	2,05
vitesse incidente v_i (v_{rec})	45,1	45,1	34,0
Δv_x mesuré (v_{rec})	$6{,}6 \pm 0{,}2$	$5{,}7 \pm 0{,}2$	$5{,}2 \pm 0{,}2$
Δv_x calculé (v_{rec})	$6{,}60 \pm 0{,}36$	$5{,}68 \pm 0{,}28$	$5{,}48 \pm 0{,}28$
angle de diffusion $\delta\theta_x$ calculé	8,4°	7,2°	9,2°

Tableau 3.2 — Comparaison entre expérience et théorie de la réflexion diffuse pour plusieurs paramètres expérimentaux. L'intensité à la surface est la même pour toutes les expériences et vaut 210 W/cm^2.

Comparison between experiment and theory for the diffuse reflection of the BEC, for different parameters. The laser intensity at the surface is 210 mW/cm^2 for all the experiments.

Nous avons répété cette expérience pour une autre valeur du désaccord et une autre hauteur de lâcher. Là encore, les résultats sont en excellent accord avec les prédictions théoriques, comme le montre le tableau 3.2. À hauteur de chute donnée, la diffusion est plus marquée à désaccord plus faible (a et b). En effet, le point de rebroussement classique est plus loin de la surface pour un déplacement lumineux plus grand ; or, la rugosité, qui est produite par l'interférence entre l'onde évanescente et les ondes diffusées qui se propagent librement, décroît moins vite quand on s'éloigne de la surface ($e^{-\kappa z}$) que l'onde purement évanescente ($e^{-2\kappa z}$). Le contraste de la rugosité est donc plus marqué à plus grande distance [79]. D'autre part, lorsque les atomes ont une vitesse incidente inférieure (expérience c comparée à b), la diffusion angulaire est plus importante pour l'argument déjà évoqué puisqu'ils pénètrent moins dans l'onde évanescente rugueuse. La largeur en vitesse après rebond peut cependant être plus faible comme c'est le cas ici en raison justement de la vitesse incidente plus faible : $\Delta v_x = \delta\theta_x\, v_i$.

Cette étude quantitative a permis pour la première fois de vérifier expérimentalement la théorie de la réflexion diffuse [80]. Il est crucial de tenir compte de la rugosité dans les expériences impliquant des atomes froids au voisinage de surface, que ce soit pour des diélectriques [68] ou des dépôts magnétiques [81]. Dans le contexte des puces à atomes, l'équipe d'Orsay a d'ailleurs démontré [82, 83] que la rugosité des fils déposés

6. Ce chiffre prend en compte l'interaction avec la paroi dans le calcul du point de rebroussement classique, ce qui n'est pas le cas dans la référence [34] qui donnait donc 6,76 v_{rec}. L'incertitude sur la prédiction provient d'une incertitude de ±0,1 GHz sur la valeur du désaccord et de ±10% sur l'intensité à la surface, 210 W/cm^2.

sur la puce était responsable de la fragmentation des condensats confinés trop près du fil, ce qui avait été observé par plusieurs équipes [84, 85, 86, 87].

3.4 Diffraction temporelle d'ondes de matières par un miroir vibrant

L'optique et l'interférométrie atomiques sont des applications naturelles des condensats de Bose-Einstein, qui constituent une source d'onde de matière cohérente. L'une des premières expériences a consisté en l'observation de franges d'interférence entre deux condensats en expansion balistique [88]. Un condensat incident sur un réseau optique est diffracté très efficacement, que ce soit dans le domaine spatial ou temporel avec un réseau pulsé. La diffraction ne fait pas en réalité appel à la cohérence du condensat, mais elle est d'autant plus efficace que la source est monochromatique, ce qui fait des condensats le système idéal pour observer la diffraction d'ondes de matière. Nous avons illustré cela par une expérience de diffraction sur un miroir vibrant. Cette expérience est proche de celle menée par l'équipe de Jean Dalibard [89], la différence étant que l'utilisation d'un condensat permet d'obtenir directement la diffraction après un seul rebond, sans qu'une phase de filtrage dans l'espace des impulsions ne soit nécessaire.

On pourrait penser que la diffusion importante lors de la réflexion sur le prisme empêche la séparation des ordres de diffraction. En réalité, comme cela est clairement apparent sur les images par absorption de la figure 3.6*a*, le nuage atomique, quoique très large dans la direction horizontale, se focalise après rebond dans la direction verticale. Cet effet est purement balistique [90, 44]. Nous avons tiré parti de cette bonne résolution verticale pour les expériences de diffraction du condensat.

La diffraction sur un miroir vibrant est due à la modulation de la phase atomique qu'impose l'oscillation du miroir à la pulsation Ω. Pour satisfaire les conditions aux limites à la surface d'un miroir infiniment raide, l'onde atomique réfléchie acquiert un facteur de phase $e^{ik_i \Delta z \cos(\Omega t)}$ où $\hbar k_i = M v_i$ est l'impulsion du paquet d'onde atomique incident. Elle se décompose donc en ordres de diffraction avec un poids dans chaque ordre $p \in Z$ donné par des fonctions de Bessel $|J_p(k_i \Delta z)|^2$, alors que l'énergie de chaque paquet est modifiée d'une quantité $p\,\hbar\Omega$.

Dans le cas d'un miroir à onde évanescente, qui n'est donc pas infiniment raide, ce résultat est modifié par la décroissance exponentielle du potentiel. L'approche semi-classique adoptée par Carsten Henkel et ses collègues [91] est bien adaptée pour décrire la modulation de la phase atomique si $k_i \gg \kappa$ et si la profondeur de modulation $\kappa \Delta z$ est faible. C'est bien le cas dans nos expériences, où l'impulsion incidente des atomes $\hbar k_i = M\sqrt{2gz_0}$ est très supérieure à $\hbar\kappa$, ou de façon équivalente, la longueur d'onde de Broglie atomique, de l'ordre d'une vingtaine de nanomètres, est très inférieure à $2\pi\kappa^{-1} = 585$ nm. De plus, la profondeur de modulation ε reste faible. Les poids attendus

dans les différents ordres de diffraction p s'écrivent alors

$$\mathcal{P}(p) = \left| J_p \left[\varepsilon \frac{k_i}{\kappa} \beta(Q) \right] \right|^2 , \tag{3.7}$$

$$\text{avec} \quad Q = \frac{\Omega}{\kappa v_i} \tag{3.8}$$

$$\text{et} \quad \beta(x) = \frac{\frac{\pi}{2}x}{\mathrm{sh}(\frac{\pi}{2}x)} . \tag{3.9}$$

Pour induire une vibration du miroir, le courant de la diode laser créant l'onde évanescente est modulé sinusoïdalement à la fréquence $\Omega = 2\pi \times 500$ kHz. Cela a essentiellement pour effet de moduler le désaccord à la résonance, et par conséquent l'amplitude du potentiel dipolaire. Dans la mesure où l'amplitude relative ε de cette modulation reste faible (inférieure à 8 % dans nos expériences), elle se traduit par une variation sinusoïdale de la hauteur effective du miroir :

$$U(z,t) = U_0\, e^{-2\kappa z}(1 + \varepsilon \cos(\Omega t)) \simeq U_0\, e^{-2\kappa z + \varepsilon \cos(\Omega t)} = U_0\, e^{-2\kappa(z - \Delta z \cos(\Omega t))} \tag{3.10}$$

avec $\Delta z = \varepsilon/(2\kappa)$. Nous avons négligé ici l'interaction avec la surface, qui joue peu dans la mesure où le point de rebroussement classique est toujours assez loin de la surface pour cette série de données ($k_L z > 1{,}2$).

L'expérience est conduite de la même manière que pour l'observation du rebond simple. On prépare un condensat de 200 000 atomes dans le piège magnétique. Ces atomes sont ensuite relâchés au-dessus du prisme, à une altitude z_0 contrôlée par les bobines de translation. L'onde évanescente modulée est allumée pendant 2,2 ms au moment du rebond, enfin on prend une image par absorption lorsque les atomes sont au voisinage de l'altitude maximale après rebond, ce qui permet de bien séparer les ordres de diffraction. L'expérience est reproduite pour différentes valeurs de la profondeur de modulation et de la hauteur de lâcher, résumées dans le tableau 3.3.

expérience	a	b	c
fréquence de modulation $\Omega/2\pi$ (kHz)	500	500	500
désaccord à résonance $\Delta/2\pi$ (GHz)	+2,1	+2,1	+2,1
modulation du désaccord $\delta\Delta/2\pi$ (MHz)	130	163	163
profondeur de modulation ε	6,2%	7,8%	7,8%
amplitude de vibration Δz (nm)	2,9	3,6	3,6
hauteur de chute z_0 (mm)	3,60	3,60	2,05
$\varepsilon \frac{k_i}{\kappa} \beta(Q)$ (argument de J_p)	1,33	1,67	0,93
temps de vol (ms)	27+27	27+27	20+20

Tableau 3.3 — Paramètres utilisés pour les trois expériences de diffraction présentées à la figure 3.9.

Parameters of the three diffraction experiments presented in figure 3.9.

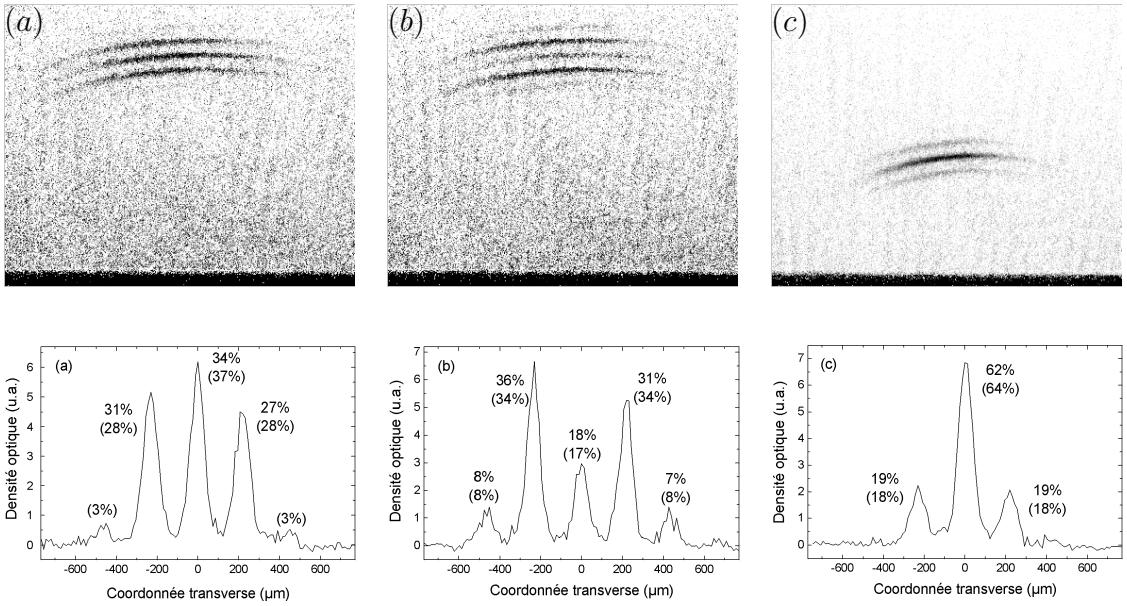

Figure 3.9 — Diffraction dans le domaine temporel d'un condensat de Bose-Einstein sur un miroir vibrant à onde évanescente. Les paramètres correspondant aux trois expériences (a), (b) et (c) sont donnés dans le tableau 3.3. Les images d'absorption, en haut, sont accompagnées en dessous d'une coupe dans la direction verticale. Le poids dans les différents ordres est indiqué à côté du pic correspondant, ainsi que la valeur théorique entre parenthèses.

Diffraction in the time domain of a BEC by a modulated evanescent wave mirror. The parameters of experiments (a), (b) *and* (c) *are given in Table 3.3. Upper row : Absorption pictures. Lower row : Corresponding vertical cuts.*

Les données expérimentales sont présentées sur la figure 3.9. On distingue clairement jusqu'à cinq ordres de diffraction, de -2 à $+2$. La position et le poids dans les différents ordres sont très bien reproduits par la théorie semi-classique [91].

3.5 Conclusion

L'objectif initial de la réalisation d'un piège bidimensionnel avec des ondes évanescentes n'a pas été atteint avec ce montage. Cela est lié d'une part à la forte rugosité de surface que nous avons constatée, d'autre part aux contraintes que le traitement de surface impose au choix des longueurs d'onde des deux faisceaux, rendant difficile l'utilisation de très grands désaccords. Avec un laser YAG et un laser Titane-Saphir et un prisme non traité, ce qui correspond à la configuration que nous avons considérée pour les calculs numériques, l'équipe de Rudi Grimm a pu piéger un gaz thermique proche du régime 2D [71]. Cependant, cet objectif initial a été le fil conducteur d'une série d'expériences intéressantes que nous avons menées avec le prisme et le condensat. D'une part, nous avons montré qu'il était possible de produire le condensat très proche d'une surface diélectrique, à 3 mm, à une époque où les expériences avec des puces à

atomes n'avaient pas encore permis la réalisation de condensats. D'autre part, nous avons étudié en détail l'interaction du condensat avec la surface rugueuse lors du rebond, en collaboration avec Carsten Henkel pour la théorie. Ce travail, qui a confirmé par l'expérience la théorie élaborée auparavant dans le groupe d'Orsay [80], s'inscrit dans le contexte plus large des interactions entre condensats et surfaces, notamment la surface des fils dans les puces à atomes. La rugosité du bord des fils est à l'origine de la fragmentation d'un condensat allongé [82, 84, 85, 86, 87], et un comportement similaire a été observé dans un piège 2D à la surface d'un diélectrique, les atomes restant confinés dans les défauts de l'onde évanescente bleue même en l'absence d'un confinement latéral par une deuxième onde rouge [68]. Enfin, nous avons montré que la rugosité du prisme n'empêche pas l'observation de la diffraction temporelle des atomes lorsque l'amplitude du déplacement lumineux à la surface est modulée dans le temps. Une expérience d'interférométrie à partir de ce que l'on peut considérer comme une séparatrice du paquet d'onde [92], impliquant plusieurs rebonds successifs, est possible en principe, la rugosité n'impliquant pas de perte de cohérence, comme cela est clair d'après les expériences de diffraction. Cependant, en raison de la chute importante de densité qui résulte de l'étalement transverse du nuage, il est plus réaliste pour une telle expérience d'utiliser une surface de rebond beaucoup plus lisse, pour conserver une densité notable après plusieurs rebonds, comme cela a été observé dans le groupe de Jean Dalibard avec un miroir concave [60].

3.6 Articles en relation avec ce chapitre

Je reproduis ici quatre articles [33, 74, 34, 93] en relation avec ce chapitre.

INSTITUTE OF PHYSICS PUBLISHING JOURNAL OF OPTICS B: QUANTUM AND SEMICLASSICAL OPTICS

J. Opt. B: Quantum Semiclass. Opt. **5** (2003) S1–S9 PII: S1464-4266(03)56474-6

Schemes for loading a Bose–Einstein condensate into a two-dimensional dipole trap

Yves Colombe[1], Demascoth Kadio[1], Maxim Olshanii[2], Brigitte Mercier[1], Vincent Lorent[1] and Hélène Perrin[1]

[1] Laboratoire de physique des lasers, CNRS-Université Paris 13, 99 av. Jean-Baptiste Clément, F-93430 Villetaneuse, France
[2] Department of Physics and Astronomy, University of Southern California, Los Angeles, CA 90089-0484, USA

Received 13 November 2002, in final form 11 February 2003
Published
Online at stacks.iop.org/JOptB/5/S1

Abstract
We propose two loading mechanisms of a degenerate Bose gas into a surface trap. This trap relies on the dipole potential produced by two evanescent optical waves far detuned from the atomic resonance, yielding a strongly anisotropic trap with typical frequencies 40 Hz × 65 Hz × 30 kHz. We present numerical simulations based on the time-dependent Gross–Pitaevskii equation of the transfer process from a conventional magnetic trap into the surface trap. We show that, despite a large discrepancy between the oscillation frequencies along one direction in the initial and final traps, a loading time of a few tens of milliseconds would lead to an adiabatic transfer. Preliminary experimental results are presented.

Keywords:

(Some figures in this article are in colour only in the electronic version)

1. Introduction

Bose–Einstein condensates (BECs) of alkali atoms [1] as sources of coherent matter waves are of considerable interest in atom optics and interferometry. The first atom interferometry experiment using a BEC was performed in 1997 [2]. Since then, interferometry has been used to probe the condensate coherence length [3], to give a signature for the Mott insulator transition in an optical lattice [4] and to test restricted geometry effects [5]. This last example is a witness to the increasing interest in BEC in reduced dimensions [6].

The 2DEG (two-dimensional electron gas) is a very rich system in condensed matter physics, giving rise for example to the fractional quantum Hall effect [7] and to anyonic quasi-particles [8]. It is also a convenient medium for electronic interferometry [9]. By analogy, a 2DAG (two-dimensional atomic gas) would give access to a new regime of quantum degeneracy [10]. Most of the theoretical work investigating this field predicts specific phenomena not encountered in the 3D geometry, such as a progressive coherence below a critical temperature and a modification of the mean field interaction [11]. The realization of a 2D condensate is also a preliminary step for the production and the manipulation of anyonic quasi-particles [12]. Finally integrated atom optics, where the matter waves can be guided in an arbitrary way, represents an important technological challenge.

The most convenient ways to realize a 2D confinement of alkali atoms use either Zeeman interaction [13] or ac Stark optical potentials [14]. The Zeeman method is based on the current-carrying micro-wires technique which has been used with success to produce BEC in quasi-1D geometries [15, 16]. This technique may be adapted to produce an exponentially decaying B field [13]. The advantage is the use of a simple device yielding a large energy spacing of the lowest-lying vibrational levels. The main drawback is the heating produced by proximity magnetic fields above the metallic surface, due to thermal fluctuations. Atoms sitting at distances below 1 μm will eventually suffer a high rate of scattering [17]. To our knowledge, no experimental demonstration of this suggested mechanism has yet been realized.

On the other hand 2D trapping with dipole forces has been performed in standing waves [18] or with atoms stopped by an evanescent wave and transferred to the nodes or anti-nodes of a far off-resonant standing wave close to a metallic or dielectric surface [19, 20]. An inhomogeneous trap in one direction is also naturally produced with two evanescent light waves and the resulting Morse-like potential is conservative for sufficiently large frequency detunings. This idea was proposed more than ten years ago by Ovchinnikov *et al* [21]. A good trap geometry is not the only issue for the realization of a 2D gas. An efficient loading of this trap is also essential. A loading scheme of a double evanescent wave trap (DEWT) based on a dissipative transfer of cold atoms has been proposed by Dalibard and Desbiolles [22] and extended for larger frequency detunings [23]. Recently, a group in Innsbruck succeeded for the first time in loading a DEWT from a dense dipole trap with 20 000 Cs atoms at a temperature as low as 100 nK [24]. All those mechanisms deal with non-condensed atoms. Our paper focuses on the loading of a DEWT from a BEC cloud. We address here two types of loading process and compare their advantages. Our approach is based on adiabatic transformations of combined magnetic plus dipole traps up to the final stage of a DEWT.

The paper is organized as follows: section 2 describes the principle of the DEWT and gives our proposed parameters; section 3 explains the method of loading starting from two different kinds of trap:

(i) the usual magnetic Ioffe–Pritchard trap or
(ii) the anti-nodes of a moving red detuned standing wave as a conveyor belt from the magnetic trap to the DEWT.

Details are given in this section about the numerical solutions of the time-dependent Gross–Pitaevskii equation (GPE). In section 4, we present the experimental apparatus and give our preliminary results: production of a ^{87}Rb BEC near a dielectric surface and transportation of a thermal cloud to this surface.

2. Principle of the double evanescent wave trap (DEWT)

Let us first recall briefly the criterion for reaching the 2D regime for atoms confined in a 3D harmonic trap, with trapping frequencies $\omega_x, \omega_y \ll \omega_z$. In the case of a degenerate Bose gas, the chemical potential μ_{3D} calculated for the 3D geometry should fulfil the inequality $\mu_{3D} \ll \hbar\omega_z$. This leads to a constraint on the atom number $N \ll N_{BEC}^{2D}$ where $N_{BEC}^{2D} = \gamma\omega_z^{3/2}/(\omega_x\omega_y)$ [6]. With the parameters of ^{87}Rb one gets $\gamma = 800\sqrt{2\pi}$ rad s^{-1}. By contrast, a 2D classical gas is obtained if $k_B T \ll \hbar\omega_z$. This makes sense if the transition temperature $k_B T_c \simeq \hbar(\omega_x\omega_y\omega_z N)^{1/3}$ also fulfils this inequality. The requirement on the atom number for a classical 2D gas is thus $N \ll N_{cl}^{2D}$ where $N_{cl}^{2D} = \omega_z^2/(\omega_x\omega_y)$ whatever the atom. N_{cl}^{2D} is less than N_{BEC}^{2D} as soon as ω_z is less than $2\pi \times 640$ kHz for ^{87}Rb, which is the case in most experiments including ours. We will discuss the validity of the 2D regime in our case later in this section.

The quasi-2D trap we describe in this paper was first proposed by Ovchinnikov *et al* [21]. It consists in two evanescent light waves produced by total internal reflection at the surface of a dielectric material (see figure 1). One of the light fields is red detuned by δ_r with respect to the atomic transition whereas the other one is blue detuned by δ_b. The angles of incidence of both beams at the dielectric–vacuum interface are chosen such that the decay length of the red field $1/\kappa_r$ is larger than the decay length of the blue field $1/\kappa_b$. The light shift produced by the two fields results in a Morse-like potential along z, with a long-range attractive potential and a short-range repulsive wall near the surface. A radial confinement (x and y directions) is achieved with appropriate waists for the red and the blue beams, typically choosing a smaller waist for the red beam. The overall potential seen by the atoms also includes the van der Waals attractive potential towards the dielectric surface.

As our goal is to load such a trap with a degenerate Bose gas, we paid particular attention to keeping the spontaneous emission rate as low as possible. The light shift of a field of intensity[3] I detuned by δ scales as I/δ whereas the spontaneous scattering rate scales as I/δ^2. At constant light shift, the use of larger detunings and therefore larger intensities is thus preferable. The practical constraints on the availability of laser sources led us to the choice of a YAG laser of a few watts at 1064 nm for the red field and a laser source of a few hundred milliwatts detuned by a few nanometres for the blue field, typically a titanium–sapphire laser. Note that the Innsbruck group came to the same conclusions [24].

We now give the expression of the 2D trapping potential for ^{87}Rb atoms in the $5S_{1/2}$ $F = 2$ state. The two trapping beams of wavelength λ_r and λ_b enter a dielectric prism of refraction index n in the xz plane where z is the direction orthogonal to the surface. The angles of incidence at the dielectric–vacuum interface are θ_r and θ_b, both above the critical angle for total internal reflection $\theta_c = \arcsin(1/n)$. The decay length of the red evanescent wave is then $\kappa_r^{-1} = \sqrt{n^2 \sin^2\theta_r - 1}\,\lambda_r/2\pi$. A similar expression holds for κ_b^{-1}.

As the detuning of the YAG laser is large as compared to the fine structure of the excited state Δ_{FS}, we can consider the transition as a $J = 0 \longrightarrow J' = 1$ transition. The light shift of the ground state due to the red field is always scalar, regardless of the polarization of the evanescent light. Therefore, we choose a TM polarization for this beam, which gives rise to a higher transmission coefficient at the dielectric–vacuum interface. We will denote by δ_r the detuning of the YAG beam with respect to the D2 line at 780 nm. In the following, we do not differentiate between δ_r and $\delta_r + \Delta_{FS}$.

On the other hand, as the detuning between the blue field and the D2 line is smaller than Δ_{FS} we have to take into account the contributions of both D1 (at 795 nm) and D2 lines to the light shift. The detuning with respect to the D2 line will be denoted as δ_b, whereas the detuning with respect to the D1 line is $\delta_b + \Delta_{FS}$. As δ_b is different from $\delta_b + \Delta_{FS}$, the light shift potential will be scalar only if the polarization of the blue evanescent field is linear. In order to ensure a uniform trapping potential for all Zeeman sub-states, we choose a TE polarization for the incoming blue wave, which ensures a linear polarization along y for the evanescent field.

We denote by P_r and P_b the powers of the red and blue beams respectively *inside* the dielectric medium, while w_r and w_b are the beam waists. The corresponding intensities inside

[3] In the following, we will employ the commonly used term 'intensity' instead of the more accurate 'irradiance' to refer to power divided by area.

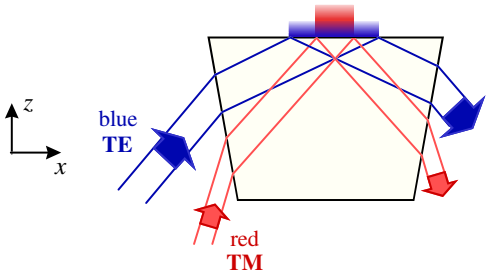

Figure 1. Principle of the 2D evanescent light trap. A red-detuned evanescent wave produces a long-range attractive exponential potential towards the surface (z axis), and a blue-detuned one prevents atomic adsorption through a short-range repulsive potential. Also shown is our choice of polarizations of the incident beams (TE or TM).

Table 1. Values of the 2D trap parameters.

	$P_{r,b}$ (W)	$w_{r,b}$ (μm)	$\lambda_{r,b}$ (nm)	$\theta_{r,b}$ (deg)	$\kappa_{r,b}^{-1}$ (nm)
Red	4	150	1064	44.6	510
Blue	0.5	170	778	50	220

the dielectric at the surface are $I_{r,b} = 2P_{r,b}\cos\theta_{r,b}/\pi w_{r,b}^2$. The intensity of each beam at $z = 0$ in the vacuum depends on its polarization (TE for the blue beam, TM for the red one).

The light shift produced by both beams reads

$$H_{\mathrm{LS}}(\boldsymbol{r}) = \hbar\Gamma[A_r \mathrm{e}^{-2\kappa_r z}\exp(-2x^2\cos^2\theta_r/w_r^2 - 2y^2/w_r^2) + A_b \mathrm{e}^{-2\kappa_b z}\exp(-2x^2\cos^2\theta_b/w_b^2 - 2y^2/w_b^2)] \quad (1)$$

where

$$A_r = t_{TM}^2 \frac{I_r}{2I_s}\frac{\Gamma}{4\delta_r} \quad (2)$$

$$A_b = t_{TE}^2 \frac{I_b}{2I_s}\left(\frac{2}{3}\frac{\Gamma}{4\delta_b} + \frac{1}{3}\frac{\Gamma}{4(\delta_b + \Delta_{FS})}\right). \quad (3)$$

Note that $A_r < 0$. The transmission coefficients for the intensity are

$$t_{TM}^2 = \frac{4n^2\cos^2\theta_r}{n^2-1}\frac{2n^2\sin^2\theta_r - 1}{(n^2+1)\sin^2\theta_r - 1} \quad (4)$$

$$t_{TE}^2 = \frac{4n^2\cos^2\theta_b}{n^2-1}. \quad (5)$$

Here, $\hbar\Gamma$ is the natural linewidth of the excited state and $I_s = 1.6$ mW cm^{-2} is the saturation intensity. The terms in $\cos\theta_{r,b}$ in the exponential appear because of the projection of the beam profile onto the dielectric surface.

The total potential includes the van der Waals interaction with the surface. One has to go beyond the Lennard-Jones potential in $1/z^3$ because the distance to the surface is comparable to $\lambda\!\!\!^{-} = \lambda/2\pi$. Therefore retardation effects cannot be ignored. Landragin [25] gives an analytical correction to the Lennard-Jones potential which approximates the exact result with a 0.6% accuracy between 0 and 10$\lambda\!\!\!^{-}$:

$$H_{\mathrm{vdW}}(z) \simeq f(z/\lambda\!\!\!^{-})H_{\mathrm{LJ}}(z) \quad (6)$$

with

$$f(u) = 0.987\left(\frac{1}{1+1.098u} - \frac{0.004\,93u}{1+0.009\,87u^3 - 0.000\,64u^4}\right) \quad (7)$$

$$H_{\mathrm{LJ}}(z) = \frac{n^2-1}{n^2+1}\frac{1}{4\pi\varepsilon_0}\frac{\langle d^2\rangle}{12}\frac{1}{\lambda\!\!\!^{-}}\left(\frac{\lambda\!\!\!^{-}}{z}\right)^3. \quad (8)$$

For rubidium in the ground state, the mean value of electric dipole squared is $\langle d^2\rangle = 28.2\,e^2a_0^2$ where a_0 is the Bohr radius and e the electron charge.

In the following we give the trap characteristics for a reasonable choice of parameters for the evanescent light, taking into account the available power of laser sources near 780 nm. The proposed values of the parameters are indicated in table 1. The dielectric medium is chosen to be BK7 glass which has a relatively low index of refraction $n = 1.51$ to minimize the van der Waals attraction towards the surface. Using this material, the critical angle for total internal reflection is $\theta_c = 41.5°$.

These values of the trap parameters lead to a very anisotropic potential above the dielectric surface. A cut of the potential along z for $x = y = 0$ is depicted in figure 2, left. The atoms are trapped at a distance $z_0 = 360$ nm from the surface. The trap depth is 180 kHz (or equivalently 9 μK) and is given by the energy difference between the bottom of the trap and the saddle points at $x = 0$, $y = \pm 195$ μm, $z = 300$ nm (see the contour plot in figure 2, right). We have checked with a 1D numerical calculation that the tunnelling from the ground state to the dielectric surface is negligible. The potential is essentially harmonic around the minimum in the x and y directions where the trapping force results from the transverse profile of both beams. The oscillation frequency is smaller along x due to the angle between the beam axis and the surface. In the z direction the trap deviates rapidly from the harmonic approximation. However, the computed oscillation frequency along z at the bottom of the trap gives a good indication of the anisotropy of the potential: $\omega_x = 2\pi \times 41$ Hz, $\omega_y = 2\pi \times 67$ Hz and $\omega_z = 2\pi \times 28$ kHz. The aspect ratio is thus 690 along x and 420 along y. With these parameters, the value of $N_{\mathrm{BEC}}^{\mathrm{2D}}$ is 1.4×10^6 and we get either $\mu_{3\mathrm{D}}/h = 10$ kHz for 10^5 atoms or 4 kHz for 10^4 atoms, to be compared to 28 kHz. The system is thus already in the 2D regime for a reasonably high number of atoms. However, $N_{\mathrm{cl}}^{\mathrm{2D}} = 3 \times 10^5$ is lower than $N_{\mathrm{BEC}}^{\mathrm{2D}}$ and the transition temperature corresponds to about 20 kHz for 10^5 atoms and 9 kHz for 10^4 atoms, which means that only thermal clouds close to the transition temperature could be considered as 2D gases.

As this trap is intended to be loaded with a degenerate Bose gas, the spontaneous scattering rate at the bottom of the trap is an important parameter. It is given by the formula

$$\Gamma_{\mathrm{scatt}} = \Gamma\left[t_{TM}^2\frac{I_r}{2I_s}\frac{\Gamma^2}{4\delta_r^2}\mathrm{e}^{-2\kappa_r z_0} + t_{TE}^2\frac{I_b}{2I_s}\left(\frac{2}{3}\frac{\Gamma^2}{4\delta_b^2} + \frac{1}{3}\frac{\Gamma^2}{4(\delta_b+\Delta_{FS})^2}\right)\mathrm{e}^{-2\kappa_b z_0}\right]. \quad (9)$$

With our choice of parameters we get $\Gamma_{\mathrm{scatt}} = 5$ s^{-1}. This gives a reasonable lifetime for a degenerate gas inside the trap.

3. Loading the 2D trap

The loading of the 2D trap with a degenerate Bose gas is one of the major points to be addressed in this type of experiment. Methods for loading similar traps with classical gases have been demonstrated before. They rely on optical pumping by evanescent waves in the vicinity of the surface [19, 24]. This

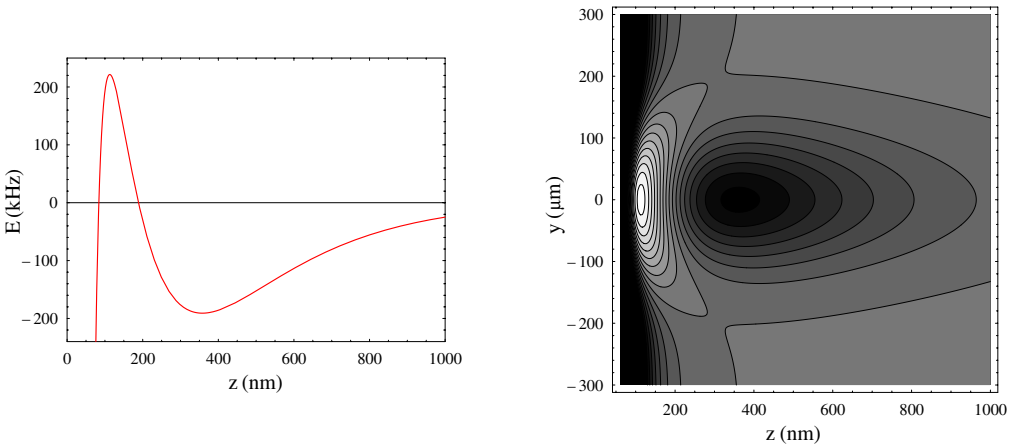

Figure 2. 2D trapping potential plotted with the values presented in table 1. Left: cut along z for $x = y = 0$. The red-detuned evanescent wave produces the long-range attractive potential, whereas the blue-detuned evanescent wave acts as a repulsive wall at short distances. The attractive van der Waals potential is dominant very close to the surface ($z < 100$ nm). Right: contour plot in the yz plane. Subsequent contours are spaced by 25 kHz; darker shades correspond to lower energies. Horizontal confinent is achieved due to the Gaussian transverse profile of the red incident beam.

kind of method is prohibited when dealing with a degenerate gas. In fact, any interaction of the atoms with resonant light should be avoided in order to preserve coherence and reduce heating. In this paper, we propose two different methods for loading the atoms from a magnetic trap, centred a few millimetres above the dielectric surface, into the DEWT. The magnetic trap we start with is a standard cigar-shaped QUIC trap [26] with frequencies $\omega_\perp = 2\pi \times 300$ Hz and $\omega_x = 2\pi \times 21$ Hz (see section 4.1). Both schemes rely on the adiabatic transfer from the magnetic trap into the surface trap. We give a brief description of the methods and present results of numerical simulations of the two transfer processes.

3.1. Scheme 1: magnetic to 2D trap transfer

The first method consists in deforming a translated magnetic trap adiabatically by switching on the evanescent light trap slowly. The atoms are first translated inside a moving magnetic trap to the vicinity of the surface. This is done by adding to the QUIC trap a pair of Helmholtz coils with a vertical axis (see section 4.2). At the same time, the blue-detuned evanescent light field is switched on in order to prevent the atoms from sticking to the surface as they come very close to it. Second, the condensate is transferred into the 2D dipole trap by switching on the red-detuned evanescent wave slowly, thus compressing the cloud strongly in the z direction. Finally, the magnetic field has to be switched off and the atoms remain trapped in the DEWT. The transfer is adiabatic if the variation of the trap frequency $\omega(t)$ fulfils along each direction the following inequality:

$$\frac{\partial \omega}{\partial t} \ll \omega^2. \tag{10}$$

This implies that the ramping time of the evanescent wave must be very large as compared to the oscillating period of the atoms in the trap.

We present here a 3D numerical calculation of part of this process using the time-dependent GPE for the macroscopic wavefunction for a condensate comprising 10^6 atoms. The starting point of the calculation is the ground state of a hybrid trap consisting of the blue-detuned evanescent light plus a magnetic harmonic trap centred at the surface ($z = 0$), see figure 3(a). We then let the wavefunction evolve due to the GPE, while switching on the red evanescent field and the van der Waals potential with an exponential time profile. The total ramping time is T_{ramp}. The calculation ends at time $t_{\text{end}} > T_{\text{ramp}}$ and does not include the magnetic field extinction.

We use the splitting method to evaluate the effect of the total Hamiltonian for a time interval $\mathrm{d}t$: if $\mathrm{d}t$ is small enough, one can let $H_r\,\mathrm{d}t$ and $H_p\,\mathrm{d}t$ commute, where H_r is the part of the Hamiltonian diagonal in the position basis (potential energy plus interactions) and H_p is diagonal in momentum (kinetic energy). The evolution during $\mathrm{d}t$ leads to

$$\psi(t + \mathrm{d}t) = T^\dagger \exp\left(\frac{-\mathrm{i}H_p\,\mathrm{d}t}{\hbar}\right) T \exp\left(\frac{-\mathrm{i}H_r\,\mathrm{d}t}{\hbar}\right)\psi(t) \tag{11}$$

where T represents a fast Fourier transform and $T^\dagger$ its inverse. We calculate the chemical potential μ and the initial wavefunction by solving the time-dependent GPE with the method of imaginary time; we propagate and renormalize $\psi(\tau)$ at each step using the equation

$$\frac{\partial \psi}{\partial \tau} = -\frac{1}{\hbar} H \psi \tag{12}$$

to get a positive chemical potential as small as possible. The corresponding wavefunction represents the ground state of the GPE and is taken as the initial state $\psi(t = 0)$ before deformation. The subsequent evolution is calculated using equation (11) (where H_r is a function of time).

The magnetic trap is chosen to be isotropic with an oscillation frequency $\omega_0 = 2\pi \times 300$ Hz (oscillation period $T_{\text{osc}} = 3.3$ ms) to reduce the calculation time. The 2D trap results from evanescent waves with decay lengths $\kappa_r^{-1} = 510$ nm and $\kappa_b^{-1} = 220$ nm. The light shift at the surface is 5.4 MHz for the blue beam and -1.4 MHz for the red one. The oscillation frequencies in the DEWT alone are $\omega_z = 2\pi \times 30$ kHz along the vertical axis, $\omega_x = 2\pi \times 30$ Hz and $\omega_y = 2\pi \times 64$ Hz in the horizontal plane. The position of the minimum of the potential well along the vertical direction is about 350 nm above the surface of the prism. As ω_x and

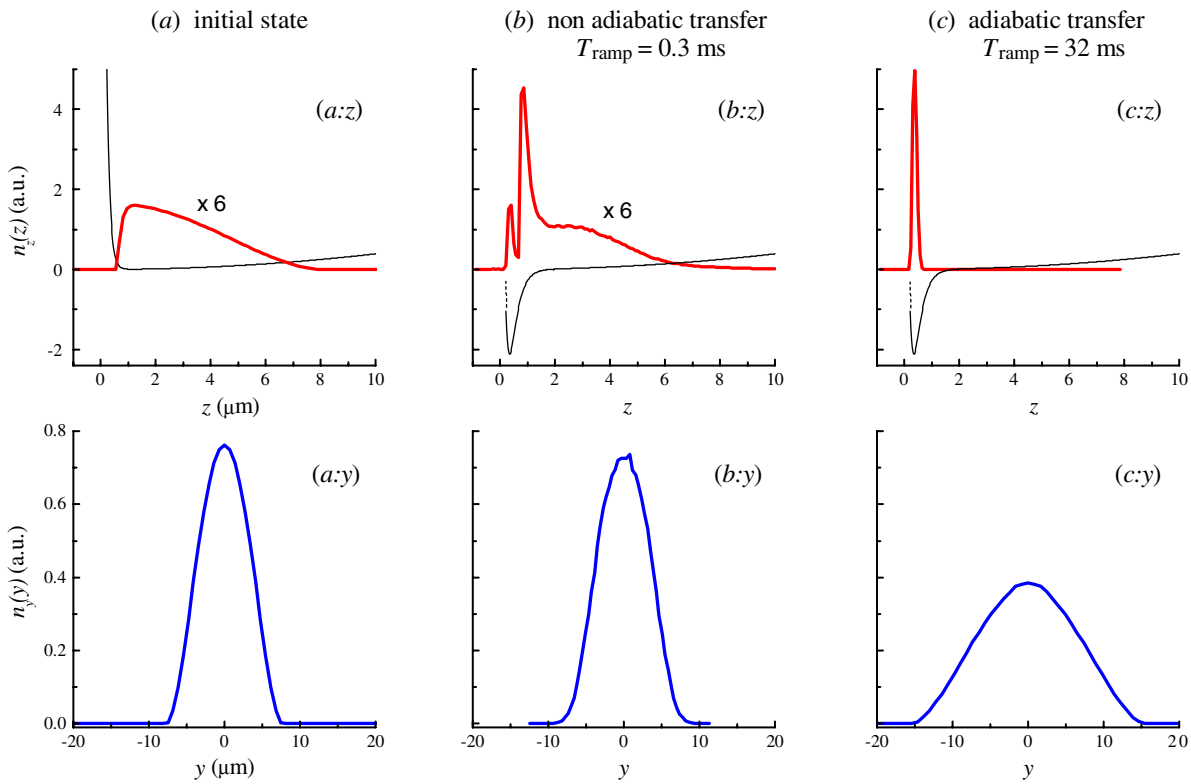

Figure 3. Integrated spatial density along x and y as a function of z ((*a*:*z*) to (*c*:*z*), thick curve) and along x and z as a function of y ((*a*:*y*) to (*c*:*y*)). Note the scaling factor in figures (*a*:*z*) and (*b*:*z*). On figures (*a*:*z*) to (*c*:*z*), the potential is also represented (thin curve). (*a*) shows the initial ground state at $t = 0$ with the red beam off. The other parts represent the atomic density after evolution with the GPE for a time t_{end} for two extreme values of T_{ramp}: for (*b*) $T_{ramp} = 0.3$ ms and $t_{end} = 2.3$ ms whereas for (*c*) $T_{ramp} = 32$ ms and $t_{end} = 42$ ms. In (*c*:*z*), a Gaussian fit of the density profile gives a $1/e^2$ radius of $\sigma = 80$ nm. The radius R obtained by fitting the y profiles with a Thomas–Fermi distribution is $R_a = 7.7$ μm, $R_b = 7.9$ μm and $R_c = 15.5$ μm for (*a*:*y*), (*b*:*y*) and (*c*:*y*) respectively.

ω_y are much smaller than ω_0, the frequency in the horizontal plane changes only slightly from ω_0 to e.g. $\sqrt{\omega_0^2 + \omega_x^2}$ and the criterion for adiabaticity is easily fulfilled horizontally.

The numerical results are shown in figure 3. Figures 3(*a*:*z*) –(*c*:*z*) represent the spatial atomic density integrated along x and y as a function of z together with the trapping potential along z. Figures 3(*a*:*y*)–(*c*:*y*) show the density integrated along x and z and plotted as a function of y. Figure 3(*a*) represents the initial atomic distribution ($t = 0$) of the 10^6 atoms, corresponding to the ground state of the hybrid magnetic plus blue evanescent wave trap. The atomic density along z is not symmetrical due to the steep wall produced by the blue beam. The spatial density for two different ramping times T_{ramp} of the red beam is given in figures 3(*b*) and (*c*).

We observe that almost all the condensate is transferred into the dipole trap for a ramping time $T_{ramp} = 32$ ms much greater than the initial oscillation period T_{osc}, figure 3(*c*). We also note that, in this case, the width of the spatial density along the horizontal direction is enlarged when adding the red beam, compare figure 3(*c*:*y*) with figure 3(*a*:*y*). Indeed when ramping up the red beam intensity slowly, the atomic cloud is compressed along the vertical axis, figure 3(*c*:*z*), and expands in the horizontal directions where the potential energy increases more slowly with distance from the centre.

On the other hand, for a very short ramping time (0.3 ms), only a few atoms are transferred into the 2D dipole trap (figure 3(*b*)). The integrated atomic density along z presents three features: we observe two density peaks with a large difference between their amplitude, plus a broad background. The centre of the smaller peak corresponds to the minimum of the dipole trap and represents the atoms which were transferred successfully. The larger peak sits at the extreme border of the dipole trap well. One can understand this with a simple picture. When we ramp up the red beam quickly, the atoms which were localized at the bottom of the initial potential with almost zero velocity suddenly acquire an energy equal to the depth of the dipole potential. They populate a very narrow band of excited states of the new well and are essentially located at the turning points of the potential. Towards the surface, the potential is very stiff and the atomic velocity changes almost instantaneously. As a result, a single density peak is visible at the right-hand turning point where the potential is much shallower. Note that the respective weight of the two peaks changes as the loading time T_{ramp} is increased: more atoms are transferred in the DEWT, see figure 4, and the second peak is reduced. The background of the distribution represents the atoms which are not much affected by the switching on of the red beam. These atoms were out of the well in the right-hand side of the potential when the red beam was ramped up. The width of the spatial density along the horizontal direction (figure 3(*b*:*y*)) does not change as compared to figure 3(*a*:*y*) due to the poor compression reached in the z direction.

The analysis of the transfer efficiency is presented in figure 4. To estimate the number of transferred atoms, we fit the peak in the z density profile corresponding to the atoms trapped in the DEWT with a Gaussian profile and compare its area to the total number of atoms. The transfer efficiency

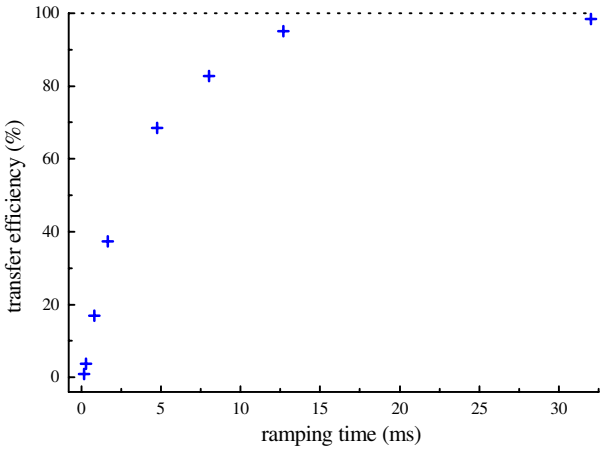

Figure 4. Transfer efficiency as a function of the ramping time. The crosses represent numerical results. The dotted line represents 100% efficiency.

increases non linearly with the ramping time. For a ramping time $T_{\text{ramp}} = 32$ ms, very large as compared to T_{osc}, the difference between the final density profiles and the ground state of the total trap (DEWT + magnetic trap) is imperceptible and the transfer is actually adiabatic. From figure 4 we infer that a 20 ms ramping time is quite enough to realize an adiabatic transfer. Note that in the adiabatic case, as we ramp the magnetic trap off very slowly, the spatial density along the z axis becomes narrower while the horizontal width becomes larger (not shown here). Indeed, the horizontal frequencies of the dipole trap ($\omega_x = 2\pi \times 30$ Hz, $\omega_y = 2\pi \times 64$ Hz) are smaller than those in the initial trap ($\omega_x = \omega_y = 2\pi \times 300$ Hz), and the anisotropy is more pronounced due to the strong confinement along z and the interactions between atoms.

3.2. Scheme 2: the atomic lift

The second method makes use of a moving standing wave to transport the atoms from the magnetic trap into the DEWT. The idea is close to the principle of the conveyor belt recently realized on a micro-chip [27]. At the beginning of the loading process, the atoms are confined in the magnetic trap and the laser fields producing the DEWT are on. The process may be decomposed into three steps.

(i) The atoms are loaded at the anti-nodes of a stationary wave into a series of horizontal planes obtained by two red-detuned counter-propagating beams along z.
(ii) The magnetic field is switched off and the atoms are lifted down towards the surface by changing the phase of one of the beams with respect to the other. The atoms accumulate in the 2D trap by continuous deformation of the potential (figure 5).
(iii) Finally, when all the atoms are in the last well near the surface, the stationary wave is switched off and the atoms remain trapped in the DEWT.

At each step, the different transfers have to remain adiabatic to avoid any heating of the atomic cloud. Step (i) should not pose particular problems as transfer of condensates into optical lattices has already been demonstrated [28]. Note that the atoms remain trapped horizontally even after the magnetic field has been switched off due to the Gaussian profile of the counter-propagating beams, with corresponding horizontal oscillation frequency ω_h. One simply has to switch off the magnetic field adiabatically, that is in a time larger than ω_h^{-1}.

To realize this first step, one can typically use a $\lambda_{\text{lift}} = 830$ nm laser diode with a power of 15 mW in each beam and a waist of 90 μm. This gives $\omega_h = 2\pi \times 60$ Hz. Provided the populated anti-nodes are far from the evanescent waves, the phase change may be very fast, and this gives the atoms a large translational velocity, v_1. When the atoms approach the surface, the velocity must be lowered, to v_2 say, because the horizontal shape of the trap changes. In fact the horizontal frequency seen by an atom changes, in the x direction for example, from ω_h to $\omega_{\max} = (\omega_h^2 + \omega_x^2)^{1/2}$ when it is first loaded in the DEWT, and then changes periodically between $\omega_{\max}$ and ω_x as the phase evolves further to load the remaining atoms. This gives the typical time constant for adiabaticity.

We tested this loading scheme qualitatively with a 3D numerical simulation analogous to the one described in the last section. We were interested mostly in the last stage where the atomic cloud distributed in several planes approaches the surface. The initial state of the calculation ($t = 0$) is the ground state of the GPE in the potential formed by the stationary wave with $\lambda_{\text{lift}} = 800$ nm plus a 1D harmonic potential along z. This potential mimics the situation immediately after the transfer from the magnetic trap into the stationary wave. The 1D potential is centred 3.4 μm above the surface and is switched off at the beginning of the evolution through the time-dependent GPE, while the 2D trap is switched on. At this point ($t = 1.1$ ms), the atoms are spread over a few planes. For an initial vertical oscillation frequency of 300 Hz and 10^5 atoms, typically 15 planes are populated. However, to reduce the calculation time, we start from a condensate in a harmonic trap with a vertical oscillation frequency of 1.6 kHz. In this case, the atoms are spread symmetrically over three planes (see figure 6). The relative phase between the two beams of the standing wave is then allowed to evolve, resulting in the two successive velocities $v_1 = 1.1$ mm s^{-1} and $v_2 = 76$ μm s^{-1}, as mentioned above.

The results of the numerical calculation are shown in figure 6. The column density integrated over x and y is plotted as a function of z at three stages of the loading process. At $t = 5.8$ ms (a) the first populated plane reaches the rim of the last well, which coincides with the 2D trap. At $t = 13.3$ ms (b) two populated planes have melted into the last well. At $t = 22.3$ ms (c) the atoms accumulate in the last well. However, it was not possible to fulfil the condition for adiabatic transfer. As a result, the final atomic density does not coincide with the ground state of the GPE in the DEWT. We shall discuss this point further in the conclusion. Moreover, when the atoms are in the last well of the standing wave before melting, they tunnel through the small barrier separating them from the trap, as can already be seen in (a), thus populating excited states of the DEWT. To limit this phenomenon, both the depth and the typical size of the wells of the standing wave must be adjusted to those of the DEWT. This condition may be a difficult point to address experimentally.

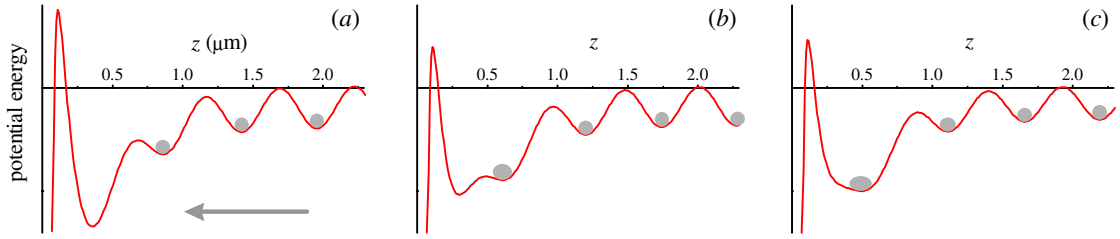

Figure 5. Principle of the atomic lift. Three different stages are shown for three values of the relative phase φ between the two beams of the standing wave. (*a*) $\varphi = 0.6\pi$; (*b*) $\varphi = 1.5\pi$; (*c*) $\varphi = 1.8\pi$.

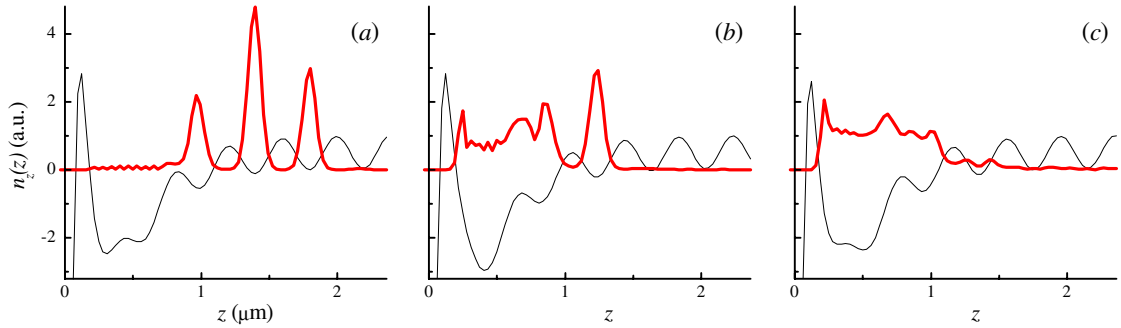

Figure 6. Results of the numerical simulation of the atomic lift: integrated spatial density along x and y as a function of z (thick curve), at three evolution times: (*a*) $t = 5.8$ ms; (*b*) $t = 13.3$ ms; (*c*) $t = 22.3$ ms. The potential is also represented (thin curve).

4. Preliminary experimental results

In this section, we present some preliminary experimental results towards loading of a degenerate Bose gas into a DEWT.

4.1. Experimental set-up

The experimental set-up, figure 7, consists of two ultra-high vacuum chambers separated vertically by 75 cm. In the upper chamber (pressure 10^{-9} Torr) the ^{87}Rb atoms are collected from a vapour in a standard magneto-optical trap (MOT) by three retro-reflected beams ($1/e^2$-diameter 25 mm each, total power 45 mW). This MOT acts as a reservoir for the second MOT in the lower cell where the pressure is below 10^{-11} Torr. The difference in vacuum pressure is ensured by a tube of length 120 mm with an internal diameter of only 6 mm. The lower MOT is set up with six independent laser beams with a $1/e^2$-diameter of 10 mm each for a total power of 45 mW.

The atoms are continuously transferred into the second cell by an original method combining pushing and guiding the atoms. The pushing beam has a power of 30 mW and is detuned by 2.5 GHz on the red side of the MOT $5S_{1/2}$, $F = 2 \longrightarrow 5P_{3/2}$, $F' = 3$ transition. It is focused 8 cm above the upper MOT to a waist of 220 μm such that its radius is 250 μm at the upper MOT and 940 μm at the lower MOT. This beam induces sufficiently large light shifts (30 MHz) so that atoms inside the beam no longer feel the MOT beams; the atoms are extracted from the upper MOT with a radiation pressure about 25 times smaller than that of a typical MOT. The advantage of this method is that the velocity of atoms remains in the capture range of the lower MOT (about 15 m s^{-1}). Furthermore, the pushing beam acts as a dipole trap which guides the atoms vertically near its axis inside the small diameter tube. The depth of this guide is about 1.4 mK at the upper MOT for the $F = 2$ state. A collinear repumping beam, tuned to the $F = 1 \longrightarrow F' = 2$ transition, ensures that the atoms remain in $F = 2$. Due to the divergence of the guiding beam the radiation pressure at the position of the lower trap is negligible. The fact that the atoms are guided while pushed towards the lower cell renders the loading process very robust against small changes in the parameters of the two MOTs.

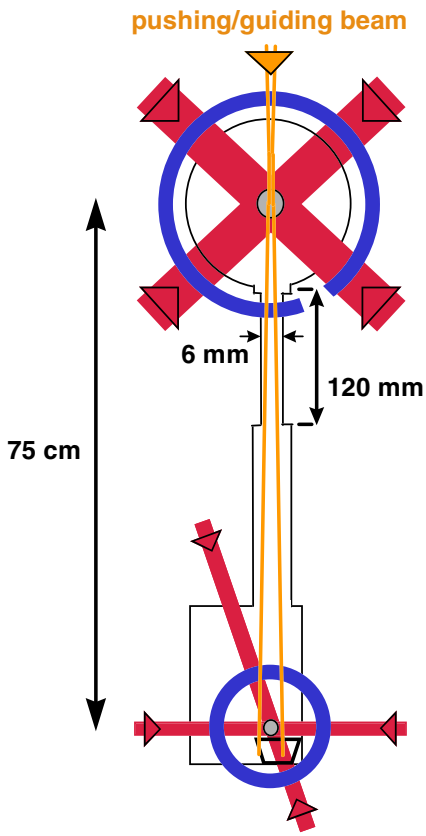

Figure 7. Schematic view of the experimental set-up.

After 30 s of loading time, the atoms are cooled by molasses cooling, compressed and pumped into the $F = 2, m_F = 2$ state. They are then transferred into a Ioffe–Pritchard, cigar-shaped magnetic trap. The coils producing the magnetic field are placed following the quadrupole and Ioffe configuration (QUIC) [26] and dissipate a total electric power of 200 W. They are cooled by thermal contact with water-cooled copper radiators. Two independent current sources are used, one for the Ioffe coil (43 A) and one for the quadrupole coils (30 A). The resulting magnetic field has a minimum B_0 of about 1 G with a field gradient $b' = 225$ G cm^{-1} and a curvature $b'' = 270$ G cm^{-2}. The resulting oscillation frequencies are 21 Hz along the axis of the cigar (x direction) and 300 Hz in the transverse yz plane for the $F = 2, m_F = 2$ state. We achieve BEC after 30 s of RF evaporative cooling.

4.2. Results

The condensate contains typically 2×10^5 atoms and is produced at the centre of the QUIC trap, just above the prism which is the support for the 2D evanescent light trap (see the bottom of figure 7). The vertical position of the prism with respect to the condensate may be adjusted mechanically. However, it is limited to at least 3 mm to maintain a correct loading efficiency of the MOT. By adding to the QUIC trap a uniform vertical magnetic field varying from 0 to 64 G the minimum of the trapping potential is moved down to the surface of the prism, as required by the first 2D-transfer scheme. This field is produced by ramping up a current from 0 to 20 A in two additional horizontal coils separated by 4 cm, each having 30 windings of mean diameter 16 cm. During the ramp, the current in the quadrupole coils of the QUIC trap is lowered by about 5%; otherwise, the trap would cross a zero of the magnetic field and the atoms would separate into two clouds. The resulting potential near the centre of the trap remains essentially unaltered apart from an increase of a factor of 1.6 in the oscillation frequency along the slow axis (from 21 to 33 Hz). This axis is also slightly tilted, in agreement with the magnetic field calculations. To illustrate the translation process, we filled the initial QUIC trap with a sample of thermal atoms at $T = 9$ μK centred 3.7 mm above the prism and imaged the atomic cloud at several steps of its journey towards the surface, figure 8. When the current in the additional coils reaches 20 A, the atoms are lost by contact with the surface in the absence of a blue-detuned evanescent wave.

As the experiment was performed with a non-condensed cloud, the next step will be to extend it to a BEC. The blue and red beams have then to be added to the experimental set-up. Preliminary experiments with a blue beam alone were realized: a bounce of thermal atoms released from the QUIC trap 3.7 mm above the prism was observed. However, the detuning $\delta_b = 2\pi \times 500$ MHz was too small for the beam to be used in a loading experiment and it will be replaced by an appropriate laser source. This should allow us to test experimentally the first transfer scheme.

5. Conclusion

In this paper, we studied two possible methods for loading a degenerate Bose gas into a strongly anisotropic trap.

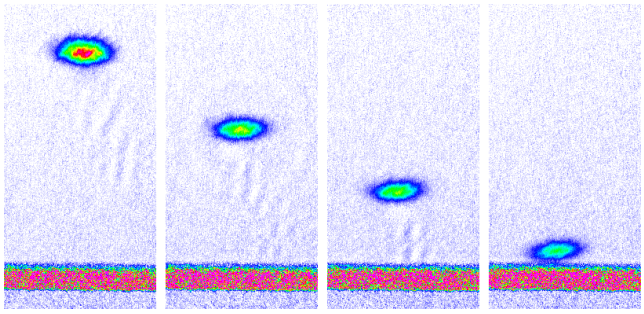

Figure 8. Absorption images of a thermal cloud at temperature 9 μK approaching the prism. Each 2.5 mm × 5 mm image is taken 4 ms after switching off the magnetic fields, at different steps of a 1 s, 0–20 A current ramp in the additional coils. The final values of the current are 0, 10, 15 and 18.4 A respectively. When reaching 20 A, the atoms are lost by contact with the surface in the absence of a blue-detuned evanescent wave.

The first method is also the simpler one. We have demonstrated experimentally with a thermal cloud the first stage corresponding to the vertical translation of the atomic cloud. We simulated the transfer from the translated QUIC trap into the DEWT. When the criterion for adiabaticity is fulfilled the transfer efficiency is close to 100%. The simulation assumed an isotropic magnetic trap with oscillation frequency $\omega_0 = 2\pi \times 300$ Hz. In the experimental situation, one of the horizontal frequencies is $\omega_{0x} = 2\pi \times 33$ Hz only and the loading time may have to be increased by a small factor. The last stage corresponds to the extinction of the magnetic field and should not pose particular problems providing that the switching time is much longer than the horizontal frequencies in the DEWT. We believe that this loading method could be implemented experimentally. The difficulty is to adjust the horizontal position of the magnetic trap to the centre of the DEWT. This can be done by changing slightly the balance between the currents in the QUIC coils.

The second method has the great advantage of compressing the atomic cloud already in the QUIC trap before the atoms are loaded into the DEWT. The translation stage towards the surface (velocity v_1) may be faster than in the last method, as the vertical oscillation frequency in the series of planes is on the order of a few tens of kilohertz instead of 300 Hz. The accumulation stage into the DEWT by a phase sweep seems to be an elegant idea. However, the phase velocity v_2 is strongly limited if one tries to fulfil the adiabaticity condition. In fact, for horizontal frequencies $\omega_h = 2\pi \times 60$ Hz in the standing wave and $\omega_x = 2\pi \times 30$ Hz in the DEWT, the frequency change between ω_x and $\sqrt{\omega_h^2 + \omega_x^2}$ has to be slower than ω_x. Therefore the velocity v_2 has to be much smaller than $\lambda_{\text{lift}}/4 \times \omega_x/2\pi = 6$ μm s^{-1} to avoid 2D breathing mode excitation. The typical time to load 15 planes is then a few seconds. This is still an order of magnitude too large to be of interest for practical applications. To reduce this time, one may either increase the horizontal frequency during the loading process, or compress the cloud initially to populate fewer horizontal planes. Another problem that will occur with this loading method is the phase noise in the standing wave. The study of its influence on the loading mechanism is out of the scope of this paper. However, a recent work in Bonn showed that is produces heating and reduces the lifetime in a standing wave trap [29].

Finally, let us note that the second method may be used in a reverse way to extract the 2DAG and study it far from the surface: once the atoms are confined in the DEWT, one can slowly switch on a standing wave and change the relative phase to lift the atoms away from the surface. It is then easier to produce a single 2D trap with a very high aspect ratio with less laser power.

Acknowledgments

We are indebted to Y Castin and D Lemoine for fruitful discussions, and to R J Butcher for a critical reading of the manuscript. We acknowledge support from the Région Ile-de-France (contract number E1213). Laboratoire de physique des lasers is UMR 7538 of CNRS and Paris 13 University.

References

[1] Anderson M H *et al* 1995 *Science* **269** 198
Davis K B *et al* 1995 *Phys. Rev. Lett.* **75** 3969
Bradley C C *et al* 1997 *Phys. Rev. Lett.* **78** 985
see also
Bradley C C *et al* 1995 *Phys. Rev. Lett.* **75** 1687

[2] Andrews M R, Townsend C G, Miesner H-J, Durfee D S, Kurn D M and Ketterle W 1997 *Science* **275** 637

[3] Bloch I, Hänsch T W and Esslinger T 2000 *Nature* **403** 166

[4] Greiner M, Mandel O, Esslinger T, Hänsch T W and Bloch I 2002 *Nature* **415** 39

[5] Dettmer S, Hellweg D, Ryytty P, Arlt J J, Ertmer W, Sengstock K, Petrov D S, Shlyapnikov G V, Kreutzmann H, Santos L and Lewenstein M 2001 *Phys. Rev. Lett.* **87** 160406

[6] Görlitz A, Vogels J M, Leanhardt A E, Raman C, Gustavson T L, Abo-Shaeer J R, Chikkatur A P, Gupta S, Inouye S, Rosenband T and Ketterle W 2001 *Phys. Rev. Lett.* **87** 130402

[7] Tsui D C, Störmer H L and Gossard A C 1982 *Phys. Rev. Lett.* **48** 1559
Laughlin R B 1983 *Phys. Rev. Lett.* **50** 1395

[8] See e.g.
MacDonald A H 1995 *Mesoscopic Quantum Physics (Les Houches 94 Summer Session)* ed E Akermans *et al* (Amsterdam: Elsevier)

[9] See e.g.
Buks E, Schuster R, Heiblum M, Mahalu D and Umansky V 1998 *Nature* **391** 871

[10] Bagnato V and Kleppner D 1991 *Phys. Rev.* A **44** 7439

[11] Petrov D and Shlyapnikov G 2001 *Phys. Rev.* A **64** 012706

[12] Paredes B, Fedichev P, Cirac J I and Zoller P 2001 *Phys. Rev. Lett.* **87** 010402

[13] Hinds E A, Boshier M G and Hughes I G 1998 *Phys. Rev. Lett.* **80** 645

[14] For an overview of these traps see
Grimm R, Weidemüller M and Ovchinnikov Y B 2000 *Adv. At. Mol. Opt. Phys.* **42** 95–170

[15] Hänsel W, Hommelhoff P, Hänsch T W and Reichel J 2001 *Nature* **413** 498

[16] Ott H, Fortágh J, Grossmann A and Zimmermann C 2001 *Phys. Rev. Lett.* **87** 230401

[17] Henkel C and Wilkens M 1999 *Europhys. Lett.* **47** 414
Henkel C and Pötting S 2001 *Appl. Phys.* B **72** 73

[18] Bouchoule I, Morinaga M, Salomon C and Petrov D S 2002 *Phys. Rev.* A **65** 033402
Vuletić V, Kerman A J, Chin C and Chu S 1999 *Phys. Rev. Lett.* **82** 1406

[19] Gauck H, Hartl M, Schneble D, Schnitzler H, Pfau T and Mlynek J 1998 *Phys. Rev. Lett.* **81** 5298

[20] Cornelussen R A, van Amerongen A H, Wolschrijn B T, Spreeuw R J C and van Linden van den Heuvell H B 2002 *Eur. Phys. J.* D **21** 347

[21] Ovchinnikov Y, Shul'ga S and Balykin V 1991 *J. Phys. B: At. Mol. Opt. Phys.* **24** 3173

[22] Desbiolles P and Dalibard J 1996 *Opt. Commun.* **132** 540

[23] Perrin H, Mercier B, Gorlicki M, Ducloy M, Keller J-C and Lorent V 2000 *IQEC'2000, 22th Int. Quantum Electronics Conf. (Nice, Sept. 2000)* p 107 (book of abstracts)

[24] Hammes M, Rychtarik D, Engeser B, Nägerl H-C and Grimm R 2002 *Preprint* physics/0208065

[25] Landragin A 1997 *PhD Thesis* Orsay University, France
Marani R, Cognet L, Savalli V, Westbrook N, Westbrook C I and Aspect A 2000 *Phys. Rev.* A **61** 053402
Wylie J M and Sipe J E 1984 *Phys. Rev.* A **30** 1185
Wylie J M and Sipe J E 1985 *Phys. Rev.* A **32** 2030

[26] Esslinger T, Bloch I and Hänsch T W 1998 *Phys. Rev.* A **58** R2664

[27] Hänsel W, Reichel J, Hommelhoff P and Hänsch T W 2001 *Phys. Rev. Lett.* **86** 608
see also
Schrader D, Kuhr S, Alt W, Müller M, Gomer V and Meschede D 2001 *Appl. Phys.* B **73** 819

[28] Pedri P, Pitaevskii L, Stringari S, Fort C, Burger S, Cataliotti F S, Maddaloni P, Minardi F and Inguscio M 2001 *Phys. Rev. Lett.* **87** 220401

[29] Alt W, Schrader D, Kuhr S, Müller M, Gomer V and Meschede D 2003 *Phys. Rev.* A at press

J. Phys. IV France **1** (2003) Pr1-1

Adiabatic transportation of a Bose–Einstein condensate to a dielectric surface

Y. Colombe[1], H. Perrin[1], B. Mercier[1] and V. Lorent[1]

[1] *Laboratoire de physique des lasers, CNRS-Université Paris 13, 99, av. Jean-Baptiste Clément, 93430 Villetaneuse, France*

Abstract

We present the adiabatic transportation of a Bose–Einstein condensate from a standard magnetic trap to a dielectric surface located 3.7 mm below. The shifting of the trapping potential is obtained by ramping up an additional homogeneous magnetic field in 100 ms. It is the first stage of the adiabatic transfer of the condensate from the initial 3D magnetic trap into a 2D evanescent light trap sitting at the dielectric surface.

1 INTRODUCTION

Bose–Einstein condensates (BECs) are coherent atomic ensembles that have become a subject of prime interest in atom optics and many-body physics. Among the various topics under study are the regimes of quantum degeneracy in 1D or 2D, which are expected to exhibit specific properties [1]. Such very anisotropic geometries are obtained in free space by magnetic fields originated from macroscopic currents [2] (1D), or by the dipole force of light in the far field domain [3] (1D and 2D). Alternatively, atoms are confined at very short distances above a surface by microscopic current-carrying wires [4] (1D) or by light in the near field domain [5] (2D). These surface traps are also a step towards integrated atom optics components that will use guided matter waves to perform interferometric measurements with high precision.

2 LOADING A 3D BEC INTO A 2D SURFACE TRAP

Our goal is to load a 2D evanescent wave trap with a regular 3D BEC. The condensate of about 200 000 ^{87}Rb atoms is produced in a standard magnetic trap, similar to the one described in [6], with radial and longitudinal oscillation frequencies $\omega_\perp = 2\pi \times 220\,\mathrm{Hz}$ and $\omega_\parallel = 2\pi \times 21\,\mathrm{Hz}$. The 2D trap, detailed in [7], will be set by two evanescent light waves in the vicinity of a dielectric surface, acting on the atoms in their ground state by ac Stark effect. One evanescent wave at $\lambda_r = 1064\,\mathrm{nm}$ provides an attractive force towards the surface, whereas the other at $\lambda_b = 778\,\mathrm{nm}$ acts as a short-range repulsive wall. The resulting potential is very flat, with oscillation frequencies $\omega_\perp = 2\pi \times 28\,\mathrm{kHz}$, $\omega_{\parallel,1} = 2\pi \times 67\,\mathrm{Hz}$ and $\omega_{\parallel,2} = 2\pi \times 41\,\mathrm{Hz}$. The centre of the quasi-2D trap lies only 360 nm above the surface. The loading of the BEC into the 2D trap consists in three stages : first, the centre of the magnetic trap is shifted down to the surface while the repulsive wave is present; second, the attractive wave is turned on in 20 ms;

eventually, the magnetic field is turned off. Numerical simulations in [7] show that this loading scheme should be adiabatic, *i.e.* achieve the transfer of the BEC into the ground state of the 2D trap.

3 ADIABATIC TRANSPORTATION OF THE BEC

We realised the first stage of the transfer by ramping up in 100 ms a vertical homogeneous magnetic field produced by two additional horizontal Helmholtz coils (Fig.1). Since the repulsive evanescent wave has not been set up, atoms are lost when reaching the surface.

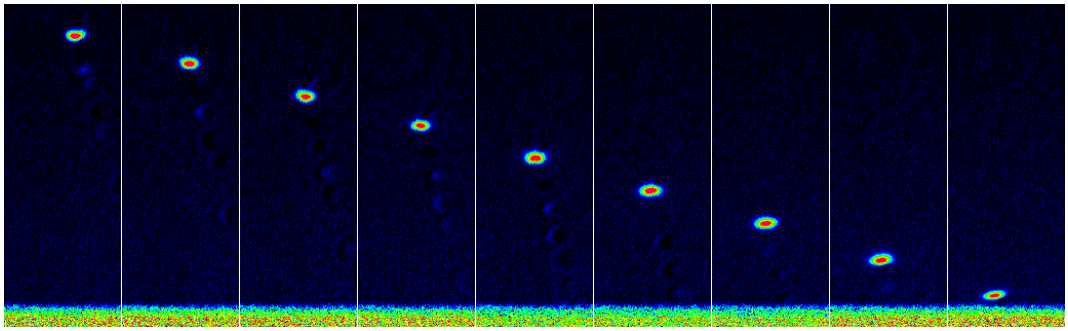

Fig. 1. Absorption images showing the magnetic transportation of a condensate over 3.7 mm in 100 ms. The final values of the current in the additional coils range from 0 to 20.2 A (not shown: atoms are lost by contact with the dielectric surface).

The ramping of the current is smoothed at the beginning and at the end of the journey to avoid any heating of the BEC. The adiabaticity of the process is checked by going through 90% of the ramp, bringing the BEC the same way back to the original trap in 90 ms, and releasing it. The time-of-flight analysis demonstrates that no losses nor heating of the condensate occur during the transportation.

ACKNOWLEDGMENTS

We would especially like to thank J. Reichel and F. Schreck for sharing their respective softwares driving the experiment and the CCD camera.

References

[1] Pricoupenko L., Perrin H. and Olshanii M., eds., Proceedings of the Euroschool on Quantum Gases in Low Dimensions, Les Houches, 15 - 25 April 2003, *J. Phys. IV*, in press.

[2] Schreck F., Khaykovich L., Corwin K.L., Ferrari G., Bourdel T., Cubizolles J. and Salomon C., *Phys. Rev. Lett.* **87** (2001) 080403.

[3] Görlitz A., Vogels J.M., Leanhardt A.E., Raman C., Gustavson T.L., Abo-Shaeer J.R., Chikkatur A.P., Gupta S., Inouye S., Rosenband T. and Ketterle W., *Phys. Rev. Lett.* **87** (2001) 130402.

[4] Hänsel W., Hommelhoff P., Hänsch T.W. and Reichel J., *Nature* **413** (2001) 498-501.

[5] Rychtarik D., Engeser B., Nägerl H.-C. and Grimm R., preprint cond-mat/0309536 (2003).

[6] Esslinger T., Bloch I. and Hänsch T.W., *Phys. Rev. A* **58** (1998) R2664-R2667.

[7] Colombe Y., Kadio D., Olshanii M., Mercier B., Lorent V. and Perrin H., *J. Opt. B: Quantum Semiclass. Opt.* **5** (2003) S155-S163.

INSTITUTE OF PHYSICS PUBLISHING JOURNAL OF PHYSICS B: ATOMIC, MOLECULAR AND OPTICAL PHYSICS

J. Phys. B: At. Mol. Opt. Phys. **39** (2006) 4649–4658 doi:10.1088/0953-4075/39/22/009

Diffuse reflection of a Bose–Einstein condensate from a rough evanescent wave mirror

Hélène Perrin[1], Yves Colombe[1], Brigitte Mercier[1], Vincent Lorent[1] and Carsten Henkel[2]

[1] Laboratoire de Physique des Lasers, Université Paris 13, 99 avenue Jean-Baptiste Clément, 93430 Villetaneuse, France
[2] Institut für Physik, Universität Potsdam, Am Neuen Palais 10, 14469 Potsdam, Germany

E-mail: henkel@uni-potsdam.de

Received 12 May 2006, in final form 5 September 2006
Published 1 November 2006
Online at stacks.iop.org/JPhysB/39/4649

Abstract
We present experimental results showing the diffuse reflection of a Bose–Einstein condensate from a rough mirror, consisting of a dielectric substrate supporting a blue-detuned evanescent wave. The scattering is anisotropic, more pronounced in the direction of the surface propagation of the evanescent wave. These results agree very well with theoretical predictions.

1. Introduction

The study of the interactions between ultracold atoms and surfaces is of major interest in the context of Bose–Einstein condensation on microchips [1, 2]. One motivation is to understand the limitations on integrated matter wave devices due to imperfect surface fabrication or finite temperature. For example, it has been shown that the quality of the wires used in microfabricated chips is directly linked to the fragmentation effects observed in Bose–Einstein condensates (BECs) trapped near a metallic wire [3]. Moreover, the thermal fluctuations of the current in a metallic surface induce spin flip losses in an atomic cloud when the distance to the surface is smaller than 10 μm typically [4].

Dielectric surfaces and evanescent waves have also been explored for producing strong confinement. They have the advantage of a strong suppression of the spin flip loss mechanism compared to metallic structures [5]. With such a system, one can realize mirrors [6], diffraction gratings [7], 2D traps [8] or waveguides [9]. Experiments involving ultracold atoms from a BEC at the vicinity of a dielectric surface have recently made significant progress, leading for instance to the realization of a two-dimensional BEC [10], to the study of atom-surface reflection in the quantum regime [11], and to sensitive measurements of adsorbate-induced surface polarization [12] and of the Van der Waals/Casimir–Polder surface interaction [13].

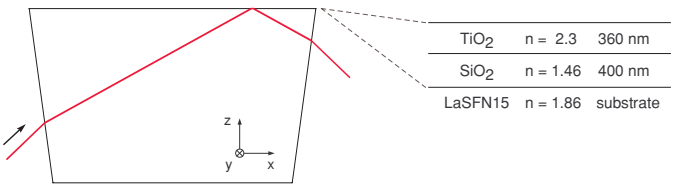

Figure 1. Dielectric prism supporting the evanescent wave. The surface is coated by two layers of successively low and high refraction index to realize a waveguide and enhance the evanescent field. For each incident polarization, TE or TM, coupling is resonant for a given incident angle. The experiments were performed with TE polarization. One denotes x as the propagation axis of the evanescent wave along the surface, y as the other horizontal axis and z as the vertical one.

In this paper, we present experimental results and a related theoretical analysis of Bose-condensed rubidium atoms interacting with the light field of an evanescent wave above a dielectric slab. The evanescent wave is detuned to the blue of an atomic transition line and provides a mirror for a BEC that is released from a trap and falls freely in the gravity field of the earth. After the bounce off the mirror, we observe a strong scattering of the atomic cloud (diffuse mirror reflection) that is due to the roughness of the slab surface where the evanescent wave is formed [14]. In our case, the phase front of the reflected matter waves is significantly distorted because the effective corrugation of the mirror is comparable to $\lambda_{\mathrm{dB}}/4\pi \cos\theta$ where λ_{dB} is the incident de Broglie wavelength and θ is the angle of incidence. This is similar to early experiments with evanescent waves [14] and with magnetic mirrors [15]. We mention that later experiments achieved a significantly reduced diffuse reflection (Arnold *et al* [16]) and were even able to distinguish a specularly reflected matter wave (Savalli *et al* [17]). The key result of our experiment is that we can quantitatively confirm the theoretical analysis developed by Henkel *et al* [18], combining independent measurements of the dielectric surface and the bouncing atoms.

The paper starts with a presentation of the experiment and an analysis of the experimental results, following [19]. We then outline an improved theoretical analysis based on [18] and discuss the momentum distribution of the reflected atoms, in particular its diffuse spread and its isotropy.

2. Set-up

The evanescent wave is produced by total internal reflection of a Gaussian laser beam at the surface of a dielectric prism. As shown in figure 1, the surface of the prism is coated by two dielectric layers, a TiO_2 layer on top of a SiO_2 spacer layer. This coating forms an optical waveguide that resonantly enhances the evanescent field above the top layer [20]; we have designed this configuration for the study of two-dimensional atom traps [21]. The incident angle of the laser beam is fixed by the resonance condition for a waveguide mode; for the transverse electric (or s) polarization we use, the incident angle is $\theta_i = 46.1^\circ$ (at the TiO_2/vacuum interface, index $n_{\mathrm{TiO_2}} = 2.3$). The resulting exponential decay length of the light field is $\kappa^{-1} = 93.8$ nm, and $I = I_0\,\mathrm{e}^{-2\kappa z}$ is the light intensity.

The mirror light is produced by a laser diode of power 40 mW detuned 1.5 GHz above the atomic D2 line ($\lambda = 780$ nm or $1/\lambda = k_L/2\pi = 12\,820\ \mathrm{cm}^{-1}$). The Gaussian beam is elliptical and produces on the surface a spot with $1/\sqrt{e}$ waist diameters of 220 μm along x and 85 μm along y (see coordinate axes in figure 1). A measurement of the reflection threshold for the atom beam, taking into account the van der Waals attraction towards the

surface (Landragin *et al* in [6]), gives access to the light intensity at the surface in the spot centre: $I_0 = 210$ W cm^{-2}. This value is lower than expected from the design of the dielectric coating; we attribute this to the losses due to the roughness of the deposited TiO_2 layer (see figure 4 below and the discussion there).

3. Atom bounce

3.1. Data

The experiment proceeds as follows: approximately 10^8 atoms are confined in the hyperfine ground state $F = 2, m_F = 2$ in a Ioffe Pritchard (IP) type magnetic trap, 3.6 mm above the evanescent mirror [21]. The magnetic trap is cigar shaped, x being its long axis. Oscillation frequencies are, respectively, $\omega_x/2\pi = 21$ Hz and $\omega_\perp/2\pi = 220$ Hz in the radial directions (y and z). The atoms are evaporatively cooled to below the condensation threshold and about $N = 3 \times 10^5$ atoms are released at $t = 0$ by switching off the magnetic trapping fields. These atoms reach the mirror after free fall at $t_{\mathrm{reb}} = 27$ ms and bounce on it with a velocity $v_i = 265$ mm s^{-1} (quasi-normal incidence, de Broglie wavelength $\lambda_{\mathrm{dB}} = 2\pi\hbar/mv_i = 17.3$ nm). Around the bouncing time t_{reb}, the mirror laser is switched on for $\Delta t = 2.2$ ms. Limiting this time window Δt prevents near-resonant photon scattering during free fall or after reflection.

The atoms are detected by absorption imaging either before or after reflection. During free fall, the cloud expands along the radial directions because potential and interaction energy is released, but its width along x remains nearly constant. The analysis of pictures taken before reflection gives access to the following parameters: fraction of condensed atoms $N_0/N = 0.4$, kinetic temperature of thermal cloud $T = 285$ nK, initial Thomas–Fermi size along x of the condensed fraction $R_x = 90$ μm and Thomas–Fermi velocity width along z: $V_\perp = 5.96$ mm s^{-1}. The condensate velocity width along x is very small; thus non-directly measurable. However, it can be inferred from the knowledge of $V_\perp$ and the oscillation frequencies in the magnetic trap, using the solution for an expanding BEC [22]; we get $V_x = \frac{\pi}{2}\frac{\omega_x}{\omega_\perp}V_\perp = 0.89$ mm s^{-1}. The observation of the centre-of-mass motion during free fall permits us to calibrate the pixel size knowing gravity's acceleration and to infer the initial position and velocity of the cloud. The magnetic field switching process communicates a small acceleration to the atoms along x, resulting in a horizontal velocity $v_x = -30.7$ mm s^{-1} ($\theta \approx 6.6°$, see figure 2, left).

After reflection, the absorption images change dramatically (figure 2). The atoms occupy the surface of a scattering sphere, hence an elastic, but strongly diffuse scattering occurs. For $t > t_{\mathrm{reb}}$, the cloud width along x increases from its initial value due to an additional velocity spread σ_{v_x}. The velocity Gaussian radius at $1/\sqrt{e}$ deduced from the pictures is 39.4 mm s^{-1}. Taking into account the initial velocity width before reflection, the spread due to diffuse reflection is $\sigma_{v_x} = 39$ mm s^{-1}, that is $6.6 \pm 0.2 v_{\mathrm{rec}}$ where $v_{\mathrm{rec}} = \hbar k_L/m = 5.89$ mm s^{-1} is the recoil velocity for Rb. This corresponds to an angular (rms) spread $\Delta\theta \approx 8.4°$.

The effect of diffuse reflection along y is more subtle to analyse, as this axis is aligned with the direction of observation. However, it is possible to extract information about σ_{v_y} from the picture. If for instance the scattering were totally isotropic, with $\sigma_{v_y} = \sigma_{v_x}$, the atomic cloud should extend asymmetrically towards $-z$ at a given position x, as the projection of a spherical shell onto a plane extends towards the inner part of the circle (see figure 3). If in contrast the scattering were to take place only along x, the cloud width along z at a given position x should be very small, with a symmetric shape.

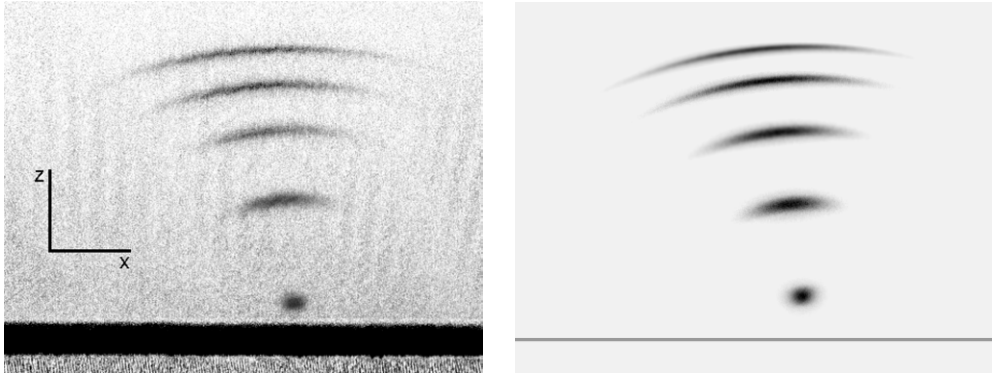

Figure 2. Left: absorption imaging pictures of a bouncing BEC with 3×10^5 atoms for different times of flight after reflection: 2 ms, 7 ms, 12 ms, 17 ms and 22 ms. The pictures, taken with a 200 μs long, resonant pulse, are merely superimposed. The wide black line in the bottom is due to the prism surface, slightly tilted from the imaging axis. Picture dimensions are 5.7 mm × 4.4 mm. Right: simulation of a bouncing BEC with 3×10^5 atoms for the same times of flight as the experimental ones, left. For this series, the velocity spread was chosen to be $\sigma_{v_y} = \sigma_{v_x}/2 = 19.5$ mm s^{-1}. The position of the mirror surface is marked by a grey line.

3.2. Simulation

To get some insight into what happens along y, we performed a numerical simulation of the atomic reflection. The simulation calculates $N = 3 \times 10^5$ individual classical atomic trajectories. The initial positions and velocities are chosen to mimic the experimentally measured parameters: 40% of the atoms are 'condensed' and are described by the initial 3D Thomas–Fermi velocity and position distribution. (We neglect the position spread along y and z because its contribution to the cloud size after a few ms of time of flight is very small.) The remaining 60% of the atoms are distributed according to Gaussian profiles for velocity and position, with widths inferred from the knowledge of temperature and trap parameters. The position and velocity of the cloud centre are fixed to the experimental values as well. The mirror is modelled as an instantaneous diffuse reflector. This assumption is reasonable as the typical time spent in the evanescent wave is small, $1/\kappa v_i = 0.35$ μs. After reflection, the atomic velocity is modified to describe both specular reflection (inversion of vertical velocity) and scattering. A random horizontal velocity is added to the reflected velocity with a Gaussian distribution. We take a $1/\sqrt{e}$ radius $\sigma_{v_x} = 39$ mm s^{-1}, as measured experimentally, and run simulations with varying σ_{v_y}. The z component of the velocity is adjusted in order to preserve kinetic energy (the scattering process is elastic, total energy is conserved). The simulation also takes into account spontaneous emission. For our parameters, the atom spontaneously emits on average 0.13 photons per bounce[3]. We randomly draw the number of photons from a Poisson distribution and add a recoil of $1 v_{\mathrm{rec}}$ in a random direction in velocity space for each emission event. After calculation of all atomic trajectories, the atomic density profile is integrated along y as in the experimental pictures. We finally apply a Gaussian blur filter (width $\sigma_{\mathrm{res}} = 9$ μm along x and 20 μm along z) to mimic the finite resolution of the experimental imaging system that we calibrated independently.

[3] This value is deduced from an integration of the number of scattered photons along the mean classical atomic trajectory, calculated from the known evanescent wave parameters. We neglect the variation of the spontaneous emission rate at the vicinity of the surface. This assumption is reasonable as the classical turning point is rather far from the surface ($k_L z_0 = 1.33$). See [23].

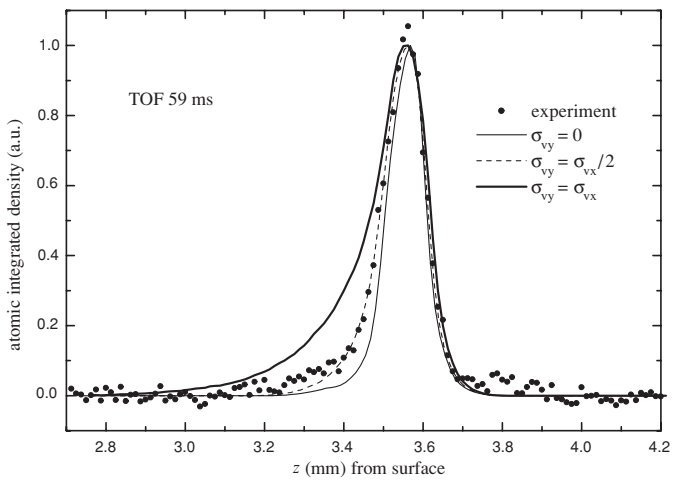

Figure 3. Atomic density profiles integrated along y and averaged along x, after 59 ms total time of flight, i.e. 32 ms after reflection. Closed circles: normalized experimental data. Lines: result of numerical calculation with a starting height of 3.59 mm above the mirror, $N_0/N = 0.4$, $V_y = V_z = V_\perp = 5.96$ mm s^{-1}, $V_x = 0.89$ mm s^{-1}, $R_x = 90$ μm, $T = 285$ nK, $v_x = -30.67$ mm s^{-1}, $v_z = 0.3$ mm s^{-1} and $\sigma_{v_x} = 39$ mm s^{-1}, values deduced from the experimental pictures. Thin line: totally anisotropic scattering ($\sigma_{v_y} = 0$); dashed line: anisotropic scattering with $\sigma_{v_y} = \sigma_{v_x}/2$; bold line: isotropic scattering ($\sigma_{v_y} = \sigma_{v_x}$). All curves are normalized to a maximum value of unity.

3.3. Anisotropic scattering

The qualitative agreement between the experimental and simulated pictures is very good as can be seen in figure 2, right. To be more quantitative for the possible values of the velocity spread σ_{v_y}, we analyse the central part of the cloud. For each time of flight, a region of size 0.8 mm $\times$ 1.5 mm along x and z respectively, centred on the maximum density of the cloud and identical for experimental and simulated pictures, is isolated and an integration of the signal is performed along x. We are left with a cut of the cloud along z, averaged over 0.8 mm along x. The experimental profile is compared to the simulated one, for different choices of σ_{v_y} after the bounce. Results are shown in figure 3 for a time of flight of 59 ms.

The experimental data clearly exclude an isotropic diffuse reflection (figure 3, bold line). They also are different from the pure one-dimensional scattering case (thin line): what fits best of all is a model intermediate between these two extremes, i.e. the scattering is only half as strong along y compared to x. The atom mirror thus has an angular reflection characteristic that is elongated in the direction parallel to the (real part of the) wave vector of the evanescent wave. Spontaneous emission plays only a minor density role for our parameters, but we found that the agreement with the experimental profiles is improved by taking it into account, in particular on the lower left wing of the peak.

3.4. Mirror corrugation

For a theoretical prediction of the anisotropic mirror reflection, we use the theory of [18] where the diffuse scattering is attributed to the interference between the evanescent wave and light diffusely scattered from the rough glass surface. Within this theory, one can compute the width of the momentum distribution of the reflected atoms provided the power spectrum

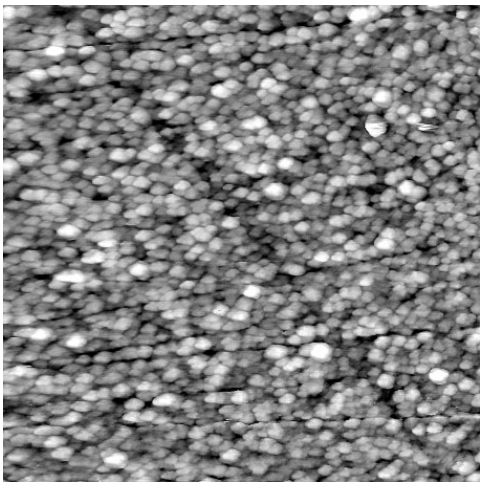

Figure 4. Typical AFM picture of the prism surface. The dimensions are 4.5 μm × 4.5 μm. The grains are the top facets of pillar-like structures characteristic of an epitaxed TiO_2 surface.

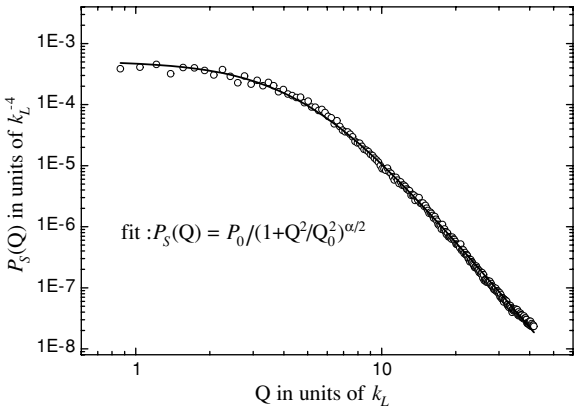

Figure 5. Open circles: power spectrum $P_S(Q)$ deduced from the AFM measurement. Solid line: fit of the data by the function given in equation (1).

of the surface roughness is known. This power spectrum is a quantitative measure of the surface quality and has been measured with an atomic force microscope (AFM). A typical 4.5 × 4.5 μm^2 portion of the surface of the coated prism is shown in figure 4. One sees the top face of pillar-like structures which are typical for epitaxially grown TiO_2 on a substrate. The AFM data yield a surface roughness $\sigma = 3.34$ nm (the rms spread of the measured surface profile). A Fourier transform of the AFM image gives access to the power spectrum $P_S(\mathbf{Q})$. (We use capitalized boldface letters for two-dimensional vectors in the mirror plane.) It is found to be isotropic (a function of Q only) and well fitted in the wave vector range $1k_L \ldots 13k_L$ by a power law with a low-frequency cut-off (see figure 5)

$$P_S(\mathbf{Q}) = \frac{P_0}{\left(1 + Q^2/Q_0^2\right)^{\alpha/2}}. \tag{1}$$

The fit gives access to the parameters $\alpha = 4.8$, $P_0 = 5.3 \times 10^{-4}\, k_L^{-4}$ and $Q_0 = 4.94 k_L$. In terms of this power spectrum, the rms surface roughness σ is given by

$$\sigma^2 = \int \frac{\mathrm{d}^2 Q}{(2\pi)^2} P_S(\mathbf{Q}), \tag{2}$$

and the fitted parameters yield $\sigma = 3.36$ nm, in excellent agreement with the value directly deduced from the rms spread of the AFM data.

3.5. Diffuse reflection theory and comparison to the data

We now show that the diffuse reflection we observe can be understood within the theory of [18]. We note first that the cloud is so dilute at the bounce that a single-atom picture is sufficient to capture the physics [24]. For a fixed incident momentum $\mathbf{p}_{\mathrm{inc}} = \mathbf{P} - \mathbf{e}_z m v_i$ near normal incidence, the reflected wavefunction can be written in the form of a plane wave with a randomly modulated phase front:

$$\psi_{\mathrm{refl}}(\mathbf{r}) = N \exp \mathrm{i}[\mathbf{p}_{\mathrm{spec}} \cdot \mathbf{r} + \delta\phi(\mathbf{R})], \tag{3}$$

where N is a normalization factor and $\mathbf{p}_{\mathrm{spec}} = \mathbf{P} + \mathbf{e}_z m v_i$. (The dependence on the angle of incidence is actually negligible for our parameters [18].) The phase $\delta\phi(\mathbf{R})$ depends on the 'impact position' $\mathbf{R}$ on the mirror, i.e., the projection of $\mathbf{r}$ onto the mirror plane. We perform an ensemble average over the realizations of the rough surface and compute the atomic momentum distribution $P_A(\mathbf{P}+\hbar\mathbf{Q})$ from the (spatial) Fourier transform of the 'atomic coherence function' (section 6 of [18])

$$\langle \psi^*_{\mathrm{refl}}(\mathbf{r}) \psi_{\mathrm{refl}}(\mathbf{r}') \rangle = N^2 \exp \mathrm{i}[\mathbf{p}_{\mathrm{spec}} \cdot (\mathbf{r}' - \mathbf{r})] \exp\left[-\tfrac{1}{2}\langle(\delta\phi(\mathbf{R}) - \delta\phi(\mathbf{R}'))^2\rangle\right], \tag{4}$$

(We take $\langle \delta\phi(\mathbf{R}) \rangle = 0$, assuming the roughness to be statistically homogeneous.) The variance of the phase shift can be found from the following formula (equations (6.15) and (5.16) of [18]):

$$\langle \delta\phi(\mathbf{R}) \delta\phi(\mathbf{R}') \rangle = \int \frac{\mathrm{d}^2 Q}{(2\pi)^2} P_S(\mathbf{Q}) |B_{\mathrm{at}}(\mathbf{Q})|^2 \, \mathrm{e}^{\mathrm{i}\mathbf{Q}\cdot(\mathbf{R}-\mathbf{R}')}, \tag{5}$$

where $B_{\mathrm{at}}(\mathbf{Q})$ is the 'atomic response function' given in equation (5.15) of [18]. For the parameters of our experiment, we find that the phase shift has a variance $\langle \delta\phi^2(\mathbf{R}) \rangle = 16.5$; large compared to unity. In this regime, [18] has shown that the reflected atomic velocity distribution approaches a Gaussian shape whose width along the x-direction, for example, is given by

$$\frac{\sigma^2_{v_x}}{v^2_{\mathrm{rec}}} = \frac{1}{k_L^2} \int \frac{\mathrm{d}^2 Q}{(2\pi)^2} Q_x^2 P_S(\mathbf{Q}) |B_{\mathrm{at}}(\mathbf{Q})|^2. \tag{6}$$

This expression gives the additional broadening of the incident velocity distribution due to the diffuse mirror reflection. We perform the integration of equation (6) numerically, with the roughness power spectrum determined previously from the AFM images (equation (1)). For simplicity, we calculate the response function $B_{\mathrm{at}}(\mathbf{Q})$ using scalar light scattering from the topmost interface only, ignoring the actual layered structure. We believe that this approximation is sufficient, at least for describing the scattering in the x-direction: as shown in [18], the atom does not change its magnetic sublevel if it scatters in this direction and if the evanescent wave is linearly polarized. These conditions are met here so that both atom and light can be described by scalar wave fields.

Within the theoretical model outlined above, the velocity spread along the propagation direction of the evanescent wave is found to be $\sigma_{v_x} = 6.76 v_{\mathrm{rec}}$. This value is in very good

agreement with the experimental value $6.6 \pm 0.2 v_{\mathrm{rec}}$. This is a very satisfying result because the theory only contains, within the approximations we made, parameters that are based on independent measurements. We believe that this is the first quantitative test of a theory of evanescent wave scattering in the diffuse regime.

3.6. Discussion of the anisotropy

We also compute the anisotropy of the reflected atoms and find a ratio $\sigma_{v_x}/\sigma_{v_y} = 2.6$, in good agreement with the value (2 ± 0.5) extracted from the experimental data. As discussed in [18], this anisotropy arises from the fact that diffuse reflection occurs predominantly by Bragg transitions where a photon is absorbed from the evanescent wave (with the wave vector $k_x = k_L n_{\mathrm{TiO_2}} \sin\theta_i$) and another photon is emitted into a diffusely scattered mode that emerges at grazing incidence into the vacuum half-space (or the inverse process). If these scattered modes are distributed isotropically in the mirror plane on a circle of radius $r_{\mathrm{sc}} k_L$, the ratio of the rms spreads would be $\sigma_{v_x}/\sigma_{v_y} = (2(n_{\mathrm{TiO_2}} \sin(\theta_i)/r_{\mathrm{sc}})^2 + 1)^{1/2}$. Taking $r_{\mathrm{sc}} = 1$, which corresponds to scattered modes emerging at grazing incidence, we again find an anisotropy ratio of $\approx$2.5. This agreement is not very surprising since the rough surface has a power spectrum much broader than the photon wavenumber k_L (figure 5). Within this simple calculation, however, we can also get a quick estimate of the impact of the dielectric coating. The choice $r_{\mathrm{sc}} = n_{\mathrm{TiO_2}} \sin(\theta_i)$ corresponds to resonant scattering into waveguide modes in the TiO_2 layer and leads to a ratio $\sigma_{v_x}/\sigma_{v_y} = \sqrt{3}$ which cannot be excluded experimentally.

4. Conclusion

In conclusion, we have observed the diffuse reflection of an ultracold atomic beam from an evanescent wave. The wave propagates on the rough surface of a dielectric prism, and light scattering leads to an atom mirror showing a significantly nonspecular reflection. The angular broadening of the reflected atom momenta, as well as their anisotropic angular distribution in the mirror plane, are in good agreement with a theory developed by Henkel *et al* [18]. It is remarkable that this agreement does not imply any free parameters since we independently measured the spectrum of the surface roughness with an AFM. In our experiment, using a BEC has mainly practical advantages. Indeed, as we mentioned above, everything can be understood within a single-atom picture, and after diffuse scattering, spatial coherence is seriously reduced, as is discussed in [18] and investigated in [25]. Nevertheless, the BEC provides crucial advantages because we achieve a very clean situation. Apart from a very low velocity spread $V_x \ll \sigma_{v_x}$, a BEC has a negligible size when impacting the evanescent wave surface. This removes the need to take into account the mirror curvature due to the Gaussian spot profile; the contribution of the initial size to the cloud width after reflection is negligible; and the losses given the finite size of the mirror (the waist of the reflected laser beam) are minimal. In fact, with a freely falling, ultracold, but thermal gas, the finite mirror size would lead to a strongly reduced signal.

Acknowledgments

We gratefully acknowledge support by the Région Ile-de-France (contract number E1213) and by the European Community through the Research Training Network 'FASTNet' under contract no. HPRN-CT-2002-00304 and the Marie Curie Research Network 'Atom Chips' under contract no. MRTN-CT-2003-505032. Laboratoire de Physique des Lasers (LPL) is Unité Mixte de Recherche 7538 of Centre National de la Recherche Scientifique and Université

Paris 13. The LPL group is a member of the Institut Francilien de Recherche des Atomes Froids.

References

[1] Hänsel W, Hommelhoff P, Hänsch T W and Reichel J 2001 *Nature* **413** 498–501

[2] Folman R, Krüger P, Schmiedmayer J, Denschlag J H and Henkel C 2002 *Adv. At. Mol. Opt. Phys.* **48** 263–356

[3] Fortágh J, Ott H, Kraft S and Zimmermann C 2002 *Phys. Rev.* A **66** 041604
Leanhardt A E, Shin Y, Chikkatur A P, Kielpinski D, Ketterle W and Pritchard D E 2003 *Phys. Rev. Lett.* **90** 100404
Schumm T, Estève J, Figl C, Trebbia J B, Aussibal C, Nguyen H, Mailly D, Bouchoule I, Westbrook C and Aspect A 2005 *Eur. Phys. J.* D **32** 171–80

[4] Jones M P A, Vale C J, Sahagun D, Hall B V and Hinds E A 2003 *Phys. Rev. Lett.* **91** 080401
Harber D M, McGuirk J M, Obrecht J M and Cornell E A 2003 *J. Low Temp. Phys.* **133** 229–38
Rekdal P K, Scheel S, Knight P L and Hinds E A 2004 *Phys. Rev.* A **70** 013811

[5] Henkel C and Wilkens M 1999 *Europhys. Lett.* **47** 414–20
Henkel C, Pötting S and Wilkens M 1999 *Appl. Phys.* B **69** 379–87

[6] Balykin V I, Letokhov V S, Ovchinnikov Y B and Sidorov A I 1988 *Phys. Rev. Lett.* **60** 2137–40
Kasevich M A, Weiss D S and Chu S 1990 *Opt. Lett.* **15** 607–9
Aminoff C G, Steane A M, Bouyer P, Desbiolles P, Dalibard J and Cohen-Tannoudji C 1993 *Phys. Rev. Lett.* **71** 3083–6
Landragin A, Courtois J Y, Labeyrie G, Vansteenkiste N, Westbrook C I and Aspect A 1996 *Phys. Rev. Lett.* **77** 1464–7

[7] Christ M, Scholz A, Schiffer M, Deutschmann R and Ertmer W 1994 *Opt. Commun.* **107** 211–7
Brouri R, Asimov R, Gorlicki M, Feron S, Reinhardt J, Lorent V and Haberland H 1996 *Opt. Commun.* **124** 448–51
Szriftgiser P, Guéry-Odelin D, Arndt M and Dalibard J 1996 *Phys. Rev. Lett.* **77** 4–7
Cognet L, Savalli V, Horvath G Z K, Holleville D, Marani R, Westbrook N, Westbrook C I and Aspect A 1998 *Phys. Rev. Lett.* **81** 5044–7

[8] Ovchinnikov Y B, Shul'ga S V and Balykin V I 1991 *J. Phys. B: At. Mol. Opt. Phys.* **24** 3173–8
Gauck H, Hartl M, Schneble D, Schnitzler H, Pfau T and Mlynek J 1998 *Phys. Rev. Lett.* **81** 5298–301
Hammes M, Rychtarik D, Engeser B, Nägerl H C and Grimm R 2003 *Phys. Rev. Lett.* **90** 173001

[9] Barnett A H, Smith S P, Olshanii M, Johnson K S, Adams A W and Prentiss M 2000 *Phys. Rev.* A **61** 023608

[10] Rychtarik D, Engeser B, Nägerl H C and Grimm R 2004 *Phys. Rev. Lett.* **92** 173003

[11] Pasquini T A, Shin Y I, Sanner C, Saba M, Schirotzek A, Pritchard D E and Ketterle W 2004 *Phys. Rev. Lett.* **93** 223201
Pasquini T A, Saba M, Jo G, Shin Y, Ketterle K, Pritchard D E, Savas T A and Mulders N 2006 Low velocity quantum reflection of Bose-Einstein condensates *Phys. Rev. Lett.* **97** 093201 (*Preprint* cond-mat/0603463)

[12] McGuirk J M, Harber D M, Obrecht J M and Cornell E A 2004 *Phys. Rev.* A **69** 062905

[13] Lin Y J, Teper I, Chin C and Vuletić V 2004 *Phys. Rev. Lett.* **92** 050404
Harber D M, Obrecht J M, McGuirk J M and Cornell E A 2005 *Phys. Rev.* A **72** 033610
Obrecht J M, Wild R J, Antezza M, Pitaevskii L P, Stringari S and Cornell E A 2006 Measurement of the temperature dependence of the Casimir-Polder force *Preprint* physics/0608074

[14] Landragin A, Labeyrie G, Henkel C, Kaiser R, Vansteenkiste N, Westbrook C I and Aspect A 1996 *Opt. Lett.* **21** 1591–3
In these experiments, some indications for anisotropic scattering after reflection of thermal atoms on an evanescent wave mirror were observed: Westbrook C and Landragin A 2005 private communication

[15] Hinds E A and Hughes I G 1999 *J. Phys. D: Appl. Phys.* **32** R119–46

[16] Arnold A S, MacCormick C and Boshier M G 2002 *Phys. Rev.* A **65** 031601

[17] Savalli V, Stevens D, Estève J, Featonby P D, Josse V, Westbrook N, Westbrook C I and Aspect A 2002 *Phys. Rev. Lett.* **88** 250404

[18] Henkel C, Mølmer K, Kaiser R, Vansteenkiste N, Westbrook C I and Aspect A 1997 *Phys. Rev.* A **55** 1160–78

[19] Perrin H, Colombe Y, Mercier B, Lorent V and Henkel C 2005 *J. Phys.: Conf. Ser.* **19** 151–7 (*Preprint* quant-ph/0509200)

[20] Kaiser R, Lévy Y, Vansteenkiste N, Aspect A, Seifert W, Leipold D and Mlynek J 1994 *Opt. Commun.* **104** 234

[21] Colombe Y, Kadio D, Olshanii M, Mercier B, Lorent V and Perrin H 2003 *J. Opt. B: Quantum Semiclass. Opt.* **5** S155–63

[22] Castin Y and Dum R 1996 *Phys. Rev. Lett.* **77** 5315–9
Kagan Y, Surkov E L and Shlyapnikov G V 1996 *Phys. Rev.* A **54** R1753–6
[23] Henkel C and Courtois J-Y 1998 *Eur. Phys. J.* D **3** 129–53
[24] Bongs K, Burger S, Birkl G, Sengstock K, Ertmer W, Rzazewski K, Sanpera A and Lewenstein M 1999 *Phys. Rev. Lett.* **83** 3577
Busch T 2003 private communication
[25] Estève J, Stevens D, Aussibal C, Westbrook N, Aspect A and Westbrook C I 2004 *Eur. Phys. J.* D **31** 487–91

PHYSICAL REVIEW A **72**, 061601(R) (2005)

Diffraction of a Bose-Einstein condensate in the time domain

Yves Colombe,* Brigitte Mercier,† Hélène Perrin, and Vincent Lorent‡
Laboratoire de Physique des Lasers, UMR 7538 du CNRS, Institut Galilée, Université Paris-Nord, Avenue J.-B. Clément, F-93430 Villetaneuse, France

(Received 29 July 2005; published 5 December 2005)

We have observed the diffraction of a Bose-Einstein condensate of rubidium atoms on a vibrating mirror potential. The matter wave packet bounces back at normal incidence on a blue-detuned evanescent light field after a 3.6 mm free fall. The mirror vibrates at a frequency of 500 kHz with an amplitude of 3 nm. The atomic carrier and side bands are directly imaged during their ballistic expansion. The locations and the relative weights of the diffracted atomic wave packets are in very good agreement with the theoretical prediction of Henkel *et al.* [J. Phys. II **4**, 1877 (1994)].

DOI: 10.1103/PhysRevA.72.061601 PACS number(s): 03.75.Be, 03.75.Dg, 42.50.Vk

The manipulation of ultracold atomic matter waves with optical or magnetic fields close to surfaces is extensively explored in the context of fabricating integrated atom optics devices. The use of the Zeeman interaction due to the magnetic field of microfabricated current carrying wires is currently the most attractive approach [1,2]. The main advantages of this method are the modularity and steadiness of the microchip fabrication. Nevertheless, some drawbacks of this technique exist since one experiences losses of atoms in magnetic traps at close distances to conducting surfaces [3–5] due to Johnson noise-induced spin flips. This loss mechanism is absent in the vicinity of dielectric surfaces, which can be used as substrates for dipole traps based on optical near fields. In 1991, Ovchinnikov *et al.* [6] made the seminal proposal of using the difference in the decay lengths of the evanescent fields created by total internal reflections of blue- and red-detuned light beams on a planar dielectric surface to create a trapping dipole potential above the surface. Hammes *et al.* demonstrated this trapping in 2002 [7]. The proposals of Barnett *et al.* [8] and Burke *et al.* [9] enlarge the optical near field trapping geometry to a richer variety of patterns: The basic idea is to take the benefit of light injected inside integrated optical structures to design evanescent field traps and guides. Having a similar compactness and versatility as the optical waveguides supporting the evanescent waves, these dipole traps and guides offer an interesting alternative to the current carrying wires on a chip technique.

In this paper we address the action of the evanescent outer part of a light mode propagating in a planar optical waveguide. The experiment performed is similar to the one realized with cold atoms by the group of Jean Dalibard in 1995 [10]. The difference mostly consists in the initial longitudinal coherence of our atomic source. In our experiment, an atomic Bose-Einstein condensate (BEC) is reflected after a free fall by the evanescent part of a blue-detuned guided optical mode, and is observed in its ballistic expansion after the bounce. The evanescent mirror is made to vibrate, which modulates the phase of the reflected wave function and diffracts the atoms in several side bands. Atoms bouncing on this potential are also dramatically scattered, which is due to the corrugated structure of the planar waveguide on a nanometer scale. A particular study of the elastic scattering of the atomic wave by the static rough mirror potential is presented elsewhere [11]. As discussed below, the diffraction in the time domain and the elastic scattering are independent phenomena and we focus here on the study of the first effect. Note that this diffraction of an atomic BEC on a vibrating mirror has similarities with atomic diffraction experiments performed with a pulsed optical standing wave [12,13].

The experimental setup is described in [14]. It is based on a double magneto-optical trap (MOT) system. From the second MOT 5×10^8 ^{87}Rb atoms are transferred into a quadrupole and Ioffe configuration (QUIC) [15] magnetic trap. An almost pure condensate of 2×10^5 atoms is obtained by radio-frequency evaporative cooling inside the QUIC trap. Below the trapped atoms stands an optical waveguide made of a 360-nm-thick layer of TiO_2 ($n_{\mathrm{guide}}=2.3$) on the top of a 400 nm SiO_2 layer ($n_{\mathrm{gap}}=1.46$). This low index gap layer is on the top surface of a high index prism made of a Schott LaSFN15 glass ($n_{\mathrm{prism}}=1.86$). The TE2 mode of the waveguide is excited through evanescent coupling of a

TABLE I. Parameters for the (a), (b), and (c) experiments: frequency modulation $\Omega/2\pi$, optical frequency detuning $\delta_0/2\pi$, detuning modulation $\Delta\delta/2\pi$, modulation depth ε, fall height z_0, and time of flight $\Delta t_{\mathrm{fall}}+\Delta t_{\mathrm{bounce}}$.

Experiment	(a)	(b)	(c)
$\Omega/2\pi$ (kHz)	500	500	500
$\delta_0/2\pi$ (GHz)	+2.1	+2.1	+1.9
$\Delta\delta/2\pi$ (MHz)	130	163	163
ε	6.2%	7.8%	8.6%
z_0 (mm)	3.6	3.6	2.05
$\Delta t_{\mathrm{fall}}+\Delta t_{\mathrm{bounce}}$ (ms)	27+27	27+27	20.5+19.5

*Present address: Sektion Physik der Ludwig-Maximilians-Universität, Schellingstrasse 4, D-80799 München, Germany.
†Present address: Laboratoire d'Optique Appliquée, Centre de l'Yvette, F-91761 Palaiseau Cedex, France.
‡Electronic address: lorent@galilee.univ-paris13.fr

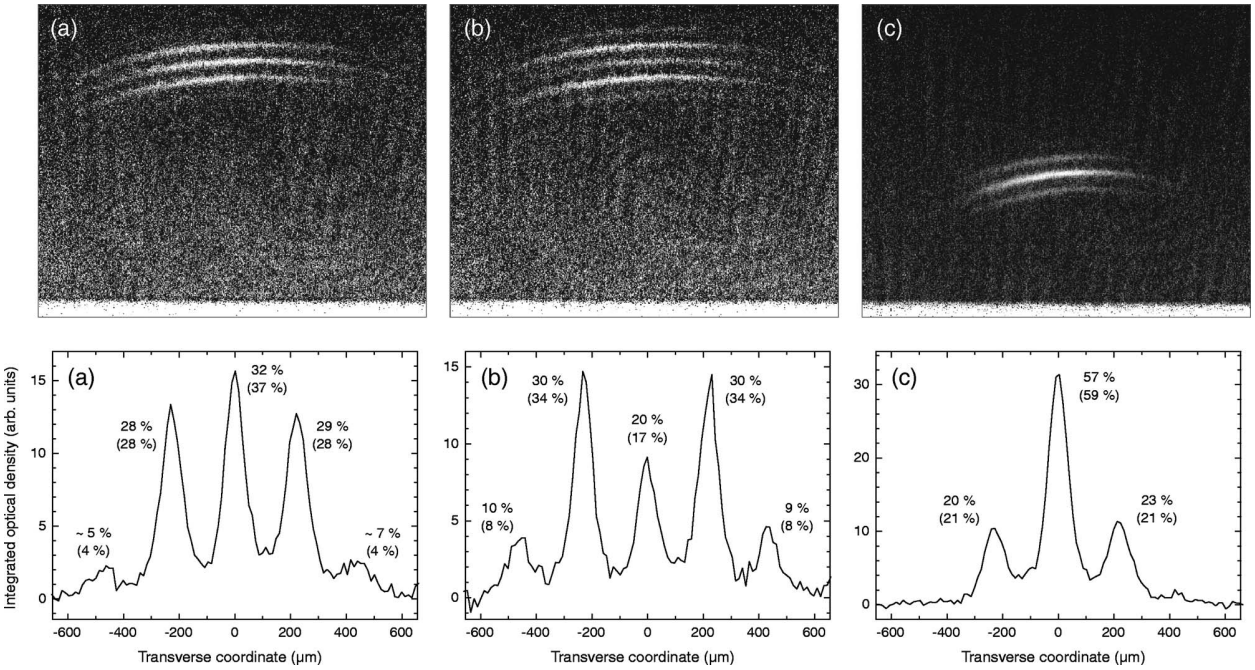

FIG. 1. Diffraction in the time domain of a ^{87}Rb BEC on a vibrating repulsive evanescent wave. The experimental parameters for (a), (b), and (c) are summarized in Table I. The circular shape of each diffracted order is due to elastic scattering of the atoms on the rough mirror potential (see text). Each absorption image is the result of a single experimental run. The camera field is 5.5 mm (horizontal) $\times$4.4 mm (vertical) and includes the top of the prism. The slight tilt of the atomic clouds is due to a small horizontal initial velocity of 30 mm/s. The values on the optical density profiles are the relative weights of the diffracted orders; expected weights are in parentheses.

P_0=50 mW diode laser beam detuned by δ_0=2.1 GHz on the blue side of the D_2 $5S_{1/2}$, $F=2\rightarrow 5P_{3/2}$ transition. The field decay length of the TE2 guided mode in the vacuum is κ^{-1} =93. The number of spontaneous photon per atom during the bounce is about 0.1 in the situation where the atoms penetrate in the evanescent field with a falling height of 3.6 mm. The vibration of the evanescent mirror is obtained by a sinusoidal modulation of the diode current. The resulting modulation depth of the ac Stark shift potential $U\propto P/\delta$ is $\varepsilon=|\varepsilon_P+\varepsilon_\delta|$, where $\varepsilon_P=\Delta P/P_0$ and $\varepsilon_\delta=-\Delta\delta/\delta_0$. The power modulation depth ε_P is measured directly with a photodiode. The detuning modulation depth ε_δ is measured by calibrating the frequency shift versus the diode current using the atomic frequency reference in a saturated absorption experiment. The modulation depth ε_P is 25 times less than ε_δ: The modulation of the reflecting potential is thus essentially due to the modulation of the detuning.

Three kinds of BEC diffraction experiments have been performed. They differ by the falling heights of the atomic cloud and by the modulation depths of mirror potential. The parameters are summarized in Table I. In the (a) and (b) experiments the atomic condensate is released from the QUIC trap centered 3.6 mm above the dielectric surface. In the (c) experiment the condensate is first magnetically transported to a height of 2.05 mm above the surface before being released from the trap [16]. The corresponding free fall times down to the dielectric surface are Δt_{fall}=27 ms in cases (a) and (b) and 20.5 ms in case (c). In addition to the incident vertical velocity, a small horizontal velocity (30 mm/s for all experiments) results in a slight tilt of the clouds after reflection. The modulation depths ε are 6.2% in (a), 7.8% in (b), and 8.6% in (c). These modulation depths correspond to vibrating amplitudes of the mirror z_{M} of 2.9 nm, 3.6 nm, and 4.0 nm, respectively. The frequency of the modulation is kept the same, $\Omega=2\pi\times 500$ kHz, throughout these experiments. The diffracted wave packets are detected by absorption imaging with a horizontal laser beam (Fig. 1, upper part). In order to accurately measure the atomic populations in the different elastically scattered diffraction orders, the optical density is integrated along circles of growing radii. The relative weights are measured on the resulting profile (Fig. 1, lower part) [17].

The diffracted populations are clearly resolved with a time of flight Δt_{bounce}=27 ms [(a) and (b)] or 19.5 ms (c) after the reflection on the evanescent mirror. The measured distances between the diffracted orders are reported in Table II. A remarkable feature of this experiment lies in the direct visualization of the side bands. The wave number separations are transferred into wave-packet separations that allow a direct and accurate measurement of the energy intervals and relative weights of the side bands. The diffraction of the matter wave by the mirror vibration and the scattering of the same matter wave by the mirror roughness are different in nature and their effects are indeed clearly separated on the absorption images. The first effect is a transfer of energy, giving birth to side bands. Given our particular condition of initial kinetic energy for say, a 3.6 mm free fall, the velocity difference between the carrier and the first side bands is $\Delta v\simeq\pm 1.5 v_{\text{rec}}$ (v_{rec} is the photon recoil velocity) with a modulation frequency of 500 kHz. The atom scattering is an elastic momentum exchange, which spreads each diffracted order over an elastic scattering sphere. Despite its large ef-

TABLE II. Expected and measured positions of the side bands relative to the carrier, in μm, for experiments (a), (b), and (c).

Diffraction orders	−2	−1	0	+1	+2
Expected: (a) and (b)	−479	−235	0	+228	+449
Measured: (a)	−470	−226	0	+221	+433
Measured: (b)	−460	−231	0	+219	+433
Expected: (c)		−228	0	+216	
Measured: (c)		−227	0	+218	

fect on the velocity distribution ($\sigma_v = 6.6 v_{\rm rec}$ along the horizontal x direction [11]), it does not prevent the observation of resolved side bands, as the two processes act in orthogonal directions. This leads us to interpret our diffraction experiments with a one-coordinate model, namely an incident plane wave at normal incidence on a perfect mirror.

Let us first consider the reflection of the plane atomic wave function on a vibrating infinite repulsive potential $U[z < z_{\rm m}(t)] = +\infty$, $U[z \geqslant z_{\rm m}(t)] = 0$ [18]. We assume that the velocity of the mirror coordinate $z_{\rm m}$ is always much less than the atomic group and phase velocities, so that the incident wave function can be written as $\psi_i(z \geqslant z_{\rm m}, t) = \exp[i(-kz - \omega t)]$. The incident and reflected waves fulfill the boundary condition $\psi_{\rm i}[z_{\rm m}(t), t] + \psi_{\rm r}[z_{\rm m}(t), t] = 0$ at any time. In the case of a harmonically vibrating mirror $z_{\rm m}(t) = z_{\rm M} \sin(\Omega t)$, the reflected wave function may be expanded as a sum of a carrier and diffracted side bands $\psi_r[z \geqslant z_{\rm m}(t), t] = \Sigma_{n=-\infty}^{+\infty} J_n(2kz_{\rm M}) \exp i[k_n z - (\omega + n\Omega)t + \pi]$, where the side band amplitudes are Bessel functions of the first kind and the atomic phase modulation amplitude is $2kz_{\rm M}$. The energy separation between side bands is $\hbar\Omega$ and the corresponding wave numbers are $k_n \simeq k + n(\Omega M/\hbar k)$ (M is the mass of the atom) as long as the energy transfer is much less than the incident kinetic energy.

In our situation the reflecting potential is an exponential whose amplitude is harmonically modulated $U(z,t) = U_0[1 + \varepsilon \sin(\Omega t)]\exp(-2\kappa z)$. Since the potential is exponential, the amplitude modulation is equivalent to an overall translation; in the case of a weak modulation depth $\varepsilon \ll 1$, this translation is also harmonic: $U(z,t) = U_0 \exp\{-2\kappa[z - z_{\rm M} \sin(\Omega t)]\}$ with $z_{\rm M} = \varepsilon/2\kappa$. The main difference between the infinitely steep and the evanescent potentials lies in the continuous variation of the incident matter wave momentum inside the potential in the last case. Henkel *et al.* have calculated the atomic phase modulation imprinted by the vibrating mirror in a semiclassical model [19]. It is assumed that the incident atomic de Broglie wavelength is much smaller than $2\pi\kappa^{-1}$, and that the classical atomic trajectory is not much affected by the vibration of the potential. In our experiment the atomic BEC cloud is released 3.6 mm or 2.05 mm above the dielectric substrate. When the atoms hit the evanescent mirror, the de Broglie wavelength $\lambda_{\rm dB}$ is, respectively, 17 nm or 23 nm. These values are indeed much smaller than $2\pi\kappa^{-1} = 585$ nm. Furthermore, our modulation depth is at maximum $\varepsilon = 8.6\%$ and ensures that the vibration barely perturbs the classical atom trajectory. Under these conditions the semiclassical approach proposed by Henkel *et al.* is valid.

The predicted diffraction weights are

$$\mathcal{P}(n) = |J_n(2kz_{\rm M}\beta(Q))|^2, \tag{1}$$

where $\beta(x) = (\pi/2)x/\sinh[(\pi/2)x]$ and $Q = (\Omega M/\hbar k)/\kappa$. Q is the ratio of the wave number interval between successive side bands and the exponential decay factor of the evanescent wave. The reduction factor $\beta(Q)$ falls exponentially for $Q > 1$, so that the maximum momentum transfer is in the order of $\hbar\kappa$ as expected from the Heisenberg uncertainty relation. The values in parentheses in Fig. 1 are the weights $\mathcal{P}(n)$ calculated by the formula (1) where the experimental values serve as inputs. The agreement between the calculated and the observed weights is within 10% accuracy in the worst case. Figure 2 illustrates the expected relative weights of the diffracted orders as a function of the modulation depth ε for atoms falling a height of 3.6 mm and a mirror modulation frequency of 500 kHz. It clearly shows that small modulation depths are the better choice to obtain a high diffraction efficiency on a few side bands.

In summary, this experiment demonstrates the diffraction of an atomic matter wave by a vibrating rough mirror potential. Despite the elastic diffusion of the atoms, the signal of

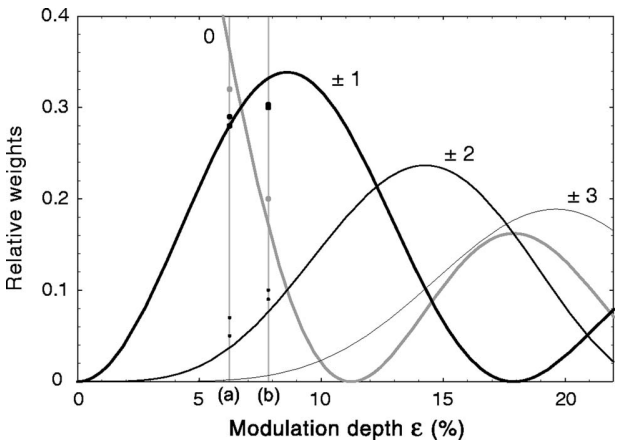

FIG. 2. Relative weight distribution over the carrier and the first six side bands of an atomic wave packet reflected off the vibrating evanescent mirror for a 500 kHz modulation as a function of the modulation depth ε. The curves are the weights $\mathcal{P}(n)$ (1) given by the semiclassical model of Henkel *et al.* [19] for ^{87}Rb atoms released 3.6 mm above the dielectric surface. The values plotted at modulations depths 6.2% and 7.8% are those of the (a) and (b) experiments, respectively (see Table I and Fig. 1).

diffraction is clear-cut because of the monochromaticity of the atomic source. However, it would be misleading to associate the quantum nature of the atomic diffraction to the Bose-Einstein phase coherence. The dynamics of the bouncing is not even determined by the density term of the Gross-Pitaevskii equation as it is in the Hannover experiment [20]; The expanding BEC evolves like a free noninteracting particle gas already 2 ms after being released from the magnetic trap. The linear Schrödinger equation correctly gives the dynamics of individual atoms, independently of a relative phase between their wave functions. Such a vibrating mirror can be used as a phase modulator in conventional atom optics: It has been implemented in a longitudinal interferometer with three consecutive bounces [21], the temporal equivalent of three grating interferometers [22,23]. In these devices, the atomic sources are considered as white light sources and great care is taken to have identical path lengths. Crossing the bridge to nonsymmetric path interferometry becomes realistic when the atomic wave comes out of a BEC. Under our experimental conditions, a two-path interferometer seems realistic under the following conditions: A first separation of order +1 and −1 followed by N and $N+1$ bounces, respectively, the final recombination being ensured by a last modulation; this would lead to a very asymmetric interferometer. With our experimental parameters, $N=7$ appears to be possible. It will require, however, the use of a superpolished substrate as a mirror and possibly a lateral confinement of the atomic wave: Up to 10 bounces have been observed with a conventional MOT atomic source at a 3 mm drop height above a curved mirror [24], and a guiding of the matter wave without perturbing the motion perpendicular to the mirror surface can be obtained with magnetic confinement [25].

ACKNOWLEDGMENTS

We thank B. M. Garraway for a careful reading of the manuscript. We acknowledge support from the FNS through the ACI-photonique program, the UE through the RTN FASTNet program under Contract No. HPRN-CT-2002-00304 and the Conseil Régional d'Ile de France.

[1] J. Reichel *et al.*, Appl. Phys. B: Lasers Opt. **72**, 81 (2001).
[2] R. Folman *et al.*, Adv. At., Mol., Opt. Phys. **48**, 263 (2002).
[3] M. P. A. Jones *et al.*, J. Phys. B **37**, L15 (2004).
[4] Y. J. Lin *et al.*, Phys. Rev. Lett. **92**, 050404 (2004).
[5] C. Henkel and M. Wilkens, Europhys. Lett. **47**, 414 (1999).
[6] Y. B. Ovchinnikov, S. V. Shul'ga, and V. I. Balykin, J. Phys. B **24**, 3173 (1991).
[7] M. Hammes, D. Rychtarik, B. Engeser, H. C. Nägerl, and R. Grimm, Phys. Rev. Lett. **90**, 173001 (2003).
[8] A. H. Barnett *et al.*, Phys. Rev. A **61**, 023608 (2000).
[9] J. P. Burke *et al.*, Phys. Rev. A **65**, 043411 (2002).
[10] A. Steane, P. Szriftgiser, P. Desbiolles, and J. Dalibard, Phys. Rev. Lett. **74**, 4972 (1995).
[11] H. Perrin, Y. Colombe, B. Mercier, V. Lorent, and C. Henkel, J. Phys.: Conf. Ser. **19**, 151 (2005); Y. Colombe, H. Perrin, B. Mercier, V. Lorent, and C. Henkel (unpublished).
[12] Y. B. Ovchinnikov *et al.*, Phys. Rev. Lett. **83**, 284 (1999).
[13] C. Keller *et al.*, Appl. Phys. B **69**, 303 (1999).
[14] Y. Colombe, D. Kadio, M. Olshanii, B. Mercier, V. Lorent, and H. Perrin, J. Opt. B: Quantum Semiclassical Opt. **5**, S155 (2003).
[15] T. Esslinger, I. Bloch, and T. W. Hänsch, Phys. Rev. A **58**, R2664 (1998).
[16] Y. Colombe, H. Perrin, B. Mercier, and V. Lorent, in *COLOQ 8*, edited by A. Aspect, J. Vigué, and B. Girard (J. Phys. IV, 2004), Vol. **119**, pp. 159–160.
[17] For each experiment, the center of the integration circles corresponds to the point of contact of the atoms with the evanescent wave, translated vertically by the distance $\frac{1}{2}g\Delta t_{\mathrm{bounce}}^2$ covered by the free fall referential that is at rest at the instant of the reflection. The wave packets are adequately fitted with Gaussian functions, which allow a measure of their relative weights and positions.
[18] The spatial width of the incident wave packet is still large enough to ensure the validity of the plane wave model.
[19] C. Henkel, A. M. Steane, R. Kaiser, and J. Dalibard, J. Phys. II **4**, 1877 (1994).
[20] K. Bongs, S. Burger, G. Birkl, K. Sengstock, W. Ertmer, K. Rzażewski, A. Sanpera, and M. Lewenstein, Phys. Rev. Lett. **83**, 3577 (1999).
[21] P. Szriftgiser, D. Guéry-Odelin, M. Arndt, and J. Dalibard, Phys. Rev. Lett. **77**, 4 (1996).
[22] D. W. Keith, C. R. Ekstrom, Q. A. Turchette, and D. E. Pritchard, Phys. Rev. Lett. **66**, 2693 (1991).
[23] E. M. Rasel, M. K. Oberthaler, H. Batelaan, J. Schmiedmayer, and A. Zeilinger, Phys. Rev. Lett. **75**, 2633 (1995).
[24] C. G. Aminoff, A. M. Steane, P. Bouyer, P. Desbiolles, J. Dalibard, and C. Cohen-Tannoudji, Phys. Rev. Lett. **71**, 3083 (1993).
[25] N. H. Dekker *et al.*, Phys. Rev. Lett. **84**, 1124 (2000).

Chapitre 4

Piégeage d'atomes habillés dans des potentiels adiabatiques

C'est en cherchant le moyen le plus efficace de transférer des atomes d'un piège magnétique vers le piège à ondes évanescentes décrit au chapitre précédent qu'un article [35] paru en 2001 dans Physical Review Letters a attiré mon attention. Les auteurs, Oliver Zobay et Barry Garraway, proposaient de combiner un champ radiofréquence (RF) et un piège magnétique habituel pour confiner des atomes dans un potentiel adiabatique, résultant de l'habillage des atomes par le champ RF. Dans ce piège, les atomes sont fortement contraints verticalement, alors que le confinement horizontal est beaucoup plus lâche, ce qui met le nuage atomique en forme de disque horizontal. De plus, l'altitude de ce disque peut être contrôlée par le choix de la fréquence RF. J'envisageai alors d'utiliser ce piège comme intermédiaire pour transporter les atomes jusqu'au piège à ondes évanescentes, en profitant d'une mise en forme préalable du nuage. Le papier de Zobay et Garraway passa relativement inaperçu à l'époque, jusqu'à ce que nous mettions en œuvre pour la première fois ce piège pour atomes habillés [36]. Depuis, un nombre croissant de groupes s'intéresse à ce type de potentiels, en particulier dans la communauté des puces à atomes [38, 41, 42].

Dans ce chapitre, je décrirai dans un premier temps le principe du piège habillé. Je donnerai quelques exemples de potentiels adiabatiques que l'on peut réaliser en combinant un champ magnétique statique et un champ RF, en utilisant ou non le rôle de la polarisation de l'onde RF : double puits [38], réseau à pas variable [94], anneau [95]... Je présenterai ensuite nos résultats expérimentaux. Je montrerai comment l'utilisation de la RF permet de piéger des atomes dans un piège quadrupolaire. Les atomes peuvent être refroidis par évaporation dans le piège habillé, et je présenterai une étude théorique de ce mécanisme. Enfin, je montrerai que l'adjonction d'une onde stationnaire au piège habillé permet d'envisager la réalisation d'un anneau à atomes [39].

4.1 Un champ RF pour habiller les atomes

Il n'est pas nouveau de combiner un champ radiofréquence avec des atomes piégés magnétiquement. C'est de cette manière que Harold Hess proposa en 1986 de refroidir des atomes confinés dans un piège magnétique [96], en éliminant sélectivement les plus énergétiques, ce qui fut réalisé expérimentalement deux and plus tard avec de l'hydrogène polarisé [97] et mena en 1995 à la condensation de Bose-Einstein des alcalins [1, 2]. Le principe est de limiter la profondeur du piège magnétique en utilisant un champ RF, dont la fréquence est résonnante avec l'écart entre niveaux magnétiques en un lieu de l'espace entourant le centre du piège, la « surface d'évaporation », que j'appellerai aussi surface résonnante dans ce chapitre. Les atomes dont l'énergie cinétique est suffisante peuvent atteindre cette zone et effectuer une transition vers un état magnétique qui est repoussé loin du centre. Les atomes restant se thermalisent alors à une température inférieure. Plus on baisse la fréquence, plus le rayon moyen de la surface d'évaporation décroît et plus les atomes restants sont froids.

Pour que le refroidissement par évaporation soit efficace, il faut que les atomes qui ont suffisamment d'énergie pour atteindre la surface d'évaporation quittent à coup sûr le piège. C'est le cas si le couplage RF est suffisant. Les atomes sont alors habillés par le champ RF et suivent adiabatiquement un potentiel qui les conduit hors du piège [98]. Ce potentiel est maximum sur la surface d'évaporation, et les atomes qui atteignent la surface continuent et quittent le piège magnétique. L'idée nouvelle d'Oliver Zobay et Barry Garraway est d'utiliser l'autre potentiel adiabatique, qui présente au contraire un minimum sur la surface résonnante, pour confiner les atomes dans une sorte de bulle. Le piège résultant se prête alors bien à un confinement en dimensions restreintes, les atomes étant piégés dans l'épaisseur de la surface résonnante, qui peut être rendue très fine.

Notons enfin que dans le domaine micro-onde, il existe un précédent historique important à ces expériences sur les atomes habillés et piégés. En 1994, Spreeuw et ses collègues ont démontré la faisabilité d'un piégeage similaire, au sein d'une cavité micro-onde, en tirant partie de l'inhomogénéité du champ micro-onde dans la cavité [99].

4.1.1 Description des états habillés

Dans tout ce chapitre, j'adopterai les notations suivantes. Le repère lié au laboratoire a pour centre O le centre du piège QUIC et pour axes x, y et z où x est l'axe long du cigare et z l'axe vertical, comme dans le chapitre 2. On prend comme axe de quantification pour le spin atomique la direction, notée $\mathbf{e}_Z$, du champ magnétique statique $B_0(\mathbf{r})\mathbf{e}_Z$. Cette direction Z dépend donc du point $\mathbf{r}$, bien que cela n'apparaisse pas explicitement dans la notation. Le champ RF est polarisé linéairement selon y dans notre expérience. On choisit comme axe Y de la base locale la direction orthogonale à la fois à Z et à y, de sorte que le champ RF puisse s'écrire $\mathbf{B}_1 \cos(\omega_{\mathrm{RF}} t)$ avec

$$\mathbf{B}_1 = B_1 \mathbf{e}_y = B_1^X(\mathbf{r})\, \mathbf{e}_X + B_1^Z(\mathbf{r})\, \mathbf{e}_Z \,. \tag{4.1}$$

La dépendance spatiale du champ RF B_1 est négligeable à l'échelle du nuage atomique. Le second terme de l'équation 4.1 ne joue pas de rôle dans le couplage RF car il est

aligné avec l'axe de quantification[1]. Le choix de la polarisation y pour l'onde RF permet d'ailleurs d'optimiser $B_1^X = B_1 \sin(\mathbf{e}_Z,\mathbf{e}_y)$, le champ statique étant orienté essentiellement dans le plan xz lorsque les atomes sont dans le piège habillé.

Le spin atomique $\mathbf{F}$ est couplé à ces deux champs. Le couplage au champ statique seul lève la dégénérescence entre les sous-niveaux magnétiques m_F du spin $F = 2$ alors que le couplage au champ RF induit des transitions entre ces niveaux. Le hamiltonien complet comporte également le terme d'énergie cinétique $\mathbf{p}^2/2M$ agissant sur l'état externe. Nous nous concentrons dans un premier temps sur l'état de spin seul en supposant l'atome fixe. Nous en déduisons les états propres pour le spin au point $\mathbf{r}$, dont l'énergie qui dépend de la position peut être prise comme un potentiel adiabatique pour l'état externe de l'atome, à condition que la condition d'adiabaticité soit vérifiée.

Le hamiltonien de l'état interne s'écrit donc :

$$H = \Omega_0(\mathbf{r})F_Z + 2\Omega_1(\mathbf{r})\cos(\omega_{\text{RF}}t)F_X \tag{4.2}$$

où l'on a posé $\hbar\Omega_0(\mathbf{r}) = g_F\mu_B B_0(\mathbf{r})$ et $\hbar\Omega_1(\mathbf{r}) = g_F\mu_B B_1^X(\mathbf{r})/2$. Le facteur 1/2 est introduit à ce stade pour souligner le fait que pour une polarisation linéaire du champ RF, seule la composante σ^+, d'amplitude Ω_1, contribue au couplage. On notera également $\omega_0 = \min(\Omega_0(\mathbf{r}))$ la fréquence résonnante au fond du piège QUIC, et $\Delta = \omega_{\text{RF}} - \omega_0$ le désaccord de la RF par rapport à l'écart entre niveaux magnétiques au fond.

Dans la limite où le couplage Ω_1 et le désaccord $\delta = \omega_{\text{RF}} - \Omega_0$ sont tous deux petits devant ω_{RF}, on peut appliquer l'approximation de l'onde tournante et ne conserver que les termes résonnants dans le couplage spin-champ[2]. On a dans ce cas

$$H = \Omega_0(\mathbf{r})F_Z + \Omega_1(\mathbf{r})e^{-i\omega_{\text{RF}}t}F_X\,. \tag{4.3}$$

Dans le référentiel tournant à la fréquence ω_{RF} autour de Z, le hamiltonien effectif est alors indépendant du temps :

$$H_{\text{eff}} = -\delta(\mathbf{r})F_Z + \Omega_1(\mathbf{r})F_X = \Omega(\mathbf{r})\mathbf{F}.\mathbf{e}_\theta\,. \tag{4.4}$$

Les états propres $|m_F\rangle_\theta$ sont ceux de la projection du spin $\mathbf{F}$ sur la direction $\mathbf{e}_\theta$ définie par

$$\begin{aligned} \mathbf{e}_\theta &= \cos\theta\,\mathbf{e}_Z + \sin\theta\,\mathbf{e}_X \\ \operatorname{tg}\theta &= -\Omega_1/\delta, \quad 0 \le \theta \le \pi \end{aligned} \tag{4.5}$$

et ont pour énergie

$$m_F\hbar\Omega(\mathbf{r}) \quad \text{avec} \quad \Omega(\mathbf{r}) = \sqrt{\delta(\mathbf{r})^2 + \Omega_1(\mathbf{r})^2}\,. \tag{4.6}$$

Ils se déduisent des états de spin des atomes piégés dans un piège magnétique par la rotation autour de Y d'un angle θ dans la base tournante $|m_F\rangle_\theta = R_Y(\theta)|m_F\rangle_Z$, qui est elle-même en rotation autour de Z à la fréquence ω_{RF} par rapport à la base locale comme l'illustre le schéma de la figure 4.1.

1. Ce terme peut en toute rigueur induire des transitions à des fréquences sous-harmoniques de ω_{RF} mais avec une amplitude réduite au moins d'un facteur $J_1(B_1^Z/B_0)$ où J_1 est une fonction de Bessel [100].

2. Le terme anti-résonnant déplace la transition de $\Omega_1^2/4\Omega_0$, 20 kHz au plus dans notre cas.

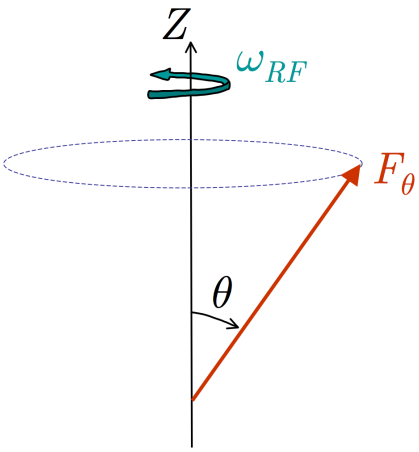

Figure 4.1 — Représentation schématique de l'état habillé : le spin atomique précesse autour du champ directeur $\mathbf{B}_0$ à la vitesse angulaire ω_{RF}. Pour $\theta = 0$ ou $\delta = -\infty$, l'état propre est confondu avec l'état de départ $|m_F\rangle_Z$ alors que pour $\theta = \pi$ ou $\delta = +\infty$ le spin a complètement basculé dans $|-m_F\rangle_Z$.

Schematic representation of the dressed state : the atomic spin precesses around the static field $\mathbf{B}_0$ *at angular velocity* ω_{RF}. *At* $\theta = 0$ *(or* $\delta = -\infty$*), the eigenstate corresponds to our initial state* $|m_F\rangle_Z$ *whereas* $\theta = \pi$ *(or* $\delta = +\infty$*) corresponds to a fully flipped state* $|-m_F\rangle_Z$.

L'état dans lequel nous plaçons les atomes pour les confiner dans le potentiel habillé est l'état $|2\rangle_\theta$, connecté à $|2\rangle_Z$ pour $|\delta| \gg \Omega_1, \delta < 0$. Il se décompose dans la base locale sur les cinq états $|m_F\rangle_Z$ selon

$$\begin{aligned} |2\rangle_\theta &= \frac{1}{4}(1+\cos\theta)^2|2\rangle_Z + \frac{1}{2}\sin\theta(1+\cos\theta)|1\rangle_Z + \sqrt{\frac{3}{8}}\sin^2\theta|0\rangle_Z \\ &\quad + \frac{1}{2}\sin\theta(1-\cos\theta)|-1\rangle_Z + \frac{1}{4}(1-\cos\theta)^2|-2\rangle_Z \end{aligned} \tag{4.7}$$

Une mesure de la décomposition de l'état habillé sur les états de la base locale permet donc de remonter à l'angle θ, comme nous le verrons au paragraphe 4.3.

4.1.2 Potentiels adiabatiques

Les atomes restent au cours de leur mouvement dans ce même état $|2\rangle_\theta$ à condition que le couplage motionnel introduit par le terme $\mathbf{p}^2/2M$ n'induise pas de transition non adiabatique entre états habillés. Au cours de leur mouvement, en effet, les atomes voient varier l'angle $\theta(\mathbf{r})$, qui dépend alors implicitement du temps. La condition d'adiabaticité s'écrit

$$|\dot{\theta}| \ll \sqrt{\delta^2 + \Omega_1^2} \quad \text{ou} \quad |\dot{\delta}\Omega_1 - \dot{\Omega}_1\delta| \ll (\delta^2 + \Omega_1^2)^{3/2}\,. \tag{4.8}$$

Cette condition impose des contraintes lors de l'allumage de l'onde RF (terme $\dot{\Omega}_1$) puis lors de la rampe en fréquence qui permet de charger le piège habillé (terme $\dot{\delta}$).

Dans la mesure où la condition d'adiabaticité est remplie, les atomes restent dans le même état habillé. L'énergie interne correspondant à cet état, qui dépend de la position, peut alors être considérée comme le potentiel adiabatique dans lequel évoluent les atomes. Je l'écrirai dorénavant sous la forme

$$U_m(\mathbf{r}) = m\hbar\sqrt{\delta(\mathbf{r})^2 + \Omega_1(\mathbf{r})^2} = m\hbar\sqrt{(\Omega_0(\mathbf{r}) - \omega_{\mathrm{RF}})^2 + \Omega_1(\mathbf{r})^2} \tag{4.9}$$

où $\Omega_1(\mathbf{r}) = \Omega_{1,\max}\sin(\mathbf{e}_Z,\mathbf{e}_y)$ et $m = m_F$. Cette expression met bien en évidence les deux sources de variation possibles du potentiel adiabatique : le désaccord à la résonance déterminé par la valeur du champ statique et les inhomogénéités de couplage dues aux changement d'orientation du champ statique. C'est ce qui fait la richesse des formes de piège que l'on peut obtenir avec les champs RF.

4.1.3 Exemples de potentiels adiabatiques

Dans un piège QUIC, la direction locale du champ statique est quasiment orthogonale à y en tous les points où se trouvent les atomes et l'on peut considérer que le terme de couplage Ω_1 est uniforme. On tire alors parti uniquement du premier terme sous la racine carrée de l'équation (4.9). Le potentiel adiabatique confine alors les atomes de façon très anisotrope, permettant la réalisation d'un gaz 2D. Je décrirai en détail cette situation au paragraphe 4.2.

Dans un piège quadrupolaire, en revanche, le couplage $\Omega_1(\mathbf{r})$ varie de façon importante sur une surface d'évaporation (un ellipsoïde de rayon r_0 dans sa petite dimension, $2r_0$ dans ses grandes dimensions) et s'annule le long de l'axe de polarisation y. Selon l'importance relative du couplage RF $F\hbar\Omega_1$ et de la gravité Mgr_0, deux situations peuvent se présenter. Si la gravité domine, les atomes sont confinés dans un piège semblable au précédent, très anisotrope, mais qui comporte des « trous » en deux points en $y = \pm r_0$ pour un quadrupole d'axe y, par lesquels les atomes les plus énergétiques peuvent s'échapper (figure 4.2*a*). La variation du couplage modifie également les fréquences d'oscillation horizontales, comme nous le verrons dans la partie 4.5. Si au contraire le couplage domine, le potentiel est minimum dans la région où se trouvent les trous. On a alors un double puits instable (figure 4.2*b*), puisque le couplage au fond des puits est insuffisant pour éviter les retournements de spin.

Si l'on ajoute un champ longitudinal à un profil quadrupolaire transverse, on peut boucher ces trous. C'est cette astuce qui a permis à l'équipe de Jörg Schmiedmayer de produire un double puits à partir d'un piège magnétique sur puce [38]. Dans cette expérience, la fréquence RF est choisie inférieure à la fréquence de résonance au centre et le terme dépendant du désaccord dans l'expression du potentiel 4.9 varie peu. En revanche, le second terme est minimum en deux points où le champ quadrupolaire est parallèle à la polarisation de la RF, ce qui produit le double puits. L'avantage important de cette technique est que l'on peut à loisir régler la distance entre les puits, simplement en jouant sur la fréquence RF. La figure 4.3 montre l'image par absorption des atomes dans le double puits, pour différentes valeurs de la fréquence RF.

Signalons également la possibilité de réaliser un réseau à pas variable, en combinant plusieurs fréquences RF [94]. Il existe également des propositions pour réaliser des

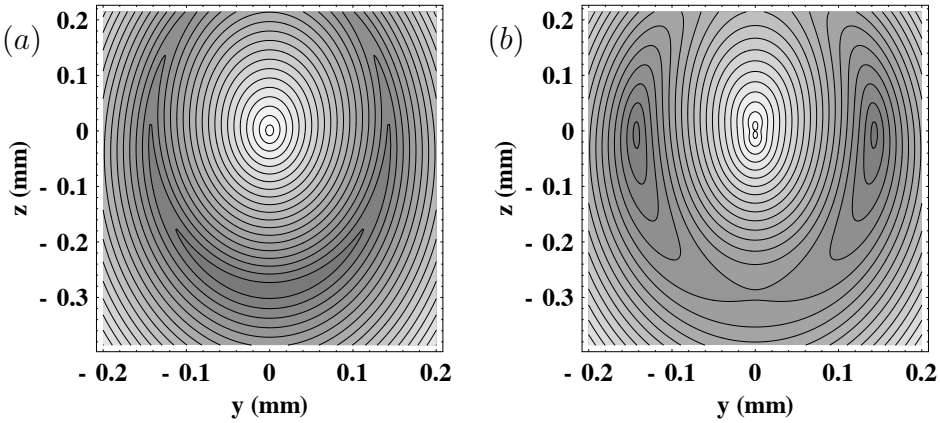

Figure 4.2 — Équipotentielles adiabatiques dans le piège quadrupolaire d'axe y habillé par une radiofréquence polarisée selon y, pour les deux situations extrêmes. (a) Couplage RF faible, $F\hbar\Omega_1 < Mgr_0$, un seul minimum existe, situé en bas de la bulle ; (b) Couplage RF important, $F\hbar\Omega_1 > Mgr_0$, il y a deux minima.

Adiabatic potentials in a quadrupolar trap of axis y dressed with a RF field linearly polarized along y, for two extreme parameter ranges. (a) Low RF coupling, $F\hbar\Omega_1 < Mgr_0$, a single minimum is present at the bottom of the bubble. (b) Large RF coupling, $F\hbar\Omega_1 > Mgr_0$, two minima coexist.

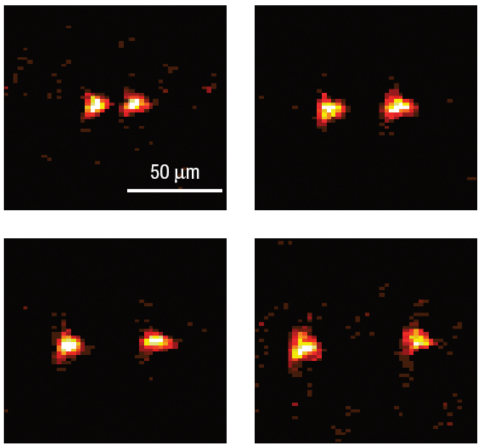

Figure 4.3 — Images par absorption d'atomes de rubidium confinés dans un double puits obtenu en habillant un champ magnétique quadrupolaire transverse. La figure est extraite de la référence [38].

Absorption images of rubidium atoms confined in a double well, obtained by dressing atoms in a quadrupolar transverse magnetic field. Figure reprinted from [38].

tores [101] ou un anneau [95], mais le procédé de chargement de ces structures reste à définir.

Enfin, la combinaison d'une bulle à atomes, réalisée par exemple dans un quadrupôle, et d'une onde stationnaire la coupant en plans successifs permet d'obtenir un

piège annulaire, que je décrirai dans la partie 4.6.

4.2 Implémentation dans un piège QUIC

Dans cette partie, je décrirai plus en détails la première réalisation de piégeage dans des potentiels RF adiabatiques [36]. Le piège obtenu est très anisotrope et permet de conserver les atomes quelques dizaines de secondes. Je discuterai également les limitations concernant la durée de vie et le taux de chauffage dans le piège.

4.2.1 Potentiel piégeant

Le potentiel obtenu avec notre piège magnétique QUIC est représenté selon la coordonnée z sur la figure 4.4. On remarque d'emblée que le confinement aux minima du piège habillé U_2 est plus fort que dans le piège statique de départ, qui est confondu avec le fond du potentiel adiabatique U_{-2}. Le potentiel global n'est cependant pas un double puits, comme le montrent les lignes équipotentielles de la figure 4.5. Il s'agit plutôt d'une bulle, et le puits de droite de la figure 4.4 est connecté au puits de gauche par les parois de la bulle.

La position du minimum de potentiel, qui correspond au puits de gauche, le plus profond en raison de la gravité, est déterminée par la valeur du champ RF. Plus la fréquence augmente, plus la résonance a lieu loin du centre du QUIC – la bulle gonfle – et plus le nuage est décalé vers le bas (figure 4.6). Son altitude est donnée par la position de la résonance $\Omega_0(\mathbf{r}) = \omega_{\mathrm{RF}}$. En notant α l'expression en terme de fréquence du gradient vertical B' de champ magnétique, $\hbar\alpha = g_F \mu_B B'$, l'altitude z_0 du piège est donnée par $\sqrt{\omega_0^2 + \alpha^2 z_0^2} = \omega_{\mathrm{RF}}$, soit

$$z_0 = -\frac{\sqrt{\omega_{\mathrm{RF}}^2 - \omega_0^2}}{\alpha} \tag{4.10}$$

4.2.2 Chargement

Le chargement du piège habillé se fait en trois étapes. Dans un premier temps, on allume le champ RF à une fréquence $\omega_{\mathrm{RF}} < \omega_0$ en dessous de la résonance au centre. Le fond du piège QUIC correspondant à 1,2 ou 1,3 MHz selon les expériences, nous nous plaçons initialement à une fréquence [3] comprise entre 0,8 et 1 MHz. Cette étape de branchement doit être suffisamment lente pour vérifier la condition d'adiabaticité (4.8), soit quelques millisecondes typiquement. Les atomes occupent alors l'état habillé $|2\rangle_\theta$ avec $\theta < \pi/2$.

On augmente ensuite lentement la fréquence RF à amplitude fixe pour traverser la résonance $\Delta = 0$. Le potentiel adiabatique de l'état $|2\rangle_\theta$ se déforme et les atomes se

3. Notons qu'en raison des harmoniques inévitables dans le signal RF amplifié, on doit vérifier $\omega_0/2 < \omega_{\mathrm{RF}} < \omega_0$ et utiliser des atomes assez froids pour qu'en tout point du nuage $\omega_{\mathrm{RF}} < \Omega_0(\mathbf{r}) < 2\omega_{\mathrm{RF}}$.

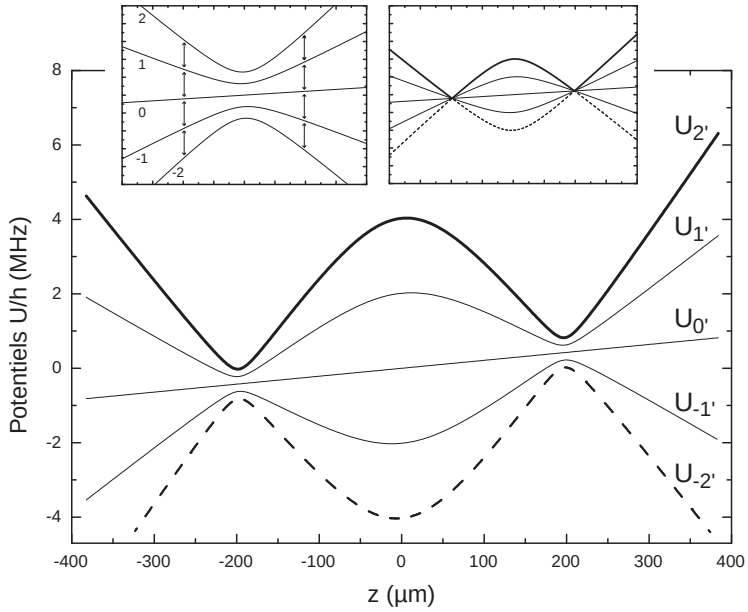

Figure 4.4 — Allure du potentiel U_m selon l'axe vertical z, en présence de la gravité. On a représenté le potentiel pour les cinq niveaux magnétiques de l'état $F = 2$ du fondamental $5S_{1/2}$ du rubidium 87. En trait gras, le potentiel U_2 dans lequel nous piégeons les atomes. En insert, à gauche, les niveaux magnétiques non perturbés dans le champ du QUIC sont couplés sur la surface résonnante par la RF, représentée par des flèches ; à droite, les mêmes niveaux dans la représentation de l'atome habillé sont dégénérés à la résonance, pour un couplage tendant vers zéro. Le couplage lève cette dégénérescence, les énergies diffèrent de la quantité $\hbar\Omega_1(\mathbf{r})$.

Sketch of the adiabatic potential U_m along the vertical axis z going through the QUIC trap centre. Gravity is taken into account. The potential is drawn for all five sublevels of $5S_{1/2}$,$F = 2$ of rubidium 87. In this chapter, the potential U_2, thick line, is discussed. Insert : Left : unperturbed bare states in the QUIC magnetic field are coupled by the RF field at the resonant surface (arrows). Right : in the dressed basis, these levels are degenerate at the resonant surface for a vanishing RF coupling. For a finite coupling, the levels are splitted by $\hbar\Omega_1(\mathbf{r})$.

déplacent lorsque ω_{RF} continue d'augmenter en suivant la loi $z_0(\omega_{\mathrm{RF}})$ donnée à l'équation (4.10). θ reste alors toujours égal à $\pi/2$ et δ à 0 même pour $\Delta > 0$, car $\Omega(\mathbf{r})$ varie avec ω_{RF}. Pour cette étape, il est intéressant de pouvoir varier la fréquence de façon arbitraire en fonction du temps, notamment en passant plus de temps autour de la résonance. Certains synthétiseurs RF permettent l'utilisation de rampes arbitraires de fréquences, ce qui est la solution idéale si le nombre de points de fréquence autorisés est suffisant. J'y reviendrai dans la partie 4.3.

Enfin, la fréquence RF est maintenue à sa valeur finale pour confiner les atomes dans le piège habillé. La figure 4.7 représente le nuage atomique lors de ces trois étapes : (a) dans le QUIC (avant la résonance), (b) à un désaccord intermédiaire et (c) à un désaccord plus important. L'efficacité globale du transfert est excellente, et l'ensemble des atomes issus du QUIC sont piégés dans le potentiel adiabatique à la fin de cette

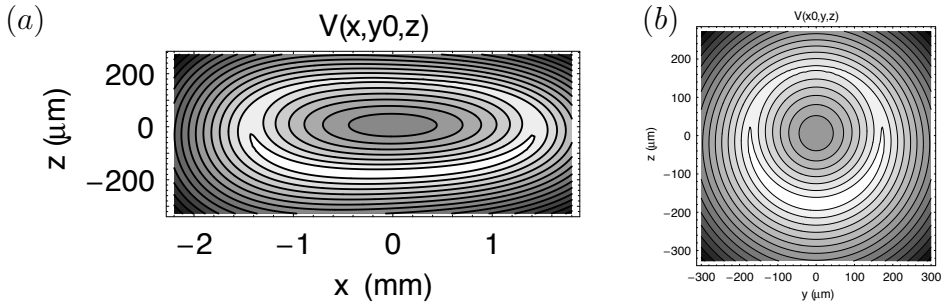

Figure 4.5 — Équipotentielles adiabatiques dans le piège QUIC habillé par la radiofréquence. (a) Coupe dans le plan $y = 0$; les échelles x et z ne sont pas identiques, par souci de lisibilité. On remarque que le minimum du potentiel est légèrement décalé vers la gauche par l'inclinaison des isomagnétiques. (b) Coupe dans le plan $x = x_0$ passant par le minimum de potentiel ($x0$,$z0$).

Isopotential lines in the adiabatic potential. (a) *Cut in the* $y = 0$ *plane, note the different scaling for* x *and* z*. The potential minimum is slightly displaced toward the left due to the shape of the isomagnetic lines.* (b) *Cut in the plane* $x = x_0$ *going through the 3D minimum.*

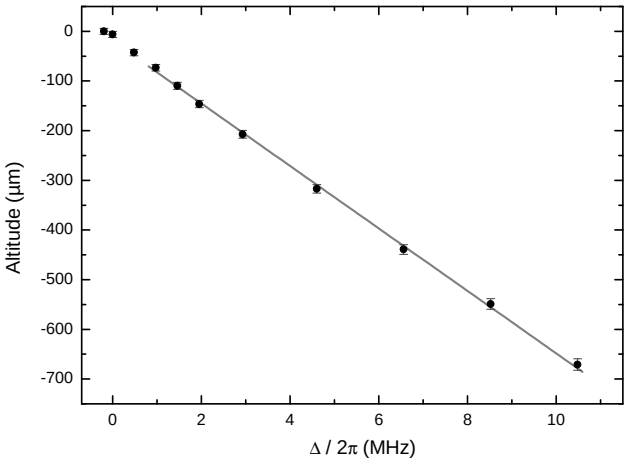

Figure 4.6 — Altitude z_0 du centre du piège habillé en fonction du désaccord RF $\Delta = \omega_{\mathrm{RF}} - \omega_0$. À faible désaccord, la dépendance est quadratique, et elle devient linéaire $z_0 \simeq -\alpha\omega_{\mathrm{RF}}$ à grand désaccord. L'ajustement de la partie linéaire redonne la valeur du gradient vertical de champ magnétique, 225 G/cm dans ce cas.

Height of the trap centre z_0 *as a function of the RF detuning* $\Delta = \omega_{\mathrm{RF}} - \omega_0$*.* z_0 *depends quadratically on* Δ *at low values of* Δ*, then linearly as* $z_0 \simeq -\alpha\omega_{\mathrm{RF}}$ *for large detunings. A linear fit gives access to the magnetic field gradient, 225 G/cm, in agreement with an independent measurement with a magnetic probe.*

procédure.

Nous avons tenté de transférer un condensat, produit dans le QUIC, dans le potentiel adiabatique. Le transfert est très efficace en terme de nombre d'atomes, cependant

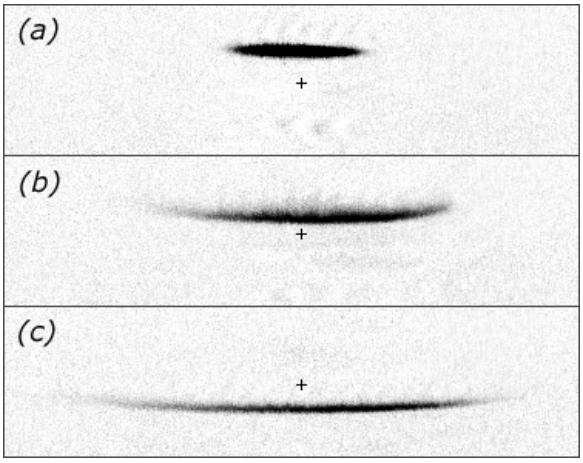

Figure 4.7 — Images par absorption du nuage d'atomes confinés dans le potentiel adiabatique basé sur le champ magnétique du piège QUIC. (a) Atomes dans le piège QUIC (sans radiofréquence) ; (b) Piège habillé avec $\Delta = 1{,}7$ MHz ; (c) Piège habillé avec $\Delta = 6{,}7$ MHz. La croix permet de repérer le déplacement des atomes lorsque la fréquence RF augmente.

Absorption pictures of rubidium atoms confined in the adiabatic potential in the QUIC magnetic field. (a) *Atoms in the QUIC trap, without RF.* (b) *Adiabatic potential with* $\Delta = 1.7$ *MHz ;* (c) *Adiabatic potential with* $\Delta = 6.7$ *MHz. The cross at the centre of the picture is fixed, the cloud is diplaced vertically as the RF frequency changes.*

il s'accompagne d'un chauffage du nuage, de sorte que les atomes ne sont plus condensés dans le piège habillé. On pourrait imputer cela à la mauvaise qualité de la source RF, qui peut exciter le mode dipolaire dans le piège habillé si la fréquence fluctue ou le mode quadrupolaire si l'intensité fluctue. Nous avons évalué ces effets, que je présenterai au paragraphe 4.3. Ils ont effectivement joué un rôle pour certaines expériences, mais sont maintenant négligeables grâce à l'utilisation d'un synthétiseur performant. Cependant le condensat est également détruit si le transfert dans le piège habillé n'est pas adiabatique, au sens de l'évolution des fréquences d'oscillation dans le piège. Cette contrainte est en effet très forte en raison de la faible valeur de la fréquence d'oscillation longitudinale ω_x. Nous pensons actuellement que c'est cet effet qui induit un chauffage lors du chargement du potentiel adiabatique. Cela sera très difficile à éliminer, mais on peut contourner ce problème en transférant un nuage plus chaud dans le piège habillé et en procédant au refroidissement des atomes *in situ*. Je décrirai l'effet de l'ajout d'un second champ RF au paragraphe 4.4

4.2.3 Caractéristiques du piège

Le champ magnétique qui sous-tend le piège habillé est celui du piège QUIC. La surface résonnante, une surface isomagnétique, forme une sorte de bulle autour du centre du piège. À basse température, les atomes ne peuplent pas l'ensemble de cette surface mais uniquement sa partie inférieure en raison de la gravité. Il en résulte un

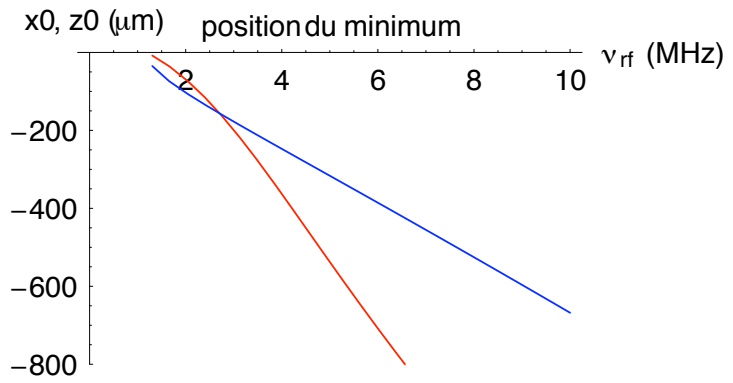

Figure 4.8 — Déplacement du minimum du potentiel adiabatique dans le piège QUIC habillé en fonction de la fréquence RF. Le décalage horizontal x_0, en rouge, est plus important que le décalage vertical (bleu) à fréquence RF élevée.

Displacement of the adiabatic potential minimum in a dressed QUIC as a function of the RF frequency. The horizontal shift x_0, red line, is larger than the vertical shift z_0, blue line, at large RF frequencies.

confinement beaucoup plus important selon la verticale que selon l'horizontale où seule la pesanteur ramène les atomes au centre.

Le piège habillé est très loin d'être un piège harmonique. L'approximation harmonique permet cependant de décrire l'anisotropie du nuage atomique et se justifie à très basse température, c'est pourquoi je donnerai dans la suite la valeur des fréquences d'oscillation. La fréquence d'oscillation verticale ω_z pour le potentiel supérieur U_F est déterminée par la forme du croisement évité. Plus précisément, si B' est la valeur *locale* du gradient de champ magnétique dans la direction verticale, on a

$$\omega_z = \alpha\sqrt{\frac{F\hbar}{M\Omega_1}} \tag{4.11}$$

où $\hbar\alpha = g_F\mu_B B'$. Cette expression a la même structure que la fréquence d'oscillation radiale dans un piège Ioffe-Pritchard, proportionnelle au gradient et inversement proportionnelle à la racine du champ biais, B_1^X dans le cas présent. Cela nous donne donc deux degrés de liberté pour augmenter la valeur de ω_z, avec le même type de contraintes que dans le QUIC sur la valeur minimale de B_1^X si l'on veut éviter les pertes par renversement du spin (pertes Majorana dans un piège magnétique, pertes Landau-Zener ici).

Les fréquences horizontales dépendent de la forme précise de la surface isomagnétique résonnante. Le mécanisme est le même que pour un pendule pesant dont la longueur de la « ficelle » est reliée à la fréquence RF. Si l'on note R_c le rayon de courbure de la surface isomagnétique dans l'une de ses directions propres, la fréquence d'oscillation dans cette direction s'écrit

$$\omega_{\text{osc}} = \sqrt{\frac{g}{R_c}}\,. \tag{4.12}$$

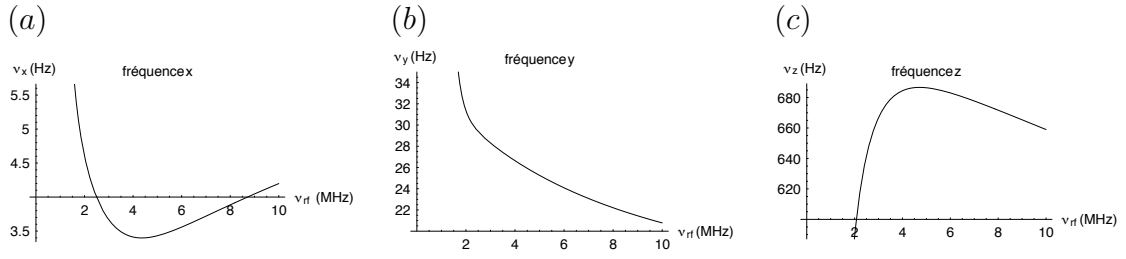

Figure 4.9 — Variation des fréquences d'oscillation dans le piège QUIC habillé par le champ radiofréquence, en fonction de la fréquence RF : Fréquences horizontales pendulaires $\omega_x/2\pi$ (a) et $\omega_y/2\pi$ (b), et fréquence verticale $\omega_z/2\pi$ liée au croisement évité (c) pour un couplage RF $\Omega_1/2\pi = 100$ kHz.

Oscillation frequencies in the dressed QUIC trap as a function of the RF frequency : Pendulum horizontal frequencies $\omega_x/2\pi$ (a) and $\omega_y/2\pi$ (b), and vertical frequency $\omega_z/2\pi$ due to the avoided crossing (c), for a RF coupling $\Omega_1/2\pi = 100$ kHz.

Dans le piège QUIC, les isomagnétiques ne sont pas symétriques par rapport au plan vertical yz, et le centre du piège habillé, situé au point le plus bas d'une isomagnétique, se décale horizontalement lorsque la fréquence RF augmente (voir figure 4.5). La figure 4.8 représente la position (x_0,z_0) du minimum de potentiel en fonction de la fréquence RF.

Les fréquences d'oscillations calculées en ce point sont données sur la figure 4.9 en fonction de $\omega_{\mathrm{RF}}/2\pi$. Les fréquences horizontales diffèrent d'un facteur 10 environ, ce qui correspond au rapport d'anisotropie du piège QUIC. Remarquons qu'elles ne dépendent pas de la valeur du couplage RF, étant imposées par la géométrie. La fréquence verticale est beaucoup plus élevée, elle est tracée ici pour un couplage $\Omega_1/2\pi$ égal à 100 kHz.

Nous avons mesuré la fréquence d'oscillation verticale par deux méthodes, soit par excitation résonnante du mode dipolaire (figure 4.10a), soit par observation directe des oscillations d'un nuage préparé hors équilibre. Dans ce dernier cas, on dépasse la fréquence RF visée lors de la rampe de chargement, et on y revient par un saut brusque de fréquence. Le nuage est alors préparé avec un décalage vertical dans le piège habillé et à vitesse nulle du centre de masse. En observant la position du centre de masse après temps de vol, on a accès à la vitesse du centre de masse dans le piège, qui oscille à la fréquence du piège à partir de la vitesse nulle (voir figure 4.10b).

De cette mesure et de la connaissance du gradient local de champ magnétique, on peut déduire l'amplitude du couplage RF en utilisant l'équation (4.11). Pour les données présentées sur la figure 4.10b, la fréquence d'oscillation est 544 Hz et le couplage RF vaut 192 kHz.

4.2.4 Durée de vie et taux de chauffage

Comme je l'ai évoqué plus haut, la fréquence d'oscillation verticale peut être contrôlée par le choix du couplage RF Ω_1. Cependant, la valeur du couplage intervient aussi dans la durée de vie des atomes dans le piège, qui peuvent effectuer des transitions

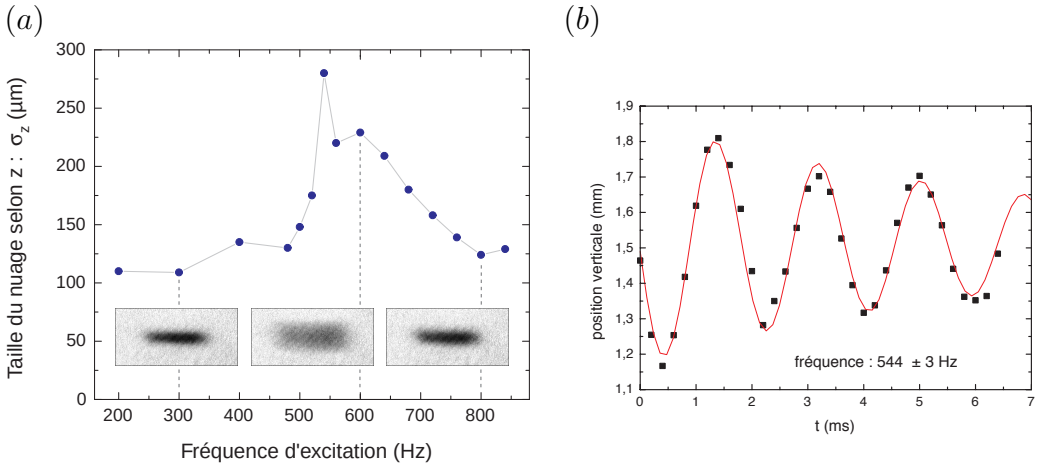

Figure 4.10 — Mesure de la fréquence d'oscillation verticale du potentiel adiabatique. (a) Excitation résonante du mode dipolaire par modulation de la fréquence RF. (b) Mesure du déplacement du nuage après temps de vol.

Measurement of the vertical oscillation frequency, either by (a) *resonant dipolar excitation by RF frequency modulation, or* (b) *direct measurement of the displacement of an oscillating cloud after a time-of-flight.*

non adiabatiques vers des états non piégés si le couplage est faible. On peut estimer la durée de vie dans le piège en calculant la probabilité de transition Landau-Zener

$$P_{\text{LZ}} = 1 - \left[1 - \exp\left(-\frac{\pi}{2}\frac{\Omega_1^2}{|\dot{\delta}|}\right)\right]^{2F} \simeq 2F \exp\left(-\frac{\pi}{2}\frac{\Omega_1^2}{|\dot{\delta}|}\right) . \tag{4.13}$$

Cette expression représente la probabilité de transition non adiabatique de l'état piégeant $|F\rangle_\theta$ vers les $2F$ autres états $|m_F\rangle_\theta$. Elle doit être très faible pour que les potentiels adiabatiques aient un sens, ce qui autorise à utiliser l'expression simplifiée du membre de droite. $\dot{\delta}$ est la variation du désaccord vu par les atomes, reliée à la vitesse à laquelle l'anti-croisement est traversé. On peut moyenner cette expression sur la distribution des vitesses dans le nuage, pour un gaz thermique et calculer un taux de perte γ, en tenant compte du fait que les atomes traversent l'anti-croisement deux fois par période [44]. Le résultat de ce calcul est représenté en termes de durée de vie γ^{-1} sur la figure 4.11 en fonction de la valeur du couplage, pour un gradient de champ magnétique local de 223,6 G/cm correspondant à celui du piège QUIC et pour plusieurs valeurs de la température. La durée de vie est plus longue pour un nuage plus froid, ce qui montre que les atomes sont soumis naturellement à un refroidissement par évaporation. Pour des atomes dans l'état fondamental dans la direction confinée par le piège adiabatique (ici la direction verticale), O. Zobay et B. M. Garraway [102] ont estimé le taux de pertes par transition Landau-Zener à $\Gamma_{\text{fond}} \simeq 2F(\omega_z/\pi)\ \exp[-\pi\Omega_1/(2\sqrt{2}\omega_z)]$. Dans toute la gamme de paramètres explorée ici, cette quantité est toujours extrêmement petite devant ω_z, Ω_1/ω_z étant typiquement supérieur à 20.

Les premières expériences ont été faites avec un synthétiseur Agilent 33250A, dont la fréquence était contrôlée par une tension externe. Elles ont montré une durée de

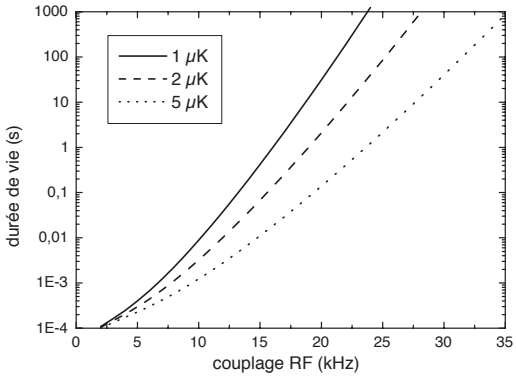

Figure 4.11 — Durée de vie limitée par les transitions non adiabatiques, calculée dans le modèle de Landau-Zener, en fonction de Ω_1. La probabilité de transition est moyennée sur la distribution de vitesse pour différentes valeurs de la température.

Lifetime associated to the non adiabatic Landau-Zener losses as a function of Ω_1*. The transition probability is averaged over the velocity distribution for different values of the temperature.*

vie courte, de l'ordre de 0,4 s, et un taux de chauffage important, à 5 μK/s. Nous nous sommes aperçus cependant que cela était dû à la mauvaise qualité de la source RF, qui peut exciter le mode dipolaire dans le piège habillé si la fréquence fluctue. En effet, ce type de synthétiseur n'est pas conçu pour effectuer des balayages de fréquences importants dans le mode de modulation externe, et le bruit ajouté par la tension se traduisait en bruit de fréquence important. Un taux de chauffage du même ordre a également été observé dans l'équipe de Brian de Marco [43] qui a récemment reproduit nos premières expériences, sans que la nature de ce chauffage soit clairement identifiée.

Nous avons ensuite utilisé deux synthétiseurs à la suite, un Stanford DS-345 pour la rampe de fréquence puis un Rohde & Schwarz SML-01 pour maintenir une fréquence fixe de très grande qualité. L'utilisation des deux synthétiseurs était justifiée par le fait que le Stanford revient à sa fréquence initiale une fois la rampe effectuée, ce qui ne convient évidemment pas à notre application. Dans cette configuration, nous avons obtenu une durée de vie bien meilleure, de 4,5 s, et un taux de chauffage non détectable [36]. Cependant, le saut de phase non contrôlé à la commutation induisait une perte d'atomes, d'autant plus importante que la différence de phase était grande.

Ces résultats ont motivé d'une part l'étude détaillée des contraintes à imposer à la source radiofréquence qui crée le piège, d'autre part la construction d'une source adaptée à ces contraintes. Pour les expériences dans le piège quadrupolaire habillé, nous avons utilisé le synthétiseur conçu et réalisé au laboratoire par l'atelier d'électronique. Avec ce synthétiseur, la durée de vie atteint 9 s avec un couplage RF de 25 kHz. Enfin, tout récemment, nous avons fait l'acquisition d'un synthétiseur Tabor WW1072, avec lequel la durée de vie rejoint celle du piège QUIC (32 s dans ces expériences) et le chauffage tombe à 88 nK/s [55].

4.3 Qualités requises pour la source RF

Les atomes piégés dans le potentiel adiabatique se trouvent exactement à la résonance de l'onde RF avec l'écart en énergie magnétique. Ils sont donc particulièrement sensibles à la qualité de la source. Je présenterai dans cette partie les sources possibles de chauffage et de pertes d'atomes qui lui sont liés et j'en déduirai une série de contraintes à respecter [55].

4.3.1 Chauffage dipolaire

Une fluctuation de fréquence de la source RF se traduit en fluctuation de la position verticale du nuage, en raison de la relation $z_0 = z_0(\omega_{\mathrm{RF}})$, donnée par exemple pour le piège QUIC à l'équation (4.10). John Thomas et ses collègues [103] ont relié le taux de chauffage dipolaire dans un piège harmonique à la densité spectrale de puissance de bruit sur la position du piège :

$$\begin{aligned} \dot{E} &= \frac{1}{4} M \omega_z^4 S_z(\nu_z), \quad \text{avec} \\ S_z(\nu) &= 4 \int_0^\infty d\tau \, \cos(2\pi\nu\tau) \langle \delta z(t) \, \delta z(t+\tau) \rangle. \end{aligned} \tag{4.14}$$

Le chauffage est sensible à une fluctuation de la position à la fréquence du piège $\nu_z = \omega_z/2\pi$ qui excite le mode dipolaire. En toute rigueur, la position selon x dépend également de la fréquence RF. Cependant, le taux de chauffage est proportionnel à la puissance quatrième de la fréquence d'oscillation, qui est de quelques Hz selon la direction x, ce qui rend négligeable la contribution au chauffage dipolaire de ce degré de liberté.

S_z est relié à la densité spectrale de puissance S_y de la fluctuation relative de fréquence RF, $y = \delta\omega_{\mathrm{RF}}/\omega_{\mathrm{RF}}$ en utilisant la relation $z_0(\omega_{\mathrm{RF}})$:

$$S_z(\nu) = \left(\omega_{\mathrm{RF}} \frac{dz_0}{d\omega_{\mathrm{RF}}} \right)^2 S_y(\nu). \tag{4.15}$$

On peut alors donner une borne supérieure au bruit de fréquence toléré pour limiter le taux de chauffage dipolaire à une valeur donnée. Par exemple, pour le piège QUIC habillé avec une fréquence RF de 3 MHz et pour une fréquence transverse du piège habillé de 1 kHz, $S_y(\nu_z)$ doit être inférieure à -118 dB·Hz^{-1} à 1 kHz pour que le chauffage linéaire reste inférieur à 0,1 μK/s. Cette contrainte est généralement satisfaite très largement par les synthétiseurs commerciaux, dont le bruit relatif de fréquence est couramment dans la gamme des -180 à -200 dB·Hz^{-1}. Cependant, le synthétiseur Agilent 33250A utilisé en mode de modulation externe de fréquence présente un bruit élevé $S_y(\nu_z) = -100$ dB·Hz^{-1} à la fréquence du piège ($\nu_z = 600$ Hz), qui explique entièrement le taux de chauffage de 5 μK/s observé dans le piège habillé, avec une fréquence RF de 3 MHz. Par comparaison, le taux de chauffage tombe à 80 nK/s avec un synthétiseur DDS commercial Tabor WW1072 [55].

Le synthétiseur « maison » présente quant à lui une stabilité de fréquence remarquable, avec un bruit de phase de -78 dB·rad^2·Hz^{-1}, qui correspond à $S_y(\nu) =$

-207 dB·Hz^{-1} à $\nu = 1$ Hz, ce qui est sa valeur maximale dans la gamme 1 Hz – 100 kHz. Le taux de chauffage correspondant est complètement négligeable, la valeur de S_y à quelques centaines de Hz étant encore inférieure à celle-ci.

Remarquons enfin que des fluctuations de courant dans les alimentations utilisées pour réaliser le piège magnétique pourraient également donner lieu à du chauffage dipolaire. Paul-Éric Pottie a mesuré le bruit relatif de courant des alimentations, qui est au plus de -125 dB·Hz^{-1} sur les pics multiples de 50 Hz (à 600 Hz par exemple). En dehors de ces pics, le bruit relatif n'excède pas -140 dB·Hz^{-1}. Cet ordre de grandeur est tel que le chauffage correspondant est négligeable, même lorsque les alimentations du quadrupôle et de la bobine Ioffe sont indépendantes.

4.3.2 Chauffage paramétrique

Il peut également exister dans le piège du chauffage paramétrique, lié à des fluctuations de la fréquence d'oscillation. S'il existe une composante de bruit résonnante à $2\nu_z$, la température des atomes croît exponentiellement avec le temps, au taux Γ_p donné par [103]

$$\Gamma_p = \pi^2 \nu_z^2 S_k(2\nu_z) = \pi^2 \nu_z^2 S_a(2\nu_z) \tag{4.16}$$

où S_a est la densité spectrale de puissance pour le bruit relatif d'amplitude, S_k le bruit sur la raideur k du piège et on a utilisé $k \propto \nu_z^2 \propto \Omega_1^{-1}$. Pour que le taux de chauffage reste en dessous de 0,01 s^{-1}, on doit avoir $S_a < -90$ dB·Hz^{-1} à 2 kHz pour une fréquence d'oscillation typique de 1 kHz. Cette valeur doit tenir compte à la fois des performances de la source, mais aussi du bruit ajouté par l'atténuateur et l'amplificateur RF utilisés, qui amène un bruit de +5 dB et +3 dB respectivement. Toutes les sources RF que nous avons utilisées présentaient un bruit relatif d'amplitude d'au plus -110 dB·Hz^{-1}, et nous n'avons jamais mis en évidence de chauffage paramétrique dans le piège habillé. Le synthétiseur « maison » est également très bon, avec un bruit d'amplitude relative de -120 dB·Hz^{-1} à 1 Hz.

4.3.3 Sauts de phase

Le spin des atomes habillés par le champ RF précesse autour du champ magnétique local à la fréquence RF, aligné avec la direction $\mathbf{e}_\theta$. Un saut de phase du champ conduit alors à un changement brutal d'orientation de $\mathbf{e}_\theta$ que le spin atomique ne peut pas suivre. Les atomes occupent un état qui se décompose sur plusieurs sous-états de spin selon le nouvel axe propre $\mathbf{e}_{\theta'}$, en particulier dans des états non piégés. Il en résulte une perte d'une partie des atomes, que l'on peut évaluer en supposant que seuls les composantes $|2'\rangle$ et $|1'\rangle$ de la nouvelle base restent piégées. La population relative restante vaut donc $p = |\langle 2|2'\rangle|^2 + |\langle 2|1'\rangle|^2$. Comme le suggère la figure 4.12, pour un saut de phase d'amplitude $\Delta\varphi$, la nouvelle direction de l'état propre fait avec l'ancienne un angle ψ tel que

$$\cos\psi = \cos^2\theta + \sin^2\theta \cos\Delta\varphi\,. \tag{4.17}$$

En particulier, à résonance au fond du piège habillé $\psi = \Delta\varphi$. Cependant, du fait de la distribution de position dans le piège, reliée à la température, tous les atomes ne

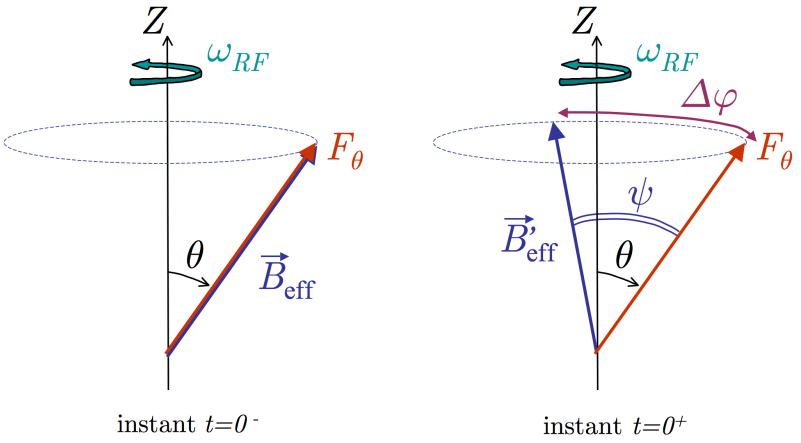

Figure 4.12 — Orientation relative du champ directeur effectif et du spin atomique, avant (à gauche) et après (à droite) un saut de phase $\Delta\varphi$. Les directions finales font entre elles un angle ψ.

Relative orientation of the effective magnetic field and the atomic spin. Left : before the phase jump, the two directions are identical. Right : after a phase jump $\Delta\varphi$, they make an angle of ψ.

sont pas à résonance et il faut moyenner la population restante $p(\psi) = \cos^8(\psi/2) + 4\cos^6(\psi/2)\sin^2(\psi/2)$ sur les valeurs possibles de θ à la température T.

Nous avons mesuré les pertes induites par un saut de phase de l'onde RF, en fonction de l'amplitude du saut. Pour cela, on commute le signal sur le synthétiseur Rohde & Schwarz utilisé à fréquence fixe à la fin de la rampe en fréquence produite par le synthétiseur Stanford. Le saut de phase est aléatoire et on le mesure *a posteriori* à l'oscilloscope. On mesure le nombre d'atomes dans le piège habillé une seconde après la fin de la rampe de chargement. Les données sont présentées sur la figure 4.13. La courbe en trait plein correspond au calcul décrit ci-dessus, en prenant une température $T = 4\ \mu$K et un couplage RF $\Omega_1/2\pi = 165$ kHz correspondant à la situation expérimentale. Le très bon accord, sans aucun paramètre ajustable, est remarquable pour ce modèle simple.

La conséquence pratique de ces mesures est l'exigence que l'on doit avoir sur la continuité de la phase de la source RF, en particulier au cours de la rampe en fréquence. L'utilisation de sources DDS — pour l'anglais « Direct Digital Synthesis » [104] — est alors particulièrement appropriée car la phase est continue par construction pour ce type de sources qui génèrent le signal point par point. Le synthétiseur Stanford est un exemple de ce type de sources, qui est aussi à la base de notre synthétiseur « maison ».

4.3.4 Sauts de fréquence

De la même manière que pour le saut de phase, un saut de fréquence $\delta\omega_{\text{RF}}$ modifie brutalement la direction de l'état propre. Cette fois, comme l'indique la figure 4.14, c'est l'angle θ qui change de $\delta\theta = \delta\omega_{\text{RF}}\,\Omega_1/(\delta^2+\Omega_1^2)$, soit au plus $\delta\theta = \delta\omega_{\text{RF}}/\Omega_1$. La population

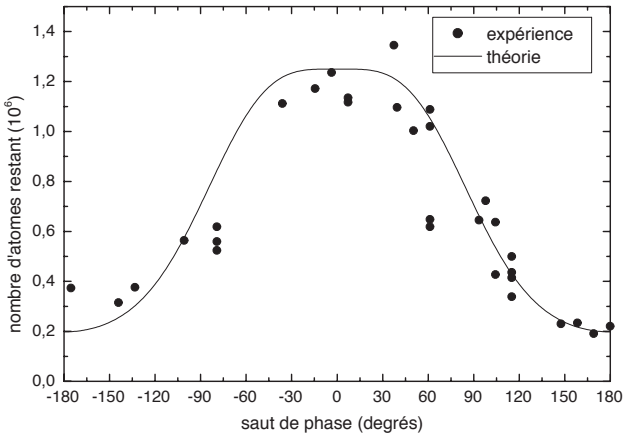

Figure 4.13 — Nombre relatif d'atomes restant dans le piège QUIC habillé après un saut de phase du champ RF. Les données expérimentales (points noirs) correspondent à une séquence à deux synthétiseurs Stanford puis Rohde & Schwarz. La fréquence finale vaut 3 MHz. Le trait plein correspond au calcul avec les mêmes paramètres de température, $T = 4$ μK, et de couplage, $\Omega_1/2\pi = 165$ kHz.

Relative atom number in the dressed QUIC after a phase jump in the RF field. Dots : Experimental data from a two-synthesizer sequence (Stanford, then Rhode & Schwarz). Full line : Corresponding theory for the known values of the temperature, $T = 4\mu K$, and the coupling strength, $\Omega_1/2\pi = 165$ kHz. The final RF frequency is 3 MHz.

restant dans l'état $|2\rangle_\theta$ habillé après un saut de fréquence vaut $\cos^{4F}(\delta\theta/2) \simeq 1 - \delta\theta^2$ pour $F = 2$, soit au moins $1 - \delta\omega_{\rm RF}^2/\Omega_1^2$.

De tels sauts de fréquence se produisent lors de la rampe en fréquence utilisée pour charger le piège, notamment si l'on utilise une rampe de fréquence arbitraire générée par un DDS. Le saut de fréquence aura alors lieu N fois si N est le nombre de points de fréquence de cette rampe. Imaginons pour simplifier que l'on effectue une rampe linéaire d'amplitude totale $\Delta\omega_{\rm RF}$ avec N valeurs successives de fréquence, de sorte que $\delta\omega_{\rm RF} = \Delta\omega_{\rm RF}/N$. La population finale dans l'état habillé $|2\rangle_\theta$ sera donc au moins de l'ordre de

$$P_2 > \left[\cos\left(\frac{\Delta\omega_{\rm RF}}{2N\Omega_1}\right)\right]^{8N} \simeq 1 - \frac{\Delta\omega_{\rm RF}^2}{N\Omega_1^2} \tag{4.18}$$

Pour un balayage de 4 MHz avec un couplage RF de 200 kHz, $N = 4000$ points de fréquence sont suffisants pour garder 90% de la population dans l'état habillé. Il en faut 16 000 en revanche si le couplage vaut 100 kHz. On a donc intérêt à effectuer la rampe à couplage plus élevé, quitte à réduire le couplage ensuite pour augmenter la fréquence d'oscillation transverse.

Pour mettre en évidence l'effet de la discrétisation des fréquences, j'ai mesuré le nombre d'atomes et la température dans le piège habillé après une seconde de pié-

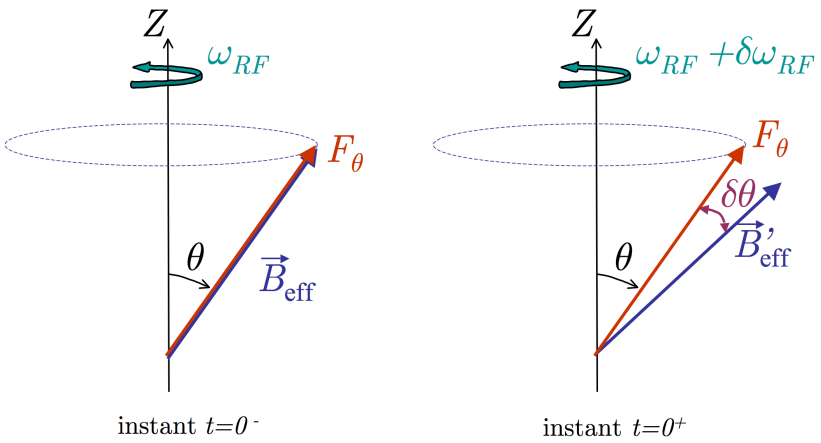

Figure 4.14 — Orientation relative du champ directeur effectif et du spin atomique, avant (à gauche) et après (à droite) un saut de fréquence $\delta\omega_{\text{RF}}$. Les directions finales font entre elles un angle $\delta\theta$.

Relative orientation of the effective magnetic field and the atomic spin. Left : before the frequency jump, the two directions are identical. Right : after a frequency jump $\delta\omega_{\text{RF}}$, they make an angle of $\delta\theta$.

geage [4], en faisant varier le nombre N de points de fréquence que comportait la rampe de chargement [55]. J'ai utilisé pour cela un synthétiseur DDS de chez Tabor Electronics (modèle WW1072), qui comporte jusqu'à 20 000 points de fréquence et présente l'avantage de maintenir en fin de rampe la fréquence finale, ce qui permet de confiner les atomes dans le piège habillé aussi longtemps qu'on le souhaite. La durée de la rampe utilisée est maintenue à 100 ms. Elle comporte une phase initiale de 12 ms à fréquence fixe (1 MHz), pendant laquelle l'amplitude de la RF est augmentée linéairement de 0 à 192 kHz, cette valeur étant déduite de la mesure de la fréquence d'oscillation dans le piège à 5 MHz (voir paragraphe 4.2.3). Le reste des points, soit 88% de N, constitue la rampe à proprement parler. La fréquence varie de 1 à 8 MHz avec un passage plus lent autour de 1,25 MHz où se trouve le fond du piège magnétique. À partir d'une séquence complète de 20 000 points, j'ai constitué des sous-séquences de 500 à 15 000 en échantillonnant la séquence de référence. Ainsi, la forme de la rampe est inchangée, seul varie le nombre de points. Les résultats présentés sur la figure 4.15*a* sont comparés avec le modèle de l'équation (4.18), en tenant compte des $0{,}88N$ points où la fréquence varie. L'accord est très bon, sachant que le modèle reste simple (rampe linéaire et amplitude RF constante).

L'effet sur la température du nuage est très clair également, comme le montre la figure 4.15*b*. Il est lié aux déplacements brusques lors de la rampe induits par un saut de fréquence. La température asymptotique vaut 8 μK pour une température initiale de 10 μK dans le piège magnétique. Cette baisse de la température est liée à la baisse de la fréquence d'oscillation moyenne quand on passe du piège magnétique au piège habillé.

4. Pour cette série d'expérience, la durée de vie dans le piège était de 25 s, ce qui permet de négliger les pertes pendant la première seconde.

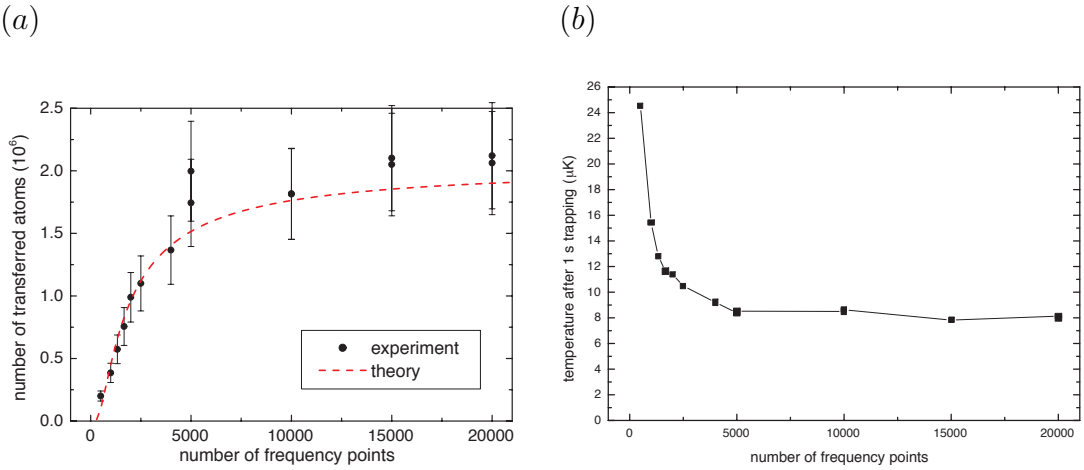

Figure 4.15 — Influence du nombre de points de fréquence de la rampe sur (*a*) le nombre d'atomes et (*b*) leur température après une seconde de piégeage dans le piège RF. Le nombre d'atomes attendu d'après l'équation (4.18) est indiqué en (*a*) par une courbe en traits pointillés.

Influence of the number of frequency points in the ramp on (*a*) *the final atom number and* (*b*) *their temperature after 1 s in the adiabatic potential. Dashed line in* (*a*) *: expected atom number deduced from Eq. (4.18).*

On s'attendrait à une baisse plus importante encore si le transfert était adiabatique.

Le nombre de points de fréquence nécessaires dans le cas présenté ici est de l'ordre de 10 000, pour obtenir 85% au moins de transfert, l'expérience indiquant même un transfert compatible avec 100% pour ce nombre de points et une rampe améliorée. Le synthétiseur Stanford permet de réaliser des balayages en fréquence arbitraires, mais ne propose que 1 500 points de fréquence. Le synthétiseur Tabor Electronics convient pour des rampes jusqu'à 7 MHz d'amplitude comme celle décrite ci-dessus. Sur ce point, le synthétiseur « maison » est idéal puisque l'on dispose de plus de 260 000 points de fréquence et une gestion de la mémoire qui permet d'économiser des points en utilisant un taux de balayage variable au cours de la séquence. On peut ainsi optimiser la résolution en fréquence au moment où elle est le plus critique et n'utiliser qu'un seul point pour maintenir la fréquence finale pendant plusieurs minutes.

4.4 Refroidissement par évaporation dans le piège habillé

Comme je l'ai mentionné plus haut, la déformation du potentiel lors du transfert du piège magnétique QUIC vers le piège habillé n'est pas adiabatique. Il est très difficile en particulier de vérifier la condition d'adiabaticité $\dot{\omega}_x \ll \omega_x^2$ dans la direction x où la fréquence d'oscillation tombe rapidement à quelques Hz seulement (voir figure 4.9), et le condensat est détruit lors du transfert. L'idéal serait alors de produire le condensat directement dans le piège habillé. Cela peut en principe être réalisé en refroidissant

les atomes dans le piège habillé, par évaporation, à l'aide d'une seconde fréquence RF ω_2 légèrement supérieure à la fréquence ω_{RF} qui crée le potentiel adiabatique [40]. J'exposerai assez en détail la théorie de ce couplage à une seconde source RF, car elle ne figure pas par ailleurs dans une des thèses de doctorat de notre équipe.

4.4.1 Principe

Discutons à présent l'effet de la seconde fréquence RF ω_2 d'amplitude Ω_2. Dans tout le paragraphe 4.4, par souci de clarté, la fréquence RF utilisée pour former le potentiel adiabatique est notée ω_1 au lieu de ω_{RF}. La figure 4.16 montre les points où chacune des fréquences couple les niveaux magnétiques successifs. Dans le référentiel du laboratoire (figure 4.16*a*), le couplage a lieu aux deux points $z_0(\omega_1)$ et $z_0(\omega_2)$. Dans le référentiel tournant à la fréquence ω_1 (figure 4.16*b*), on s'attend à ce que les états propres du potentiel adiabatique soient couplés aux endroits où la différence de fréquence $\Delta_2 = \omega_2 - \omega_1$ correspond à l'écart entre les énergies des états habillés. Cela est vrai aux points $z_0(\omega_2)$ mais aussi en des points symétriques par rapport à $z_0(\omega_1)$, situé à l'intérieur de la surface résonnante à ω_1. Nous verrons que ces nouvelles résonances, correspondant à l'absorption d'un photon à ω_2 et l'émission stimulée de deux photons à ω_1, apparaissent naturellement dans une description des états dans la base habillée. Le résultat de ce couplage est, comme dans le cas habituel du refroidissement par évaporation dans un piège magnétique, de limiter la profondeur du potentiel adiabatique à une valeur contrôlée par la seconde fréquence RF, que l'on peut approcher de ω_1 pour forcer l'évaporation.

4.4.2 Couplage des états habillés

Les états de spin, en présence des deux champs de fréquence différente, sont couplés entre eux de façon complexe, et dans le cas général la solution doit être obtenue numériquement. Cependant, dans le cas où l'un des couplages Ω_1 domine, un traitement analytique approché donne d'excellents résultats.

On considère donc qu'au champ Ω_1 de fréquence ω_1, polarisé linéairement selon y, on ajoute un autre champ Ω_2 de fréquence ω_2, de même polarisation. On note $\delta_1(\mathbf{r}) = \omega_1 - \Omega_0(\mathbf{r})$. Avec les mêmes notations qu'au paragraphe 4.1 et à l'équation (4.2), le hamiltonien dans le référentiel du laboratoire est à présent

$$H = \Omega_0(\mathbf{r})F_Z + 2\Omega_1 \cos(\omega_1 t)F_X + 2\Omega_2 \cos(\omega_2 t)F_X \,. \tag{4.19}$$

On suppose ici pour alléger la discussion que le couplage ne dépend pas de la position. Une variation du couplage avec la position pourrait être ajoutée sans modifier les résultats généraux.

On se place ensuite dans le référentiel tournant à la fréquence ω_1 autour de Z et on applique la rotation autour de Y pour retrouver les états habillés discutés au 4.1. On néglige alors les termes qui varient rapidement (approximation de l'onde tournante), aux fréquences $2\omega_1$ ou $\omega_1 + \omega_2$, mais on conserve le terme à la fréquence $\Delta_2 = \omega_2 - \omega_1$. On obtient :

$$H_{\text{eff}} = \Omega(\mathbf{r})F_\theta + \Omega_2 \cos(\Delta_2 t)F_X - \Omega_2 \sin(\Delta_2 t)F_Y \tag{4.20}$$

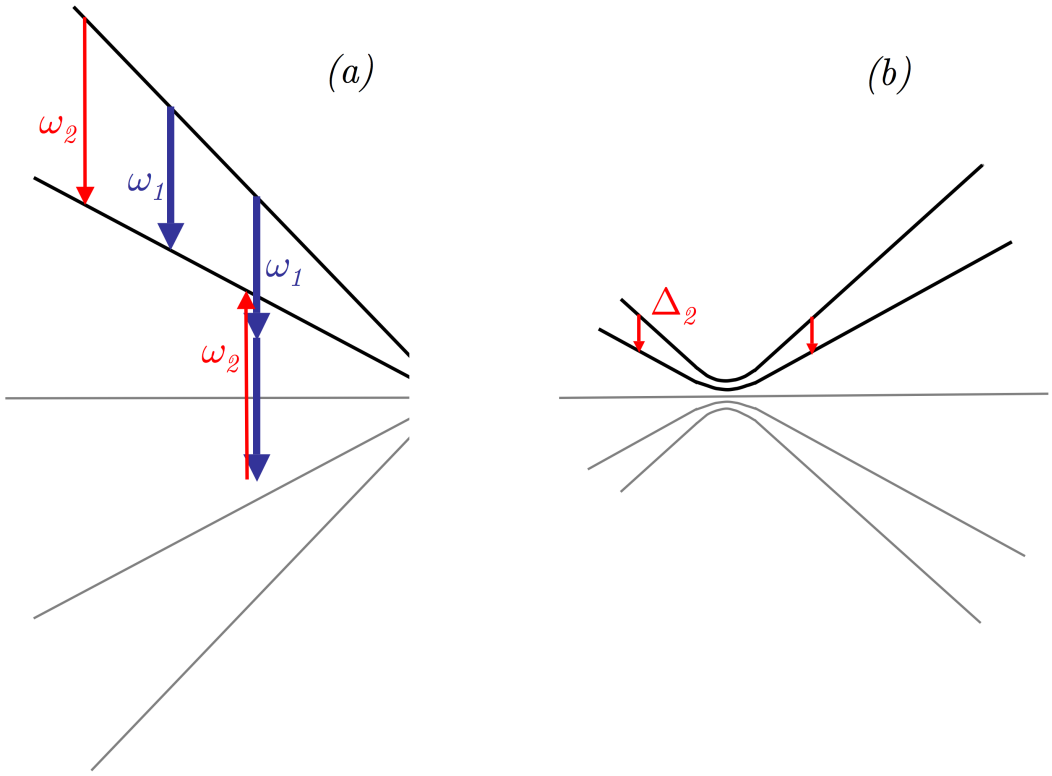

Figure 4.16 — Energie des états magnétiques non couplés (a) et potentiels adiabatiques (b) en fonction de z, en présence de deux champs RF de fréquences différentes, $\omega_2 > \omega_1$. À la résonance pour ω_1, la dégénérescence est levée et l'écart entre états habillés est $\hbar\Omega_1$. Le second champ RF ω_2 induit des transitions de part et d'autre du centre du potentiel adiabatique (*i.e.* de la surface résonnante à ω_1). A gauche, la résonance ordinaire avec émission d'un photon à ω_2, à droite, la résonance extraordinaire impliquant deux photons ω_1 supplémentaires. La longueur des flèches dans la figure (b) correspond à $\Delta_2 = \omega_2 - \omega_1$.

Energy of the uncoupled magnetic states (a) and the adiabatic potentials (b) as a function of z, in the presence of a two RF fields, with $\omega_2 > \omega_1$. In addition to the expected transitions at ω_1 and ω_2, a symmetric transition appears on the other side of the resonant surface, involving more photons. In the dressed basis (b), the length of both arrows is $\Delta_2 = \omega_2 - \omega_1$.

où θ, F_θ et $\Omega(\mathbf{r}) = \sqrt{\delta_1^2 + \Omega_1^2}$ sont définis comme au 4.1.

Ce hamiltonien est en réalité celui d'un spin F en présence d'un couplage RF à la fréquence Δ_2. Il correspond au schéma de la figure 4.16b. La direction X, contrairement à Y, n'est pas orthogonale à la direction $\mathbf{e}_\theta$. On complète alors la base par un vecteur $\mathbf{e}_{\theta\perp} = \mathbf{e}_\theta \times \mathbf{e}_Y$. En ne conservant que les termes du couplage orthogonaux à $\mathbf{e}_\theta$, il vient :

$$H_{\text{eff}} = \Omega(\mathbf{r})F_\theta - \Omega_2 \cos\theta(\mathbf{r}) \cos(\Delta_2 t) F_{\theta\perp} - \Omega_2 \sin(\Delta_2 t) F_Y \,. \tag{4.21}$$

Il est alors naturel d'appliquer une seconde fois l'approximation de l'onde tournante, pour les atomes habillés soumis à ce couplage. Cela est justifié si le désaccord effectif

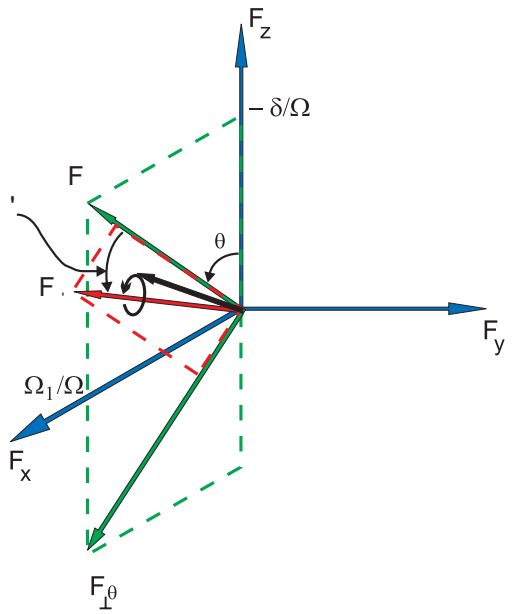

Figure 4.17 — Base des états doublement habillés. Le spin des atomes confinés dans le potentiel adiabatique est aligné selon F_θ. Il bascule selon $F_{\theta'}$ sous l'effet de la seconde RF, dans le référentiel tournant autour de F_θ à la fréquence Δ_2.

Basis of the doubly dressed states. The spin of the atoms confined in the adiabatic potential is aligned along F_θ. It flips along $F_{\theta'}$ in the presence of the second RF field, in a basis rotationg around F_θ at frequency Δ_2.

$\delta_2(\mathbf{r}) = \Delta_2 - \Omega(\mathbf{r})$ et le couplage Ω_2 sont petits devant la fréquence effective Δ_2. Plaçons-nous dans le cas où $\Delta_2 > 0$. Dans le référentiel en rotation à la fréquence Δ_2 autour de $\mathbf{e}_\theta$ et en ne conservant que les termes résonnants, on obtient le hamiltonien indépendant du temps décrivant les états *doublement habillés*[5] :

$$H'_{\text{eff}} = -\delta_2(\mathbf{r})F_\theta - \frac{\Omega_2}{2}\left(1+\cos\theta(\mathbf{r})\right)F_{\theta\perp} = \Omega'(\mathbf{r})F_{\theta'}\,. \tag{4.22}$$

Cette expression est analogue à (4.4), avec un couplage dépendant explicitement de la position via $\theta(\mathbf{r})$. Les états doublement habillés $|m_F\rangle_{\theta'}$ sont les états propres de $F_{\theta'}$, la projection du spin sur la direction $\mathbf{e}' = \cos\theta'\mathbf{e}_\theta + \sin\theta'\mathbf{e}_{\theta\perp}$, représentée sur la figure 4.17. $\Omega'(\mathbf{r}) = \sqrt{\delta_2^2 + \Omega_2^2(1+\cos\theta)^2/4}$ est l'écart en fréquence entre états doublement habillés, avec $\operatorname{tg}\theta' = -\Omega_2(1+\cos\theta)/(2\delta_2)$.

De part et d'autre du point où se concentrent les atomes, d'altitude $z_0(\omega_1)$ ou d'angle $\theta = \pi/2$, il y a deux résonances aux points $\mathbf{r}$ tels que $|\Delta_2| = \Omega(\mathbf{r})$, c'est-à-dire pour

$$\theta(\mathbf{r}) = \theta_0 = \operatorname{Arccos}\left(\frac{\sqrt{\Delta_2^2 - \Omega_1^2}}{\Delta_2}\right) \quad \text{et} \quad \theta(\mathbf{r}) = \pi - \theta_0\,. \tag{4.23}$$

5. Dans le cas où $\Delta_2 < 0$, c'est-à-dire où la seconde RF ω_2 a une fréquence inférieure à la première ω_1, il faut tourner à la fréquence Δ_2 autour de $-F_\theta$ ou bien à la fréquence $-\Delta_2 = |\Delta_2|$ autour de F_θ, le désaccord vaut $\delta_2(\mathbf{r}) = |\Delta_2| - \Omega(\mathbf{r})$ et le couplage vaut $\Omega_2/2 \times (1-\cos\theta(\mathbf{r}))$.

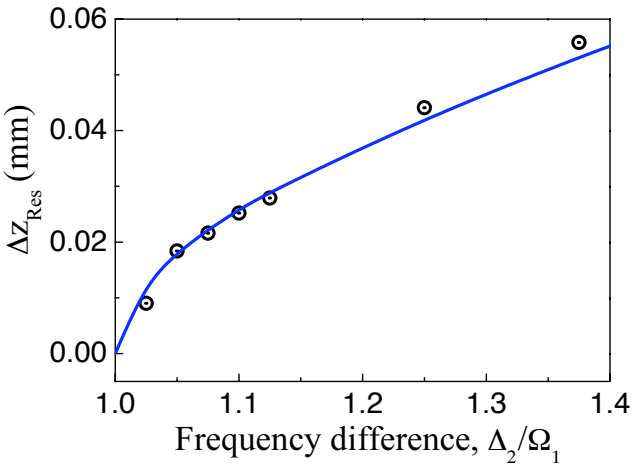

Figure 4.18 — Ecart vertical entre les deux résonances, ordinaire et extraordinaire, en fonction de la différence de fréquence Δ_2 en unités de Ω_1. En points, le calcul exact de la référence [40], en trait plein le résultat du modèle, Eq.(4.25).

Vertical separation between the outer and the inner resonances, as a function of the frequency difference Δ_2 in units of Ω_1. Dots : exact calculation [40]. Full line : model of Eq.(4.25).

Le couplage est différent pour ces deux points, valant respectivement

$$\frac{\Omega_2}{2}\left(1+\sqrt{1-\frac{\Omega_1^2}{\Delta_2^2}}\right) \quad \text{et} \quad \frac{\Omega_2}{2}\left(1-\sqrt{1-\frac{\Omega_1^2}{\Delta_2^2}}\right) . \tag{4.24}$$

Sous cette forme, ces expressions sont aussi valables pour $\Delta_2 < 0$. J'appellerai *résonance ordinaire* celle qui correspond à $\theta = \theta_0$, et *résonance extraordinaire* la seconde. La résonance ordinaire correspond à l'émission d'un photon à ω_2 dans la base non couplée, à gauche sur la figure 4.16. En effet, à grande valeur de Δ_2 par rapport à Ω_1, $\theta_0 \simeq 0$ pour $\Delta_2 > 0$, la résonance extraordinaire a une amplitude tendant vers 0 et la résonance se produit seulement à la position $z_0(\omega_2)$ avec un couplage Ω_2. Cela correspond simplement au cas où F_θ se confond avec F_Z et où la seconde rotation à $\omega_2 - \omega_1$, combinée à la rotation à ω_1 autour de F_Z, consiste tout simplement en une rotation à ω_2 autour de F_Z, comme si la première onde n'était pas présente [6]. Cela revient à traiter indépendamment l'effet des deux fréquences RF. Cette résonance unique se trouve à gauche sur la figure 4.16 pour $\omega_2 > \omega_1$ et à droite dans le cas contraire.

Lorsque Δ_2 se rapproche de Ω_1, ou de manière équivalente lorsque ω_2 ne diffère de ω_1 que par une fraction de Ω_1, le fait que les atomes soient habillés par la première RF à ω_1 prend toute son importance. Les transitions ont lieu entre états habillés et non simplement entre états magnétiques de la base non couplée. La résonance extraordinaire

6. Dans le cas où $\Delta_2 < 0$, la seconde rotation à $\omega_2 - \omega_1$ se fait bien aussi autour de F_Z, qui se confond alors avec $-F_\theta$.

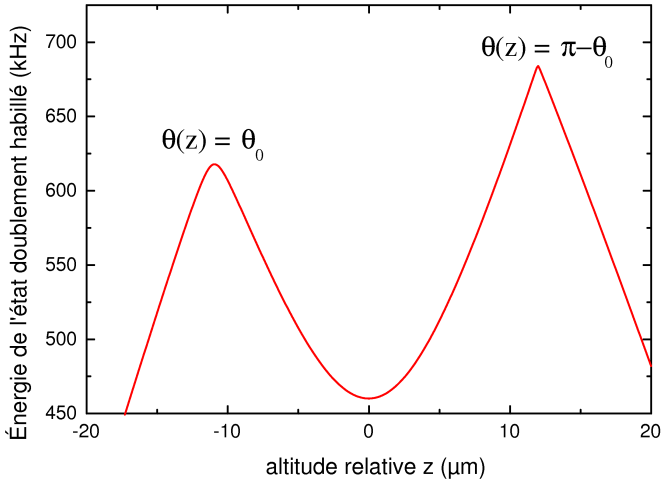

Figure 4.19 — Énergie potentielle des atomes dans l'état doublement habillé $|2\rangle_{\theta'}$. On a pris $\omega_1 = 2\pi\times 5\,\text{MHz}$, $\Omega_1 = 2\pi\times 100\,\text{kHz}$, $\omega_1 = 2\pi\times 5{,}2\,\text{MHz}$, $\Omega_2 = 2\pi\times 10\,\text{kHz}$. Les deux résonances correspondent aux conditions $\theta(z) = \theta_0$ et $\theta(z) = \pi - \theta_0$.

Adiabatic potential of the doubly dressed state $|2\rangle_{\theta'}$, with $\omega_1 = 2\pi \times 5\,MHz$, $\Omega_1 = 2\pi \times 100\,kHz$, $\omega_1 = 2\pi \times 5.2\,MHz$, $\Omega_2 = 2\pi \times 10\,kHz$. The two resonances at $\theta(z) = \theta_0$ and $\theta(z) = \pi - \theta_0$ set the trap depth.

apparaît et son amplitude augmente aux dépens de la résonance ordinaire à mesure que Δ_2 se rapproche de Ω_1. On a alors deux voies d'évaporation possibles de part et d'autre du fond du potentiel adiabatique, comme le suggère la figure 4.16. Si l'on note $\hbar\alpha/(g_F\mu_B)$ le gradient local du champ magnétique du QUIC, les deux résonances sont séparées de

$$\Delta z = \frac{2\sqrt{\Delta_2^2 - \Omega_1^2}}{\alpha} \tag{4.25}$$

Pour $\Delta_2 = \Omega_1$, les deux résonances se rejoignent et on couple le fond du puits adiabatique avec les niveaux non piégés, qui sont connectés adiabatiquement aux niveaux piégés au centre du QUIC. Remarquons d'ailleurs qu'il n'y a pas de résonance pour $|\Delta_2| < \Omega_1$ puisque les états adiabatiques sont séparés d'au moins Ω_1. Si l'on revient alors à la condition de validité de la seconde approximation de l'onde tournante, on peut dire qu'elle est valable si $\Omega_2 \ll \Omega_1$ et autour des résonances, de telle sorte que $|\delta_2(\mathbf{r})| \ll \Omega_1$. Cela suffit d'ailleurs à décrire complètement l'effet de la seconde RF, de $\delta_2 = 0$ à $|\delta_2| > \Omega_2$.

Carlos Garrido Alzar a effectué un calcul exact de la probabilité de départ de l'état habillé $|2\rangle_\theta$ induit par une impulsion RF à la fréquence ω_2 [40]. La figure 4.18 montre la position des résonances obtenue par ce calcul, comparée au modèle des atomes doublement habillés, Eq.(4.25). L'accord excellent démontre la validité de cette approche. Le même calcul est également en très bon accord avec le modèle pour ce qui concerne

la valeur relative du couplage aux deux points résonnants, selon l'équation (4.24).

4.4.3 Potentiels doublement adiabatique

Nous venons de voir que la seconde approximation de l'onde tournante était valable à faible valeur du couplage Ω_2. Cependant, cette valeur peut être suffisante pour que les atomes en mouvement dans le potentiel adiabatique induit par la première fréquence RF suivent adiabatiquement l'état habillé $|2\rangle_{\theta'}$, état propre de $F_{\theta'}$. C'est d'autant plus vrai pour la résonance ordinaire dont l'amplitude est la plus grande, du moins tant que l'on ne s'approche pas du fond du puits. On peut alors recalculer le potentiel adiabatique pour tenir compte des deux ondes RF. Les atomes doublement habillés ont pour énergie $m_F\hbar\Omega'(\mathbf{r})$. Le potentiel adiabatique correspondant à $m_F = -2$ est représenté sur la figure 4.19.

La mise en œuvre expérimentale du refroidissement par évaporation dans le piège RF habillé est en cours au laboratoire. Nous avons en effet obtenu début 2008 des conditions favorables au refroidissement, avec une durée de vie dans le piège habillé de 30 s environ et un taux de chauffage limité à 50 nK/s. Nous avions fait des essais de refroidissement dès 2003, mais le taux de chauffage présent à l'époque dans le piège [36] ne permettait pas de procéder au refroidissement du nuage. Depuis, l'équipe de J. Schmiedmayer à Heidelberg [7] a observé un refroidissement dans le double puits

7. Ce groupe a depuis déménagé à Vienne en Autriche.

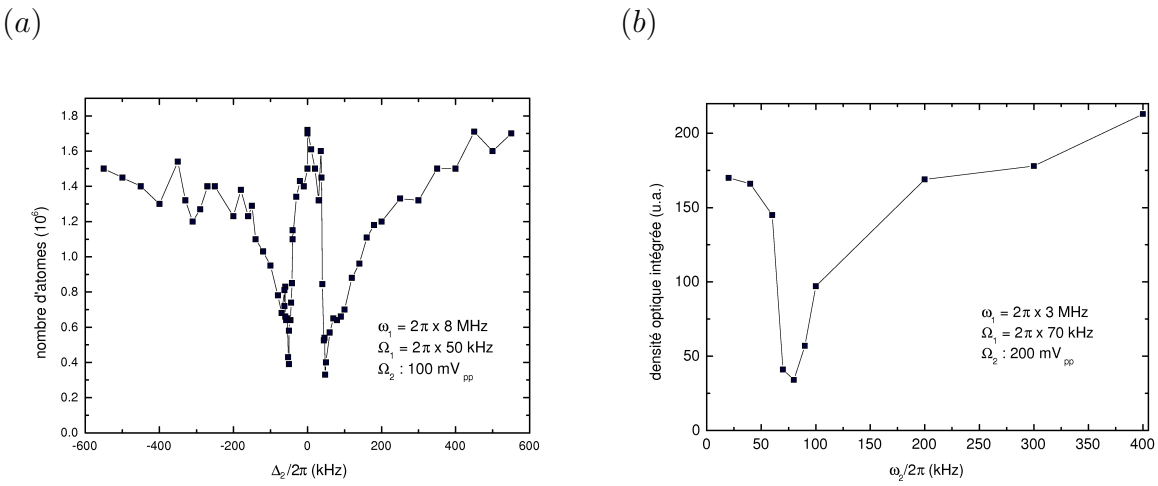

Figure 4.20 — Spectroscopie dans le piège habillé. À gauche, les deux pics correspondent aux résonances à $\Delta_2 = \pm\Omega_1$. L'élargissement est lié à la température dans le piège, qui autorise des transitions à Δ_2 plus élevé. À droite, le spectre est obtenu au voisinage de la fréquence de Rabi $\Omega_1 = 2\pi \times 50$ kHz.

Spectroscopy of the dressed trap. Left : Resonances at $\Delta_2 = \pm\Omega_1$. The peaks are broadened by the temperature in the trap, allowing transitions at energy differences larger than $\hbar\Omega_1$. Right : Low frequency spectrum around $\Omega_1 = 2\pi \times 50$ kHz.

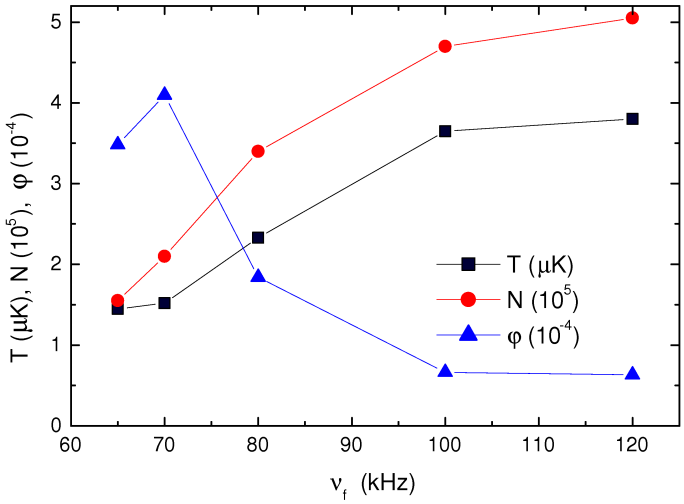

Figure 4.21 — Refroidissement par évaporation dans le potentiel adiabatique du piège QUIC habillé. La fréquence du champ RF du piège est $\omega_1 = 2\pi \times 8$ MHz, sa fréquence de Rabi est $\Omega_1 = 2\pi \times 50$ kHz. La seconde source RF pour l'évaporation est créée par une antenne identique à celle de la première RF, placée en face, de l'autre côté de la cellule en verre. Son amplitude est de 400 $\mathrm{mV_{pp}}$, ce qui correspond à $\Omega_2 \sim 2\pi \times 1$ kHz. Sa fréquence est réduite en 4 s de 600 kHz à une fréquence finale variable. La figure représente la variation du nombre d'atomes N, de la température T et de la densité dans l'espace des phases lorsque l'on fait varier la fréquence finale.

Evaporative cooling in the adiabatic potential. For this experiment, the parameters were : $\omega_1 = 2\pi \times 8$ MHz, $\Omega_1 = 2\pi \times 50$ kHz and a second RF amplitude of 400 $\mathrm{mV_{pp}}$ at the input of the second antenna, corresponding to $\Omega_2 \sim 2\pi \times 1$ kHz. This antenna is placed just in front of the dressing antenna, across the glass cell. The frequency ω_2 is reduced within 4 s of a linear ramp from 600 kHz to an adjustable final value. The variation of the atom number N, the temperature T and the phase space density is plotted against this final evaporation frequency value.

habillé, dans des conditions sensiblement différentes : les atomes sont essentiellement dans l'état $|2\rangle_z$, d'énergie dépendant de la position grâce au déplacement lumineux d'un champ RF en-dessous de la résonance. Le refroidissement par un second champ RF fonctionne alors simplement comme dans un piège magnétique classique.

Dans notre piège où les atomes sont placés à la résonance avec le champ RF, le refroidissement par un second champ restait à prouver. Nous avons d'ores et déjà observé l'effet d'une sonde RF d'amplitude faible, qui induit des pertes d'atomes dépendant de sa fréquence. La figure 4.20 montre le nombre d'atomes restant dans le piège habillé après 6 s d'application d'une seconde radiofréquence à une valeur fixe, proche soit de ω_1, comme cela a été discuté plus haut, soit de Ω_1, l'écart entre niveaux dans le piège habillé au fond du piège. L'élargissement de la raie et son aspect asymétrique sont dûs à la distribution thermique des atomes dans le piège et dépendent donc de la température. Pour refroidir les atomes, il faut maintenant appliquer une rampe en fréquence à cette seconde source RF, soit autour de ω_1, soit à basse fréquence autour de Ω_1.

L'efficacité du refroidissement dépendra ensuite également du taux de collisions, qui est sensiblement plus faible dans le piège habillé que dans le piège QUIC, en raisons des faibles fréquences d'oscillation horizontales.

Très récemment, en novembre 2008, nous avons effectivement observé le refroidissement d'un ensemble d'atomes dans le piège habillé. Nous avons utilisé pour cela une rampe linéaire en fréquence à basse fréquence, autour de $\omega_2 = \Omega_1$. L'avantage de ce choix est que le couplage avec la seconde RF est équilibré pour les deux résonances, ordinaire et extraordinaire. La rampe est appliquée sur le flanc de la distribution en énergie observée sur la figure 4.20, entre 600 kHz et une fréquence finale variable. Les données de la figure 4.21 indiquent non seulement une baisse de la température pendant les 4 secondes que dure la rampe, mais également une augmentation de la densité dans l'espace des phases [8], mettant en évidence un refroidissement du nuage. Ces résultats sont très encourageants pour l'utilisation des pièges radiofréquences à résonance, qui supportent donc bien la technique éprouvée du refroidissement par évaporation.

4.5 Piège quadrupolaire habillé

L'utilisation d'un champ RF permet de confiner des atomes ultra froids dans le champ d'un piège quadrupolaire. Ce type de piège présente en principe un « trou » au centre, l'intensité du champ magnétique y étant nulle. Cela induit des pertes d'atomes par transition Majorana, d'autant plus importantes que les atomes sont froids et passent du temps près du centre. En présence d'un champ RF intense, le minimum de potentiel se trouve sur un ellipsoïde iso-magnétique ajustable par le choix de la fréquence RF, ce qui permet d'éloigner les atomes de ce trou. La gravité rassemble les atomes au bas de cet ellipsoïde. La durée de vie dans un tel piège n'est plus limitée par les pertes Majorana liée à l'amplitude RF, si elle est choisie suffisamment grande, et l'on est ramené à la situation d'un piège du type Ioffe-Pritchard. La figure 4.2*a* représente les équipotentielles dans un piège quadrupolaire habillé.

Nous avons testé cette configuration de piégeage. Les atomes sont d'abord transférés dans le piège QUIC habillé [9] comme cela est expliqué au paragraphe 4.2.2, puis le courant de la bobine Ioffe est ramené à zéro de sorte que les atomes sont transférés dans un piège quadrupolaire habillé en suivant les surfaces isomagnétiques. Lors du transport, une moitié des atomes est perdue, le minimum du piège QUIC initial se scindant en deux zéros qui se déplacent dans des directions opposées [47]. Le transport s'accompagne également d'un chauffage du nuage, de 3 à 8 μK typiquement. Nous enregistrons ensuite le nombre d'atomes dans le piège quadrupolaire habillé au cours du temps, ainsi que la température de ces atomes. L'expérience est décrite en détail dans la référence [37] et les résultats sont présentés sur la figure 4.22.

Les données mettent en évidence une baisse de la température, jusqu'à une valeur limite atteinte après quelques secondes, accompagnée d'une baisse non exponentielle du nombre d'atomes. Cela est caractéristique d'une évaporation spontanée des atomes

8. La densité dans l'espace des phases est estimée grossièrement en utilisant les fréquences d'oscillations du piège habillé dans la limite harmonique.

9. C'est le synthétiseur « maison » qui a été utilisé dans cette série d'expériences.

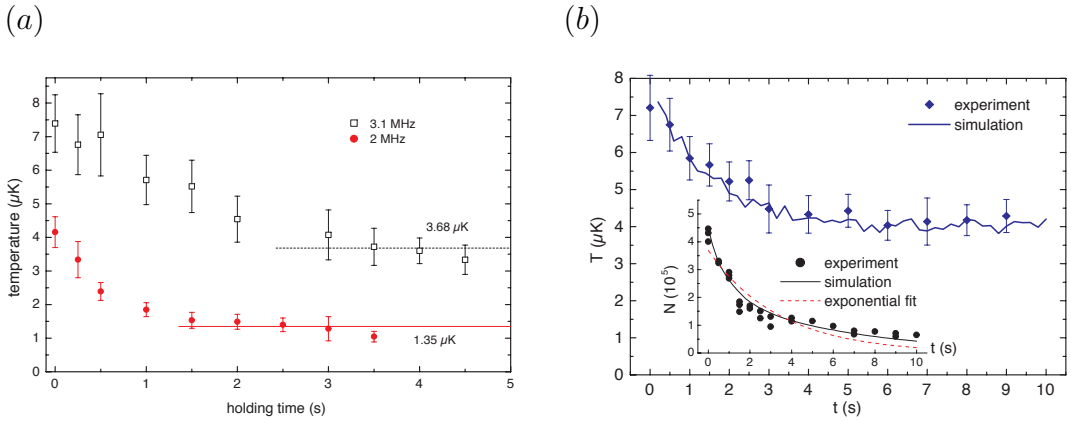

Figure 4.22 — Evolution de la température du nuage dans le piège quadrupolaire habillé. (a) Température obtenue expérimentalement pour un couplage RF de 40 kHz et deux valeurs de la fréquence RF. La température limite est plus faible dans le cas d'une fréquence de 2 MHz, pour laquelle la bulle est plus petite et les atomes sont plus proches des trous. (b) Comparaison, pour un couplage de 260 kHz et une fréquence RF de 3,1 MHz, de la température et du nombre d'atomes mesurés avec ceux prédits par une simulation Monte-Carlo. On note que la décroissance du nombre d'atomes en fonction du temps n'est pas bien ajustée par une simple exponentielle.

Evolution of the temperature with time in a dressed quadrupole trap. (a) *The limit temperature is lower for a smaller RF frequency of 2 MHz, as the trap bottom is closer from the two holes.* (b) *Comparaison of the temperature and the atom number evolution with a numerical Monte-Carlo simulation, for a coupling of 260 kHz and a RF frequency of 3.1 MHz. Inset : the atom number decreases in a non exponential way.*

les plus énergétiques. En effet, bien que l'énergie nécessaire pour atteindre le centre du piège magnétique soit très au-delà de la température des atomes (2 ou 3 MHz selon les expériences, soit 100 à 150 μK), il existe tout de même deux « trous » par lesquels les atomes peuvent s'échapper, dont l'emplacement est visible sur la figure 4.2b. Ces trous sont dus à la variation du couplage RF avec l'angle entre champ statique et polarisation RF décrit au paragraphe 4.1.3. La polarisation du champ RF étant linéaire et horizontale, il existe deux points sur l'équateur de l'ellipsoïde iso-magnétique en lesquels le champ magnétique statique est aligné avec le champ RF, ce qui annule le couplage. Les atomes peuvent s'échapper par ces points, dont l'énergie diffère de celle du fond par Mgz_0 uniquement, qui est inférieure à 30 μK dans les expériences décrites ici.

L'hypothèse d'une évaporation spontanée des atomes par les trous du couplage RF est étayée par deux arguments. D'une part, la température limite dépend de la profondeur du potentiel. Nous avons en effet reproduit l'expérience pour deux valeurs de la fréquence RF, qui détermine le rayon de la bulle et donc la hauteur à franchir pour les atomes depuis le fond de la bulle pour atteindre l'un des trous. La figure 4.22a

montre que la température limite est réduite si le rayon de la bulle l'est. Le rapport entre profondeur du puits et température finale vaut entre 7 et 12, ce qui est compatible avec une évaporation spontanée [105].

D'autre part, j'ai comparé les courbes expérimentales avec une simulation Monte-Carlo classique qui évalue le nombre d'atomes et la température dans le piège au cours du temps. On calcule l'évolution et la probabilité de collision de paquets d'atomes de taille 2^n, qui sont dupliqués lorsque la moitié des paquets a disparu [106, 107]. J'avais déjà utilisé cette méthode lors de ma thèse, en collaboration avec Jean Dalibard. Le point délicat est de définir un critère de perte des atomes, puisque les pertes de type Landau-Zener sont probabilistes. J'ai pris le parti de déterminer qu'un atome est perdu à coup sûr lorsque la probabilité de transition Landau-Zener dépasse une valeur donnée P_c, et n'est pas perdu sinon. La probabilité est évaluée pour chaque atome à chaque instant puisqu'elle dépend de sa vitesse et de la valeur locale du couplage. Les résultats présentés sur la figure 4.22*b* sont obtenus avec $P_c = 0{,}9$. Ils reproduisent bien à la fois la décroissance en température et les pertes d'atomes, validant ainsi l'hypothèse d'une évaporation spontanée dans le piège habillé.

Peut-on conclure à un refroidissement dans le piège ? L'incertitude de la mesure de la température et la difficulté d'obtenir la densité atomique *in situ* ne nous permettent pas de trancher de façon catégorique. La densité dans l'espace des phases semble légèrement augmenter pendant les deux premières secondes, puis baisser au-delà. Il est certain que les conditions initiales de densité et température n'étaient pas très favorables dans cette série d'expériences. Avec un chargement amélioré, on pourrait probablement utiliser cette fuite naturelle par les trous comme moyen de refroidir les atomes par évaporation. Il suffirait alors de réduire la fréquence RF au cours du temps pour forcer le processus. Remarquons enfin que l'on peut éviter la présence de trous dans le plan équatorial en utilisant un champ RF de polarisation circulaire. Il n'y a plus alors qu'un point de fuite au sommet de la bulle, ce qui limite grandement les pertes.

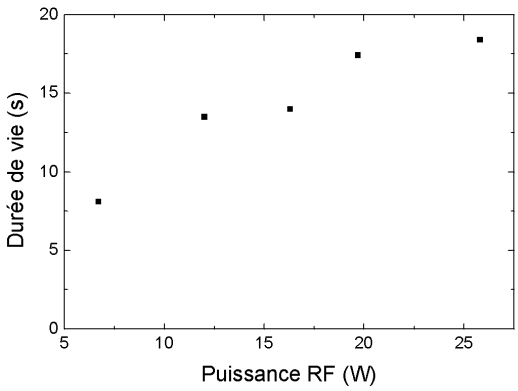

Figure 4.23 — Durée de vie du piège quadrupolaire habillé chargé directement à partir du piège magnéto-optique, en fonction de la puissance RF utilisée.

Lifetime of the dressed quadrupole trap, loaded directly from the MOT, as a function of the RF power.

Récemment, nous avons mis au point une technique permettant de charger des atomes depuis le piège quadrupolaire initial directement dans le piège quadrupolaire habillé, sans passer par une étape dans le piège QUIC. Ce n'est *a priori* pas évident : en effet, le procédé habituel de chargement dans le potentiel adiabatique, décrit au paragraphe 4.2.2, suppose l'existence d'un minimum de champ magnétique non nul, ce qui n'est pas le cas dans un piège quadrupolaire. Pour contourner cette difficulté, nous appliquons la séquence décrite ci-dessous :

1. charger le piège magnéto-optique en présence d'un champ magnétique vertical, de sorte que le centre du piège soit décalé de 2 mm vers le bas par rapport au zéro du piège quadrupolaire ;
2. après une phase de mélasse réalisée tous champs éteints, on pompe optiquement les atomes en présence d'un champ homogène selon x ;
3. on allume le champ RF à une fréquence inférieure à la résonance pour ce champ de pompage homogène ; les atomes sont alors dans un état habillé ;
4. on allume progressivement le champ quadrupolaire et on fait simultanément une rampe sur la fréquence RF, de sorte que la position résonnante reste toujours à la même altitude, 2 mm en dessous du centre du piège quadrupolaire ;
5. une fois la valeur maximale du courant atteinte, on peut éteindre les bobines produisant le champ homogène selon x.

Pour que ce chargement soit efficace, il faut une amplitude RF assez élevée. En effet, il faut monter le courant rapidement dans les bobines de champ quadrupolaire lors de l'étape 4 pour ne pas perdre les atomes, qui ne sont piégés que grâce au gradient du champ magnétique. Nous avons observé que le nombre d'atomes transférés augmente avec la puissance RF, et ce jusqu'à 25 W, qui est la puissance maximale que nous ayons testée. La durée de vie dans le potentiel adiabatique est également fonction croissante de la puissance RF, comme le montre la figure 4.23. De plus, nous avons vérifié que les résultats sont meilleurs lorsque la polarisation RF est circulaire d'axe vertical, ce qui évite le problème discuté plus haut des trous dans le potentiel adiabatique.

Ces résultats en sont à leurs débuts, le chargement induisant pour le moment un chauffage du nuage atomique. Cependant, la perspective de charger les atomes directement dans le piège quadrupolaire habillé est intéressante, et le refroidissement par évaporation peut être mis en œuvre selon la technique décrite au paragraphe 4.4.

4.6 Piège annulaire

Comme je l'ai mentionné au paragraphe 4.1.3, les potentiels adiabatiques offrent une grande variété dans les formes de pièges réalisables, en particulier de pièges non harmoniques. À la suite d'une discussion avec Rudi Grimm à l'école des Houches du printemps 2003, nous avons proposé avec Yves Colombe de combiner le piège adiabatique avec une onde stationnaire de direction verticale pour former un ou des anneaux pour atomes. En effet, l'intersection de la bulle donnée par le piège RF avec les plans imposés par l'onde stationnaire donne une série pièges annulaires à la verticale les uns

des autres. La fréquence d'oscillation verticale peut être élevée, car elle est donnée par le confinement dipolaire lumineux de l'onde stationnaire, dont la longueur caractéristique est de l'ordre de la longueur d'onde λ du laser utilisé. Ainsi, ce piège serait bien adapté pour étudier la persistance d'un courant permanent dans un gaz restreint en dimension 2. L'étude détaillée du piège a été faite dans la thèse d'Olivier Morizot en collaboration avec Barry Garraway [39].

Nous avons considéré le cas d'un piège magnétique quadrupolaire d'axe vertical. En effet, nous avons vu plus haut que le zéro de champ magnétique au centre de ce piège n'est plus problématique en présence du champ RF. De plus, la symétrie d'axe vertical alliée au choix d'une polarisation RF circulaire d'axe z assure que l'anneau a une forme circulaire et non elliptique. Le rayon de l'anneau est alors le rayon horizontal de la bulle, soit $r_0 = \omega_{\mathrm{RF}}/\alpha$ où α est défini comme au paragraphe 4.2 par $\hbar\alpha = g_F \mu_B B'$ et B' est le gradient du piège quadrupolaire selon les axes faibles (les axes horizontaux). Un grand avantage de ce système est que ce rayon est réglable directement par le choix de la fréquence RF. De plus, les fréquences de piégeage axiale et verticale sont ajustables indépendamment, l'une étant imposée par le potentiel adiabatique et l'autre par le piège optique. Si l'on note w le diamètre à $1/\sqrt{e}$ du faisceau vertical au foyer, P la puissance totale et $U_0 \propto P/(w^2\delta)$ le déplacement lumineux moyen induit au centre du faisceau par l'onde stationnaire désaccordée de δ, l'expression des fréquences d'oscillations est :

$$\omega_\rho = \alpha\sqrt{F\frac{\hbar}{M\Omega_1}} \tag{4.26}$$

$$\omega_z = \frac{2\pi}{\lambda}\sqrt{\frac{4U_0}{M}}\, e^{-r_0^2/w^2}. \tag{4.27}$$

Cette totale indépendance des fréquences d'oscillation verticale et horizontale est valable si le désaccord de l'onde stationnaire est positif par rapport à la transition atomique (désaccord bleu) car les atomes se trouvent alors dans un nœud de l'onde stationnaire et l'effet radial du laser est négligeable. Cela ne serait pas vérifié avec un désaccord rouge, le profil Gaussien du faisceau participant alors au piégeage radial.

L'ordre de grandeur des fréquences d'oscillation que l'on peut atteindre dans les directions verticales et radiales est de 4 à 40 kHz et de 500 à 1500 Hz respectivement. Le piège annulaire, représenté sur la figure 4.24 par l'une de ses équipotentielles, a la forme d'un anneau de Saturne. Pour un condensat dont le potentiel chimique est typiquement de l'ordre du kilohertz se pose naturellement la question de la dimensionnalité du gaz piégé.

Pour déterminer la dimension du gaz, il faut comparer les énergies du système aux fréquences de confinement du piège. Pour un condensat de Bose-Einstein, c'est le potentiel chimique qui donne l'échelle typique en énergie. En le comparant à ω_z ou ω_ρ, on peut identifier trois régimes en fonction du nombre d'atomes. On note dans la suite $\bar{\omega} = \sqrt{\omega_\rho \omega_z}$.

3D On a un condensat tridimensionnel si le potentiel chimique μ_{3D} obtenu avec cette hypothèse est supérieur à chacune des fréquences d'oscillation. L'expression du

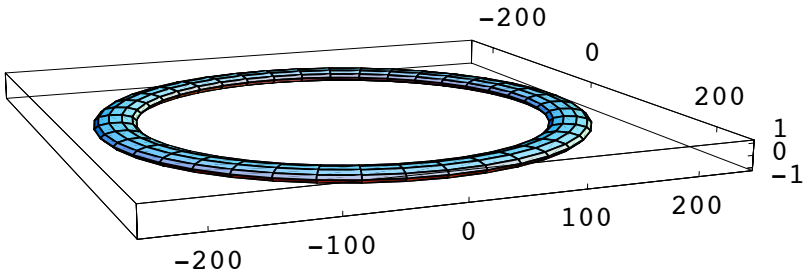

Figure 4.24 — Allure du piège annulaire, dont une équipotentielle est représentée ici. Les paramètres sont ceux de la table 4.1. L'échelle verticale a été dilatée d'un facteur 10 pour rendre visible l'épaisseur du piège, dans la direction de l'onde stationnaire.

Isopotential surface of the ring trap, with the parameters of Table 4.1. The vertical scale, in the direction of the standing wave, is amplified by a factor 10 for clarity.

potentiel chimique en dimension 3 pour un condensat dans l'anneau est [39]

$$\mu_{3D} = \hbar\bar{\omega}\sqrt{\frac{2Na}{\pi r_0}}, \tag{4.28}$$

a étant la longueur de diffusion. On doit alors avoir $N > N_{3D}$ pour être dans ce régime, où $N_{3D} = \frac{\pi r_0}{2a}\frac{\omega_z}{\omega_\rho}$. Pour les paramètres présentés à la table 4.1, $N_{3D} = 2{,}4 \times 10^6$. Ce nombre est assez élevé par rapport au nombre d'atomes que nous obtenons typiquement dans le condensat. Le piège est donc bien indiqué pour observer un gaz en dimension restreinte.

2D Lorsque $N < N_{3D}$, l'expression de μ n'est plus valable. On fait alors l'hypothèse que le degré de liberté vertical est gelé pour obtenir l'expression du potentiel chimique à 2D :

$$\mu_{2D} = \hbar\bar{\omega}\left(\frac{\omega_\rho}{\omega_z}\right)^{1/6}\left(\frac{3Na}{4\sqrt{\pi}r_0}\right)^{2/3}. \tag{4.29}$$

Cette expression est valable pour $\hbar\omega_\rho < \mu_{2D} < \hbar\omega_z$, soit pour[10] $N > N_{2D}$ avec $N_{2D} = \frac{4\sqrt{\pi}r_0}{3a}\sqrt{\frac{\omega_\rho}{\omega_z}}$. L'ordre de grandeur de ce nombre critique d'atomes est $N_{2D} = 15\,000$ pour les paramètres proposés. Le régime 2D paraît être le plus naturellement accessible expérimentalement.

1D Pour un nombre d'atomes encore inférieur $N < N_{2D}$, on entre dans le régime 1D où le mouvement radial est gelé lui aussi[11]. La densité linéique le long de l'anneau est constante et l'expression du potentiel chimique est très simple :

$$\mu_{1D} = \hbar\bar{\omega}\frac{Na}{\pi r_0}. \tag{4.30}$$

10. On devrait aussi écrire la condition $\mu_{2D} < \hbar\omega_z$. Elle est la même que la condition $N < N_{3D}$, à un facteur numérique près de l'ordre de l'unité.

11. Ici encore, la condition $\mu_{1D} < \hbar\omega_\rho$ conduit à la même valeur pour le nombre critique d'atomes, à un facteur numérique près proche de 1.

Le nombre d'atomes doit être assez faible pour atteindre ce régime, ce qui nécessite une détection appropriée.

Discutons à présent les sources possibles de perte d'atomes ou de chauffage, afin d'optimiser le choix des paramètres RF et lasers. Le taux de photons diffusés spontanément par l'onde stationnaire « bleue » est relié à la taille du nuage dans la direction z :

$$\Gamma_{\rm sc} = \frac{\Gamma}{2}\frac{M\omega_z^2\langle z^2\rangle}{\hbar\delta}. \tag{4.31}$$

Dans l'état fondamental selon z, on obtient $\Gamma_{\rm sc} = \Gamma\,\omega_z/4\delta$ alors que pour un gaz thermique 3D $\Gamma_{\rm sc} = \Gamma\,k_BT/2\hbar\delta$.

D'autre part, la durée de vie est limitée — outre par la qualité du vide — par les transitions non adiabatiques (pertes Landau-Zener). On peut en estimer le taux dans un gaz thermique à la température T, comme pour la figure 4.11, en moyennant la probabilité de transition Landau-Zener $P_{\rm LZ}(v_\rho)$ sur la distribution des vitesses dans la direction radiale v_ρ et en remarquant qu'un atome traverse le croisement évité deux fois par période :

$$\Gamma_{\rm LZ} = \frac{\omega_\rho}{\pi}\,\langle P_{\rm LZ}(v_\rho)\rangle \simeq \frac{\omega_\rho}{\pi}\,2F\sqrt{\frac{M}{2\pi k_BT}}\int dv_\rho\, e^{-\frac{Mv_\rho^2}{2k_BT}}\, e^{-\frac{\pi\Omega_1^2}{2\alpha v_\rho}}\,. \tag{4.32}$$

On a utilisé l'équation (4.13) avec $|\dot\delta| = \alpha|v_\rho|$. En toute rigueur, il faudrait considérer aussi les pertes Landau-Zener dans l'état fondamental, mais elles sont toujours négligeables avec les paramètres expérimentaux usuels pour lesquels $\Omega_1 \gg \omega_\rho$, comme nous l'avons vu au paragraphe 4.2.4.

Remarquons enfin que l'on peut négliger le couplage tunnel d'un puits de l'onde stationnaire à l'autre, puisque la gravité lève la dégénérescence en énergie entre deux puits voisins. On a plutôt alors des oscillations de Bloch de très faible amplitude.

Le choix des paramètres expérimentaux se fait en se donnant une profondeur souhaitée pour le piège et une valeur maximale acceptable pour $\Gamma_{\rm sc}$ et $\Gamma_{\rm LZ}$ à une température donnée, et en déduisant de ces contraintes les valeurs possibles des paramètres du laser et du champ RF. Il est aisé de montrer que la taille transverse du faisceau doit vérifier $w = \sqrt{2}r_0$ pour maximiser à la fois la fréquence d'oscillation dans la direction verticale et la profondeur du piège. D'autre part, on a intérêt à choisir la puissance laser la plus grande possible pour augmenter le désaccord et limiter la diffusion de photons spontanés, et le gradient de champ magnétique le plus élevé possible pour un meilleur confinement radial. Fixons donc ces deux grandeurs à des valeurs accessibles dans l'expérience actuelle, soit la puissance laser à 0,5 W pour le laser Titane Saphir à notre disposition, et le gradient de champ à $B' = 150$ G/cm, valeur actuelle de notre piège quadrupolaire. Choisissons alors de limiter $\Gamma_{\rm sc}$ à 0,1 s^{-1} et $\Gamma_{\rm LZ}$ à 0,01 s^{-1}, et de fixer la profondeur du piège $V_0 = 2U_0/e$ à 5 μK par exemple. La température des atomes est limitée à 2 μK typiquement dans un potentiel de cette profondeur. La contrainte sur $\Gamma_{\rm sc}$ nous donne le désaccord δ minimal, donc la longueur d'onde λ du laser. La taille au col du faisceau se déduit de U_0. Le rayon optimal de l'anneau vaut $r_0 = w/\sqrt{2}$, ce qui fixe la fréquence RF. Enfin, on choisit Ω_1 pour limiter les pertes Landau-Zener à la

Paramètre expérimental	Valeur	Paramètre du piège	Valeur
puissance laser P	0.5 W	rayon r_0	198 μm
longueur d'onde λ	767 nm	profondeur V_0	4.9 μK
taille du col w	280 μm	fréquence ν_z	40 kHz
fréquence Rabi $\Omega_1/2\pi$	20 kHz	fréquence ν_ρ	1,1 kHz
fréquence $\omega_{\mathrm{RF}}/2\pi$	2080 kHz	taux Γ_{sc} à 2 μK	0,106 s^{-1}
gradient de champ B'	150 G/cm	taux Γ_{LZ} à 2 μK	0,005 s^{-1}

Tableau 4.1 — Paramètres expérimentaux typiques pour le piège annulaire, et paramètres du piège résultant de ce choix. L'onde stationnaire serait obtenue avec un laser Titane-Saphir.

Typical parameters for a ring trap, with a standing wave produced by a Titanium-Sapphire laser.

valeur désirée. En appliquant cette procédure, on obtient les paramètres du tableau 4.1.

Nous avons proposé un schéma de chargement du piège annulaire à partir d'un piège magnétique du type de celui que nous utilisons pour préparer le condensat [39]. Il est possible également de partir d'un piège TOP, dont la géométrie est particulièrement adaptée, les bobines produisant le champ tournant pouvant être utilisées pour obtenir un champ RF de polarisation circulaire [108]. Enfin, j'ai mentionné au paragraphe 4.5 les expériences préliminaires que nous avons menées pour habiller directement les atomes d'un piège quadrupolaire, ce qui permettrait de charger assez simplement le piège annulaire depuis ce piège quadrupolaire habillé.

Le nombre de puits de l'onde stationnaire peuplés par des atomes peut être modifié en faisant se croiser les faisceaux lasers sous un angle 2θ, ce qui change la période du réseau en $\lambda/(2\sin\theta)$. C'est ce qui a permis à Jean Dalibard et à son équipe de faire varier le nombre de puits peuplés, dans une expérience mettant en évidence les propriétés de gaz dégénérés en dimension 2 [29]. Cette possibilité a été utilisée pour produire deux gaz 2D proches l'un de l'autre et diagnostiquer la transition de Kosterlitz-Thouless par une mesure interférentielle. Ce principe peut être appliqué de la même manière au piège annulaire que nous proposons.

Pour l'heure, le piège annulaire tel qu'il est décrit ici n'a pas encore été réalisé expérimentalement. En revanche, à la suite de notre proposition, une variante où l'onde stationnaire est remplacée par une nappe de lumière a été mise au point à Oxford dans l'équipe de Chris Foot [108].

Un piège en forme d'anneau est idéal pour étudier la superfluidité, rendant possible l'établissement d'un courant permanent. Ce phénomène, bien connu pour l'hélium superfluide [109] et les supraconducteurs [110], a été mis en évidence récemment avec un condensat dans un piège TOP percé d'un faisceau laser désaccordé vers le bleu [111]. Les atomes étaient mis en rotation par transfert du moment angulaire d'un faisceau Laguerre-Gauss lors d'une transition Raman. Cette technique est utilisable dans l'anneau décrit dans ce chapitre. Il est également possible de mettre en rotation les atomes directement, en faisant tourner une déformation du piège à la manière de la cuillère à

atomes mise au point dans l'équipe de Jean Dalibard [112]. Nous avons proposé pour cela de déformer le piège magnétique quadrupolaire, en ajoutant deux paires de bobines parcourues par des courants en quadrature [39]. Il est aussi possible de tirer parti de l'anisotropie du couplage RF, décrite au paragraphe 4.1.3, et de la faire tourner, comme cela est proposé dans la référence [108].

4.7 Conclusion

Depuis la proposition théorique d'Oliver Zobay et Barry Garraway en 2001, et la démonstration expérimentale que nous en avons faite deux ans plus tard, notre compréhension de ce nouveau type de piège s'est beaucoup améliorée. Les potentiels adiabatiques se sont popularisés, notamment auprès des équipes utilisant des puces à atomes, qui tirent parti du gradient de champ magnétique élevé accessible dans ces structures. Le refroidissement par évaporation est utilisé dans ces pièges [40, 101], qui permettent de confiner des condensats. Pour le moment cependant, le condensat ne survit pas à une rampe de fréquence RF qui croise la résonance au fond du piège magnétique statique [36, 43], mais est préservé pour un champ RF de fréquence fixe branché adiabatiquement à une valeur inférieure à cette résonance [38]. La modularité des potentiels adiabatiques a fait leur succès [39, 95, 94, 113].

Dans l'équipe, nous avons proposé et étudié de nouvelles géométries comme le piège quadrupolaire habillé. La géométrie annulaire est particulièrement intéressante pour l'étude de la superfluidité, et nous orientons l'expérience dans cette direction. Afin de mettre en place les faisceaux devant produire l'onde stationnaire nécessaire au confinement vertical (cf. paragraphe 4.6), l'accès optique doit être amélioré. Pour ce faire, nous avons décidé de reconstruire l'enceinte expérimentale. Ce changement est bienvenu car la plupart des éléments de l'actuelle enceinte ont été mis en place il y a neuf ans et les performances ultra-vide commencent à se dégrader. La nouvelle enceinte, plus ramassée, permettra d'avoir accès aux trois axes optiques dans une cellule en quartz, dont l'un avec une grande ouverture angulaire ($\pm 40°$ verticalement, $\pm 60°$ horizontalement). De plus, le champ quadrupolaire sera produit par deux bobines d'axe vertical, ce qui introduit une invariance par rotation compatible avec la réalisation d'un piège annulaire horizontal. La future enceinte comportera deux chambres ultravides séparées par un vide différentiel, et les atomes seront transportés de la zone du piège magnéto-optique à la zone du piège magnétique par une paires de bobines en mouvement, placées sur un rail. Enfin, il est prévu à terme de charger le piège magnéto-optique à partir d'un piège magnéto-optique bi-dimensionnel, ce qui permettra d'augmenter la cadence des expériences.

4.8 Articles en relation avec ce chapitre

Je reproduis ici cinq articles [36, 39, 40, 37, 55] en relation avec ce chapitre.

EUROPHYSICS LETTERS 15 August 2004

Europhys. Lett., **67** (4), pp. 593–599 (2004)
DOI: 10.1209/epl/i2004-10095-7

Ultracold atoms confined in rf-induced two-dimensional trapping potentials

Y. Colombe, E. Knyazchyan, O. Morizot, B. Mercier,
V. Lorent and H. Perrin

Laboratoire de physique des lasers, CNRS-Université Paris 13
99 avenue Jean-Baptiste Clément, F-93430 Villetaneuse, France

(received 1 March 2004; accepted 7 June 2004)

PACS. 42.50.Vk – Mechanical effects of light on atoms, molecules, electrons, and ions.
PACS. 03.75.-b – Matter waves.
PACS. 32.80.Pj – Optical cooling of atoms; trapping.

Abstract. – We present the experimental implementation of a new trap for cold atoms proposed by O. Zobay and B. M. Garraway (*Phys. Rev. Lett.*, **86** (2001) 1195). It relies on adiabatic potentials for atoms dressed by a rf field in an inhomogeneous magnetic field. This trap is well suited to confine atoms tightly along one direction to produce a two-dimensional atomic gas. We transferred ultracold atoms into this trap, starting either from thermal samples or Bose-Einstein condensates. In the latter case, technical noise during the loading stage caused heating and prevented us from observing 2D BECs.

It is well known that Bose-Einstein condensation (BEC) of homogeneous gases cannot occur in dimensions less than 3 [1]. However, 2D condensation is possible inside a power law external confining potential [2]. Crossover from 3D condensation to 2D and 1D has been experimentally demonstrated by measuring the aspect ratios of atomic clouds released from anisotropic traps [3]. Quantum gases in low dimensions and particularly in 2D are of much interest for several reasons. It is predicted that the coherence and the mean-field interaction are strongly influenced by the trap parameters in the tightening direction [4]. These properties are of crucial importance for integrated atom optics [5, 6]. In 2D, the appearance of (1/2)-anyons quasiparticles has been predicted in a rotating trap [7]. The first step towards the creation of these quasiparticles is to generate BEC in the lowest Landau level. This has been recently realized in a 3D rotating trap [8]. By the centrifugal force the BEC approaches the two-dimensional regime.

There should be a dramatic improvement of this kind of experiments if the trapped gas is two-dimensional at the start. A 2D gas is obtained by strongly confining atoms along one direction. There are several ways to produce such a "2D trap". One is to use rapidly decaying fields supported by a surface, which provides very naturally a strong transverse confinement. The decaying field may be either optical, as for the double-evanescent-wave trap [9, 10], or magnetic as in the Zeeman effect surface trap [11]. 2D BEC was recently achieved in a trap combining the use of a single evanescent wave and gravity [12]. However, the use of surface

traps may lead to perturbation of the atomic cloud due, for instance, to the roughness of the trapping potential, as pointed out in [12]. This effect is similar to the condensate fragmentation observed in atom chips [13]. This is a disadvantage for experiments similar to [8]. The use of an optical standing wave is a natural way to produce 2D traps far from any surface [14, 15]. The drawback of this method is that the atoms are filled in many pancake traps, unless the lattice period is chosen large enough. We present here the experimental implementation of a single pancake trap sitting in free space.

A new quasi-2D trap was proposed by Zobay and Garraway [16, 17]. It relies on the adiabatic potentials seen by an atom sitting in an inhomogeneous magnetic field $\boldsymbol{B}_0(\boldsymbol{r})$ and dressed by a radio-frequency field. The same potentials are implied in rf-induced evaporative cooling; in that case, they are used to limit the depth of the trap.

To realize the trapping potential, we start from the magnetic trap we use for producing a Bose-Einstein condensate. ^{87}Rb atoms in the $5S_{1/2}$, $F = 2$ state sit in this inhomogeneous magnetic field and experience an m_F-dependent magnetic potential $m_F(V_0 + V_{\mathrm{trap}}(\boldsymbol{r}))$. This is a trapping potential for the state $F = 2$, $m_F = 2$ we work with. V_0 corresponds to the offset magnetic field B_0 at the center of the magnetic trap $\boldsymbol{r} = (0, 0, 0)$. When a rf field $B_1 \cos(\omega_{\mathrm{rf}} t)$ of Rabi frequency $\Omega = g\mu_{\mathrm{B}} B_1/2\hbar$ —where $g = 1/2$ and μ_{B} is the Bohr magneton— is applied to the atoms in the strong-coupling regime, the atomic levels present an avoided crossing at the points where the rf frequency ω_{rf} is resonant with the frequency difference between the m_F states, that is when $V_0 + V_{\mathrm{trap}}(\boldsymbol{r}) = \hbar\omega_{\mathrm{rf}}$. The new potentials experienced by the dressed atoms read $m_F V(\boldsymbol{r})$, where

$$V(\boldsymbol{r}) = \sqrt{(V_{\mathrm{trap}}(\boldsymbol{r}) - \hbar\Delta)^2 + (\hbar\Omega)^2}\,. \tag{1}$$

In this last equation, we introduced the rf detuning $\hbar\Delta = \hbar\omega_{\mathrm{rf}} - V_0$ with respect to the rf transition in the center of the magnetic trap. In this semi-classical approach, the eigenstates $\phi_{m_F}(\boldsymbol{r})$ corresponding to these energies are still spin states, along a direction tilted from the local direction of the magnetic field at point $\boldsymbol{r}$ by an angle θ, where $\cos\theta = -\Delta/\sqrt{\Delta^2 + \Omega^2}$ and $\sin\theta = \Omega/\sqrt{\Delta^2 + \Omega^2}$. In the lab frame, the tilted eigenstate is rotating with pulsation ω_{rf} around the local direction of the magnetic field. The state ϕ_{m_F} is identical to the uncoupled magnetic substate $-m_F$ at infinite positive detuning Δ, and to m_F when Δ is getting very large and negative. Note that they are eigenstates only for the internal degrees of freedom, $\boldsymbol{r}$ being fixed. A motional induced coupling may lead to Landau-Zener transitions between these states when $\boldsymbol{r}$ changes, which may be avoided by using a large enough rf coupling Ω.

For atoms in the ϕ_2 dressed state, this potential presents a minimum at the points where $V_{\mathrm{trap}}(\boldsymbol{r}) = \hbar\Delta$. The locus of these points is the surface where the norm of the magnetic field has a given value —or, equivalently, an iso-B surface. If, for instance, the magnetic trapping potential is harmonic, the iso-B surfaces are ellipsoids. The atoms are thus forced to move onto an "egg shell", their motion being very limited in the direction orthogonal to the shell. This "atomic bubble" is not easily observable, however: The atoms fall at the bottom of the shell due to gravity. As the typical radius of the shell increases, the atomic cloud becomes essentially two-dimensional. A cut of the potential including gravity is represented in fig. 1. It shows that along the vertical z-axis, only one side of the shell will be occupied by the atomic cloud, as soon as the temperature is lower than the energy difference between the top and the bottom of the shell.

We now will discuss the trap characteristics in the case of our experiment. The atomic cloud we start with is confined in a cigar shape QUIC magnetic trap [18]. The long axis of the cigar is horizontal and is denoted as x. This is also the direction of the offset magnetic field of 1.8 G, corresponding to $V_0/h = 1.3$ MHz. y is the other horizontal axis along which

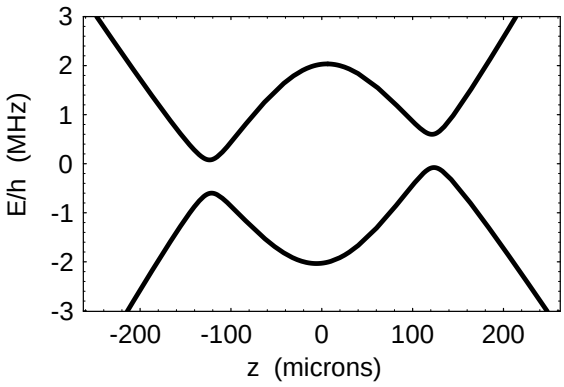

Fig. 1 – Cut along the z-axis of the total potential $mgz + m_F V(\boldsymbol{r})$ with $m_F = 2$ (upper curve) and $m_F = -2$ (lower curve). The lower-state potential (corresponding to state ϕ_{-2}) is used during evaporative cooling, where the depth is limited by the rf coupling. For the upper state (ϕ_2), the potential minimum sits at the bottom of a shell (at $z = z_0$). Parameters are: $\Delta/2\pi = 1\,\mathrm{MHz}$ and $\Omega/2\pi = 170\,\mathrm{kHz}$. The initial magnetic potential is the one of our QUIC trap (see text).

the magnetic rf field is aligned [19]. Finally, z is the vertical axis. The oscillation frequencies at the bottom of the QUIC trap are $\omega_x/2\pi = 21\,\mathrm{Hz}$ and $\omega_y/2\pi = \omega_z/2\pi = 200\,\mathrm{Hz}$. The QUIC trap is symmetric with respect to the $y = 0$ plane. Initially, the atoms are confined in the upper magnetic state $F = 2$, $m_F = 2$. To load the atoms from this 3D trap into the bottom of a shell, we simply chirp a rf field from below the resonance at the center of the QUIC trap $V_0/\hbar$ to the desired value of Δ. The atoms thus always stay in the upper state we start in, as soon as the Rabi frequency is large enough for them to follow adiabatically the dressed state ϕ_2.

The cloud is located on an iso-B surface [20], centered at position x_0, y_0, z_0, where $y_0 = 0$ and z_0 is the lowest height which fulfills $V_{\mathrm{trap}}(x_0, 0, z_0) = \hbar\Delta$. As V_{trap} depends only slightly on x near the cloud position, z_0 is essentially given by $V_{\mathrm{trap}}(0, 0, z_0) = \hbar\Delta$. The oscillation frequency in the strongly confined z-direction may be inferred from the Rabi frequency Ω and the vertical gradient $\alpha(z_0)$ at position z_0 of the trap potential, defined by: $V_{\mathrm{trap}}(0, 0, z) \simeq \hbar\Delta + (z - z_0)\,\alpha(z_0)$. With these notations, the oscillation frequency in the tightly confining direction z reads:

$$\omega_{\mathrm{trans}} = |\alpha(z_0)|\sqrt{\frac{2}{m\hbar\Omega}}\,. \tag{2}$$

In a QUIC trap, the radial gradient α is constant except in a small region around the minimum at $z = 0$. The transverse oscillation frequency can still be controlled using the Rabi frequency Ω. However, the Rabi frequency cannot be chosen arbitrarily small because of Landau-Zener losses.

The horizontal frequencies ω_1 and ω_2 corresponding, respectively, to the x and y directions directly depend on the local shape of the iso-B surface. In the yz plane, due to the axial symmetry of the QUIC trap [21], the iso-B lines are circles and ω_2 is merely the pendulum pulsation:

$$\omega_2 = \sqrt{\frac{g}{|z_0|}}\,. \tag{3}$$

In the xz plane, the iso-B lines are very elongated due to the cigar shape of the QUIC trap and they are more complicated [20]. ω_1 is much smaller than ω_2 and cannot be expressed

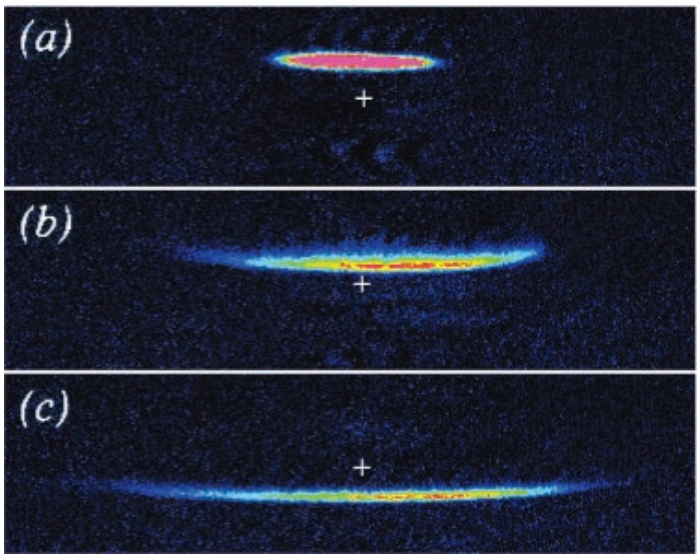

Fig. 2 – Successive absorption images of thermal clouds in the xz plane as the detuning Δ is increased. (a) QUIC trap. (b) $\Delta/2\pi = 1.7\,\mathrm{MHz}$, $z_0 = -130\,\mu\mathrm{m}$. (c) $\Delta/2\pi = 6.7\,\mathrm{MHz}$, $z_0 = -450\,\mu\mathrm{m}$. The white cross is a fixed reference in each picture. The pictures are taken as the rf and the magnetic trap are still on. The Rabi frequency was $\Omega/2\pi = 180\,\mathrm{kHz}$. The atomic clouds contain typically 10^6 atoms at a temperature of $5\,\mu\mathrm{K}$. Dimensions of images are 4.5 mm (horizontal) $\times$1.2 mm (vertical).

analytically. Its order of magnitude is given by approximating the iso-B lines by ellipses:

$$\omega_1 \simeq \sqrt{\frac{g}{|z_0|}}\frac{\omega_x}{\omega_z}\,. \tag{4}$$

As $|z_0|$ increases with Δ, ω_1 and ω_2 may be controlled via Δ and ω_{trans} via Ω; one can easily find a set of parameters such that $\omega_{\mathrm{trans}} \gg \omega_1,\, \omega_2$.

The experimental setup has been described elsewhere [22]. In brief, if consists of a double MOT system, the atoms being continuously loaded from an upper vapor MOT into a lower MOT sitting in a low-pressure glass cell. After a transfer into the magnetic QUIC trap, the atoms are cooled down to the condensation threshold in 30 s by evaporative cooling (in the ϕ_{-2} dressed state). We then switch off the evaporation rf and switch on the trapping rf at a frequency below the resonance frequency in the center of the trap (1.3 MHz). This ensures that the atoms will be transferred into the ϕ_2 state, which is connected with the bare $m_F = 2$ state at very large negative detuning. ω_{rf} is chirped from $2\pi \times 1\,\mathrm{MHz}$ to the desired value of the detuning Δ in typically 150 ms. The rf field is produced by a circular antenna of axis y, fed by a rf synthesizer followed by either a 5 W or a 25 W amplifier. The Rabi frequency $\Omega/2\pi$ may be adjusted via a rf attenuator between 0 and 180 kHz and has been calibrated experimentally. We checked that the initial negative detuning of 300 kHz was large enough to populate only the ϕ_2 state when switching on the rf in a 2 ms linear ramp, at $\Omega/2\pi = 180\,\mathrm{kHz}$.

The series of absorption images shown in fig. 2 illustrate the deformation of the atomic cloud as it is transferred into the egg shell trap. Starting from the QUIC trap, the cloud is translated along z when Δ increases (as z_0 depends on Δ) and is deformed at the same time: It is compressed in the z direction whereas it is relaxed along x. The curvature of the trap, due to the iso-B surface curvature, is clearly visible. The vertical position of the cloud z_0 is a linear function of Δ as soon as $\Delta/2\pi$ exceeds 1 MHz, as one would expect for a constant magnetic-field gradient. The measurements give access to the gradient α which corresponds to 225 G/cm.

In order to better characterize the egg shell trap, the oscillation frequency along z was measured at a given value of $\Omega/2\pi = 180\,\mathrm{kHz}$ and $\Delta/2\pi = 2\,\mathrm{MHz}$. The vertical oscillation frequency may be estimated to 550 Hz, knowing α and Ω. To measure it, we excited the dipolar resonance at ω_{trans} by modulating with a 5 kHz depth the detuning $\Delta/2\pi$ and thus the trap position z_0 for 150 ms. The vertical size of the cloud after a 10 ms time of flight was measured and plotted as a function of the excitation frequency. We found a peak centered at 600 Hz with a HWHM width of 80 Hz, in good agreement with the expected value. The small discrepancy is likely to be due to the approximate knowledge of the Rabi frequency Ω.

The vertical oscillation frequency (600 Hz) corresponds to a temperature of 30 nK. As the 3D transition temperature for 10^5 atoms in this trap is about 50 nK, pure thermal clouds confined in the adiabatic trap always remain three-dimensional. However, the situation is different for a BEC where we shall compare the chemical potential μ to the vertical oscillation frequency. The atom number, the cloud position z_0 and the oscillation frequency ω_{trans} were measured in order to estimate μ. ω_1 and ω_2 were given a value deduced from the measured z_0. For an extreme detuning $\Delta/2\pi = 8.7\,\mathrm{MHz}$, we have $z_0 = -560\,\mu\mathrm{m}$ and oscillation frequencies $600\,\mathrm{Hz} \times 21\,\mathrm{Hz} \times 2\,\mathrm{Hz}$. For 10^5 atoms, assuming Thomas-Fermi theory in 3D, this yields a chemical potential $\mu/h = 400\,\mathrm{Hz}$ which is smaller than the vertical oscillation frequency. Therefore a condensate confined in this trap would present a 2D character.

However, we did not obtain a 2D condensate in this anisotropic trap. When starting with a BEC, we observed a heating during the loading phase, which destroyed the BEC. We investigated the heating rate and lifetime of the egg shell trap using thermal gases initially prepared at $0.75\,\mu\mathrm{K}$ typically in the QUIC trap. The atoms were transferred into the egg shell trap within 150 ms. After a variable holding time at a constant rf frequency (plateau) of 3 MHz in the anisotropic trap, a time-of-flight image was taken 7 ms after releasing the atoms from the trap. We measured the cloud size along x and z. The experiment was repeated using two different schemes for producing the rf field: i) Either we produced the rf ramp and the rf plateau with the same synthesizer (Agilent 33250A) used in a voltage-controlled frequency mode (FM mode), ii) or we used a first DDS-synthesizer (Direct Digital Synthesis, Stanford DS345) for ramping the frequency and switched to another synthesizer (Rohde & Schwarz SML01) used at constant frequency (3 MHz) for the plateau. Note that the relative phase is not controlled at the switching.

For both schemes, we observed a strong heating along the vertical direction during the loading rf ramp. The vertical temperature deduced from a time-of-flight measurement increased to about $4\,\mu\mathrm{K}$, whereas the horizontal temperature remained almost unchanged. We attribute this heating either to the frequency noise on the rf signal when a synthesizer is used in FM mode for scheme i) (see below) or to the discrete frequency steps in the case of the DDS ramp ii). During the following holding time at constant rf frequency, the heating and lifetime were very different for the two schemes. In scheme i), the heating was about $5\,\mu\mathrm{K/s}$ and the $1/e$-lifetime was limited to 360 ms. These features are clearly limited by the noise on the rf signal in FM mode: For our Agilent 33250A synthesizer used in this mode, we indeed measured a jitter at a given rf frequency during 1 s ranging from about 8 Hz FWHM for a 2 MHz modulation depth (which we use to produce a 2 MHz sweep between 1 and 3 MHz) to about 100 Hz FWHM for a 10 MHz modulation depth. These figures have to be compared to its sub-mHz spectral width if this same synthesizer were used in a fixed frequency mode. Note that these values strongly depend on the synthesizer. On the contrary, for scheme ii) we observed a thermalization between the x and z directions in about 340 ms (fig. 3) but no heating during holding time, and could obtain lifetimes as high as 4.5 s. This lifetime may be due to Landau-Zener transitions to untrapped states. In addition, the random phase jump occurring at the switching between ramping and holding rf synthesizers had a dramatic effect on the

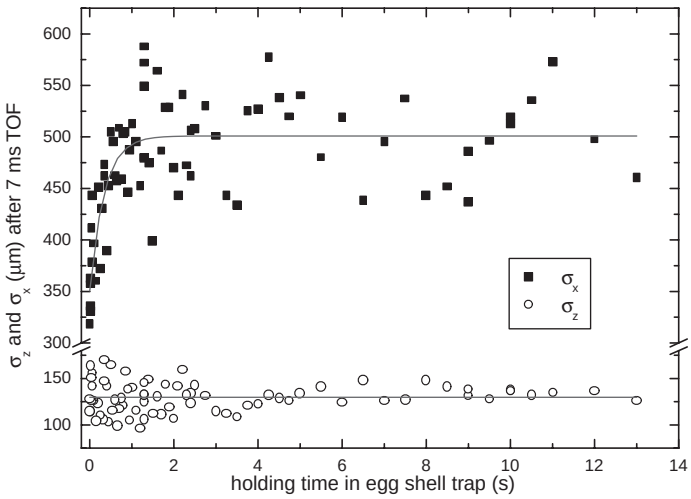

Fig. 3 – Evolution of the cloud sizes along x (filled squares) and z (open circles) with the holding time in the egg shell trap after 7 ms time of flight. At this value, the expanding cloud is still anisotropic. The x data are fitted with an exponential function. The deduced thermalization time is 340 ms. The equilibrium temperature measured along z as deduced from the mean σ_z value is 3.6 μK.

atom number; when the phase jump was close to π (phase reversal) we observed a strong atom loss with typically five times less atoms remaining trapped as compared to quasi-continuous phase occurrences.

In conclusion, we were able to trap ultracold atoms in a new kind of anisotropic trap, produced with the same tools broadly used for obtaining a BEC, that is a magnetic trap and a rf field. This trap may be well suited for confining BECs in lower dimensions. We confined thermal clouds in this egg shell trap without noticeable heating and measured a lifetime up to 4.5 s. Defects in the rf sweep during the loading stage induced heating and prevented us from producing a 2D BEC in this trap. The heating originates from excitations along the transverse axis, either due to frequency noise of the synthetizer used in FM mode or to discrete frequency steps when using a DDS synthetizer; we currently work towards getting rid of these technical limitations and producing a BEC in the 2D regime. Another issue will then arise, as the loading phase is likely to produce excitations along the long axis x of the egg shell trap, with oscillation frequency on the order of a few Hz only. To avoid these longitudinal excitations, we experimented evaporative cooling directly inside the egg shell trap using scheme i) together with an additional rf field as proposed in [16]. This could be a suitable means to achieve BEC in this trap, starting with a thermal cloud. However, this cooling mechanism could not overcome the noise-induced heating present during the holding phase in scheme i). This evaporative method applied to scheme ii) should give positive results.

Finally, the principle of adiabatic trapping may be associated to optical fields in order to produce new trapping geometries. In association with a red detuned vertical standing wave, the egg shell trap could be a way to load a single optical antinode [23]. Once the atoms fill a single antinode, a further increase of the rf detuning Δ pushes the atoms along the iso-B shell outwards the centre of the pancake. One ends up with a ring trap of about 1 mm in diameter, with high oscillation frequencies along the two transverse directions due either to the vertical standing wave or to the rf-induced avoided crossing of the Zeeman sublevels. Neutral atoms were already confined in cm scale magnetic storage rings [24]. Our 1D ring would have no local coupling to an external atomic source, and hence no local defect. It represents a tool well adapted to the study of permanent superfluid current.

* * *

We gratefully acknowledge support by the Région Ile-de-France (contract number E1213) and by the European Community through the Research Training Network "FASTNet" under contract No. HPRN-CT-2002-00304. Laboratoire de physique des lasers is UMR 7538 of CNRS and Paris 13 University.

REFERENCES

[1] Hohenberg P. C., *Phys. Rev.*, **158** (1967) 383; Mermin N. D. and Wagner H., *Phys. Rev. Lett.*, **17** (1966) 1133; Mermin N. D., *Phys. Rev.*, **176** (1968) 250.
[2] Bagnato V. and Kleppner D., *Phys. Rev. A*, **44** (1991) 7439.
[3] Görlitz A. *et al.*, *Phys. Rev. Lett.*, **87** (2001) 130402.
[4] Petrov D. S., Holzmann M. and Shlyapnikov G. V., *Phys. Rev. Lett.*, **84** (2000) 2551.
[5] Ott H., Fortágh J., Schlotterbeck G., Grossmann A. and Zimmermann C., *Phys. Rev. Lett.*, **87** (2001) 230401.
[6] Hänsel W., Hommelhoff P., Hänsch T. W. and Reichel J., *Nature*, **413** (2001) 498.
[7] Paredes B., Fedichev P., Cirac J. I. and Zoller P., *Phys. Rev. Lett.*, **87** (2001) 010402.
[8] Schweikhard V., Coddington I., Engels P., Mogendorff V. P. and Cornell E. A., *Phys. Rev. Lett.*, **92** (2004) 040404.
[9] Ovchinnikov Y., Shul'ga S. and Balykin V., *J. Phys. B*, **24** (1991) 3173.
[10] Hammes M., Rychtarik D., Engeser B., Nägerl H.-C. and Grimm R., *Phys. Rev. Lett.*, **90** (2003) 173001.
[11] Hinds E. A., Boshier M. G. and Hughes I. G., *Phys. Rev. Lett.*, **80** (1998) 645.
[12] Rychtarik D., Engeser B., Nägerl H.-C. and Grimm R., *Phys. Rev. Lett.*, **92** (2004) 173003.
[13] Fortágh J., Ott H., Kraft S., Günther A. and Zimmermann C., *Phys. Rev. A*, **66** (2002) 041604(R); Leanhardt A. E., Shin Y., Chikkatur A. P., Kielpinski D., Ketterle W. and Pritchard D. E., *Phys. Rev. Lett.*, **90** (2003) 100404.
[14] Bouchoule I., Morinaga M., Salomon C. and Petrov D., *Phys. Rev. A*, **65** (2002) 033402; Vuletić V., Kerman A. J., Chin C. and Chu S., *Phys. Rev. Lett.*, **82** (1999) 1406.
[15] Burger S., Catialotti F. S., Fort C., Maddaloni P., Minardi F. and Inguscio M., *Europhys. Lett.*, **57** (2002) 1.
[16] Zobay O. and Garraway B. M., *Phys. Rev. Lett.*, **86** (2001) 1195.
[17] Zobay O. and Garraway B. M., *Phys. Rev. A*, **69** (2004) 023605.
[18] Esslinger T., Bloch I. and Hänsch T. W., *Phys. Rev. A*, **58** (1998) R2664.
[19] To optimize the rf coupling, the rf magnetic field has to be aligned in a direction orthogonal to the local static magnetic field at the position of the atoms inside the egg shell trap, which in our experiment remains in the xz plane as the rf detuning is increased.
[20] The iso-B lines are plotted for a QUIC trap in [18].
[21] The deviation from a circle in the yz plane is less than 2% for a radius of 2 mm.
[22] Colombe Y., Kadio D., Olshanii M., Mercier B., Lorent V. and Perrin H., *J. Opt. B*, **5** (2003) S155.
[23] Grimm R., private communication.
[24] Sauer J. A., Barrett M. D. and Chapman M. S., *Phys. Rev. Lett.*, **87** (2001) 270401; Arnold A. S. and Riis E., *J. Mod. Opt.*, **49** (2002) 959; see also the proposal: Arnold A. S., *J. Phys. B*, **37** (2004) L29.

Ring trap for ultracold atoms

Olivier Morizot, Yves Colombe, Vincent Lorent, and Hélène Perrin
Laboratoire de Physique des Lasers, CNRS-Université Paris 13, 99 Avenue Jean-Baptiste Clément, F-93430 Villetaneuse, France

Barry M. Garraway
Department of Physics and Astronomy, University of Sussex, Brighton BN1 9QH, United Kingdom
(Received 2 December 2005; published 23 August 2006)

We propose a toroidal trap designed for ultracold atoms. It relies on a combination of a magnetic trap for rf-dressed atoms, which creates a bubble-like trap, and a standing wave of light. This trap is well-suited for investigating questions of low dimensionality in a ring potential. We study the trap characteristics for a set of experimentally accessible parameters. A loading procedure from a conventional magnetic trap is also proposed. The flexible nature of this ring trap, including an adjustable radius and adjustable transverse oscillation frequencies, will allow the study of superfluidity in variable geometries and dimensionalities.

DOI: 10.1103/PhysRevA.74.023617 PACS number(s): 03.75.Nt, 32.80.Pj

I. INTRODUCTION

In recent years, much work has been devoted to study theoretically and experimentally ultracold neutral atoms in very elongated traps, where the atomic cloud approaches the one-dimensional regime [1–8]. The situation under consideration is usually a one-dimensional harmonic oscillator, either a single trap [2–5] or a series of such harmonic traps [6–8]. New physics appears if the trap is now closed onto itself, with periodic boundary conditions. Guiding a matter wave on a torus is now thoroughly investigated by several groups [9–13]. The motivations are clearly towards the realization of inertial sensors and gyroscopes on one side even if a torus geometry is also of great advantage in the measurement of quantal phases. On the other side a torus trap filled with a degenerate atomic gas is also a source of inspiration for fundamental questions related to the coherence and superfluid properties of this trapped atomic wave [14]. Gupta *et al.* have produced a Bose-Einstein condensate in a ring-shaped magnetic waveguide [12] for the purpose of observing persistent quantized circulation and related propagation phenomena. In a similar way Arnold *et al.* [13] successfully seeded an atomic storage ring of large diameter ($\sim$10 cm). In the pursuit of tighter trapping potentials, other proposals investigate the use of optical dipole forces [15] or the conjunction of static magnetic and electric fields [16]. The toroidal trap geometry and loading we propose here is based on an adiabatic transformation of a radio-frequency two-dimensional trapping potential [17] by the addition of a standing optical wave in a vertical direction. The obtained toroidal trap will exhibit the shape of a Saturnian ring in the case where the optical trapping in the vertical direction provides a tighter confinement than the radial rf trapping. This hollow disk shape offers a new situation to study vortices since its internal diameter is orders of magnitude larger than the healing length of an atomic condensate. It may then exhibit a geometry that allows an irrotational motion without disruption inside the trap.

Our proposed ring trap has considerable flexibility allowing a variation of the dimensionality of the trap and several methods of control. A one-dimensional cold-atom regime can be reached with the trap in its tightest form. With a relaxation of the radial trapping (or increase in atom number) the trap allows a two-dimensional pancake ring of atoms. At this point we note that we can also create a vertical stack of such traps (utilizing the periodicity of the standing wave). This approach has proven to be of interest for detecting a small signal from each trap by increasing the signal-to-noise ratio compared to individual, identical, traps [6,7]. Finally, a three-dimensional regime can, of course, be reached with sufficient numbers of atoms, but in addition a more polodially symmetric potential can be formed by reducing the vertical confinement.

The paper is organized as follows: in Sec. II the concept and construction of this trap is described and in Sec. III we describe the dimensional characteristics of the trap. In Secs. IV and V we discuss factors that affect the feasibility of the trap, such as its finite lifetime, and we show that the trap is realizable with existing technology (Sec. V) and that it is possible to load the trap efficiently (Sec. VI). An outlook and conclusion are given in Sec. VII. Details of calculations of needed chemical potentials are presented in Appendixes A and B.

II. TRAP DESCRIPTION

This trap is the superposition of two different traps, an egg shell trap (ZG-trap) relying on a magnetic trapping field and rf coupling, combined with a standing wave of light. The principle of the rf-dressed potentials was explained elsewhere [17,18], but let us recall here the main features, for instance in the case of ^{87}Rb, $F=2$ ground state. An inhomogeneous magnetic field of norm $B(\mathbf{r})$ presenting a local minimum B_0 (the base of a magnetic trap) is used together with a rf coupling between m_F Zeeman substates created by an oscillating magnetic field $B_{\mathrm{rf}}\cos(\omega_{\mathrm{rf}}t)$. This results in a dressing of the m_F states, as represented in Fig. 1, and the potential experienced by the upper adiabatic state reads

$$V_d(\mathbf{r}) = F\{[V_B(\mathbf{r}) - V_{\min} - \hbar\,\Delta]^2 + (\hbar\Omega)^2\}^{1/2}. \qquad (1)$$

Here, $m_F=F=2$ for ^{87}Rb and $V_B(\mathbf{r})=g_L\mu_B B(\mathbf{r})$ is the potential created by the magnetic trap alone for $F=2, m_F=1$,

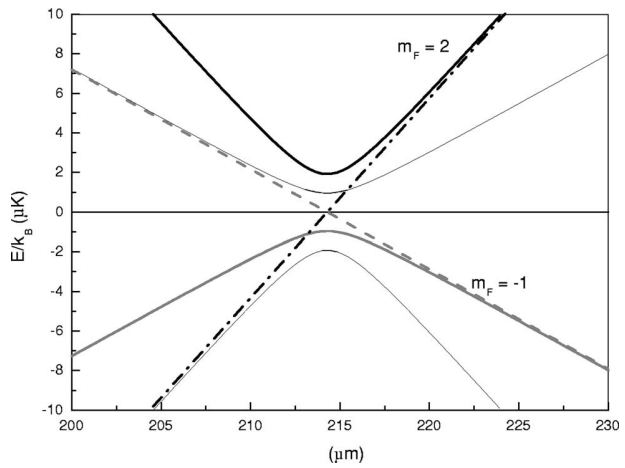

FIG. 1. Energy of the dressed levels in the magnetic quadrupole trap described in the paper, plotted along the radial coordinate, in the vicinity of the potential minimum at $\rho=r_0$. The five dressed sublevels for a $F=2$ spin state are plotted, as well as two bare states for comparison (bare state $m_F=-1$ is shown dashed and $m_F=2$ dash-dotted). The ring trap we discuss in this paper is based on the upper dressed potential $m_F=F=2$, for the radial trapping (bold solid line). Values for the field gradient and rf and Rabi frequencies are given in Table I.

where g_L is the Landé factor and μ_B the Bohr magneton. The potential at the bottom of this magnetic trap is $V_{\min}=g_L\mu_B B_0=\hbar\omega_0$. The detuning $\Delta=\omega_{\rm rf}-\omega_0$ is the difference between the rf applied frequency and the resonant frequency at the magnetic potential minimum, and $\Omega=g_L\mu_B B_{\rm rf}/2\hbar$ is the Rabi frequency of rf coupling [19]. The potential minimum of this trap sits on an iso-B surface, as $V_d(\mathbf{r})$ has a minimum for $V_B(\mathbf{r})=\hbar\Delta$, that is on the surface defined by $g_L\mu_B B(\mathbf{r})=\hbar\Delta$. In the following, we will concentrate on the case of a quadrupolar trap with z as the symmetry axis [20]. Note that in this case the magnetic field in the center is zero, so that $\Delta=\omega_{\rm rf}$ and $V_{\min}=0$. Let b' be the field gradient in the radial direction, and let us define α as $\alpha=g_L\mu_B b'/\hbar$. In this case, an atom is in a dressed state with potential

$$V_d(\rho,z)=F\hbar\,[(\alpha\sqrt{\rho^2+4z^2}-\Delta)^2+\Omega^2]^{1/2} \tag{2}$$

and the relevant iso-B surface is an ellipsoid of equation $\rho^2+4z^2=r_0^2$, where $\rho^2=x^2+y^2$ and the radius r_0 is related to Δ through $r_0=\Delta/\alpha$, typically much greater than a micrometer. In the presence of gravity, the atoms fall to the bottom of this shell: the resulting trapped cloud is in a quasi-two-dimensional (2D) geometry. This situation was recently demonstrated experimentally in a Ioffe-Pritchard type trap [21]. It was also used in an atom chip experiment for producing a double well potential [22].

Let us now add an optical standing wave to this egg shell trap, along the vertical z direction, blue detuned by $\delta>0$ with respect to an atomic dipolar transition [23] and with identical linear polarization for the two laser beams (Fig. 4). The light shift creates a periodic potential of period $\lambda/2$ where λ is the light wavelength. Along z, the atoms are then confined in a series of parallel planes. In a given plane, their

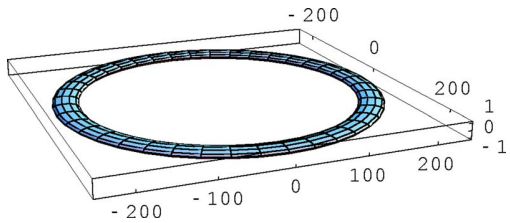

FIG. 2. (Color online) A view of the ring trap. An isopotential surface is plotted for the parameters of Table I, in the harmonic approximation. The length unit is 1 μm. The vertical direction was amplified ten times for clarity. The overall trap shape is that of a Saturnian ring.

altitude is fixed to $z=z_0$ better than a fraction of λ. As a result, if they also experience the adiabatic rf potential in a quadrupole trap, the atoms sit on a circle, the intersection of that plane and the iso-B ellipsoid, defined by $\rho=R$ of radius $R=\sqrt{r_0^2-4z_0^2}$ much greater than λ (Fig. 2). This is the circular trap we are interested in.

The total potential for the atoms may be written as

$$V(\rho,z)=V_d(\rho,z)+U_0[1-\cos(2kz)]e^{-2\rho^2/w^2}+mgz, \tag{3}$$

where $k=2\pi/\lambda$ is the wave vector of one of the counter-propagating light beams, U_0 is the mean light shift of the standing wave on axis, and w the $1/\sqrt{e}$ diameter. Gravity was taken into account by the last term. U_0 is assumed to be large enough for the tunnel effect between successive planes to be negligible (see Sec. IV). Note that the potential does not depend on the azimuthal angle θ. For the $D2$ transition of ^{87}Rb, the expression for U_0 is

$$U_0=\frac{2}{3}\frac{\Gamma}{\delta}\frac{2P}{8\pi w^2 I_s}\hbar\Gamma, \tag{4}$$

where $\Gamma=2\pi\times 5.89$ MHz is the natural linewidth of the transition, P the total laser power, and $I_s=1.6$ mW/cm^2 is the saturation intensity. The factor $2/3$ accounts for the transition coefficients of the $D2$ line for a linear polarization.

Let us focus on the plane situated around $z=0$, so that $z_0=0$ and $R=r_0$. In principle, the trapping potential mixes the radial (ρ) and axial (z) coordinates. However, the constraints on ρ and z are such that the potential may be written to a good approximation as a sum of independent potentials $V_\rho(\rho)$ and $V_z(z)$ for the radial and axial coordinates, respectively. Indeed, due to the presence of the standing wave, $|z|$ is restricted to values less than $\lambda/4$, typically 100 nm. This is small as compared to $d=\Omega/\alpha$, the length scale associated with the rf coupling [see Eq. (2)] which is on the order of a few micrometers. The z dependence may thus be omitted in V_d. In the same way, ρ extends over d which is small as compared to the waist w. This waist should be chosen of the order of the radius r_0 (see Sec. V), that is a few hundred micrometers, and then ρ may simply be replaced by r_0 in the expression of the light shift. Within these assumptions, the single particle Hamiltonian becomes separable in ρ and z and one can calculate independently oscillation frequencies along z and ρ around $z=0$ and $\rho=r_0$ for an atom of mass m:

TABLE I. Typical set of parameters for the realization of the ring trap. The laser used for the standing wave may be a titanium sapphire laser.

Parameter	Value
Laser power P	0.5 W
Laser wavelength λ	771 nm
Beam waist w	300 μm
rf Rabi frequency $\Omega/2\pi$	20 kHz
rf frequency $\Delta/2\pi$	2250 kHz
Magnetic field gradient b'	150 G/cm

$$\omega_\rho = \alpha\sqrt{F\frac{\hbar}{m\Omega}}, \tag{5}$$

$$\omega_z = \frac{2\pi}{\lambda}\sqrt{\frac{4U_0}{m}}e^{-r_0^2/w^2}. \tag{6}$$

Thus the total potential for the atoms, Eq. (3), can be written approximately as

$$V(\rho,z) = F\hbar\,\Omega + \frac{1}{2}m\omega_\rho^2(\rho - r_0)^2 + \frac{1}{2}m\omega_z^2 z^2, \tag{7}$$

which is illustrated for an iso-potential surface in Fig. 2. [In Eq. (7) we neglect a slight vertical shift in the position of the minimum of the potential due to gravity. This does not significantly affect the vibrational frequency for typical parameters given below.] For the parameters proposed in Table I and used in the rest of the paper, we obtain oscillation frequencies of $\omega_\rho/2\pi=1.1$ kHz and $\omega_z/2\pi=43$ kHz, with a ring diameter of 430 μm.

III. CONDITIONS FOR REACHING THE LOW DIMENSIONAL REGIME

An interesting feature of this ring trap is its high oscillation frequency in the transverse direction. It is thus relevant to raise the question of dimensionality of a degenerate gas confined in this trap. This question has acquired a growing interest in the last 5 years, and is related, for instance, to the creation of anyons [24] or the fermionization of the excitations in the bosonic cloud [25]. Already in a 3D elongated condensate, the coherence properties are affected by the geometry [1,4,26,27]. To estimate in which regime (1D, 2D, or 3D) the gas has to be considered, we compare the chemical potential, calculated in the Thomas Fermi approximation under a given dimensionality assumption, to the trapping oscillation frequencies. The three regimes (3D, 2D, or 1D) correspond, respectively, to $\mu > \hbar\omega_z$, $\hbar\omega_\rho < \mu < \hbar\omega_z$, and $\mu < \hbar\omega_\rho$. The crossover between one regime and another may be given in terms of atom number in the trap. Detailed calculations of the chemical potential in the different regimes are given in Appendix A.

Let us first estimate the 3D Thomas-Fermi chemical potential. It can be calculated from the normalization of the condensate wave function in the Thomas-Fermi approximation. The 3D interaction strength is $g_{3D}=4\pi\hbar^2 a/m$, $a=5.4$ nm being the 3D scattering length. In the harmonic approximation for the toroidal potential, where Eq. (7) is valid, the chemical potential is given by the formula of Eq. (A5) [28]:

$$\mu_{3D} = \hbar\,\bar{\omega}\sqrt{\frac{2Na}{\pi r_0}}, \tag{8}$$

where $\bar{\omega}=\sqrt{\omega_\rho\omega_z}$ is the geometric mean of the oscillation frequencies and N the atom number. This expression is meaningful if the gas is 3D, that is if $\mu_{3D} > \hbar\omega_z$. In terms of atom number, it can be expressed as $N > \frac{\pi r_0}{2a}\frac{\omega_z}{\omega_\rho}$, that is $N > 2.4\times 10^6$ for the choice of the parameters given in Table I. This number is sufficiently high that it is feasible to have a condensate which is at least in a two-dimensional regime, without any difficulty in imaging it. With 10^5 atoms, for instance, the chemical potential corresponds to $\mu_{3D}/h=8.9$ kHz, which is below the highest oscillation frequency of 43 kHz. The total energy per atom does not allow us to populate transverse (z) excitations, and the vertical degree of freedom is frozen. Such a degenerate gas would thus be at least in the 2D regime and the chemical potential has to be recalculated within a 2D hypothesis.

In the 2D case, the interaction strength is modified and reads $g_{2D}=g_{3D}/(\sqrt{2\pi}l_z)=2\sqrt{2\pi}\hbar^2 a/(ml_z)$ where $l_z=\sqrt{\hbar/(m\omega_z)}$ is the size of the ground state of the harmonic oscillator in the frozen direction [29]. Again, the chemical potential in 2D is deduced from normalization of the integrated density to the atom number in the Thomas-Fermi regime, Eq. (A8):

$$\mu_{2D} = \hbar\,\bar{\omega}\left(\frac{\omega_\rho}{\omega_z}\right)^{1/6}\left(\frac{3Na}{4\sqrt{\pi}r_0}\right)^{2/3}. \tag{9}$$

The gas would be in the 1D regime if the 2D chemical potential is of the order of, or less than the radial oscillation frequency ω_ρ. This corresponds to an atom number $N < \frac{4\sqrt{\pi}r_0}{3a}\sqrt{\frac{\omega_\rho}{\omega_z}}$, that is $N < 1.5\times 10^4$ for the proposed parameters. A uniform 1D gas of density $n_1=N/(2\pi r_0)$ would have an interaction strength $g_{1D}=g_{3D}/(2\pi l_z l_\rho)=2\hbar^2 a/(ml_z l_\rho)$ [29] with $l_\rho=\sqrt{\hbar/(m\omega_\rho)}$, and a chemical potential μ_{1D} in the trap, with

$$\mu_{1D} = \hbar\,\bar{\omega}\frac{Na}{\pi r_0}. \tag{10}$$

Again, this expression is valid if the kinetic energy is negligible as compared to the mean-field energy. However, even if this is the case, longitudinal excited states (along the ring) are likely to be populated as the excitation frequency is only of the order of 1 mHz. With such a 1D system, the gas could be in the Tonks-Girardeau regime [25,30] if the parameter $\gamma=mg_{1D}/(\hbar^2 n_1)$ is much larger than 1. For our parameters, this would correspond to very few atoms, i.e., much less than the $\gamma=1$ limit of 850 atoms. With a larger atom number (a few thousand), we should instead have a quasicondensate with a fluctuating phase [29].

In conclusion to this section, let us stress that an atomic cloud confined in the ring trap proposed in this paper would

easily be in the 2D regime, the vertical (z) degree of freedom being frozen. With the parameters of Table I, it would be true for an atom number between 1.5×10^4 and 2.4×10^6. The 1D regime is achievable with a smaller number of atoms, but the Tonks-Girardeau regime would require a few hundred atoms only, and the detection of the atomic cloud would then be an issue.

IV. LIFETIME IN THE RING TRAP

In the ring trap, the lifetime may be limited by several processes, apart from the collisions with the background gas. In this section, we discuss these losses for the ground-state or for thermal atoms.

First, as the atoms are confined in a rf-dressed state, they may undergo nonadiabatic Landau-Zener transitions to an untrapped spin state due to motional coupling. This will happen along the radial axis, where the potential changes more rapidly. The transition rate Γ_{LZ} may be estimated by averaging over the velocity distribution the transition probabilities P_{LZ} for a given radial velocity v_ρ [31]:

$$P_{LZ}(v_\rho) = 1 - \left[1 - \exp\left(-\frac{\pi\Omega^2}{2\alpha v_\rho}\right)\right]^{2F} \simeq 2Fe^{-\pi\Omega^2/2\alpha v_\rho}. \tag{11}$$

The loss rate to other spin states is deduced from this transition probability by multiplying by twice the radial oscillation frequency, as the transition may occur at each crossing. With the parameters given above, the transition rate is limited to $\Gamma_{LZ}=\langle P_{LZ}(v_\rho)\rangle\omega_\rho/\pi\simeq0.075\ \mathrm{s}^{-1}$ for a thermal cloud of temperature 3 μK. For atoms in the vibrational ground-state of the dressed potential, the approach of Ref. [18] and its Eq. (10) may be generalized to a F spin state as done in Ref. [31]. The transition rate is then approximately $\Gamma_{gs}\simeq2(F\omega_\rho/\pi)\exp[-\pi\Omega/(2\sqrt{2}\omega_\rho)]$. This leakage is negligible for the parameters of Table I.

Second, we shall consider the issue of tunneling of the atoms between the vertical lattice sites. For a horizontal lattice – that is, without the effect of gravity – the tunneling amplitude per atom J is related to the lattice depth. In the tight binding limit, where the lattice depth $V_0=2U_0e^{-2r_0^2/w^2}$ is much higher than the recoil energy $E_R=h^2/(2m\lambda^2)$, J scales approximately as $(V_0/E_R)^{1.05}e^{-2.12\sqrt{V_0/E_R}}$ [32]. In the case discussed here, $V_0=32E_R$ and the tunneling rate J/h is only 1.3 Hz. This rate is even smaller when gravity is taken into account, as it splits the degeneracy between neighboring ground states by a value $mg\lambda/2h=1/\tau_B=822$ Hz (τ_B is the Bloch period). For the given lattice depth, we are deeply in the adiabatic limit and the atoms remain in the ground state band and experience Bloch oscillations: if one starts with atoms in a single lattice well (a Wannier state), after a Bloch period they are all back in the same well. Moreover, the amplitude of these Bloch oscillations in space is very small (2 nm). Only finite size effects, lattice imperfections, or excitations to the first excited band would prevent the exact return to the initial condition. Tunneling should not be an issue for this trap, at least for the parameters mentioned above.

Finally, photon scattering may lead to heating and trap losses. These processes are quite small for blue detuned lattice light because the atoms only significantly scatter photons when they leave the very center of a lattice well. In a given well, the scattering rate per atom is related to the cloud spreading $\langle z^2\rangle$ and can be expressed as

$$\Gamma_{\mathrm{sc}} = \frac{\Gamma}{2}\frac{m\omega_z^2\langle z^2\rangle}{\hbar\delta}. \tag{12}$$

This simplifies to $\Gamma_{\mathrm{sc}}=\Gamma\omega_z/4\delta$ in the ground state of the vertical motion, and to $\Gamma_{\mathrm{sc}}=\Gamma k_BT/2\hbar\delta$ for a thermal gas. The corresponding calculated values are $\Gamma_{\mathrm{sc}}=0.08\ \mathrm{s}^{-1}$ for the ground state and $\Gamma_{\mathrm{sc}}=0.25\ \mathrm{s}^{-1}$ for a thermal gas at 3 μK, or equivalently a heating rate of 30 and 90 nK/s, respectively [33].

V. CHOICE OF THE EXPERIMENTAL PARAMETERS

In this section we propose a strategy for an optimal choice of the laser, magnetic field, and rf field parameters. A correct choice of these experimental parameters should allow one to have a ring trap as large as possible, with high vertical and transverse oscillation frequencies, and reasonable values for magnetic, rf, and optical fields, while minimizing the spontaneous photon scattering rate and tunneling between neighboring wells. With this objective, it appears that the magnetic gradient and the laser power should be chosen as large as possible: only technical issues will limit this choice. We thus fix these parameters to values easily obtainable experimentally, that is a laser power of 0.5 W, available, for instance, from a titanium sapphire laser, and a magnetic gradient $b'=150$ G/cm, corresponding to a gradient of 300 G/cm in the axis of the quadrupole coils, already realized in a previous experiment [34]. b' is related directly to the parameter α introduced in Sec. II.

An important remark concerns the choice of the beam waist w, for a desired ring radius r_0. There is an optimal choice, maximizing the lattice depth and consequently the vertical oscillation frequency. The waist should be equal to $w=\sqrt{2}r_0$, the $\sqrt{2}$ coefficient corresponding to the maximum of the function $\frac{1}{x}e^{-1/x^2}$, as can be deduced from Eq. (6). This fixes the relation between the light shift in the beam center U_0 and the lattice depth: $V_0=2U_0/e$.

Once these values are fixed, we impose constraints on the possible losses or heating rates discussed in Sec. IV, that is on the tunneling rate J, the scattering rate Γ_{sc}, and the Landau-Zener transition rate Γ_{LZ}. We set these rates, respectively, to a given J_0, to some small fraction ε of the natural linewidth ($\Gamma_{\mathrm{sc}}=\varepsilon\Gamma$) and to $\Gamma_{LZ}=\gamma$. Now, the choice of J imposes the standing wave depth V_0 (see Sec. IV), as well as the vertical oscillation frequency ω_z, directly related to V_0 and E_R through $\hbar\omega_z=2\sqrt{V_0E_R}$. This in turn gives the detuning to be chosen for limiting the photon scattering rate in the ground state to $\varepsilon\Gamma$: $\delta=\omega_z/4\varepsilon$ (see Sec. IV). The light shift U_0 is known from its fixed relation with V_0, and as the laser power P and the detuning δ have been chosen, the waist w can be deduced from the knowledge of U_0. From w one gets $r_0=w/\sqrt{2}$ and the rf detuning $\Delta=\alpha r_0$. The only remaining

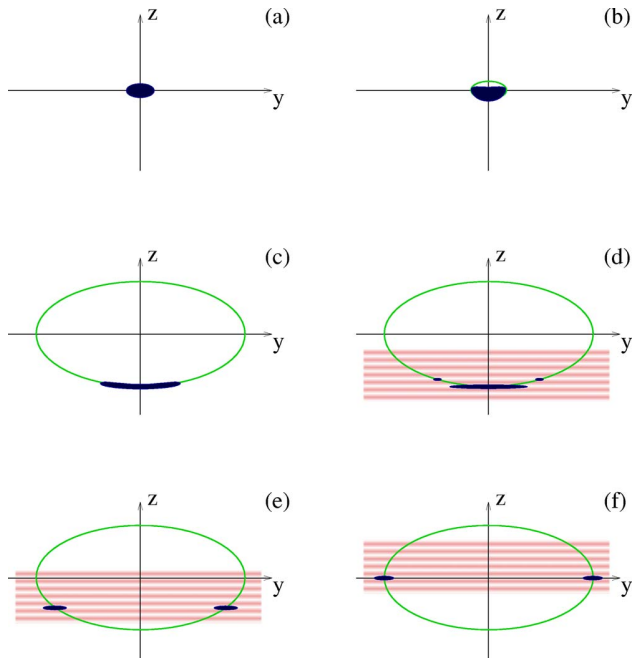

FIG. 3. (Color online) Outline illustration of stages in the loading of the ring trap. The z axis is in the vertical direction and we assume a cylindrical symmetry about this axis. In (b)–(f) the elliptical line indicates the location (in the y-z plane) of the rf resonance. In (d)–(f) the horizontal bands indicate the presence of the standing light wave. Then: (a) We take as the starting point a BEC in a magnetic trap. (b) Shortly after transfer to the dressed rf trap the condensate fills a location around the rf resonance, but is not yet excluded from the trap center. (c) After rf expansion [stage (ii)] the condensate lies at the bottom of the "egg shell." (d) The application of the optical standing wave results in a potential which confines the condensate to a couple of potential wells (corrugations). (e) The standing wave is moved upwards and the condensate ring is formed and expanded outwards and upwards. (f) Final position of the condensate ring at maximum radius. All three potentials, magnetic, dressed rf, and optical are required to maintain the ring.

parameter is then the rf Rabi frequency Ω, which is chosen to fit the desired value of γ.

We applied this procedure to desired values of $J/h=1$ Hz, $\Gamma_{sc}=0.1$ s^{-1}, and $\gamma=0.1$ s^{-1} at 3 μK to obtain the typical parameter values suggested in Table I.

VI. LOADING

A condensate in the proposed ring trap would cover quite a small volume spread over a relatively large area, and as a result the method used to load the atoms into the trap needs to be considered carefully. This is because of the mismatch between the starting point, a condensate in a magnetic trap, which may be spheroidal and localized, and the end point, a condensate in a ring trap which has essentially no overlap with the starting point at all.

There may be several approaches to loading the proposed ring trap. Based on a previous experiment [34], which used a QUIC trap, our proposed loading method takes place in at least five stages [(i–v) below] and is illustrated in Fig. 3. In the following we refer to a BEC for convenience. The steps are the same for a cold atom cloud, but a condensate has an advantage of compactness.

(i) Dressed trap loading: Starting with the magnetic trap, Fig. 3(a), the condensate is first transferred to the field-dressed atom trap (ZG-trap) by an established loading procedure [17,21] in which a rf field is steadily increased in intensity at a fixed, negative, detuning (relative to the magnetic trap center) and subsequently ramped up in frequency to positive detuning [see Fig. 3(b)]. This accomplishes a transfer to field-dressed potentials, like those in Eq. (2), which are subsequently expanded outwards from the trap center as seen in Fig. 3(c). [This rf expansion is discussed further in (ii), below.]

In the resulting trap the condensate lies in an electromagnetic potential which confines it to the surface of an ellipsoid, or egg shell, as in Sec. II. This surface is represented by the ellipse in Figs. 3(b)–3(f). However, gravity, and the absence of the optical potential, ensures that the condensate occupies just the lower part of the ellipsoid surface, when the ellipsoid is sufficiently large, as seen in Fig. 3(c). As mentioned in Sec. II the egg shell is defined, for a particular rf frequency, by the surface of resonance between the magnetic sublevels and the rf. Thus the size of the ellipsoid, or egg shell, depends on the rf frequency; so as the rf frequency is increased, the part of the condensate at the bottom of the egg shell moves downwards and becomes flatter. This is the rf expansion phase and is represented by the transition from Fig. 3(b) to Fig. 3(c).

(ii) rf expansion: During the rf expansion the pendulum frequency reduces considerably. Numerical simulations of this kind of expansion, as part of a loading process, were carried out in Ref. [18]. To give an example for the current ring trap, we may consider 10^5 atoms in the dressed trap. We will also have an underlying magnetic trap with the parameters given in Sec. V and a rf intensity leading to the same dressed trapping frequency $\omega_{trans}=2\pi\times 2.26$ kHz at the final rf frequency. With the rf thus chosen the condensate would be at a distance of $z_0=107$ μm below the magnetic trap center, and the final horizontal oscillation frequency (given in Appendix B) is $\omega_{1,2}=\sqrt{g/4z_0}$ with a value of approximately 24 Hz. Thus, since this is the lowest horizontal frequency during expansion, the time scale for the expansion needs to be considerably longer than the corresponding characteristic time scale $1/24\sim 42$ ms. If it is not, there will be lateral excitations. Since the condition for adiabaticity is that $\dot{\omega}_{1,2}\ll\omega_{1,2}^2$ [18], we can make an estimate for the required expansion time by solving the equation $\dot{\omega}_{1,2}=-\epsilon\omega_{1,2}^2$,where ϵ represents an amount of nonadiabaticity that can be tolerated. Thus an overestimate of the expansion time is $1/(\epsilon\omega_{1,2})$ if the value of $\omega_{1,2}$ is the final horizontal oscillation frequency. (This neglects the initial horizontal oscillation frequency in comparison with the final value.) Then a tolerance of $\epsilon\sim 1\%$ leads to an expansion time of 0.7 s.

The condensate would thus be flattened. The aim is to flatten it sufficiently to be able to load it as efficiently as possible into a single corrugation of the optical potential cre-

ated by the blue-detuned standing wave. The best case would be if the condensate could be flattened to match its width in the optical potential. In practice we would expect difficulties with this step. Physical constraints on the size of the magnetic coils and the fields they produce mean that it can be hard to make a condensate with many atoms sufficiently thin, without retaining some of the curvature of the egg shell. Thus a curved standing wave would be ideal, since it would match better the shape of the curved condensate. However, from the experimental point-of-view this would be complicated to set up and adjust. Thus we will consider a planar standing wave in what follows. In this case it means that when the standing wave is applied the condensate may be sliced into a number of rings and a central disk. Figure 3(d) shows a disk and just one such ring as an example. Each ring would be formed from condensate collected within a distance given by the well separation of the optical potential (i.e., within a range of $\lambda/2$).

Since the aim is to study the condensate properties in one of the rings, it is important to estimate the fraction of condensate that might be lost from the principal ring in the loading process. An estimate can be formed by considering the Thomas-Fermi approximation for the condensate density in the egg-shell trap. A simple model of the trap consists of a radial potential $m\omega_{trans}{}^2(r-R)^2/2$ representing the shell with a local curvature R, a local oscillation frequency ω_{trans} in the "shell," and a simplified gravitational potential (see Appendix B).

Again, as a numerical example, we consider 10^5 atoms in the dressed trap with the rf at its final value so that the condensate lies at a distance of 107 μm below the magnetic trap center. Then the Thomas-Fermi solution, see Appendix B, gives a condensate with a maximum total thickness of 0.60 μm, a horizontal full width of 56 μm, and a height (from the resonance point) of 0.92 μm. The height and maximum thickness are in the region of twice the proposed optical well separation of $\lambda/2 \sim 0.39$ μm. The number of atoms caught in the loading process can be estimated by integrating the Thomas-Fermi solution over a vertical distance of $\lambda/2$. In this example we numerically find that at best 60% of atoms could be loaded into a single well, and roughly three other rings are populated to a lesser extent.

In this example the condensate is already close to a two-dimensional regime. If we increase the displacement of the condensate, by increasing the rf frequency and keeping other parameters constant, we find that there is a slight reduction in thickness and height, but even at a displacement of 200 μm the thickness is 0.53 μm with the other parameters as given. Increasing the rf in this way also has side effects, such as a reduction in the lateral oscillation frequency $\omega_{1,2}=\sqrt{g/z_0}/2$ and consequent increased loading time. We note that if curvature *were* more of a problem than thickness, the situation could be improved by the application of red-detuned light to attract the atoms, temporarily, into the center. Such a horizontal confinement may cause some increase in (vertical) thickness, for a given number of atoms, and so there may still have to be a trade-off between the curvature of the condensate and its thickness. An increase in either thickness, or curvature, could result in atoms being spread amongst several other optical wells when the standing wave is applied.

(iii) Improve magnetic trap geometry: As soon as the condensate has moved away from the center of the magnetic trap, it is advantageous to improve the magnetic configuration by removing any bias fields needed in the original magnetic trap. For example, with a QUIC trap configuration we can achieve a quadrupole field by turning off the Ioffe coil. This will result in a circularly symmetric ring trap at the final stage, and by doing this while the condensate is still fairly localized, we again reduce the demands of adiabaticity on the time scales of the system. (As soon as the condensate has moved away from the center of the trap there is no longer any need to worry about any Majorana transitions.)

(iv) Application of optical potential: Now the blue-detuned standing wave can be applied and as many atoms as possible are trapped in a single well, or corrugation, of the optical potential. Figure 3(d) shows a case where a single other well is also populated. The light is switched on relatively slowly so as not to cause any excitation of the condensate.

We note that the option exists, at this point in the loading sequence, to remove unwanted atoms from some of the optical wells by applying an rf "scalpel." However, this procedure would require an adiabatic unloading and reloading of the dressed rf trap, which can be done, but adds to the overall loading time.

(v) Ring expansion: The final stage of the loading process is to form the condensate ring by changing the vertical position of the blue-detuned potential well relative to the rf resonance point, or egg shell. If we consider the standing wave as comprised of two traveling waves, this can be done by simply changing the phase of one of the traveling wave components. When this is done the standing wave pattern can be moved upwards. As this happens, the confinement to the egg shell of the rf trap ensures the formation of a ring of condensate. The ring expands outwards as it is raised upwards [Fig. 3(e)]. During this expansion the orientation of the softer rf trapping changes from the vertical to the horizontal and the condensate will adopt the shape of a Saturnian ring which becomes narrower when the rf trapping is fully in the horizontal direction.

Clearly, the ring reaches a point of maximum circular radius when its center is at the center of the quadrupole trap. However, we note that while the magnitude of the magnetic field remains constant, the orientation of the magnetic field changes as the ring is raised. Since the orientation of the magnetic field is important in the orientation of the antenna (see Ref. [19]) this would necessitate switching between different antennas at about the half-way point. A problem that then emerges is that the rf trapping becomes asymmetrical as soon as the ring starts to expand, and consequently, until the switching occurs, the ring is squeezed more tightly in one direction. A better solution to the problem of the orientation of the antenna avoids any switching by utilizing a rf magnetic field rotating in the horizontal plane. This field can be generated by two rf coils at right angles to each other (Fig. 4). When the condensate is at the bottom of the egg-shell potential, the magnetic field is basically vertical and provided the rf field is rotating in the correct direction the rf

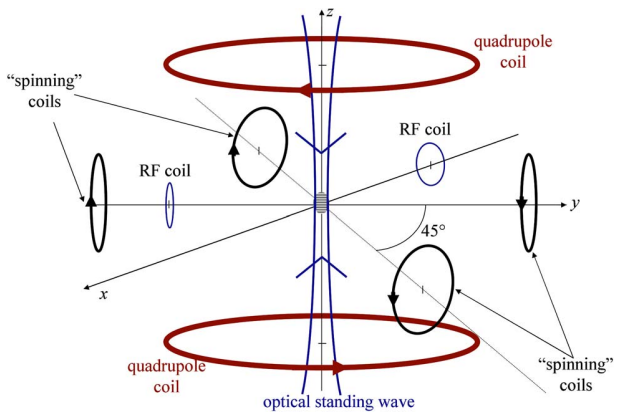

FIG. 4. (Color online) Coils and laser configuration for producing and exciting the ring trap. The trap is the combination of a vertical light standing wave (blue beam on the figure) and an egg shell rf trap (see Sec. II). This egg shell trap relies on a magnetic field gradient (produced by the quadrupole coils) and rf coupling between Zeeman sublevels (two rf coils in quadrature as described in Sec. VI). The additional "spinning" coils could be used for exciting the rotation of the atoms inside the ring trap (see Sec. VII).

dressed trapping is fully effective. When the condensate is at the horizontal extremum of the egg shell, i.e., forming a ring, the magnetic field is horizontal and at each point on the ring the rotating field always has one ineffective component and an effective component perpendicular to the local static magnetic field. As a result the rf trapping is uniform around the ring without needing to switch. The reduced effective amplitude can be compensated by an increase in rf power as the ring expanded to its full radius.

Finally, we note that instead of raising the standing wave pattern, the ring could also be expanded by a further increase of the rf detuning. This would force the ring outwards at the same vertical position, i.e., at 107 μm below the magnetic trap center in the example given.

VII. CONCLUSION

In this paper we have seen how a ring trap for cold atoms can be made from a combination of magnetic, rf, and optical fields. It is the combination of these fields which makes possible a trap with sufficient tightness that it could hold 2D and even 1D condensates. Many of the physical parameters of the trap are the result of practical compromises which have been tested in this paper. For example, the leakage in the optical trap component is traded off against practical laser power and reduced photon scattering. The leakage of the rf trapping component is traded off against its tightness. The number of atoms should be sufficiently high that it can be easily imaged. Additional calculations have shown that a small tilting of the trap will not adversely affect it. The ring trap also has to have a loading scheme and a possibility has been presented in this paper which involves careful orientation of the rf antennas to maintain rf trapping as the atom ring is formed. A set of feasible parameters for the trap has been presented which still leaves room for later optimization and yet would allow the demonstration of the ring trap and low-dimensional effects.

Once the atom ring is created it could be excited, or manipulated, with the application of a periodic perturbation. Optical "paddles" can be used to good effect (see, e.g., Ref. [35]), but another way to do this would be with a rotating deformation of the ring. This can be achieved with the magnetic field from two pairs of coils, each of which is in an anti-Helmholtz configuration with its axis oriented in the horizontal plane and at a 45° angle to the axis of the other pair (Fig. 4). Each pair of coils can perturb the circular shape of the ring trap on its own. It can be shown that one pair of these coils results in an ellipse with a difference in radii of

$$\delta r_0 \simeq \frac{3}{2}\frac{\delta b'}{b'} r_0, \tag{13}$$

where $\delta b'$ is the magnetic field gradient produced along the axis of the coils. By applying a time-dependent function to the current of the *pairs* of coils the elliptical trap can be continuously rotated. This may initiate a collective movement, or excitation, of the trapped cloud or condensate as has been explored in some theoretical papers [36–41]. As well as studying persistent currents the trap makes an interesting topology to study solitons in three and less dimensions [38]. Furthermore, it would be possible to study the implosion of an atom ring, and the effect of repulsive interactions, by switching off the rf coupling. The magnetic field would then cause some components of the BEC to be expelled, and some to be drawn into the center where the atom ring would be turned inside-out after some effect of the interactions.

As mentioned in the Introduction the setup for this ring trap also makes it possible to have multiple ring traps by utilizing the periodicity of the standing wave. Interferences between multiple rings could be obtained either by releasing the vertical confinement alone—and maintaining the rf shell—or by releasing both vertical and horizontal confinement to allow a full expansion of the degenerate gas. It would also make it possible to image vortices and phase fluctuations in a 2D ring (similarly to the imaging of sheets in Ref. [42]). In the same way the sudden loss of just the vertical confinement can create some interesting dynamics in the shell as the rings overlap.

In this trap the rf dressed-state trapping and the tight optical confinement can be adjusted independently of each other. Thus our ability to convert between a ring trap and a pancake trap (without the rf) allows a study of the interplay between persistent currents and vortices as the restricted geometry of the trap is changed, as well as an exploration of how superfluidity is connected to BEC, and other quantum gases [14], during such a geometric crossover.

Since this paper was submitted we have become aware of two other proposals for smaller ring traps [43,44] which utilize dressed-state rf trapping in different ways.

ACKNOWLEDGMENTS

We acknowledge fruitful discussions with Rudi Grimm. This work was supported by the Région Ile-de-France (Contract No. E1213) and by the European Community through

the Research Training Network "FASTNet" under Contract No. HPRN-CT-2002-00304 and Marie Curie Training Network "Atom Chips" under Contract No. MRTN-CT-2003-505032. Laboratoire de Physique des Lasers is UMR 7538 of CNRS and Paris 13 University. The LPL group is a member of the Institut Francilien de Recherche sur les Atomes Froids. B. M. Garraway is a visiting professor at Paris 13 University.

APPENDIX A: THOMAS-FERMI SOLUTION FOR THE RING TRAP IN 3D, 2D, AND 1D

In this section, we give a detailed calculation of the chemical potential in the Thomas-Fermi approximation for the ring trap in the harmonic approximation, depending on the dimension. Let us first consider the 3D case. The 3D density is related to the ring trapping potential (7) through

$$n_{3D}(\rho,z) = \frac{\mu_{3D} - \frac{1}{2}m\omega_\rho^2(\rho - r_0)^2 - \frac{1}{2}m\omega_z^2 z^2}{g_{3D}} \tag{A1}$$

in the region of space where this quantity is positive. This region is defined by $(\rho - r_0)^2/R_\rho^2 + z^2/R_z^2 < 1$, where R_ρ and R_z are related to μ_{3D} through $\mu_{3D} = \frac{1}{2}m\omega_\rho^2 R_\rho^2 = \frac{1}{2}m\omega_z^2 R_z^2$. Due to the trap rotational invariance, the atomic density does not depend on the polar angle θ. The chemical potential is given by normalization of the integrated density to the atom number:

$$N = 2\pi \int_{-R_z}^{R_z} dz \int_{r_0 - R_\rho\sqrt{1-z^2/R_z^2}}^{r_0 + R_\rho\sqrt{1-z^2/R_z^2}} \rho\, d\rho\, n_{3D}(\rho,z) \tag{A2}$$

or, after a substitution $u = (\rho - r_0)/R_\rho$, $v = z/R_z$

$$\frac{Ng_{3D}}{\mu_{3D}} = 2\pi r_0 R_z R_\rho \int_{-1}^{1} dv \int_{-\sqrt{1-v^2}}^{+\sqrt{1-v^2}} du \left(1 + \frac{R_\rho}{r_0}u\right)(1 - v^2 - u^2). \tag{A3}$$

The term in R_ρ/r_0 cancels after integration over u because of parity, while the leading term is doubled. After integration, one finds

$$Ng_{3D} = \pi^2 r_0 R_\rho R_z \mu_{3D}. \tag{A4}$$

It leads to the following expression for the chemical potential for a degenerate cloud confined in the ring in the 3D regime:

$$\mu_{3D} = \hbar\,\bar{\omega}\sqrt{\frac{2Na}{\pi r_0}}. \tag{A5}$$

Here, we have used the expressions for R_ρ and R_z given above, the 3D interaction coupling constant $g_{3D} = 4\pi\hbar^2 a/m$, and the geometric mean of the oscillation frequencies $\bar{\omega} = \sqrt{\omega_\rho \omega_z}$.

If now the vertical degree of freedom is frozen, the gas enters the 2D regime. The condensate wave function is the product of the harmonic oscillator ground state along z, of size $l_z = \sqrt{\hbar/(m\omega_z)}$, and a 2D wave function in the plane, satisfying a 2D Thomas-Fermi equation. The expression for the chemical potential should be calculated from integration of the 2D density, deduced from this equation in the harmonic approximation:

$$n_{2D}(\rho) = \frac{\mu_{2D} - \frac{1}{2}m\omega_\rho^2(\rho - r_0)^2}{g_{2D}} \tag{A6}$$

for ρ such that this expression is positive. Here, the 2D coupling constant is given by $g_{2D} = g_{3D}/(\sqrt{2\pi} l_z) = 2\sqrt{2\pi}\hbar^2 a/(m l_z)$ [29]. Again, if R_ρ is such that $\mu_{2D} = \frac{1}{2}m\omega_\rho^2 R_\rho^2$, we can write

$$\frac{Ng_{2D}}{\mu_{2D}} = 2\pi r_0 R_\rho \int_{-1}^{1} du \left(1 + \frac{R_\rho}{r_0}u\right)(1 - u^2). \tag{A7}$$

Only the leading term contributes for parity reasons and we have $Ng_{2D} = \frac{8\pi}{3} r_0 R_\rho \mu_{2D}$. Using the relation between R_ρ and μ_{2D} and the expression of the interaction coupling constant, the expression for the chemical potential in the 2D regime reads

$$\mu_{2D} = \hbar\,\bar{\omega}\left(\frac{\omega_\rho}{\omega_z}\right)^{1/6}\left(\frac{3Na}{4\sqrt{\pi} r_0}\right)^{2/3}. \tag{A8}$$

For a 1D gas, both z and ρ degrees of freedom are frozen, with a respective size l_z and $l_\rho = \sqrt{\hbar/(m\omega_\rho)}$. The ground state has a uniform density along the ring $n_{1D} = N/(2\pi r_0)$, in the Thomas-Fermi approximation, and we have $g_{1D} n_{1D} = \mu_{1D}$. The interaction coupling constant is given by $g_{1D} = g_{3D}/(2\pi l_z l_\rho) = 2\hbar^2 a/(m l_z l_\rho)$ [29]. We obtain directly the chemical potential from this set of equations, as

$$\mu_{1D} = \hbar\,\bar{\omega}\frac{Na}{\pi r_0}. \tag{A9}$$

APPENDIX B: THOMAS-FERMI SOLUTION FOR THE TIGHT SHELL TRAP

Before the optical potential is applied in the loading process the trap potential is that of a dressed rf shell trap in the presence of gravity which results in the atoms collecting at the bottom of the shell. In order to estimate the capture efficiency when the optical potential is applied we utilize the density in the rf trap from the three-dimensional Thomas-Fermi solution. Thus positive densities satisfy $n(r,\theta) = [\mu - V(r,\theta)]/g_{3D}$ where $g_{3D} = 4\pi\hbar^2 a/m$. We then approximate the potential for the atoms, Eq. (3) with $U_0 = 0$, by

$$V(r,\theta) = \frac{1}{2}m\omega_{trans}^2(r - R)^2 + mgR(1 - \cos\theta). \tag{B1}$$

This potential assumes a tight binding to a shell with a local radius of curvature R. For the ellipsoid geometry of Sec. II this means $R = 4z_0 = 2r_0$. The shell binding frequency ω_{trans} also has the value local to the bottom of the shell and is assumed independent of radial distance r and angle θ. This independence is not strictly true because the effective rf amplitude and field gradient vary with angle. For a given effective rf amplitude, and for the ellipsoidal geometry of Sec. II the frequency ω_{trans} at the bottom of the trap is twice radial rf

trapping frequency ω_ρ in the ring [Eq. (5)]. The gravitational sag of the shell is also neglected, and varies with position, but this is expected to be small for realistic parameters.

To find the chemical potential we may use a 3D harmonic approximation since the shell approximation is already a radial harmonic potential and the maximum value for θ, for parameters given, is 0.07 rad, allowing the angular part to be harmonic, too. The angular frequency $\omega_{1,2}$ is the same as the pendulum frequency, i.e., $\omega_{1,2}=\sqrt{g/R}=\sqrt{g/(4z_0)}$. Thus we may use the standard 3D harmonic result [45]

$$\mu=\frac{\hbar\tilde{\omega}}{2}\left(\frac{15Na}{a_0}\right)^{2/5}, \tag{B2}$$

with the geometric mean of the oscillation frequencies $\tilde{\omega}=(\omega_{trans}g/R)^{1/3}$, and $a_0=\sqrt{\hbar/m\tilde{\omega}}$. The chemical potential found from all the approximations given above agrees well with a numerical integration and is used, with the Thomas-Fermi solution, to estimate the number of atoms loaded into the optical potential.

[1] D. S. Petrov, G. V. Shlyapnikov, and J. T. M. Walraven, Phys. Rev. Lett. **85**, 3745 (2000); D. S. Petrov, G. V. Shlyapnikov, and J. T. M. Walraven, *ibid.* **87**, 050404 (2001).

[2] A. Görlitz, J. M. Vogels, A. E. Leanhardt, C. Raman, T. L. Gustavson, J. R. Abo-Shaeer, A. P. Chikkatur, S. Gupta, S. Inouye, T. Rosenband, and W. Ketterle, Phys. Rev. Lett. **87**, 130402 (2001).

[3] S. Dettmer, D. Hellweg, P. Ryytty, J. J. Arlt, W. Ertmer, K. Sengstock, D. S. Petrov, G. V. Shlyapnikov, H. Kreutzmann, L. Santos, and M. Lewenstein, Phys. Rev. Lett. **87**, 160406 (2001).

[4] S. Richard, F. Gerbier, J. H. Thywissen, M. Hugbart, P. Bouyer, and A. Aspect, Phys. Rev. Lett. **91**, 010405 (2003).

[5] I. Shvarchuck, Ch. Buggle, D. S. Petrov, K. Dieckmann, M. Zielonkowski, M. Kemmann, T. Tiecke, W. von Klitzing, G. V. Shlyapnikov, and J. T. M. Walraven, Phys. Rev. Lett. **89**, 270404 (2002).

[6] H. Moritz, T. Stöferle, M. Köhl, and T. Esslinger, Phys. Rev. Lett. **91**, 250402 (2003).

[7] B. L. Tolra, K. M. O'Hara, J. H. Huckans, W. D. Phillips, S. L. Rolston, and J. V. Porto, Phys. Rev. Lett. **92**, 190401 (2004).

[8] B. Paredes, A. Widera, V. Murg, O. Mandel, S. Fölling, I. Cirac, G. V. Shlyapnikov, T. W. Hänsch, and I. Bloch, Nature (London) **429**, 277 (2004).

[9] J. A. Sauer, M. D. Barrett, and M. S. Chapman, Phys. Rev. Lett. **87**, 270401 (2001).

[10] A. S. Arnold and E. Riis, J. Mod. Opt. **49**, 959 (2002); A. S. Arnold, J. Phys. B **37**, L29 (2004).

[11] S. Wu, W. Rooijakkers, P. Striehl, and M. Prentiss, Phys. Rev. A **70**, 013409 (2004).

[12] S. Gupta, K. W. Murch, K. L. Moore, T. P. Purdy, and D. M. Stamper-Kurn, Phys. Rev. Lett. **95**, 143201 (2005).

[13] A. S. Arnold, C. S. Garvie, and E. Riis, Phys. Rev. A **73**, 041606 (2006).

[14] F. Bloch, Phys. Rev. A **7**, 2187 (1973); and see G. M. Kavoulakis, Y. Yu, M. Ögren, and S. M. Reimann, e-print cond-mat/0510315, and references therein.

[15] E. M. Wright, J. Arlt, and K. Dholakia, Phys. Rev. A **63**, 013608 (2000).

[16] A. Hopkins, B. Lev, and H. Mabuchi, Phys. Rev. A **70**, 053616 (2004).

[17] O. Zobay and B. M. Garraway, Phys. Rev. Lett. **86**, 1195 (2001).

[18] O. Zobay and B. M. Garraway, Phys. Rev. A **69**, 023605 (2004).

[19] This expression for Ω is valid if the $B_{\rm rf}$ field is orthogonal to the local static magnetic field; if this is not the case, only its orthogonal component contributes to Ω. See, e.g., Yves Colombe, Ph.D. thesis, Université Paris 13, 2004.

[20] The principle of the circular trap is also valid with other kinds of magnetic traps, in particular Ioffe-Pritchard traps. Depending on the axis chosen for the standing wave, the trap may be elliptical instead of circular.

[21] Y. Colombe, E. Knyazchyan, O. Morizot, B. Mercier, V. Lorent, and H. Perrin, Europhys. Lett. **67**, 593 (2004).

[22] T. Schumm, S. Hofferberth, L. M. Andersson, S. Wildermuth, S. Groth, I. Bar-Joseph, J. Schmiedmayer, and P. Krüger, Nat. Phys. **1**, 57 (2005).

[23] A red detuned light would also be a possible choice. However, the photon scattering rate would be higher in this case.

[24] B. Paredes, P. Fedichev, J. I. Cirac, and P. Zoller, Phys. Rev. Lett. **87**, 010402 (2001).

[25] M. D. Girardeau, J. Math. Phys. **1**, 516 (1960).

[26] M. Hugbart, J. A. Retter, F. Gerbier, A. F. Varón, S. Richard, J. H. Thywissen, D. Clément, P. Bouyer, and A. Aspect, Eur. Phys. J. D **35**, 155 (2005).

[27] D. Hellweg, L. Cacciapuoti, M. Kottke, T. Schulte, K. Sengstock, W. Ertmer, and J. J. Arlt, Phys. Rev. Lett. **91**, 010406 (2003).

[28] We neglect here the radius variation, which would give a correction of order $R_\rho/r_0<10^{-2}$.

[29] See e.g., D. S. Petrov, D. M. Gangardt, and G. V. Shlyapnikov, in *Proceedings of Quantum Gases in Low Dimensions*, edited by L. Pricoupenko, H. Perrin, and M. Olshanii [J. Phys. IV **116**, 3 (2004), and references therein.] Note that the expression for g_{2D} on p. 11 should be corrected by a factor of $\sqrt{\pi}$ so that it reads $g=2\sqrt{2\pi}\hbar^2a/(ml_0)$.

[30] L. Tonks, Phys. Rev. **50**, 955 (1936); M. D. Girardeau, *ibid.* **139**, B500 (1965); M. Olshanii, Phys. Rev. Lett. **81**, 938 (1998).

[31] N. V. Vitanov and K.-A. Suominen, Phys. Rev. A **56**, R4377 (1997).

[32] A. M. Rey, Ph.D. thesis, University of Maryland, 2004.

[33] R. Grimm, M. Weidemüller, and Yu. B. Ovchinnikov, Adv. At., Mol., Opt. Phys. **42**, 95 (2000).

[34] Y. Colombe, D. Kadio, M. Olshanii, B. Mercier, V. Lorent, and H. Perrin, J. Opt. B: Quantum Semiclassical Opt. **5**, S155 (2003).

[35] K. W. Madison, F. Chevy, W. Wohlleben, and J. Dalibard, Phys. Rev. Lett. **84**, 806 (2000).

[36] J. Javanainen, S. M. Paik, and S. M. Yoo, Phys. Rev. A **58**, 580 (1998).
[37] L. Salasnich, A. Parola, and L. Reatto, Phys. Rev. A **59**, 2990 (1999).
[38] J. Brand and W. P. Reinhardt, J. Phys. B **34**, L113 (2001).
[39] J. Javanainen and Y. Zheng, Phys. Rev. A **63**, 063610 (2001).
[40] E. Nugent, D. McPeake, and J. F. McCann, Phys. Rev. A **68**, 063606 (2003).
[41] A. B. Bhattacherjee, E. Courtade, and E. Arimondo, J. Phys. B **37**, 4397 (2004).
[42] S. Stock, Z. Hadzibabic, B. Battelier, M. Cheneau, and J. Dalibard, Phys. Rev. Lett. **95**, 190403 (2005).
[43] I. Lesanovsky, T. Schumm, S. Hofferberth, L. M. Andersson, P. Krüger, and J. Schmiedmayer, Phys. Rev. A **73**, 033619 (2006).
[44] T. Fernholz, R. Gerritsma, P. Krüger, and R. J. C. Spreeuw, e-print physics/0512017.
[45] F. Dalfovo, S. Giorgini, L. P. Pitaevskii, and S. Stringari, Rev. Mod. Phys. **71**, 463 (1999).

Evaporative cooling in a radio-frequency trap

Carlos L. Garrido Alzar,[1,*] Hélène Perrin,[1] Barry M. Garraway,[2] and Vincent Lorent[1]
[1]*Laboratoire de Physique des Lasers, CNRS-Université Paris 13, Villetaneuse, France*
[2]*Department of Physics and Astronomy, University of Sussex, Brighton BN1 9QH, United Kingdom*
(Received 31 August 2006; published 17 November 2006)

A theoretical investigation for implementing a scheme of forced evaporative cooling in radio-frequency (rf) adiabatic potentials is presented. Supposing the atoms to be trapped in a combination of a dc magnetic field and a rf field at frequency ω_1, the cooling procedure is facilitated using a second rf source at frequency ω_2. This second rf field produces a controlled coupling between the spin states dressed by ω_1. The evaporation is then possible in a pulsed or continuous mode. In the pulsed case, atoms with a given energy are transferred into untrapped dressed states by abruptly switching off the ω_2 coupling. In the continuous case, it is possible for energetic atoms to adiabatically follow the doubly dressed states and escape out of the trap. Our results also show that when ω_1 and ω_2 are separated by at least the Rabi frequency associated with ω_1, additional evaporation zones appear which can make this process more efficient.

DOI: 10.1103/PhysRevA.74.053413 PACS number(s): 32.80.Pj, 39.25.+k

I. INTRODUCTION

In recent years, the investigation of quantum gases in low-dimensional trapping geometries has significantly attracted the attention of the physics research community. This growing interest is motivated, partially, by the current possibilities that the extremely rapid progress in integrated atom optics has opened for the manipulation of Bose-Einstein condensed (BEC) atoms. This development allows the study of crucial problems associated with the strong modifications that the fundamental properties of these quantum systems experience due to the reduced dimensionality. For instance, a one-dimensional (1D) Bose gas in the Tonks-Girardeau regime mimics a system of noninteracting spinless fermions [1–3]; in 2D, the superfluidity emerges due to the vortex binding-unbinding Berezinskii-Kosterlitz-Thouless phase transition [4,5], recently observed [6].

For the study of the BEC low-dimensional physics, trapping configurations of different nature and topology have been proposed and used. For example, the 3D to 1D crossover was explored by Görlitz *et al.* [7] in an elongated Ioffe-Pritchard type direct-current (dc) magnetic trap, the phase defects of a BEC were investigated in a quasi-2D trap based on a 1D optical lattice [8] and, in atom chip experiments, dc current-carrying wires are usually employed to confine atoms in highly anisotropic traps [9]. Although these trapping configurations have demonstrated their relevance for studying quantum gases in low dimensions, adiabatic potentials [10], resulting from a combination of dc and radio-frequency (rf) magnetic fields, are also becoming a very attractive and promising tool [11–16].

The rf traps share the versatility and flexibility of the above mentioned trapping schemes and, moreover, they are relatively easy to implement and control. In the first implementation of these traps [11], ultracold atoms were confined in a 2D geometry. A rf adiabatic potential has also been used as a beam splitter, allowing the demonstration of matter-wave interference on an atom chip [12]. Ring-shaped traps, and other more complex trapping geometries using adiabatic potentials have also been considered [13–16].

Given the topology of the rf trapping potential, and because of technical limitations in some cases, the loading of the trap with Bose-Einstein condensed atoms, preserving the quantum degeneracy, can be a challenging task. In this situation, it is of relevance to consider the possibility of evaporative cooling of atoms *directly* in these low-dimensional rf traps. This is the subject that will be addressed in this paper, taking into account the interaction of the atoms with two radio-frequency fields. When dealing with more than one rf frequency, an analytical solution for the atomic spin dynamics can be found by treating the individual successive interactions of the rf fields with the atoms [17] or by considering the two fields simultaneously, provided one of the fields is rather weak [18]. We will study how a weak second radio-frequency source can be used to perform an evaporation.

We will see that the forced evaporation of rf-trapped atoms can be accomplished in two ways. First, the spin evolution induced by this second rf source can be quenched by switching off the field, i.e., by using a pulsed rf source. Secondly, we can allow an adiabatic following of doubly dressed states which requires the second rf source to be continuous rather than pulsed. This last scheme is similar to the standard evaporative cooling method used in static magnetic traps [19–21].

This paper is organized as follows. In Sec. II we will discuss the geometry of the system and the singly dressed states of the rf trap. In Sec. III, the evolution of the system is determined in three different ways: numerically, using a first order Magnus series approximation, and by using a second rotating wave approximation which leads to a double dressing of the atoms by two rf fields. Section IV is devoted to the application of the results of Sec. III to the study of evaporative cooling in the rf trap. Finally, we give a summary and conclusion in Sec. V.

II. ADIABATIC POTENTIAL CONFINEMENT

The underlying idea of the confinement of ultracold atoms using rf adiabatic potentials is presented in detail in Refs. [10,15], Ref. [11] being a report on the experimental inves-

*Electronic address: leonardo@galilee.univ-paris13.fr

tigation of such a trapping scheme. For this reason, instead of discussing how this trapping actually takes place in depth, we will rather make use of the already known results that are relevant in order to consider the problem of evaporative cooling in these traps.

The treatment presented in this paper is valid for any value of the spin F. However, for concreteness the numerical results will be given for ^{87}Rb in the Zeeman state $m=+2$ of the $5S_{1/2}$, $F=2$ hyperfine ground state level. We will suppose that the atoms are confined in a QUIC magnetic trap [22,23] produced by a dc magnetic field $\mathbf{B}_{\mathrm{dc}}(\mathbf{r})$. The atomic clouds trapped in this configuration are anisotropic (cigar-shaped along x) and we will take the offset magnetic field produced by the Ioffe coil [22] to be oriented along the x direction. In the following, the axes in the lab frame will be labeled by lower case letters xyz. The z axis is in the vertical direction and y is the horizontal direction perpendicular to the cigar axis. The axes in the local frame attached to the dc magnetic field will be labeled by capital letters XYZ. Moreover, we will assume that the direction of the dc magnetic field defines the local Z quantization axis. The Larmor frequency of the atomic spin precession in this dc field will be denoted $\omega_0(\mathbf{r})=g_F\mu_B B_{\mathrm{dc}}(\mathbf{r})/\hbar$. Here, g_F and μ_B are the Landé factor and the Bohr magneton, respectively.

Now, we apply to this confined atomic system two rf fields (produced by antennae), both of them polarized along y and of angular frequencies ω_1 and ω_2. The respective Rabi frequencies Ω_1 and Ω_2 define the coupling along the X direction. In principle the resulting rf coupling now depends on position due to the spatially varying orientation of the dc magnetic field. However, we will neglect this variation in the rest of the paper. This approximation of uniform Ω_1 and Ω_2 does not invalidate the obtained results, as the spin dynamics can be treated locally. In principle, the results can be generalized by parametrically introducing the spatial dependence of the coupling throughout the analysis. Having in mind that the second rf field will be rather weaker than the first one, we transform into the frame rotating at ω_1 and perform the rotating wave approximation (RWA). The Hamiltonian that describes the spin dynamics can thus be written as (see the derivation in the Appendix)

$$H(\mathbf{r},t) = H_A(\mathbf{r}) + \Omega_2[F_X\cos(\Delta t) + F_Y\sin(\Delta t)], \qquad (1)$$

where $F_X(F_Y)$ is the atomic angular momentum in the $X(Y)$ direction, $\Delta=\omega_2-\omega_1$, $H_A(\mathbf{r})=\Omega(\mathbf{r})F_\theta$ is the adiabatic Hamiltonian associated with the rf confinement, and $\Omega(\mathbf{r}) \equiv \sqrt{\delta(\mathbf{r})^2+\Omega_1^2}$ defines the energy separation between the adiabatic levels. In the absence of Ω_2, the flip angle θ and the detuning $\delta(\mathbf{r})$ are given by $\tan(\theta)\equiv-\Omega_1/\delta(\mathbf{r})$, with $\theta \in [0,\pi]$ and $\delta(\mathbf{r})=\omega_1-\omega_0(\mathbf{r})$, respectively. We have considered that the component F_Z of the atomic angular momentum is aligned with the local Z component of the dc magnetic field vector. Strictly, these Rabi frequencies are not spatially homogeneous as mentioned above. However, they can be treated as such over the spatial extension of the atomic cloud [11].

Graphically, the spin evolution given by Eq. (1), in the case $\Omega_2=0$, is represented in Fig. 1. It can be seen in this figure that the tilted angular momentum F_θ results from a rotation of F_Z around F_Y and is given by

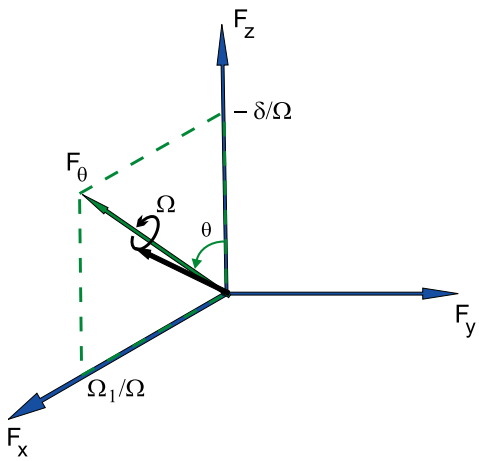

FIG. 1. (Color online) At a given location $\mathbf{r}$, δ and Ω_1 define the angle θ by which F_Z is rotated. The spin (black arrow) therefore precesses around an axis given by F_θ (green arrow) at a frequency Ω.

$$F_\theta = \cos(\theta)F_Z + \sin(\theta)F_X = \mathcal{R}_Y(\theta)F_Z\mathcal{R}_Y^\dagger(\theta), \qquad (2)$$

where the rotation matrix $\mathcal{R}_Y(\theta)=\exp(-i\theta F_Y/\hbar)$ can be expressed in the basis $\{-2,\ldots,+2\}$ of the bare states.

In Fig. 2(a), the energies of the bare states are plotted as a function of the position z, where the energy variation is due to the dc magnetic field $\mathbf{B}_{\mathrm{dc}}(\mathbf{r})$. This spatial dependence has been calculated for a value $x=x_{\min}=6.9$ mm corresponding to the position where the QUIC magnetic field is minimal in our experimental setup [11]. Moreover, we have taken $y=0$ and a Rabi frequency $\Omega_1/2\pi=400$ kHz. The arrows shown in that figure, in blue for ω_1 and in red for ω_2 (each frequency stands to the right of its respective arrows), indicate the locations where the corresponding rf fields resonantly couple the states in the laboratory frame. On the other hand, the spatial z dependence of the adiabatic states internal energies is shown in Fig. 2(b) where the states are labeled, from top to bottom: $|+2_A\rangle$, $|+1_A\rangle$, $|0_A\rangle$, $|-1_A\rangle$, and $|-2_A\rangle$. We can also see in this last figure the avoided level crossings at the positions where ω_1 (taken equal to $2\pi\times3.19$ MHz in this

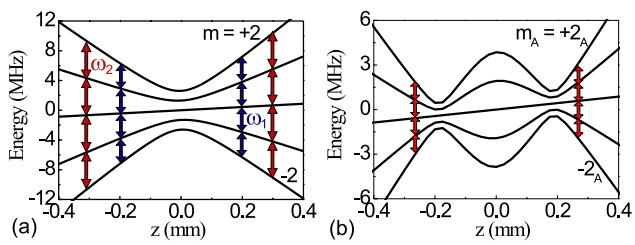

FIG. 2. (Color online) Spatial z dependence of the energy of the uncoupled (a) and dressed (b) states for $x=x_{\min}$ and $y=0$. At the avoided level crossings, the energy splitting between the levels is Ω_1. Gravity has been taken into account in both cases and $\omega_2 > \omega_1$.

example and from now on) resonantly couples the bare states.

In order to consider only the confinement ($\Omega_2=0$) using the adiabatic potentials shown in Fig. 2(b), let's suppose that initially we have a $m=+2$ spin polarized ultracold atomic sample. In this situation, the trapping potential corresponding to the bare state $|+2\rangle$ can be adiabatically deformed into the one associated with the dressed state $|+2_A\rangle$. Such a transformation can be performed by changing the detuning $\delta(\mathbf{r})$ from red to blue at constant Rabi frequency Ω_1 [10,11] or, by increasing Ω_1 at a constant red detuning [12]. Here, by adiabatic deformation we mean that the angular precession frequency $\Omega(\mathbf{r})$ of the spin in Fig. 1 must be much larger than the rate at which the angle θ changes [$|\dot{\theta}| \ll \Omega(\mathbf{r})$]. Using the loading schemes just mentioned, it is possible to obtain highly anisotropic rf traps with trapping frequencies, in the strongest confinement direction, ranging from several hundreds of Hz up to a few kHz.

Having described the main properties of the adiabatic confinement, let us now address the following issues. Assuming intuitively the existence of the resonances represented by the arrows in Fig. 2(b), we would like to know precisely where they are located and how strong they are. Another relevant point to be taken into account concerns the effect of these resonances at the rf trap center when, numerically, ω_1 and ω_2 are close to each other. Moreover, it will be interesting to find out the different parameter values for which the second rf field induces transitions between the adiabatic states, in the perturbative limit with $\Omega_2 \ll \Omega_1$, leading to a possible implementation of evaporative cooling in rf traps.

III. DYNAMICS OF THE SYSTEM

In this section we will study the dynamics of the system using three different methods. In the first case, the exact numerical solution of the time-dependent Schrödinger equation (TDSE) will be found. Secondly, an approximated analytical treatment will be presented (Magnus approximation) in order to interprete the exact results derived numerically. Finally, we will present an analytic solution based on a second rotating wave approximation which will be the basis of the analysis presented in Sec. IV. Since the evolution of the atomic external and internal degrees of freedom takes place on very different time scales, here we will decouple the two dynamics and consider only the time evolution of the internal degrees of freedom.

A. Numerical solution

The evolution of the state vector $|\Psi(t)\rangle$ with the Hamiltonian (1) was solved numerically, in the interaction picture, using a fourth order Runge-Kutta algorithm. In this case, the state vector can be very efficiently propagated in time [24] and we checked the accuracy by monitoring the normalization of the state vector and varying the time step. The first question we would like to address here is supposing that an atom is initially in the trapped dressed state $|+2_A\rangle$, what is the probability $P_{2A}=|\langle 2_A|\Psi(\mathbf{r},t)\rangle|^2$ of finding it in that *same* state as time goes by? We will also be interested in how this

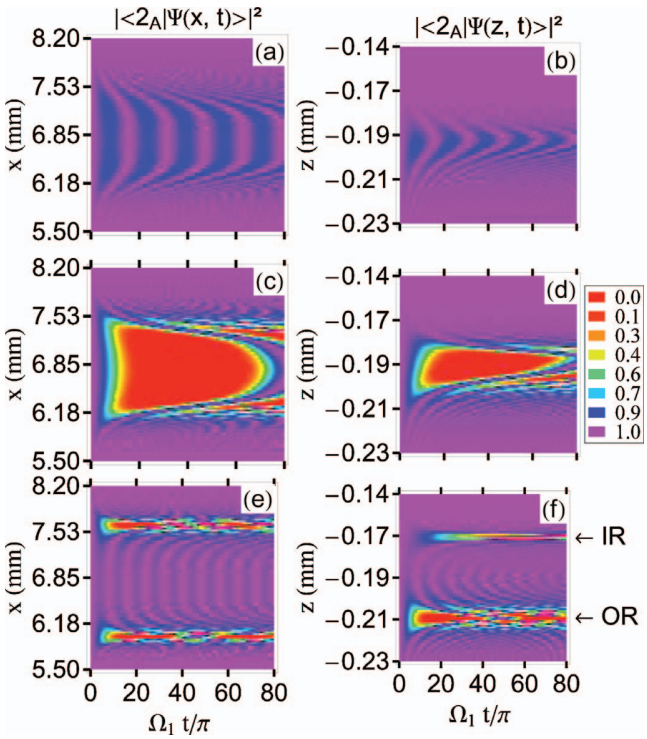

FIG. 3. (Color online) Probability for an atom to remain in the initial rf trapped state $|+2_A\rangle$. The values of Δ are, respectively, $0.875\Omega_1$ in (a) and (b), Ω_1 in (c) and (d), and $1.25\Omega_1$ in (e) and (f). The rf trap frequency $\omega_1/2\pi$ is set to 3.19 MHz. The x-t (z-t) dependence of P_{2A} is calculated at $z_{\min}=-0.19$ mm ($x_{\min}=6.9$ mm). In (f) the labels OR and IR indicate the locations of the outer and inner resonances, respectively.

probability changes for an atom located in different places in the trap. The preliminary answer to these questions is presented in Fig. 3, where the probability we are interested in is plotted for three different values of Δ, the difference between the radio frequencies ω_2 and ω_1.

In Fig. 3, and from now on, we use Ω_1 as a frequency unit, having in mind to keep it constant in a given experimental situation. The value of Ω_2 has been taken equal to $0.05\Omega_1$, small enough in order to be in the perturbative limit, as will be shown later. This value of Ω_2 will be used in all the following results unless a different one is explicitly stated. In the left column of Fig. 3, the x and time dependence of P_{2A} are calculated at the points $y=0$ and $z_{\min} \approx -0.19$ mm, with this value of z corresponding to the location of the left avoided level crossing in Fig. 2(b). To obtain the right column of Fig. 3, we use for x the value $x_{\min} \approx 6.9$ mm, very close to the location where the QUIC trap has its minimum in the x direction.

In Fig. 3 the three values of Δ have been chosen to illustrate some key characteristics of the spin dynamics. As the energy separation between the adiabatic levels at the avoided level crossings is exactly Ω_1, we observe resonant behavior at the rf trap bottom for $\omega_2=\omega_1+\Omega_1$, i.e., when $\Delta=\Omega_1$ [see Figs. 3(c) and 3(d)]. Similarly, for $\Delta<\Omega_1$ we have a red-detuned interaction everywhere [Figs. 3(a) and 3(b)]. In this case we observe weak modulations of P_{2A} that are essentially

determined by a beating between the Δ and $\Omega(\mathbf{r})$ frequency components. For $\Delta > \Omega_1$ [Fig. 3(e) and 3(f)] we have a blue-detuned interaction around the minima $x_{\min}$ and $z_{\min}$. Away from the center a resonance occurs, as expected, at approximately the location in the trap where ω_2 resonantly couples the bare states [see Fig. 2(a)]. This is the outer resonance labeled OR in Fig. 3(f). However, there is another feature we would like to stress. Namely, the presence of the inner resonance IR clearly seen in the z dependence of P_{2A} in Fig. 3(f). Note that the avoided level crossing (rf trap center) is at $z_{\min}$. Looking back to Fig. 2(a) and having in mind that $\omega_2 > \omega_1$, the existence of this second resonance IR in Fig. 3(f) at $z > z_{\min}$ may be counterintuitive, at least in the undressed picture. As we will see, its relative strength is fully determined by the rotation angle θ. Note that because of the loose confinement in the x direction [11], the dynamics in the y-z plane does not change much from one location to another in the x axis. However, this dynamics is very sensitive to changes in z (or y) and therefore, the results for the x dependence of the probability P_{2A} in Figs. 3(a), 3(c), and 3(e) can be significantly different when another z location is considered.

B. Interpreting the numerical results using a first order Magnus series approximation

Searching for the understanding of the physical picture behind the numerical results presented in Fig. 3, let us consider the first order Magnus series approximation [25,26] to the solution of the TDSE. This approximation is basically the formal solution of the TDSE neglecting the two-time commutators of the Hamiltonian. This Hamiltonian is given in the interaction picture by

$$H'(t) = \exp(i\Omega t F_\theta/\hbar) H(t) \exp(-i\Omega t F_\theta/\hbar). \tag{3}$$

In Eq. (3), we have dropped the $\mathbf{r}$ dependence in Ω and F_θ for the sake of notational simplification. Noting Fig. 1 and introducing $F_{\perp\theta} = \mathcal{R}_Y(\theta) F_X \mathcal{R}_Y^\dagger(\theta) = \cos(\theta) F_X - \sin(\theta) F_Z$ (see Fig. 6), which is the angular momentum vector perpendicular to F_θ and F_Y, we find

$$\begin{aligned} H'(t) = \Omega_2 \{ & \sin(\theta)\cos(\Delta t) F_\theta \\ & + [\sin(\Delta t)\sin(\Omega t) + \cos(\theta)\cos(\Delta t)\cos(\Omega t)] F_{\perp\theta} \\ & + [\sin(\Delta t)\cos(\Omega t) - \cos(\theta)\cos(\Delta t)\sin(\Omega t)] F_Y \}. \end{aligned} \tag{4}$$

In this case, the time evolution of a given initial dressed spin state $|\Psi(0)\rangle$ is represented by the rotation

$$|\Psi(t)\rangle = \exp[-i\Xi(t)\cdot\mathbf{F}/\hbar] |\Psi(0)\rangle, \tag{5}$$

where the scalar product $\Xi(t)\cdot\mathbf{F}$ stands for $\Xi_\theta(t) F_\theta + \Xi_{\perp\theta}(t) F_{\perp\theta} + \Xi_Y(t) F_Y$, where $\Xi_\theta(t)$, $\Xi_{\perp\theta}(t)$, and $\Xi_Y(t)$ are a measure of the projections of the spin $|\Psi(t)\rangle$ precession axis onto the axes F_θ, $F_{\perp\theta}$, and F_Y, respectively (for simplicity we will just call them projections). Taking into account Eq. (4), the definition of the exponential argument in Eq. (5) is

$$\Xi(t)\cdot\mathbf{F} = \int_0^t dt' H'(t'), \tag{6}$$

leading to the following expressions for the projections:

$$\Xi_\theta(t) = \frac{\Omega_2}{\Delta} \sin(\theta)\sin(\Delta t), \tag{7}$$

$$\Xi_{\perp\theta}(t) = \Omega_2 \left\{ \cos^2(\theta/2) \frac{\sin[(\Delta-\Omega)t]}{\Delta-\Omega} - \sin^2(\theta/2) \frac{\sin[(\Delta+\Omega)t]}{\Delta+\Omega} \right\}, \tag{8}$$

$$\Xi_Y(t) = 2\Omega_2 \left\{ \cos^2(\theta/2) \frac{\sin^2[(\Delta-\Omega)t/2]}{\Delta-\Omega} + \sin^2(\theta/2) \frac{\sin^2[(\Delta+\Omega)t/2]}{\Delta+\Omega} \right\}. \tag{9}$$

By inspecting Eqs. (7)–(9), we can see the time-dependent terms resulting from a beating between frequency components at Δ and $\Omega(\mathbf{r})$. These beats are seen as the modulation (interference-like patterns) of P_{2A} observed in Fig. 3. In particular, we see in these equations that there will be some interesting behavior when $\Delta = \pm\Omega$. In either case the condition is realized by two values of θ: θ_0 and $\pi - \theta_0$ with $\theta_0 = \arcsin(\Omega_1/\Delta)$. If $\Delta \neq \pm\Omega$, the coefficients $\Xi_i(t)$ are oscillatory with finite amplitudes. However, when $\Delta = \Omega$ at $\theta = \theta_0$, for instance, $\Xi_{\perp\theta}(t)$ shows a linear tendency in time of the form $\Omega_2 \cos^2(\theta_0/2) t$ while the other two components are negligible. This suggests that the spin will essentially rotate at a frequency $\Omega_2 \cos^2(\theta_0/2)$ around the axis $F_{\perp\theta}$. Starting from an eigenstate of F_θ, as in Sec. III A, the spin will be completely flipped after a half period. This rotation corresponds to the outer resonance OR in Fig. 3(f). At the location $\theta = \pi - \theta_0$, the same resonant behavior occurs with a rotation frequency $\Omega_2 \sin^2(\theta_0/2)$. This corresponds to the inner resonance IR in Fig. 3(f). In the case when ω_2 is smaller than ω_1, we have the resonant condition $\Delta = -\Omega$ and we have the same behavior except that the character of the inner and outer resonances is now reversed.

Away from the resonant conditions just described the analysis of Eqs. (7)–(9) is more complicated and consequently we evaluate these equations numerically. Some results for the time evolution of the populations of the adiabatic states $|0_A\rangle$ and $|2_A\rangle$ are given in Fig. 4. We show both Magnus approximation (dashed lines) and the exact numerical solution (circles) for comparison. As can be seen, if we constrain the dressed spin dynamics to half of the first period, we obtain a very good agreement between the first order Magnus series and the exact numerical results. After this time we see dephasing between the two evolutions and, even more dramatic, an important disagreement in the amplitude of the observed oscillations. These two behaviors are somehow expected because at time instants very far from $t=0$ the contribution of the next order terms in the Magnus series becomes more relevant [26]. In Sec. III C we can find a better approximation (using a second RWA) to the numerical solution which is shown in Fig. 4 with solid lines.

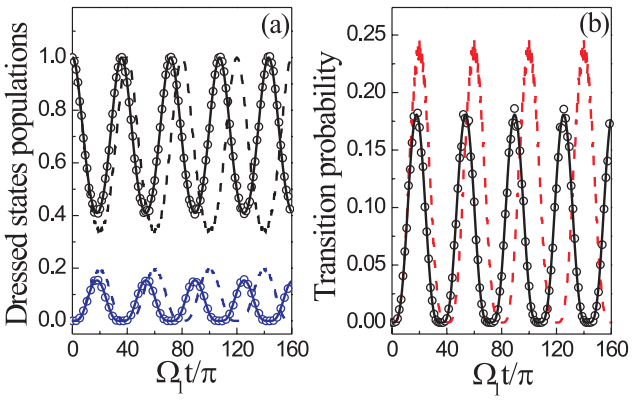

FIG. 4. (Color online) Occupation probability of the dressed states $|2_A\rangle$ (black upper traces) and $|0_A\rangle$ (blue lower traces) (a). In (b) the probability for an atom to be in the untrapped dressed states is shown. The circles show exact numerical results (Sec. III A), the dashed lines from the Magnus approximation (Sec. III B), and the solid lines from the second RWA (Sec. III C). The calculation has been done at the rf trap bottom $(x_{\min},0,z_{\min})$ for $\Delta=1.05\Omega_1$ and $\Omega_2=0.05\Omega_1$.

Another test for the validity range of the first order Magnus series approximation is presented in Fig. 5, where the population of the dressed state $|2_A\rangle$ and the probability of leaving the rf trap are shown. In this figure the results of the numerical treatment and those from the Magnus series are represented by the points and the solid lines, respectively. To obtain the results in Fig. 5, the initial adiabatic spin state has evolved during a time interval approximately equal to one half of the first oscillation period observed in Fig. 4, in short, up to $\Omega_1 t=20\pi$ that is $t=\pi/\Omega_2$. In addition to the good agreement that both methods show in the regions of less interest for us, we can notice the four resonances in the z dependence. The inner peaks are rather smaller than the outer ones, indicating that we have a position-dependent resonant coupling.

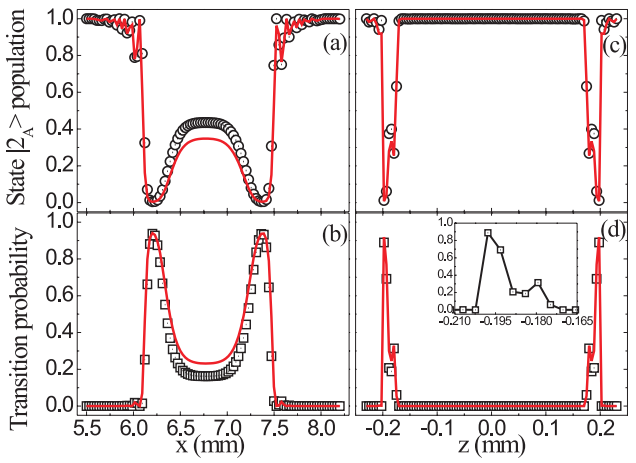

FIG. 5. (Color online) Population of the dressed state $|2_A\rangle$ versus position in the x (a) and z (c) directions at $\Omega_1 t=20\pi$. The probability for an atom to be in the untrapped dressed states is shown in (b) for the x and in (d) for the z spatial dependence (solid line: Magnus solution, circles and squares: numerical solution). As before, $\Delta=1.05\Omega_1$ and $\Omega_2=0.05\Omega_1$. The inset shows a zoom of the resonances around the avoided level crossing at $z_{\min}\approx-0.19$ mm. The solid line in the inset is just to guide the eyes.

C. Effective Hamiltonian from a second rotating wave approximation

The first order Magnus approximation predicts well the location of the resonances and their spin rotation frequency. However, it fails to describe correctly the dynamics away from the resonance points $\Delta=\pm\Omega$. To tackle this problem, we used a different approach and derived more generally applicable analytical expressions. The approach is based on a second rotating wave approximation, performed on Eq. (1) and expressed through the rotation $\bar{H}(t)=\mathcal{R}_\Delta H(t)\mathcal{R}_\Delta^\dagger$, where $\mathcal{R}_\Delta=\exp(i\Delta t F_\theta/\hbar)$. This transformation leads to the time-dependent Hamiltonian $\bar{H}(t)$ given by

$$\bar{H}(t)=-[\Delta-\Omega-\Omega_2\sin(\theta)\cos(\Delta t)]F_\theta+\Omega_2[\cos(\theta)\cos^2(\Delta t)+\sin^2(\Delta t)]F_{\perp\theta}+\Omega_2[1-\cos(\theta)]\sin(\Delta t)\cos(\Delta t)F_Y, \tag{10}$$

where all the parameters appearing in it have already been introduced. We note that this equation is valid for any value of Δ, including those close to Ω_1, i.e., when ω_1 and ω_2 are not so different from each other. Now we apply a second rotating wave approximation, which is valid provided that the "detuning" $\Delta-\Omega$ and the maximum coupling Ω_2 are much less than the "carrier frequency" Δ. We finally obtain from Eq. (10) the effective Hamiltonian

$$\bar{H}_\Delta=-(\Delta-\Omega)F_\theta+\frac{\Omega_2}{2}[1+\cos(\theta)]F_{\perp\theta}. \tag{11}$$

This last equation provides a new compact and powerful description of the spin dynamics in the dressed trap in the presence of a second rf field. As an example we have shown in Fig. 4 the spin evolution (solid lines) predicted with the effective Hamiltonian which is in excellent agreement with the exact numerical calculations.

The form of the effective Hamiltonian (11) is completely equivalent to that of H_A in Eq. (A7). If we look, for instance, at the vectorial representation of the spin in the case of a single rf field (Fig. 1), then in the presence of the second rf field one gets the picture shown in Fig. 6, where now $F_{\theta\Delta}=\cos(\theta_\Delta)F_\theta+\sin(\theta_\Delta)F_{\perp\theta}$ plays a similar role as F_θ did before. The angle θ_Δ is then

$$\tan(\theta_\Delta)\equiv-\frac{\Omega_2[1+\cos(\theta)]}{2(\Delta-\Omega)},\quad \text{with } \theta_\Delta\in[0,\pi]. \tag{12}$$

We can view the resulting precession as a second dressing of the dressed spin states [18]. One can obtain the doubly dressed states by diagonalizing the Hamiltonian (11). The corresponding eigenenergies of these states are given by multiples of $\hbar\Omega_\Delta$ where clearly

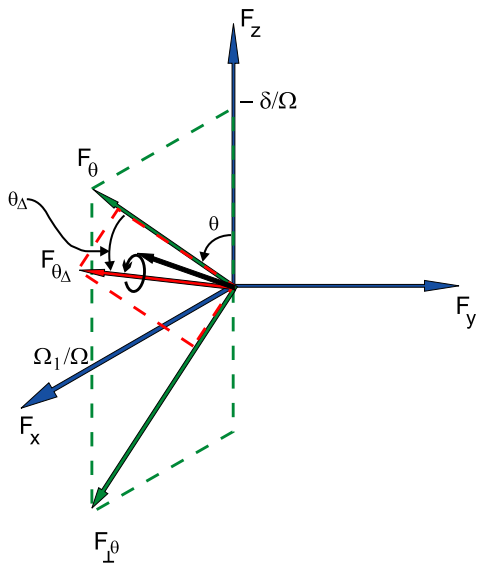

FIG. 6. (Color online) In the presence of the second rf field and applying a second RWA, the spin (black arrow) precesses around an axis obtained when first, ω_1 tilts F_Z by θ getting F_θ, and then ω_2 tilts F_θ by θ_Δ getting $F_{\theta\Delta}$.

$$\Omega_\Delta = \sqrt{(\Delta - \Omega)^2 + \frac{\Omega_2^2}{4}[1 + \cos(\theta)]^2}. \tag{13}$$

The spin oscillation frequency observed in Fig. 4 is precisely Ω_Δ. On resonance, the period of these Rabi oscillations induced by the coupling in Eq. (11) is then $T=4\pi/\Omega_2[1+\cos(\theta)]$ in agreement with the prediction of the Magnus approximation.

Looking at Fig. 6 we realize that $\theta_\Delta=\pi/2$ corresponds to resonant coupling with a maximum transition probability to a state orthogonal to the eigenstates of F_θ. This happens when $\Omega=\Delta$ [see Eq. (12)]. As in the Magnus case, this condition is realized by the two values $\theta_0=\arcsin(\Omega_1/\Delta)$ and $\pi-\theta_0$ with $\theta_0 \in [0,\pi/2]$. Recalling that when $\theta=\pi/2$ we are exactly at the avoided level crossings in Fig. 2(b), θ_0 indicates the location of the outer resonances OR while $\pi-\theta_0$ takes care of the inner ones IR.

IV. EVAPORATION

A. General remarks

In the following two subsections we will consider two schemes for implementing the evaporative cooling. First, we will look at a pulsed scheme in which a fraction of the atoms are spin flipped out of the trapped state by a sudden switch off of the second rf field. Then, secondly, we will examine a continuous scheme in which hot atoms are removed from the rf trap by adiabatically following a doubly dressed state. In both these schemes the hot atoms that are going to be removed have to reach the resonances at θ_0 or $\pi-\theta_0$. If we can neglect the gravitational potential, the energy of these atoms should be larger than about $F\hbar(\Delta-\Omega_1)$ with respect to the bottom of the dressed rf trap. This approximation, valid for relatively small Ω_2, can be refined using Eq. (13) and taking gravity into account. As an example, for our typical experimental setup [11] and $\Omega_2=0.05\Omega_1$, this energy is equivalent to temperatures of 0.21, 6.1, and 11 μK for Δ equal to $1.05\Omega_1$, $1.25\Omega_1$, and $1.4\Omega_1$, respectively.

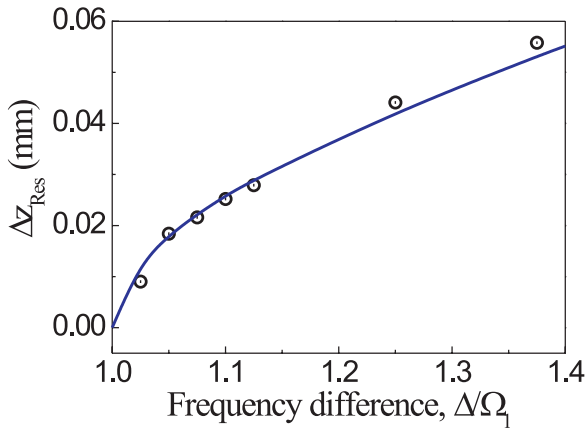

FIG. 7. (Color online) Distance between neighboring inner and outer resonances around an avoided level crossing. The circles are from the numerical calculation and the solid line is obtained using Eq. (14) with $b'=203$ G/cm. The points were obtained at $t=\pi/\Omega_2$ by measuring the distance between the resonances as seen in the inset of Fig. 5(d).

These limiting energies imply, of course, that the atom cloud will have a finite size determined by the location of the inner and outer resonances. In Fig. 7 we investigate the distance $\Delta z_{\rm res}$ between the neighboring inner and outer resonances as a function of Δ. As expected, the distance between the resonances goes to zero when Δ is reduced. In fact, since $\Omega_2 \ll \Delta$, and if we assume a constant magnetic field gradient b', we can derive the approximate form of $\Delta z_{\rm res}$ from $\Delta=\Omega$ as

$$\Delta z_{\rm res} = 2\frac{\sqrt{\Delta^2 - \Omega_1^2}}{\alpha}, \tag{14}$$

where $\alpha=g_F\mu_B b'/\hbar$.

The last point we would like to consider here concerns the inner resonance observed in the z direction. One positive aspect about this resonance is that when Δ is such that both the inner and outer resonances are close to the bottom of the dressed rf trap, the atomic cloud trapped in the adiabatic state $|2_A\rangle$ can be evaporated from both sides. However, the negative point is that some atoms are transferred by the inner resonance into the state $|-2_A\rangle$ and trapped around $z=0$. If these atoms come back to the region of the avoided level crossing, then they will be energetic enough that heating of the coldest atoms will take place via interatomic collisions. Note that for the rf dressed trap geometry discussed here gravity favors the evaporation through the outer resonance because a lower atomic energy is required than for the inner resonance.

B. Pulsed evaporative cooling

We first look at the pulsed evaporation scheme, which has as its main idea the extraction of hot atoms, in a controlled way, from the rf trap at the resonance locations. We can do

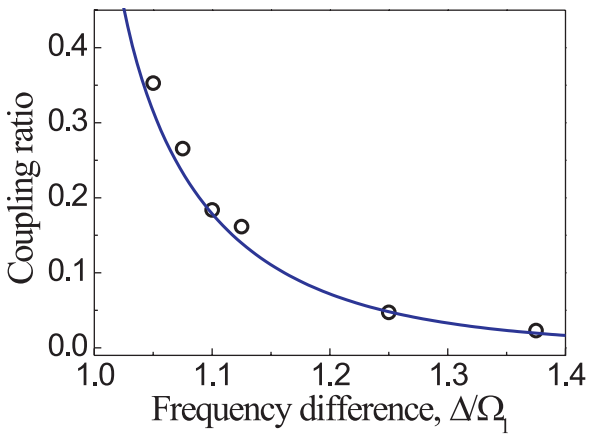

FIG. 8. (Color online) Ratio between the coupling strengths at the locations of the inner and outer resonances. The exact numerical solution is represented by the points whereas the solid line is derived from the second RWA with $\Delta=\Omega$. For Δ large compared to Ω_1, the coupling at the inner resonances goes to zero.

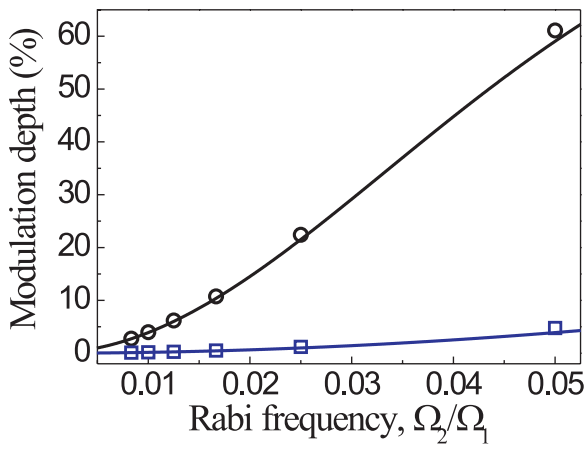

FIG. 9. (Color online) Modulation of the dressed state $|2_A\rangle$ population at the trap center for $\Delta=1.05\Omega_1$ (black open circles) and $1.25\Omega_1$ (blue open squares). The solid lines are calculated analytically from the second RWA treatment.

this because at these locations we have large transition probabilities between the rf dressed states as seen in Figs. 3(e) and 3(f). These transitions have been already analyzed, first, by using the Magnus approximation (Sec. III B) and, secondly, by using the second RWA (Sec. III C). They have also been interpreted with the vector picture in Fig. 6 as rotations about $F_{\theta\Delta}$. Hence we can see that if at a given time instant t the precession axis of $|\Psi(t)\rangle$ has zero projection onto F_θ, then this state vector will be orthogonal to the initial dressed rf state and consequently, a transition has taken place. Clearly, the second rf field can transfer hot atoms out of the initial trapped dressed state. The pulse has to be repeated several times during the trap oscillation period to ensure an efficient evaporation of all the atoms with sufficient energy to reach the resonances. The pulsed evaporative cooling scheme requires that we can discriminate between hot and cold atoms by affecting as little as possible the atoms in the region of the rf trap center. This implies a careful choice of the pulse duration and amplitude as will be discussed below.

We already noted that in some situations it may not be desirable to evaporate via the inner resonance (Sec. IV A). One way we can avoid this resonance in the pulsed scheme is to carefully chose the time duration of the pulse. For example, we can see in Fig. 3(f) that the depletion at the inner resonance (IR) takes place later compared to the outer resonance (OR). This happens because, independently of the orientation of the dc magnetic field, the coupling with the Rabi frequency Ω_2 in Eq. (11) is spatially inhomogeneous since θ depends on $\mathbf{r}$. To investigate this inhomogeneity for different values of Δ, we have chosen in Fig. 8 a particular value $t=\pi/\Omega_2$ and explore the ratio of the probability of being in the untrapped states at the two resonances. This is shown in the figure as a function of the frequency difference Δ. The second RWA can predict this relative effectiveness of the inner and outer resonances. From Eq. (11) this ratio can be determined analytically for $\Delta=\Omega$ and it is plotted in Fig. 8 with a solid line. The calculation of the numerical results in Fig. 8 is done as follows. For a given value of Δ a figure similar to Fig. 5(d) is plotted. Then, the ratio of the inner peak height to the outer peak height is found. This is the coupling strength ratio we are interested in. Since there is an excellent agreement between the exact solution and the solid line in Fig. 8, we can state that indeed the second RWA works well in the parameter range we have explored. Notice that for $\Delta \gg \Omega_1$ we recover the expected result that only the resonant coupling at the frequency ω_2 will occur between the bare states. For intermediate values of Δ, we can clearly see that the particular choice $t=\pi/\Omega_2$ for the pulse duration allows a good discrimination between the resonances IR and OR. In the final evaporation stage, where $\Delta \gtrsim \Omega_1$, if we wish to limit the IR excitation it is necessary to adapt the pulse duration.

As mentioned above we should avoid introducing transitions at the dressed rf trap centre. Because of such transitions we can see in Figs. 3(a), 3(b), 3(e), and 3(f) that, even when the detuning for coupling adiabatic states is red or blue ($\Delta<\Omega_1$ or $\Delta>\Omega_1$), the population of the initial trapped dressed state $|2_A\rangle$ is in fact modulated at the center of the rf trap (avoided level crossing). Such a modulation can produce unwanted losses and, to study this process, we introduce the modulation depth. This quantity is defined as the contrast of the oscillations presented in Fig. 4(a) as the black points (numerical result). In Fig. 9 we plot the modulation depth as a function of the Rabi frequency of the evaporation rf field, and for two different values of Δ. As expected, the modulation depth increases with Ω_2 since larger rf power is available for coupling the adiabatic states. Also not very surprising, this modulation is more pronounced when Δ is such that ω_2 couples adiabatic states close to the position of the avoided level crossing.

Taking into account the result presented in Fig. 9, we devised a strategy which affects as little as possible the coldest atoms, while doing the evaporation. The idea is to ramp Ω_2 and Δ simultaneously to preserve a fixed modulation depth at the rf trap center [27]. In Fig. 10 such a ramp is presented, where we have allowed for a 3% modulation level of the coldest atoms population. Note that the reduction of

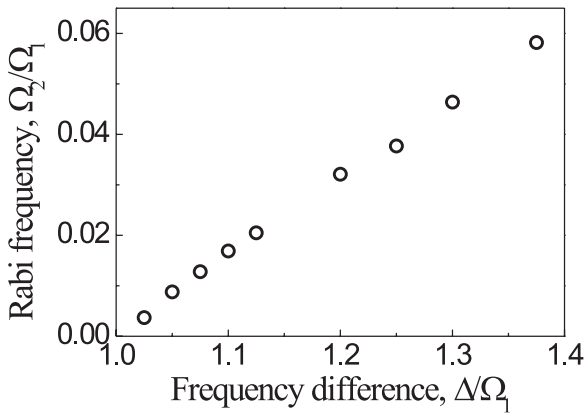

FIG. 10. Optimized Rabi frequency as a function of the frequency difference Δ. In this optimization, the population modulation at the rf trap center is limited to 3%.

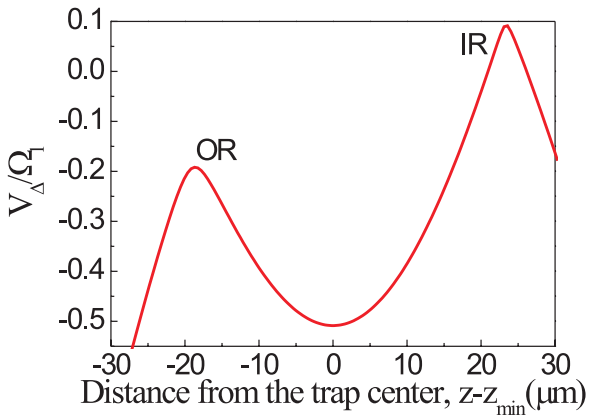

FIG. 11. (Color online) Doubly dressed potential V_Δ shown as a function of distance $z-z_{\min}$ from the dressed rf trap center at $z_{\min}$ for $\Omega_2=0.05\Omega_1$ and $\Delta=1.25\Omega_1$ as in Figs. 3(e) and 3(f). The potential is only shown in the region of the singly dressed rf resonance where $\delta=0$, with the associated inner and outer doubly dressed resonances indicated with IR and OR as in Fig. 3(f). Only the relevant, i.e., lowest, state is shown for $F=2$ and gravity was taken into account in this figure. The vertical unit corresponds to about 20 μK for the value of Ω_1 given in Sec. II.

Ω_2 has to be taken into account for the optimization of the pulse duration.

In fact, since Ω_2 and Δ can be controlled independently, we can make individual ramps for each one of these parameters and manipulate independently the position and strength of the evaporation resonances. Taking into account that there is a finite modulation of the atomic population at the rf trap center, even for Δ very different from Ω_1, we propose using a limited number of rf pulses to cool down the sample. For example, a pulsed evaporative cooling scheme has been developed demonstrating the achievement of the collisional regime in a beam of neutral atoms [28]. However, this pulsed scheme uses pulses longer than the trap oscillation period unlike the scheme proposed here.

C. Continuous evaporative cooling

Our second scheme for the evaporative cooling of atoms in the dressed rf trap uses the second rf field in a continuous rather than pulsed mode. This situation is closer to the normal case of the evaporation of atoms in a dc magnetic trap by a single rf field. Here, we simply use the second rf field as a tool to control the dressed rf trap depth. This trap depth corresponds to the energy required to reach the resonances (with respect to the dressed rf trap bottom) as considered in Sec. IV A.

In the usual case of continuous rf evaporation it is useful to look at the system using dressed states. In our situation, the equivalent relevant basis is given by doubly dressed states. As remarked earlier, these are found by diagonalizing $\bar{H}_\Delta$, Eq. (11), or we can write

$$\bar{H}_\Delta = \Omega_\Delta F_{\theta\Delta}, \tag{15}$$

with the frequency Ω_Δ as given in Eq. (13). This frequency determines the doubly dressed potential $\hbar\Omega_\Delta(\mathbf{r})$ which we would like the atoms to follow for the evaporation to proceed. If we include gravity the resulting potential $V_\Delta(\mathbf{r})$ is given by

$$V_\Delta(\mathbf{r}) = -F\hbar\Omega_\Delta(\mathbf{r}) + Mgz. \tag{16}$$

An example of this potential is given in Fig. 11 which shows the minimum at $z=z_{\min}$ (i.e., at $\theta=\pi/2$ or $\delta=0$), where the cold atoms will eventually collect, as well as the resonance regions IR and OR which form the "lips" of the doubly dressed trap over which the hotter atoms must pass. (During the usual evaporation process the "lips" are subsequently lowered by ramping the rf frequency and the same procedure can be carried out here with the second rf field.)

For this picture to be valid, we must have an adiabatic following of the vector $F_{\theta\Delta}$ as the atoms move about the trap. A general condition for this can be expressed as

$$\left|\frac{d\theta_\Delta}{dt}\right| \ll \Omega_\Delta, \tag{17}$$

where θ_Δ is given in Eq. (12) and the right-hand member of the inequality (17) is seen to be just the energy separation between the doubly dressed levels. In practice this condition is rather easily satisfied for a singly dressed rf trap (see, for example, Ref. [11]), which is relevant for the bottom of the doubly dressed trap as illustrated in Fig. 11. However, in order to also satisfy the adiabatic following condition (17) at the resonances, we will find a new constraint that Ω_2 should not be *too* small. The analysis of adiabaticity is conveniently carried out in terms of a Landau-Zener parameter Λ such that Eq. (17) implies that $\Lambda \gg 1$. To proceed, we use the definition (12) of θ_Δ in order to compute its time derivative assuming that only θ is time dependent. Calculating the time derivative and evaluating Eq. (17) at the outer resonance location θ_0, we find that in terms of the Landau-Zener parameter $\Lambda = \Omega_\Delta/|\dot{\theta}_\Delta|$ the adiabatic condition reads

$$\Lambda = \frac{\Omega_2^2[1+\cos(\theta_0)]^2}{4|\dot{\delta}_0|\cos(\theta_0)} \gg 1, \tag{18}$$

where $\dot{\delta}_0$ is the time derivative of the detuning $\delta(\mathbf{r})$ evaluated at θ_0, and is proportional to an atom velocity. From the ex-

pression for Λ we can see that as soon as Ω_2 is reduced, only the slow atoms will have their spin adiabatically following the axis $F_{\theta\Delta}$, and in fact, for motion linearized over the resonance, the multistate Landau-Zener analysis [20] shows that the probability for an atom to be lost from the adiabatic state in a single pass is $1-[1-\exp(-\pi\Lambda)]^{2F}$. For the parameters of Fig. 11, the energy of the atoms E (measured from the trap bottom in temperature units) would have to have a value of $E/k_B=20$ μK for the probability of a non-adiabatic crossing to reach about 10^{-5} for the OR.

It is clear that if we switch from the outer resonance OR (at $\theta=\theta_0$) to the IR (at $\theta=\pi-\theta_0$) the adiabaticity condition (18) will be different. This is connected to both the spatially dependent coupling $\Omega_2[1+\cos(\theta)]/2$, and the effect of gravity, which as seen in Fig. 11 make the IR "lip" higher. The weaker coupling at the inner resonance also means that the dynamics is less adiabatic at this point. In fact for fairly "hot" atoms one can contrive that the resonance OR is rather adiabatic while the resonance IR is rather diabatic. Together with the effect of gravity, this would mean that atoms can be evaporated out of the OR resonance while adiabatic coupling through the IR resonance is prevented. As explained in Sec. IV A this can be useful to partially prevent the return of evaporated atoms to the resonance regions with subsequent collisions and heating. However, we note that if we want to reduce the final temperature by steadily reducing Δ, the couplings at the two resonances become more equal (as in the pulsed scheme) and less discrimination between the two evaporation zones is possible.

V. CONCLUSIONS

We have seen that we can employ a doubly dressed basis [18] for the analysis of a dressed rf trap with two rf fields provided the second rf field is sufficiently weak. Using this arrangement of fields we can create a scheme for the evaporative cooling of atoms in a singly dressed rf trap in a continuous mode. In contrast with the traditional continuous forced evaporation scheme the idea of evaporative cooling based on the application of rf pulses with properly chosen durations and frequencies is also developed for a dressed rf trap. The duration of such pulses is essentially determined by the power of the rf field used for the evaporation, although the optimal pulse length changes from one location to another in the adiabatic trapping potential. When the trapping and evaporative cooling radio frequencies are comparable, we found that the evaporation also happens via additional resonances. Even if these resonances can enhance the evaporation process in both the pulsed and continuous schemes, we have to be careful that atoms evaporated through these resonances do not come back and heat the cold atomic cloud. In this respect, the advantage of the pulsed scheme is to provide an additional control of the transition probability at the inner resonance via the pulse duration. However, the effect of gravity is to favor the evaporation via the outer resonance OR which is then located at a position of lower energy. Although the importance of this effect may depend on the particular trapping geometry (pancake, ring traps), the evaporation schemes proposed in this paper are quite general and should allow an efficient cooling of atoms directly in the various rf traps which have been proposed or realized [11–16].

The main application of the work in this paper is to the evaporative cooling of atoms in a dressed trap. However, there are also applications concerning noise and stability of dressed rf traps where the carrier frequency ω_1 is not perfectly monochromatic. This can be due, for instance, to contamination by stray fields. Then it is clear that if the frequency components next to the carrier are in the range of, let us say, $\Delta=1.01\Omega_1-1.05\Omega_1$, they will empty the rf trap if they have enough power to do so or, in the best case, they will raise the temperature of the atoms. This means that if we look at the second rf source as a noise term (a sideband in the frequency spectrum), the results presented here can be used to estimate the damage it causes.

After submission of this work we became aware of an experimental paper using a second rf source in a dressed rf trap [29].

ACKNOWLEDGMENTS

We acknowledge the financial support of the Région Ile-de-France (Contract No. E1213). C.L.G.A. acknowledges support within Marie Curie program ("Atom Chips," Grant No. MRTN-CT-2003-505032). BMG thanks the University Paris 13. Laboratoire de Physique des Lasers is UMR 7538 of CNRS and University Paris 13. The LPL group is a member of the Institut Francilien de Recherche des Atomes Froids (IFRAF).

APPENDIX: DERIVATION OF $H(\mathbf{r},t)$

We will start the derivation of Eq. (1) by considering that the total magnetic field experienced by the atoms consists of three contributions or terms. One coming from the inhomogeneous dc magnetic field $\mathbf{B}_{\rm dc}(\mathbf{r})$ of the QUIC trap, a second term oscillating at the frequency ω_1, $\mathbf{B}_1(\mathbf{r},t)=B_{01}\mathbf{e}_1\cos(\omega_1 t)$, associated with the adiabatic trapping potential, and a third term of frequency ω_2, $\mathbf{B}_2(\mathbf{r},t)=B_{02}\mathbf{e}_2\cos(\omega_2 t)$, responsible for the evaporative cooling in the rf trap. Here, B_{01} and B_{02} are the amplitudes of the fields whereas $\mathbf{e}_1$ and $\mathbf{e}_2$ are unit polarization vectors. Using these definitions and denoting by $\mathbf{F}$ the atomic angular momentum operator, the total Hamiltonian of our physical system $H_T(\mathbf{r},t)$ can be approximated by

$$H_T(\mathbf{r},t)=g_F\mu_B\mathbf{F}\cdot[\mathbf{B}_{\rm dc}(\mathbf{r})+\mathbf{B}_1(\mathbf{r},t)+\mathbf{B}_2(\mathbf{r},t)]/\hbar, \quad \text{(A1)}$$

where g_F and μ_B are the Landé factor and the Bohr magneton, respectively. If we assume that at every point $\mathbf{r}$ the direction of the dc magnetic field defines the local Z quantization axis then, for X polarized rf fields, Eq. (A1) takes the form

$$H_T(\mathbf{r},t)=\omega_0(\mathbf{r})F_Z+V_1(\mathbf{r},t)+V_2(\mathbf{r},t). \quad \text{(A2)}$$

In Eq. (A2) $\omega_0(\mathbf{r})=g_F\mu_B B_{\rm dc}(\mathbf{r})/\hbar$ is the Larmor precession frequency. The interaction Hamiltonian $V_j(\mathbf{r},t)$ is defined by the expression

$$V_j(\mathbf{r},t)=\Omega_j(\mathbf{r})F_X(e^{i\omega_j t}+e^{-i\omega_j t}), \quad j=1,2 \quad \text{(A3)}$$

where $\Omega_j(\mathbf{r}) \equiv g_F \mu_B B_{0j}/(2\hbar)$ is the Rabi frequency.

Given $H_T(\mathbf{r},t)$, the dynamics of an atomic spin state $|\phi(\mathbf{r},t)\rangle$ is governed by the Schrödinger equation

$$i\hbar \frac{d|\phi(\mathbf{r},t)\rangle}{dt} = H_T(\mathbf{r},t)|\phi(\mathbf{r},t)\rangle, \tag{A4}$$

which in the frame rotating at the frequency ω_1, becomes

$$i\hbar \frac{d|\psi(\mathbf{r},t)\rangle}{dt} = [-\delta(\mathbf{r})F_Z + \mathcal{R}_1^\dagger V_1(t)\mathcal{R}_1 + \mathcal{R}_1^\dagger V_2(t)\mathcal{R}_1]|\psi(\mathbf{r},t)\rangle. \tag{A5}$$

In Eq. (A5) we have introduced the detuning $\delta(\mathbf{r}) = \omega_1 - \omega_0(\mathbf{r})$, the rotating frame operator $\mathcal{R}_1 = \exp(-i\omega_1 t F_Z/\hbar)$, and the rotated state $|\psi(\mathbf{r},t)\rangle = \mathcal{R}_1^\dagger|\phi(\mathbf{r},t)\rangle$. If we consider the bare state basis $\{|-2\rangle, |-1\rangle, |0\rangle, |+2\rangle, |+1\rangle\}$ of a spin-2 system, the matrix form of the rotated interaction Hamiltonians $\mathcal{R}_1^\dagger V_1(t)\mathcal{R}_1$ and $\mathcal{R}_1^\dagger V_2(t)\mathcal{R}_1$ are, respectively, given by

$$\Omega_1(\mathbf{r})\begin{pmatrix} 0 & 1 & 0 & 0 & 0 \\ 1 & 0 & \sqrt{\frac{3}{2}} & 0 & 0 \\ 0 & \sqrt{\frac{3}{2}} & 0 & \sqrt{\frac{3}{2}} & 0 \\ 0 & 0 & \sqrt{\frac{3}{2}} & 0 & 1 \\ 0 & 0 & 0 & 1 & 0 \end{pmatrix}$$

and

$$\Omega_2(\mathbf{r})\begin{pmatrix} 0 & e^{i\Delta t} & 0 & 0 & 0 \\ e^{-i\Delta t} & 0 & \sqrt{\frac{3}{2}}e^{i\Delta t} & 0 & 0 \\ 0 & \sqrt{\frac{3}{2}}e^{-i\Delta t} & 0 & \sqrt{\frac{3}{2}}e^{i\Delta t} & 0 \\ 0 & 0 & \sqrt{\frac{3}{2}}e^{-i\Delta t} & 0 & e^{i\Delta t} \\ 0 & 0 & 0 & e^{-i\Delta t} & 0 \end{pmatrix},$$

where $\Delta = \omega_2 - \omega_1$ and we have made use of the rotating wave approximation (RWA) by discarding the terms that oscillate at $2\omega_1$ and $\omega_1 + \omega_2$. In general, we find the dynamics of $|\psi(\mathbf{r},t)\rangle$ in Eq. (A5) to be described by the Hamiltonian

$$H(\mathbf{r},t) = H_A(\mathbf{r}) + \Omega_2[F_X \cos(\Delta t) + F_Y \sin(\Delta t)], \tag{A6}$$

where the adiabatic Hamiltonian $H_A(\mathbf{r})$ is defined as

$$H_A(\mathbf{r}) = -\delta(\mathbf{r})F_Z + \Omega_1 F_X. \tag{A7}$$

The time-independent Hamiltonian (A7) can be rewritten as $H_A(\mathbf{r}) = \Omega(\mathbf{r})F_\theta$ if we define $\Omega(\mathbf{r}) = \sqrt{\delta(\mathbf{r})^2 + \Omega_1^2}$, $\cos(\theta) = -\delta(\mathbf{r})/\Omega(\mathbf{r})$, $\sin(\theta) = \Omega_1/\Omega(\mathbf{r})$, and $F_\theta = \cos(\theta)F_Z + \sin(\theta)F_X$.

[1] L. Tonks, Phys. Rev. **50**, 955 (1936).
[2] M. Girardeau, J. Math. Phys. **1**, 516 (1960).
[3] B. Paredes *et al.*, Nature (London) **429**, 277 (2004).
[4] V. L. Berezinskii, Sov. Phys. JETP **32**, 493 (1971); **34**, 610 (1972).
[5] J. M. Kosterlitz and D. J. Thouless, J. Phys. C **6**, 1181 (1973).
[6] Z. Hadzibabic *et al.*, Nature (London) **441**, 1118 (2006).
[7] A. Görlitz *et al.*, Phys. Rev. Lett. **87**, 130402 (2001).
[8] S. Stock *et al.*, Phys. Rev. Lett. **95**, 190403 (2005).
[9] R. Folman *et al.*, Adv. At., Mol., Opt. Phys. **48**, 263 (2002).
[10] O. Zobay and B. M. Garraway, Phys. Rev. Lett. **86**, 1195 (2001); Phys. Rev. A **69**, 023605 (2004).
[11] Y. Colombe *et al.*, Europhys. Lett. **67**, 593 (2004).
[12] T. Schumm *et al.*, Nat. Phys. **1**, 57 (2005).
[13] O. Morizot *et al.*, Phys. Rev. A **74**, 023617 (2006).
[14] Ph. W. Courteille *et al.*, J. Phys. B **39**, 1055 (2006).
[15] I. Lesanovsky *et al.*, Phys. Rev. A **73**, 033619 (2006).
[16] T. Fernholz *et al.*, physics/0512017.
[17] N. F. Ramsey, Phys. Rev. **100**, 1191 (1955).
[18] Z. Ficek and H. S. Freedhoff, Phys. Rev. A **53**, 4275 (1996). See also, H. Freedhoff and T. Quang, Phys. Rev. Lett. **72**, 474 (1994); H. S. Freedhoff and T. Quang, J. Opt. Soc. Am. B **10**, 1337 (1993); C. Cohen-Tannoudji and S. Reynaud, J. Phys. B **10**, 2311 (1977).
[19] H. F. Hess, Phys. Rev. B **34**, R3476 (1986); H. F. Hess *et al.*, Phys. Rev. Lett. **59**, 672 (1987).
[20] N. V. Vitanov and K.-A. Suominen, Phys. Rev. A **56**, R4377 (1997).
[21] O. J. Luiten, M. W. Reynolds, and J. T. M. Walraven, Phys. Rev. A **53**, 381 (1996).
[22] T. Esslinger, I. Bloch, and T. W. Hänsch, Phys. Rev. A **58**, R2664 (1998).
[23] B. Lu and W. A. van Wijngaarden, Can. J. Phys. **82**, 81 (2004).
[24] J. C. Tremblay and T. Carrington, Jr., J. Chem. Phys. **121**, 11535 (2004).
[25] W. Magnus, Commun. Pure Appl. Math. **7**, 649 (1954).
[26] K. F. Milfeld and R. E. Wyatt, Phys. Rev. A **27**, 72 (1983).
[27] Another strategy to reduce the population transfer in the rf trap center could be to include this requirement in the optimization of the pulse duration.
[28] T. Lahaye and D. Guéry-Odelin, Eur. Phys. J. D **33**, 67 (2005).
[29] S. Hofferberth *et al.*, Nat. Phys. **2**, 710 (2006). This paper shows randomization of the relative phase of the double-well condensate when a second rf field is applied.

J. Phys. B: At. Mol. Opt. Phys. **40** (2007) 4013–4022 doi:10.1088/0953-4075/40/20/004

Trapping and cooling of rf-dressed atoms in a quadrupole magnetic field

O Morizot, C L Garrido Alzar, P-E Pottie, V Lorent and H Perrin

Laboratoire de physique des lasers, CNRS-Université Paris 13, 99 avenue Jean-Baptiste Clément, F-93430 Villetaneuse, France

E-mail: perrin@lpl.univ-paris13.fr

Received 26 June 2007, in final form 29 August 2007
Published 2 October 2007
Online at stacks.iop.org/JPhysB/40/4013

Abstract
We observe the spontaneous evaporation of atoms confined in a bubble-like radio frequency (rf)-dressed trap (Zobay and Garraway 2001 *Phys. Rev. Lett.* **86** 1195; 2004 *Phys. Rev.* A **69** 023605). The atoms are confined in a quadrupole magnetic trap and are dressed by a linearly polarized rf field. The evaporation is related to the presence of holes in the trap, at the positions where the rf coupling vanishes, due to its vectorial character. The final temperature results from a competition between residual heating and evaporation efficiency, which is controlled via the height of the holes with respect to the bottom of the trap. The experimental data are modelled by a Monte Carlo simulation predicting a small increase in phase-space density limited by the heating rate. This increase was within the phase-space density determination uncertainty of the experiment.

(Some figures in this article are in colour only in the electronic version)

1. Introduction

Ultracold atoms in versatile traps are the subject of extensive study. Developing alternative trap geometries enables the exploration of new physical situations. Among the most remarkable results obtained with atoms in non-harmonic traps, one may cite the observation of superfluid to Mott insulator transition in optical lattices [2], Josephson oscillations in a double well [3] or trapping in a ring geometry [4]. Recently, radio-frequency (rf) fields were used together with a static magnetic field to produce a quasi-2D trap [1, 5, 6] and a double well [7]. Other trapping geometries were proposed, based on this promising rf-dressing technique, such as rings [8, 9] or lattices [10]. One presents here the implementation of rf-dressing inside a quadrupole magnetic trap.

Quadrupole traps are usually not popular for ultracold atom trapping due to Majorana losses at the centre, where the field vanishes. The losses are avoided in TOP traps by adding

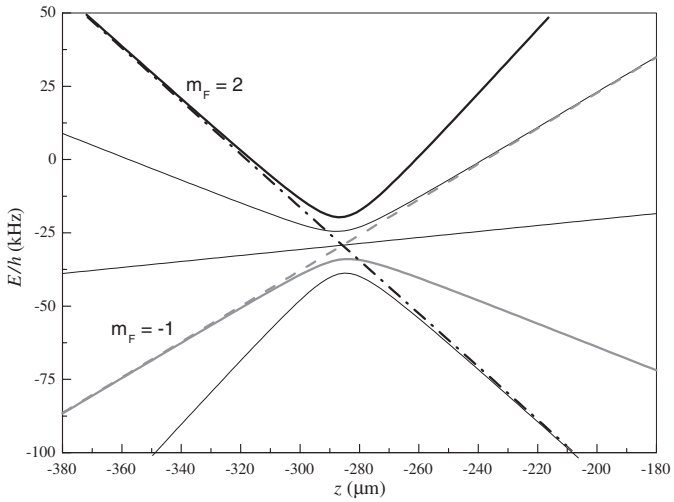

Figure 1. Energy of the dressed levels of ^{87}Rb in the magnetic quadrupole trap described in the paper, plotted along the vertical coordinate z, in the vicinity of the potential minimum at $z = -r_0$. The parameters are $\omega_{\rm rf} = 2\pi \times 3.1$ MHz, $b' = 150$ G cm^{-1} and $\Omega_1 = 2\pi \times 100$ kHz. The five dressed sublevels for a $F = 2$ spin state are plotted, as well as two bare states for comparison, $m_F = -1$, dashed, and $m_F = 2$, dash-dotted. The atoms are trapped in the upper dressed potential $m_F = F = 2$. Gravity was taken into account.

a rotating uniform magnetic field, at a frequency in the 10 kHz range [11]. In the trap presented in this paper, the magnetic field oscillates at a few MHz, resulting in an rf-dressed quadrupole trap. The atoms are then located away from the region of a zero magnetic field. Still, the rf polarization is responsible for the existence of regions of zero rf coupling. This results in a leakage of the higher kinetic atomic population. In this paper, we give evidence for a temperature decrease and a non-exponential atom number loss, characteristic for an evaporation process, for different experimental parameters.

2. Trap description

The trap relies on rf coupling between Zeeman sublevels in an inhomogeneous static magnetic field. The basic idea of the rf-dressed potentials was first proposed by Zobay and Garraway [1] and experimentally demonstrated a few years later [5]. We will recall here the main features of this trap and develop further the consequences of an inhomogeneous rf coupling.

A static trapping magnetic field $B(\mathbf{r})\mathbf{e}_{\rm B}(\mathbf{r})$ presenting a local minimum B_0 is used together with a rf oscillating magnetic field $B_{\rm rf}\cos(\omega_{\rm rf}t)\mathbf{e}_{\rm y}$. The rf field is detuned by $\Delta = \omega_{\rm rf} - \omega_0$ from the coupling frequency $\omega_0 = g_{\rm L}\mu_{\rm B}B_0/\hbar$ at the static magnetic field minimum, where $g_{\rm L}$ is the Landé factor and $\mu_{\rm B}$ the Bohr magneton. The linearly polarized rf field couples the Zeeman substates $|F, m_F\rangle$ and $|F, m'_F\rangle$ with $m'_F = m_F \pm 1$ at the positions where the magnetic splitting is close to the rf frequency. In the limit of a large coupling, this results in a dressing of the m_F levels into adiabatic states whose energy are represented on figure 1. In the following, we will concentrate on the upper adiabatic state, undergoing a potential

$$V_{\rm d}(\mathbf{r}) = F((V_{\rm B}(\mathbf{r}) - \hbar\omega_{\rm rf})^2 + \hbar^2\Omega^2(\mathbf{r}))^{1/2}. \tag{1}$$

This expression is obtained within the rotating wave approximation. Here, $m_F = F = 2$ in the case of ^{87}Rb in its $5s_{1/2}$ ground state. $V_{\rm B}(\mathbf{r}) = g_{\rm L}\mu_{\rm B}B(\mathbf{r})$ is the magnetic energy shift

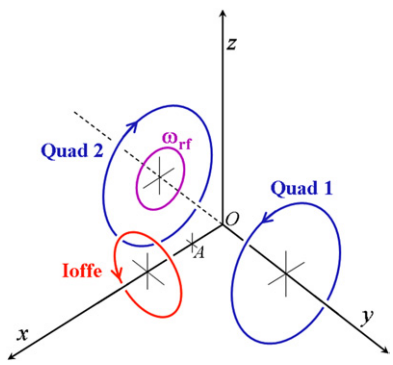

Figure 2. Simplified scheme of the trap. After accomplishing evaporative cooling in the QUIC trap (Quad + Ioffe coils) centred at position A, the atoms are loaded into the dressed rf trap (Quad + Ioffe + rf coils). The current in the Ioffe coil is then slowly ramped down to zero for transferring the atoms into the dressed trap based on the quadrupole field of axis y (Quad + rf coils). The rf field polarization is aligned along the axis of the quadrupole.

between two adjacent Zeeman sublevels, and

$$\Omega(\mathbf{r}) = \Omega_1 \sin(\mathbf{e}_y, \mathbf{e}_B(\mathbf{r})) \tag{2}$$

is the Rabi frequency of rf coupling, of maximal amplitude $\Omega_1 = g_L \mu_B B_{rf}/(2\hbar)$. Ω_1 is independent of $\mathbf{r}$ to a very good approximation. As deduced from this formula, the rf coupling vanishes at the points where the static field is parallel to the radio frequency polarization $\mathbf{e}_y$, that is along the y-axis. We will see later on that in the case of a quadrupole static magnetic field, these points appear as two 'holes' on the equator of our bubble-like trap.

The simplest situation occurs when the rf coupling $\Omega(\mathbf{r})$ is uniform. Then, for a positive detuning $\Delta > 0$, the dressed potential $V_d(\mathbf{r})$ is minimum all over an iso-B surface, defined by $V_B(\mathbf{r}) = g_L \mu_B B(\mathbf{r}) = \hbar\omega_{rf}$. This is no longer true if Ω varies in space, due to the spatial dependence of the orientation of the static field: this breaks the invariance on the iso-B surface, leading to a finite number of minima related to the minima of $\Omega(\mathbf{r})$. On the other hand, gravity tends to push the atoms towards the bottom of the iso-B surface. To describe correctly the potential geometry, we thus need to take both effects into account. As we will see, the potential minima will not always sit exactly on the iso-B surface, but they will be close to it in most relevant experimental cases.

We concentrate in the following on the case of a quadrupole trap with an horizontal symmetry axis. This axis is labelled y in our experimental setup, see figure 2, and is the same as the rf polarization. Let b' be the magnetic field gradient in the radial direction of coordinate $\rho = (x^2 + z^2)^{1/2}$, and let us define α as $\alpha = g_L \mu_B b'/\hbar$. One has $\mathbf{B}(\mathbf{r}) = b'(\rho \mathbf{e}_\rho - 2y\mathbf{e}_y)$ and therefore $\Omega(\mathbf{r}) = \Omega_1 \rho/\sqrt{\rho^2 + 4y^2}$. In this situation, an atom in the uppermost dressed state $m_F = F$ undergoes the potential

$$V_{tot}(x, y, z) = mgz + F\hbar\sqrt{(\alpha\sqrt{\rho^2 + 4y^2} - \omega_{rf})^2 + \frac{\rho^2}{\rho^2 + 4y^2}\Omega_1^2}, \tag{3}$$

where m is the atomic mass and mgz the gravitational potential. The relevant iso-B surface is then an ellipsoid of equation $\rho^2 + 4y^2 = r_0^2$, where r_0 is related to ω_{rf} through $r_0 = \omega_{rf}/\alpha$. The rf coupling vanishes along the y-axis, where the magnetic field is parallel to the rf polarization.

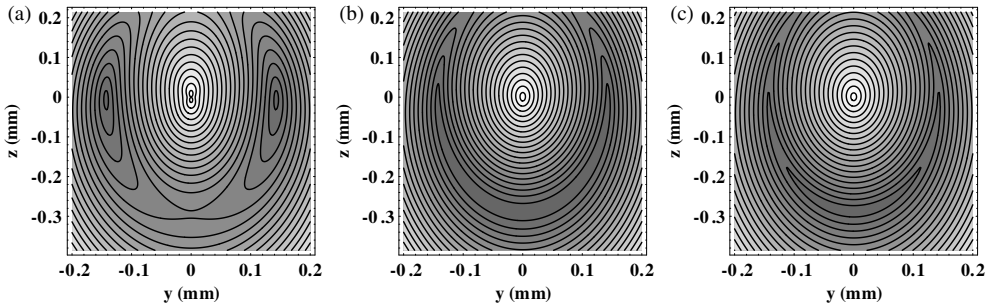

Figure 3. Contour plot of the potential for ^{87}Rb atoms in the yz plane, for different values of the rf coupling relative to $\omega_{\rm rf}$. The parameters are $\omega_{\rm rf}/2\pi = 3.1$ MHz and a magnetic gradient of 150 G cm^{-1} in the z-direction, such that $\beta = 9.85$ and $\omega_{\rm rf}/\beta = 2\pi \times 305$ kHz. (*a*) Large coupling $\omega_{\rm rf}/\Omega_1 < \beta$ ($\Omega_1/2\pi = 1$ MHz); the two minima are located at the position of the holes. (*b*) Intermediate coupling $\omega_{\rm rf}/\Omega_1 = \beta$ ($\Omega_1/2\pi = 305$ kHz). (*c*) Small coupling $\omega_{\rm rf}/\Omega_1 > \beta$ ($\Omega_1/2\pi = 100$ kHz); a single minimum is present at the bottom of the shell.

To visualize the potential, let us first remark that the extrema are located in the vertical plane $x = 0$. In this plane, $\rho = |z|$. One can rewrite $V_{\rm tot}(y, z)$ in units of mgr_0 as

$$V_{\rm tot}(x = 0, y, z)/(mgr_0) = \frac{z}{r_0} + \beta\sqrt{\left(\frac{\sqrt{z^2+4y^2}}{r_0} - 1\right)^2 + \frac{z^2}{z^2+4y^2}\frac{\Omega_1^2}{\omega_{\rm rf}^2}}. \quad (4)$$

The parameter $\beta = F\hbar\alpha/mg$ is the ratio of the magnetic and the gravitational force. It should be larger than 1 for the magnetic trap to compensate gravity and in our experiment $\beta \simeq 10$. Therefore, the behaviour of the second term in the potential expression is dominant. Indeed, the exact study of the minima position of $V_{\rm tot}$ shows that for $\beta \gg 1$, the minima lie very close to the iso-B surface $\rho^2 + 4y^2 = r_0^2$. To discuss qualitatively the potential geometry, we will thus assume that the atoms sit exactly on this ellipsoid, which cancels the first term under the square root. We are left with

$$V_{\rm tot}(z)/(mgr_0) \simeq \frac{z}{r_0} + \beta\frac{|z|}{r_0}\frac{\Omega_1}{\omega_{\rm rf}}, \qquad \text{with} \quad |z| \leqslant r_0. \quad (5)$$

Depending on the ratio $\omega_{\rm rf}/\Omega_1$ of the rf frequency to the rf coupling, two different situations may occur: for $\omega_{\rm rf}/\Omega_1 < \beta$, or equivalently $mgr_0 < F\hbar\Omega_1$, the coupling inhomogeneity is the dominant effect, and the potential minima sit at the points where the coupling term is the smallest. This corresponds to the positions where $\rho = 0$, that is at the intersections of the iso-B ellipsoid and the y-axis (see figure 3(a)). Note that at these points, the rf coupling vanishes, leading to spin-flip losses into untrapped states. In the following, we will refer to these two points as to the 'holes'. On the other hand, for $\omega_{\rm rf}/\Omega_1 > \beta$, or $mgr_0 > F\hbar\Omega_1$, gravity dominates and there is a single potential minimum at the very bottom of the ellipsoid, far from the holes (figure 3(c)). In this single well, and in the harmonic approximation, the oscillation frequencies up to first order in $1/\beta$ [1] are

$$\omega_x = \sqrt{\frac{g}{r_0}}. \quad (6)$$

[1] The exact value of the oscillation frequencies contains other terms of orders at least $1/\beta^2$. They can be calculated analytically, but are negligible in our experimental conditions where $\beta \simeq 10$.

$$\omega_y = 2\sqrt{\frac{g}{r_0}}\sqrt{1 - \frac{F\hbar\Omega_1}{mgr_0}} = 2\omega_x\sqrt{1 - \beta\frac{\Omega_1}{\omega_{\rm rf}}}. \tag{7}$$

$$\omega_z = \alpha\sqrt{\frac{F\hbar}{m\Omega_1}} = \omega_x\sqrt{\beta\frac{\omega_{\rm rf}}{\Omega_1}}. \tag{8}$$

The vertical oscillation frequency was derived in [1]. One easily identifies the pendulum frequency along x. Along y, the pendulum frequency is modified by the inhomogeneous coupling. We remark that these oscillation frequencies are valid only for small amplitude oscillations around the potential minimum, the trap as a whole being far from harmonic.

For values of $\omega_{\rm rf}/\Omega_1$ close to β, one will face a situation where the potential is almost flat in the crescent defined by $z < 0$, $x = 0$ and $z^2 + 4y^2 = r_0^2$ (figure 3(b)). The gravitational energy mgr_0 at the holes is indeed exactly equal to the energy shift $F\hbar\Omega_1$ induced by the rf at the bottom of the iso-B surface, and ω_y as expressed above goes to zero. However, this intermediate region is extremely narrow for $\beta \gg 1$, with a width in the parameter $\omega_{\rm rf}/\Omega_1$ on the order of $3/(2\beta)$ around β, and in practice one deals only with one of the two extreme situations, a or c. Note that in any case the zero magnetic field region, responsible for Majorana spin flips in the centre of conventional quadrupole traps, plays a minor role in an rf-dressed quadrupole trap. The energy barrier is at least $F\hbar\omega_{\rm rf}$, much larger than the thermal energy of the atomic cloud.

In our experiment, $\omega_{\rm rf}/\Omega_1$ is larger than β (typically $\omega_{\rm rf}/2\pi \simeq 3$ MHz and $\Omega_1/2\pi <$ 260 kHz), and we are always in the case of a single minimum. Therefore, due to gravity, ultracold atoms remain trapped near the bottom of the ellipsoid and only marginally explore the non-coupling regions. This single-well situation was demonstrated experimentally in a Ioffe–Pritchard type trap [5]. The opposite situation was used in an atom chip experiment for producing a double well potential [7]. In the experiment described in this paper, we bring into light the non-negligible effect of the two holes for an ultracold atomic cloud, even in the situation where a single minimum is present.

3. Experimental sequence

The experimental setup has been described in detail elsewhere [12, 13]. The atoms in the state $F = 2, m_F = +2$ are first loaded into a static magnetic trap, in a quadrupole and Ioffe configuration (QUIC) [14], see figure 2, Quad and Ioffe coils. In this trap, the atoms are confined near the magnetic field minimum, position A of figure 2, situated 7 mm away from the quadrupole centre O in the direction of the Ioffe coil. Then, a 30 s radio frequency ramp is applied to evaporatively cool them down to just above the condensation threshold. We deliberately do not reach condensation and rather work with ultracold clouds, with a temperature of typically 4 μK, in order to explore the leakage through the pierced part of the iso-B bubble as explained later. The evaporation rf source is then switched off and the trapping rf field, polarized along y, is turned on at a frequency lower than the resonance frequency in the trap centre, 1.3 MHz. Note that for this purpose, a nonzero minimum magnetic trap is necessary. The rf frequency is then adiabatically ramped up to the desired value of $\omega_{\rm rf}$ within typically 150 ms, as detailed in [5]. This way, the atoms are always following the upper dressed state, corresponding to $m_F = F = +2$ in the dressed basis. At the end of this step, they are confined in a dressed rf trap relying on the QUIC static magnetic field.

The QUIC trap stage is necessary to obtain an ultracold sample and load it efficiently into the dressed rf trap. The atoms are then transferred into a dressed quadrupole trap, which

presents points of strictly zero rf coupling at any value of ω_{rf}. The current in the Ioffe coil is therefore decreased in order to reach a quadrupole configuration within a time interval of about 450 ms. During this process, the minimum of the static magnetic field quickly goes to zero and is split into two zero field points separating along the x-axis. One point is going back 7 mm away from A to the position O of the initial quadrupole centre whereas the other one is going from A to infinity in the opposite direction (see [14], figure 2). During this transfer, the atomic cloud remains in the dressed trap, situated just below the static magnetic minimum, and is split into two clouds according to the deformation of the iso-magnetic surfaces. The first stage of the Ioffe current decreasing is controlled carefully in order that at least half of the atoms follow the right direction, towards the initial quadrupole centre O. At the end of this stage, about 4×10^5 atoms at a higher temperature of 8 μK are confined in an rf-dressed quadrupole trap. The QUIC-to-quadrupole transfer of the rf-dressed atoms is a critical step and is very sensitive to initial conditions. This procedure is at the origin of a scattering in the values of atom number and temperature.

The rf field is produced by a home made synthesizer [15]. The Rabi frequency Ω_1 corresponding to a given voltage amplitude is evaluated as follows. The rf antenna, normally dedicated to rf trapping, is used for evaporative cooling in the QUIC trap for this measurement. An evaporation ramp is applied down to a given final rf frequency. The threshold frequency below which all atoms are expelled from the magnetic trap is recorded. For an arbitrary weak rf power, this threshold frequency corresponds to the Zeeman splitting ω_0 at the bottom of the QUIC magnetic trap. However, the recorded threshold frequency is larger, as the magnetic levels are deformed due to dressing by the rf photons. We use the observed value as input in the calculation of the dressed potential, including gravity, and search for the Rabi frequency value making the potential flat, just unable to hold the atoms. We repeat this procedure for different voltage amplitudes at the synthesizer to calibrate the rf power.

4. Experimental results

After the atoms have been transferred to the rf-dressed quadrupole trap, they remain stored for a variable time τ after which the magnetic field and rf coupling are simultaneously switched off. An absorption image of the cloud is taken after a 7.5 ms ballistic expansion. From these measurements, the evolution of the atom number and the temperature with the storage time τ is deduced. The temperature is related to the vertical size after the expansion of the atomic cloud. In principle, it also depends on the initial vertical size, which is not entirely negligible due to the curved shape of the trap. However, we neglect the initial size, which overestimates the real temperature by about 20%, as deduced from the comparison with a numerical simulation (see the following section).

We observe a rapid decreasing of the temperature during the first few seconds. The experiment was repeated at $\Omega_1/2\pi = 40$ kHz for two different values of ω_{rf} (see figure 4). For $\omega_{rf}/2\pi = 2$ MHz, we find a final temperature $T_1 = 1.35$ μK whereas it does not get lower than $T_2 = 3.68$ μK for $\omega_{rf}/2\pi = 3.1$ MHz. For the largest rf coupling value $\Omega_1/2\pi =$ 260 kHz, the temperature decrease, can be observed over more than 10 s (see the experimental points on figure 5), with a first drop in temperature followed by a transition to a slower but still decreasing evolution.

These results, together with the non-exponential decrease of the atom number, see inset of figure 5, reveal an evaporation process via Landau–Zener losses through the holes along the rf coil axis in the equatorial plane. The final temperature is related to the trap depth, calculated

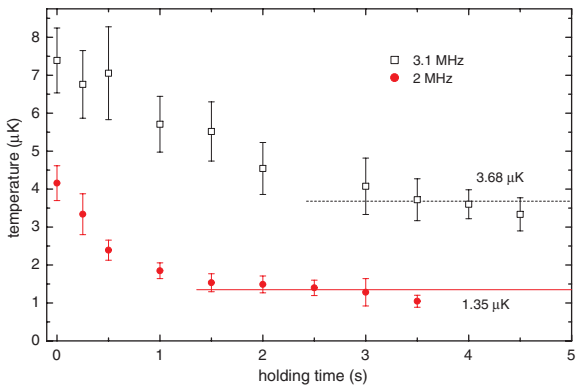

Figure 4. The temperature T, measured as described in the text, as a function of time with $\Omega_1 = 2\pi \times 40$ kHz and for different values of the RF frequency $\omega_{\rm rf}/2\pi = 2$ MHz (closed circles) and 3.1 MHz (open squares). Each point is an average over two to three data points. The error bars take into account the point dispersion as well as an experimental uncertainty of 10%. T drops over the first trapping seconds, and then stabilizes to a value $T = 1.35$ μK (resp. 3.68 μK) indicated by the horizontal lines, deduced from the average of the five (resp. four) last points.

between the trap bottom and the position of the holes and depending on the rf frequency through

$$U_0 = mgr_0 - F\hbar\Omega_1 = \frac{mg\omega_{\rm rf}}{\alpha} - F\hbar\Omega_1. \tag{9}$$

The trap depth is $U_0/k_{\rm B} = \Theta_1 = 26.7$ μK (resp. $\Theta_2 = 15.7$ μK) for a 3.1 MHz (resp. 2 MHz) rf frequency and a Rabi frequency $\Omega_1/2\pi = 40$ kHz. The final temperature compared to the trap depth gives $\Theta_1/T_1 = 7.3$ and $\Theta_2/T_2 = 11.6$. The overestimation of temperature makes these values a lower bound to the depth to temperature ratio. A ratio of 8 to 10 is considered typical for a spontaneous evaporation process in an harmonic trap [16].

In principle, the evaporation could also come from losses through the centre of the quadrupole, however the energy $F\hbar\alpha r_0 = F\hbar\omega_{\rm rf}$ required to cross the central region of the quadrupole trap is much higher than the energy U_0 necessary to explore the uncoupled region, making this process very unlikely.

Finally, the possible non-adiabatic Landau–Zener losses in the avoided crossing region at the bottom of the ellipsoid, where the atoms mostly sit, can be neglected. Indeed, the probability of spin-flipping in this zone for a given velocity v reads [17]

$$P_{\rm LZ} = 1 - \left[1 - \exp\left(-\frac{\pi}{2}\frac{\Omega_1^2}{\alpha v}\right)\right]^{2F}. \tag{10}$$

If one averages equation (10) over the whole velocity distribution for an rf coupling $\Omega_1 =$ 30 kHz, smaller than was ever used in the experiment, and a temperature in the dressed trap $T = 10$ μK, one finds a lifetime $\tau_{\rm LZ}$ due to Landau–Zener losses as high as 100 s, which is even larger than the lifetime due to collisions with the background gas. Landau–Zener losses at the trap bottom are then obviously not responsible for the losses and temperature decrease.

5. Numerical simulation

In order to confirm our interpretation of the experimental results, we performed a numerical simulation of the cloud classical dynamics with the parameters of the experiment, for a coupling $\Omega_1/2\pi = 260$ kHz, a rf frequency $\omega_{\rm rf}/2\pi = 3.1$ MHz and a trapping time ranging

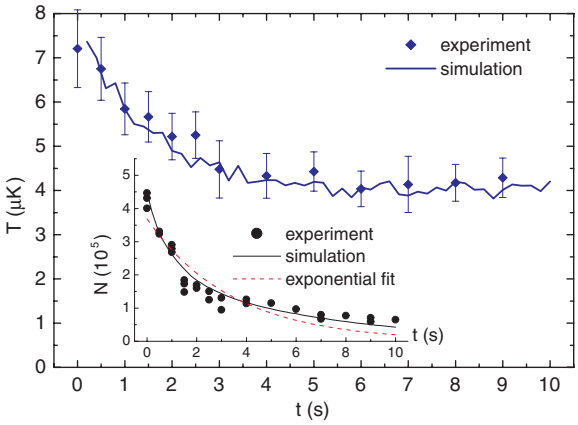

Figure 5. Temperature, deduced from the size σ_z after a 7.5 ms time-of-flight, as a function of the holding time in the rf-dressed quadrupole trap. The experimental data, closed diamonds with error bars as in figure 4, are compared to the numerical simulation, thick line. (Inset) Evolution of the atom number in the same conditions: the experimental data, circles, are compared to the simulation, line and to a pure exponential fit, dashed red line. For these experiments and the related simulation, the parameters are $\omega_{\rm rf}/2\pi = 3.1$ MHz and $\Omega_1 = 2\pi \times 260$ kHz.

between 0 and 10 s. The simulation calculates the evolution of a cloud of atoms initially trapped on the iso-B surface, at temperature T_i, above condensation threshold. Collisions between trapped atoms are taken into account through a method developed by Bird [18], while collisions with the background gas are described through a lifetime of 60 s. A possible linear heating rate H is taken into account in the simulation by increasing each velocity component v_i by $2v_i H\,{\rm d}t/T$ after a time step ${\rm d}t$. The Landau–Zener losses are more difficult to model. The use of a random number to decide, with a local probability distribution, if an atom is lost or not would be time consuming. Instead, the holes are modelled by a deterministic loss term: the atoms are considered lost if the Landau–Zener probability at this point $P_{\rm LZ}(\mathbf{r}, v)$ exceeds a critical value $P_{\rm c}$. Due to the exponential dependence of the Landau–Zener non-adiabatic coupling on the rf Rabi frequency, this occurs essentially in a region very close to the two holes.

Figure 5 gives a plot of the temperature for different holding times in the dressed trap. The temperature is deduced in the same conditions as in the experiment, from the cloud size after a 7.5 ms time-of-flight, and the two values are thus directly comparable. The simulation fits at best the experimental data for the choice $P_{\rm c} = 0.9$ and $H = 300$ nK s^{-1}. The Landau–Zener probability $P_{\rm c}$ mainly determines the initial rate of temperature decrease. Once this value is fixed, the heating rate H imposes the final saturation temperature, resulting from the equilibrium between evaporation and residual heating. The simulation reproduces well the features of spontaneous evaporation, namely temperature reduction and non-exponential atomic losses (see dotted line in the inset of figure 5). These features completely disappear if the holes are suppressed.

The peak phase-space density φ in the rf-dressed trap is computed from the simulated data. To be able to compare this figure with the experiment, we used in both cases the estimation $\varphi \simeq N(\hbar\bar{\omega}/k_{\rm B}T)^3$, where T is calculated from the vertical width after time-of-flight as explained above. Here, $\bar{\omega}$ is the geometric mean of the oscillation frequencies of the rf-dressed trap, equations (6)–(8). This estimate only gives the order of magnitude for the phase-space density, as the formula is correct only for a harmonic trap and the trap is far from

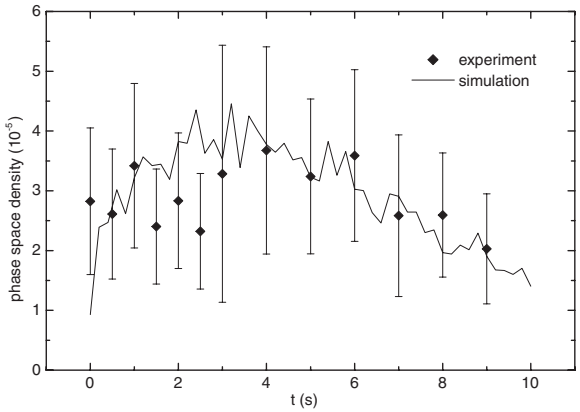

Figure 6. Estimated phase-space density for the data series of figure 5, from the experimental data, diamonds, and the simulation, line. The parameters are $\omega_{\rm rf}/2\pi = 3.1$ MHz and $\Omega_1 = 2\pi \times 260$ kHz. The error bars take into account data dispersion and an experimental uncertainty of 40%, resulting from uncertainties in atom number and temperature.

being harmonic. The results are displayed on figure 6, for the same parameters as used in figure 5. For these parameters, $\bar{\omega}/2\pi = 60.6$ Hz. The simulation shows a first increase of about 50% within the first 3 s, followed by a regular decrease due to residual heating. The experimental data give values for φ of the same order, but are too scattered for demonstrating unambiguously a phase-space density increase. This is due to the sensitivity of the estimate for φ to the temperature value T, which is determined with a large uncertainty.

6. Conclusion

In this paper, we demonstrate trapping of ultracold atoms in a quadrupole magnetic configuration. The atoms are prevented to escape through the centre by rf dressing of the atomic state, which results in a confining adiabatic potential. Non-exponential losses associated with a temperature decrease are observed in this trap, giving evidence for spontaneous evaporation. These losses are attributed to the presence of zero rf-coupling zones in the trap, due to rf polarization. The experimental data are interpreted with the help of a numerical simulation, well reproducing the main features. The evaporation results in a drop in temperature, which saturates due to a residual heating in the trap. This technical heating clearly prevents an increase in phase-space density. Cooling in the trap may be improved in different ways. The observed spontaneous evaporation could be forced by reducing the rf frequency $\omega_{\rm rf}$ with time, thus limiting the trap depth. Still, it seems that a necessary approach would be to use a second independent rf field to spin flip selectively the more energetic atoms, as in conventional evaporative cooling [19, 20]. Ultimately, the quadrupole geometry with a symmetry axis oriented in the vertical direction is ideal for the realization of a isotropic quasi-2D degenerate gas [21] or an atomic ring [8].

Acknowledgments

We acknowledge fruitful discussions with Barry Garraway. This work was supported by the Région Ile-de-France (contract number E1213) and by the European Community through the Research Training Network 'FASTNet' under contract No HPRN-CT-2002-00304 and

Marie Curie Training Network 'Atom Chips' under contract No MRTN-CT-2003-505032. Laboratoire de physique des lasers is UMR 7538 of CNRS and Paris 13 University. The LPL group is a member of the Institut Francilien de Recherche sur les Atomes Froids.

References

[1] Zobay O and Garraway B M 2001 *Phys. Rev. Lett.* **86** 1195
Zobay O and Garraway B M 2004 *Phys. Rev.* A **69** 023605
[2] Greiner M, Mandel O, Esslinger T, Hänsch T W and Bloch I 2002 *Nature* **415** 39
[3] Albiez M, Gati R, Fölling J, Hunsmann S, Cristiani M and Oberthaler M K 2005 *Phys. Rev. Lett.* **95** 010402
[4] Gupta S, Murch K W, Moore K L, Purdy T P and Stamper-Kurn D M 2005 *Phys. Rev. Lett.* **95** 143201
[5] Colombe Y, Knyazchyan E, Morizot O, Mercier B, Lorent V and Perrin H 2004 *Europhys. Lett.* **67** 593
[6] White M, Gao H, Pasienski M and DeMarco B 2006 *Phys. Rev.* A **74** 023616
[7] Schumm T, Hofferberth S, Andersson L M, Wildermuth S, Groth S, Bar-Joseph I, Schmiedmayer J and Krüger P 2005 *Nat. Phys.* **1** 57
[8] Morizot O, Lorent V, Perrin H and Garraway B M 2006 *Phys. Rev.* A **74** 023617
[9] Lesanovsky I, Hofferberth S, Schmiedmayer J and Schmelcher P 2006 *Phys. Rev.* A **74** 033619
[10] Courteille Ph W, Deh B, Fortágh J, Günther A, Kraft S, Marzok C, Slama S and Zimmermann C 2006 *J. Phys. B: At. Mol. Opt. Phys.* **39** 1055
[11] Petrich W, Anderson M H, Ensher J R and Cornell E A 1995 *Phys. Rev. Lett.* **74** 3352
[12] Colombe Y, Kadio D, Olshanii M, Mercier B, Lorent V and Perrin H 2003 *J. Opt. B: Quantum Semiclass. Opt.* **5** S155
[13] Dimova E, Morizot O, Stern G, Garrido Alzar C L, Fioretti A, Lorent V, Comparat D, Perrin H and Pillet P 2007 *Eur. Phys. J.* D **42** 299
[14] Esslinger T, Bloch I and Hänsch T W 1998 *Phys. Rev.* A **58** R2664
[15] Morizot O, De Lapeyre De Bellair J, Wiotte F, Lopez O, Pottie P-E and Perrin H 2007 Agile low phase noise radio-frequency sine wave generator applied to experiments on ultracold atoms *Preprint* 0704.1974
[16] Luiten O J, Reynolds M W and Walraven J T M 1996 *Phys. Rev.* A **53** 38
[17] Vitanov N V and Suominen K-A 1997 *Phys. Rev.* A **56** R4377
[18] Bird G A 1994 *Molecular Gas Dynamics and the Direct Simulation of Gas Flows* (Oxford: Clarendon/Oxford University Press)
[19] Garrido Alzar C L, Perrin H, Garraway B M and Lorent V 2006 *Phys. Rev.* A **74** 053413
[20] Hofferberth S, Lesanovsky I, Fischer B, Verdu J and Schmiedmayer J 2006 *Nat. Phys.* **2** 710
[21] Pitaevskii L P and Rosch A 1997 *Phys. Rev.* A **55** R853

Eur. Phys. J. D **47**, 209–214 (2008)
DOI: 10.1140/epjd/e2008-00050-2

THE EUROPEAN PHYSICAL JOURNAL D

Influence of the Radio-Frequency source properties on RF-based atom traps

O. Morizot, L. Longchambon, R. Kollengode Easwaran, R. Dubessy, E. Knyazchyan, P.-E. Pottie, V. Lorent, and H. Perrin[a]

Laboratoire de physique des lasers, CNRS-Université Paris 13, 99 av. Jean-Baptiste Clément, 93430 Villetaneuse, France

Received 9 January 2008 / Received in final form 19 February 2008
Published online 19 March 2008 –

Abstract. We discuss the quality required for the RF source used to trap neutral atoms in RF-dressed potentials. We illustrate this discussion with experimental results obtained on a Bose-Einstein condensation experiment with different RF sources.

PACS. 39.25.+k Atom manipulation – 32.80.Pj Optical cooling of atoms; trapping

1 Introduction

Radio-frequency (RF) fields are used in cold atom experiments for different purposes: for instance, evaporative cooling performed in a magnetic trap relies on RF field coupling between the different atomic magnetic states [1,2]. This technique led to the first observation of Bose-Einstein condensation (BEC) [3,4]. RF pulses are used for dissociating ultracold molecules produced from ultracold gases through Feshbach resonances [5]. More recently, RF fields have been used together with static magnetic fields for trapping ultracold atoms at a temperature of a few μK in unusual geometries [6,7]. There is a growing interest for these "RF-based traps" among atomic physicists, for creating double well traps on atom chips [8–10] as well as proposing new kinds of confining potentials [11–14]. In both cases, a single frequency RF signal must be frequency swept over some range, often larger than the initial frequency, following a precise time function lasting several seconds. Typically the RF frequency is varied between 1 MHz and a few tens of MHz in 0.1 s to 10 s in a first ramping stage, and held at the final frequency for seconds in a plateau stage. Commercial RF generators meet reasonably well the usual requirements for evaporative cooling, even if a better resolution in arbitrary frequency ramps would be appreciated. However, in the case of RF-based trapping, the requirements are stronger. The main difference between these two situations is that in evaporative cooling the cold atomic sample is located away from the region of efficient coupling, whereas in the RF-based trapping scheme the coldest atoms sit exactly at the point where the RF field has the largest effect. The quality of the RF source is then much more important than for evaporative cooling. Indeed, the cloud position is directly related to the value of the RF field frequency, whereas the trap restoring force, or equivalently the oscillation frequency ν_t in the harmonic approximation, is linked to the RF amplitude. As a result, any amplitude noise, frequency noise or phase noise of the RF signal during the ramp or the plateau leads to heating of the cold atomic cloud [7,15]. These considerations motivated the detailed study presented in this paper.

This paper is organised as follows: in Section 2 we give explicit expressions for the heating of the cold atom sample for frequency and amplitude noise in the case of RF-based trapping. Section 3 is devoted to experimental results, with a comparison between different RF sources tested on the BEC experiment.

2 Requirements on the RF source for RF-based trapping

In this paper, we will focus on the RF-dressed trap that is experimentally produced in our laboratory [7]. The main conclusions may easily be extended to other RF-dressed trap geometries.

The trap confines the atoms in all three space dimensions. The trapping force arises from the interaction between the atoms and the linearly polarized RF field $B(t) = B_{\mathrm{RF}} \cos(2\pi\nu_{\mathrm{RF}} t)$ in the presence of an inhomogeneous static magnetic field B_{dc}. This interaction dresses the atoms with RF photons and results in a transverse confinement of the dressed atoms to an isomagnetic surface. The atoms are free to move along this confining surface, resulting in our case in a kind of "bubble trap" [6]. Due to gravity, however, they are concentrated at the bottom of the surface. Their motion is pendulum-like in the horizontal directions, and imposed by the RF interaction

[a] e-mail: perrin@lpl.univ-paris13.fr

along the vertical z axis. This last direction is thus the most sensitive to the RF field properties (frequency ν_{RF}, amplitude B_{RF}) and we will therefore concentrate on the vertical motion in the following. Along this direction, heating or atomic losses may arise from frequency or amplitude noise, phase jumps or discrete frequency steps during the RF ramp.

2.1 Frequency noise: dipolar excitation heating

Very generally, for atoms in a one dimensional harmonic trap with a trapping frequency ν_z, any effect producing a jitter in the trap position z results in linear heating through dipolar excitation. The average energy of the cold atomic cloud E increases linearly as [16]:

$$\dot{E} = \frac{1}{4} M \omega_z^4 S_z(\nu_z) \tag{1}$$

where $\omega_z = 2\pi\nu_z$, M is the atomic mass and S_z is the one-sided Power Spectral Density (PSD) of the position fluctuations δz, defined as the Fourier transform of the time correlation function [16]

$$S_z(\nu) = 4 \int_0^\infty d\tau \cos(2\pi\nu\tau) \langle \delta z(t) \delta z(t+\tau) \rangle. \tag{2}$$

In our 3D trap, the time variations of energy, E, and temperature, T, are related by $\dot{T} = \dot{E}/3k_B$. In principle, $\dot{E}$ is the sum of three contributions of the type (1) for all three directions. However, the vertical heating is always much larger than the horizontal ones in this RF-based trap, and we will neglect the minor contributions in the following.

The vertical trap position z is a function $z = Z(\nu_{\mathrm{RF}})$ of the RF frequency ν_{RF}. As a result, S_z is directly proportional to S_{rel}, the PSD of relative frequency noise of the RF source:

$$S_z(\nu) = \left(\nu_{\mathrm{RF}} \frac{dZ}{d\nu_{\mathrm{RF}}} \right)^2 S_{\mathrm{rel}}(\nu). \tag{3}$$

The function Z depends on the geometry of the static magnetic field. In a quadrupolar field, for instance, Z is linear with ν_{RF} and its derivative is a constant. From equations (1) and (3), we infer that the linear heating rate is proportional to $S_{\mathrm{rel}}(\nu_z)$.

To fix orders of magnitude, within the static magnetic field of our Ioffe-Pritchard trap [7], ν_z may be adjusted between 600 and 1500 Hz and the typical temperature of the cold rubidium 87 atoms ranges from 0.5 to 5 μK. For Bose-Einstein condensation experiments, a linear temperature increase below 0.1 $\mu\mathrm{K\,s^{-1}}$ is desirable [17]. This rate corresponds to $\sqrt{S_z(\nu_z)} = 0.3\ \mathrm{nm}/\sqrt{\mathrm{Hz}}$ for an intermediate trap frequency of 1000 Hz and $\nu_{RF} = 3$ MHz, which in turn corresponds to a one-sided PSD of relative frequency fluctuations of the RF source $S_{\mathrm{rel}}(\nu_z) = -118\ \mathrm{dB\,Hz^{-1}}$.

2.2 Amplitude noise: parametric heating

Fluctuations of the RF field amplitude B_{RF} are responsible for parametric heating in the vertical direction. The trapping frequency ν_z is inversely proportional to $\sqrt{B_{\mathrm{RF}}}$ [6]:

$$\nu_z = \left(\frac{dZ}{d\nu_{\mathrm{RF}}} \right)^{-1} \sqrt{\frac{2F\hbar}{M\gamma B_{\mathrm{RF}}}}. \tag{4}$$

Here, γ is the gyromagnetic ratio of the atom and F is the total atomic spin ($F = 2$ for rubidium 87 in its upper hyperfine state). The atoms are assumed to be polarised in their extreme $m_F = F$ substate. Amplitude noise then results in an exponential increase of the cloud temperature with a rate Γ given by

$$\Gamma = \pi^2 \nu_z^2 S_a(2\nu_z) \tag{5}$$

where S_a is the PSD of the relative RF amplitude noise [16]. In order to perform experiments with the BEC within a time scale of a few seconds, Γ should not exceed $10^{-2}\ \mathrm{s^{-1}}$ [17]. Again, for a typical oscillation frequency of 1000 Hz, this corresponds to $S_a < -90\ \mathrm{dB\,Hz^{-1}}$. This requirement is rather easy to match and does not limit the choice of the RF source, as –110 $\mathrm{dB\,Hz^{-1}}$ is commonly reached with commercial synthesizers. However, particular care must be taken in the choice and installation of the RF amplifier usually used after the source.

2.3 Phase jumps

Controlling the phase of the RF source is not a crucial point for evaporative cooling, but becomes an issue in the case of RF-based traps, where it is associated with trap losses. In the latter situation, the atomic spin follows an effective magnetic field precessing at the RF frequency around the dc magnetic field, with a precession angle $2\pi\nu_{\mathrm{RF}}t$ and a nutation angle θ. A phase jump results in a sudden change $\Delta\varphi$ in the precession angle, the atomic spin being then misaligned with the new direction the effective field. Some of the atoms end up with a spin oriented incorrectly and escape the trap.

The atomic loss after a phase jump $\Delta\varphi$ may be estimated in the following way. The nutation angle θ is linked to RF frequency and amplitude through $\tan(\theta) = (B_{\mathrm{RF}}/2)/(B_{\mathrm{dc}} - 2\pi\hbar\nu_{\mathrm{RF}}/g_F\mu_B)$ [18]. g_F and μ_B are the Landé factor and the Bohr magneton, respectively. θ is position dependent, as is the value of the dc magnetic field B_{dc}. After the phase jump, the new effective field makes an angle ψ with the former one, where $\sin(\psi/2) = \sin(\theta)\sin(\Delta\varphi/2)$. At a given position, the probability $p(\psi)$ of keeping an atom in the new dressed state is then given by its overlap with the initial spin eigenstate, $p(\psi) = [\cos(\psi/2)]^{4F}$. In the case of rubidium 87 in the $F = 2$ hyperfine ground state, starting polarized in the $m_F = 2$ dressed state, $p(\psi) = \cos^8(\psi/2)$. The fraction $P(\Delta\varphi)$ of the atoms remaining in the right state is then an average of $\langle p(\psi) \rangle_\theta$ over the cloud size. For example, a phase jump of 10^{-2} rad will result at most in a loss of a fraction 10^{-4} of the atoms in states other than $m_F = 2$.

For a single phase jump, as illustrated experimentally in Section 3, the phase jump amplitude should then remain below 0.1 rad for limiting the losses to 1%. However,

even much smaller phase jumps should be avoided, if they are repeated. This is difficult to achieve with an analog synthesizer over a wide frequency sweep. By contrast, Direct Digital Synthesis (DDS) technology is well adapted to this requirement [19].

2.4 Frequency steps

The drawback of DDS technology is that, although the phase is continuous, the frequency is increased in successive discrete steps $\delta\nu$. A sudden change in the RF frequency also results in atomic losses, through the same mechanism as for phase jumps. The effective magnetic field rotates, at most, by the small angle $\delta\theta$ given by $\delta\theta = 2\pi\delta\nu/(\gamma B_{\mathrm{RF}}/2)$. For a linear ramp with N steps over a frequency range $\Delta\nu = N\delta\nu$, the fraction of atoms remaining after the full ramp is of order $[\cos(\delta\theta/2)]^{4FN}$. Given the expression for $\delta\theta$, this reads:

$$\left[\cos\left(\frac{2\pi\Delta\nu}{N\gamma B_{\mathrm{RF}}}\right)\right]^{4FN} \simeq 1 - \frac{F}{2N}\left(\frac{4\pi\Delta\nu}{\gamma B_{\mathrm{RF}}}\right)^2. \quad (6)$$

Thus, for the remaining fraction to be larger than 95%, the number of frequency steps should be larger than $N_{\min}$, where $N_{\min} = 10F(4\pi\Delta\nu/\gamma B_{\mathrm{RF}})^2$. For example, for a 2 MHz ramp with a typical RF amplitude of 200 mG, it yields $N_{\min} = 16\,000$.

In addition to this loss effect, a sudden change in the RF frequency results in a sudden shift of the position of the RF-dressed trap. This may cause dipolar heating of the atoms, especially if this frequency change occurs every trap period. The frequency steps should thus be as small as possible, a few tens Hz to a hundred Hz typically.

3 Results

3.1 Experimental set-up

As mentioned in Section 2, the RF signal is used for producing a bubble-like trap, where ultracold rubidium atoms are accumulated at the bottom of the surface. The trap is very anisotropic with stronger confinement in the vertical direction [7]. For the RF-dressed trap to be efficiently loaded from a Ioffe-Pritchard static magnetic trap, the RF frequency ν_{RF} is ramped up from 1 MHz to a final fixed frequency ν_{RF}^{end} ranging from 2 to 10 MHz. The static magnetic field, necessary both for magnetic trapping and RF-induced trapping, is always present. A typical ramp is shown on Figure 1. The frequency is ramped more slowly around 1.3 MHz, corresponding to the resonant frequency at the centre of the magnetic trap where adiabaticity of spin rotation is more difficult to obtain. At the end of this ramp, which may last between 75 ms and 500 ms, the RF frequency is held between 0.1 and 10 s for recording the lifetime and heating rate of the atoms in the RF-based trap.

In order to control the RF amplitude, a programmable RF attenuator Minicircuits ZAS-3 is driven by an analog output channel of a National Instrument PC card PCI-6713. This attenuator adds 5.1 dB of amplitude noise. At the output of the attenuator, the RF signal is amplified by a HD Communications Corp. class-AB amplifier HD19168. Its gain is 40 dB and its noise figure is typically +7 dB according to the manufacturer specifications. This 12 dB total excess noise was still too low for the amplitude noise to have a significant effect on the atoms, and we did not observe any parametric heating in our experiments. The RF field is then produced by a small circular antenna of 3 cm diameter. The field is linearly polarised and its amplitude B_{RF} may be adjusted between 70 and 700 mG.

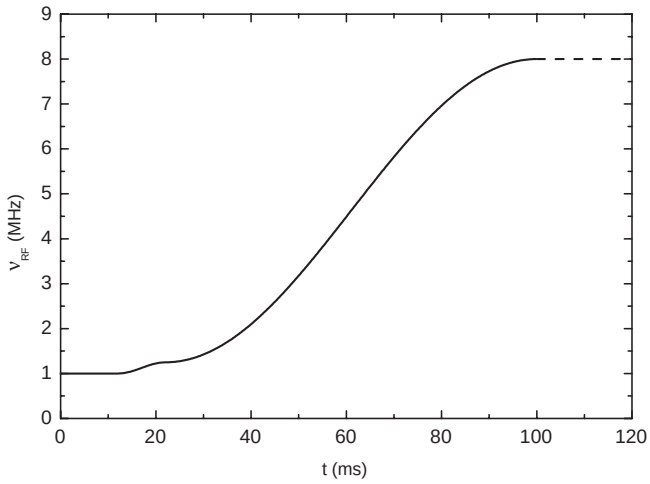

Fig. 1. Typical shape of a radio-frequency ramp applied to the ultracold atomic sample. In the present example ν_{RF} is increased from 1 to 8 MHz within 88 ms, after a 12 ms stage where the frequency is maintained at 1 MHz for adiabatic switching of the RF source. At the end of the ramp, the RF frequency is maintained at its final value for some holding time in the RF-based trap, dashed line.

In the following, we present three kinds of measurements performed with different RF sources. First, we investigate the effect of a single phase jump at the end of the ramp on the trapped atom number, for a fixed holding time. Second, the number of frequency steps during the ramp is varied and the final number of atoms is recorded together with the temperature. Finally, the holding time is varied to measure the lifetime and heating rate in the RF-based trap, for three different RF-sources. The atom number and the temperature are measured after a ballistic expansion of 10 ms by absorption imaging on a CCD camera.

3.2 Phase jump

The effect of a phase jump is tested in the following way. The RF frequency is swept from 1 MHz to 3 MHz with a Stanford DS-345 DDS. The 1500 points frequency ramp is non linear, with a slower zone around the resonance crossing at 1.3 MHz in the spirit of the typical ramp depicted on Figure 1. The RF antenna is then switched to a second independent synthesizer, a Rohde & Schwartz

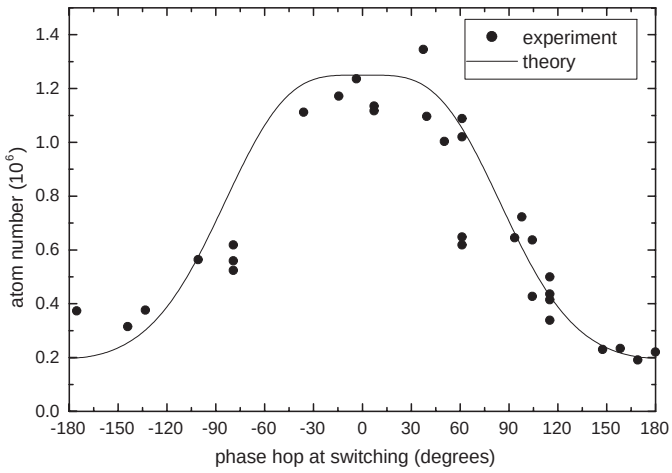

Fig. 2. Number of atoms remaining 1 s after switching between the two synthesizers as a function of the phase jump. Experimental data, full circles, are compared to a calculation, full line, with an RF amplitude of 470 mG and a temperature of 4 μK.

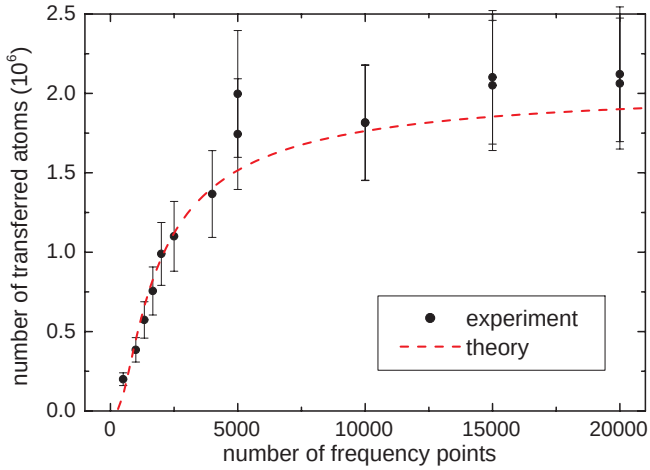

Fig. 3. (Color online) Number of atoms remaining 1 s after the transfer ramp, as a function of the number of frequency points in the arbitrary ramp. Circles: experimental data. Dashed line: prediction of the model of equation (6).

SML-01 maintained at a fixed frequency of 3 MHz for the full holding time (dashed line of Fig. 1). The phase difference is not controlled at the switching, but is monitored for each experiment with an oscilloscope. The final atom number is recorded after a 1 s holding time. The results are presented on Figure 2, full circles. For the maximum phase jump, π, 80% of the atoms are lost. This figure depends on the atomic temperature, the losses being higher at lower temperature, and is well reproduced by theory, as shown on Figure 2, black line. The theoretical curve is calculated for the experimental RF amplitude of 470 mG by averaging the loss probability over the positions of the atoms, as deduced from a thermal distribution at the measured temperature of 4 μK. The fact that the trap is able to hold two of the five spin components of the $F = 2$ hyperfine state is taken into account, by using $p(\psi) = \cos^8(\psi/2) + 4\cos^6(\psi/2)\sin^2(\psi/2)$, see Section 2.3 for the definition of the probability $p(\psi)$. The overall amplitude is set to the initial atom number in the magnetic trap before transfer into the RF-based trap, measured independently. We find a very good agreement between the experimental results and the simple theory developed above, with no adjustable parameter.

3.3 Frequency steps

As discussed in Section 2.4, the transfer efficiency is expected to depend on the number of frequency steps in the ramp, when a DDS device is used. To evaluate the number of required steps, we repeated the following procedure, varying only the number of frequency points in the arbitrary ramp. The atoms were cooled in the magnetic trap down to 10 μK. After an adiabatic switching of the RF up to $B_{\mathrm{RF}} = 550$ mG in 12 ms, the RF frequency was ramped from 1 MHz to 8 MHz in 88 ms to transfer the atoms in the RF-based trap. The number of transferred atoms and their temperature was recorded after 1 s in the trap. This time was short as compared to the lifetime in the RF-based trap, which reached 25 s for this experiment. The arbitrary ramp is depicted on Figure 1. It consisted in a constant plateau of 12 ms followed by two connected cosine branches of 10 ms and 78 ms respectively, in order to cross the resonance at 1.25 MHz more slowly. For these experiments, the sine-wave output of a Tabor Electronics DDS synthesizer, model WW1072, was used. The number of frequency points N was varied between 500 and 20 000 which is the maximum value for this device. These frequency lists were constructed by removing uniformly a fraction of the points of a reference arbitrary ramp of 20 000 points. Only 88% of these points really contributed to the frequency ramp, as 12% of them were used for maintaining a constant frequency for the initial switching stage.

The results for atom number and temperature are presented on Figures 3 and 4 respectively. The initial atom number in the magnetic trap was measured to be $2.05 \pm 0.2 \times 10^6$. Two regimes are clearly identified. Below $N = 5\,000$, the number of transferred atoms increases almost linearly with N. Above this value, more than 80% of the atoms are transferred into the RF-based trap, and the number of atoms detected for N larger than 15 000 is even equal to the initial atom number. To compare with the theory of Section 2.4, the expected value of the transferred number given by both the measured initial atom number and equation (6) is plotted together with the data, dashed line. The number of frequency steps considered in the calculation is $0.88N$, as the initial points at constant frequency do not induce losses. The theory reproduces well the overall behaviour, even if it slightly underestimates the transfer efficiency at large N. In particular, it predicts a transfer efficiency reaching 80% for $N = 7\,000$. The transfer efficiency is expected to reach 93% for $N = 20\,000$, which is consistent with the experiment within the uncertainty.

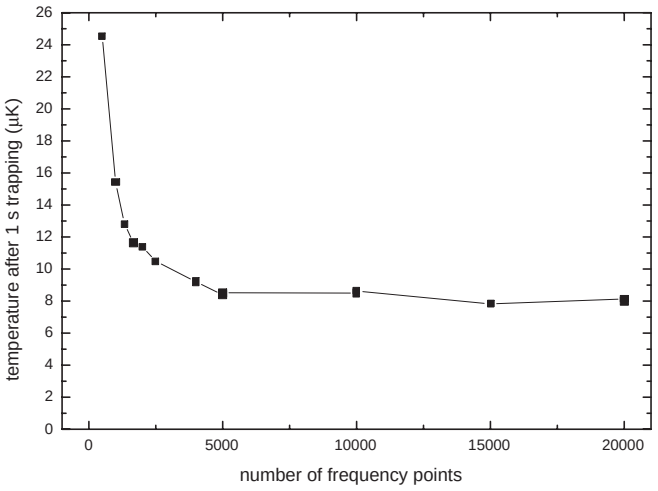

Fig. 4. Temperature of the transferred atoms, measured 1 s after the end of the transfer ramp, as a function of the number of frequency points in the arbitrary ramp. The initial temperature in the magnetic trap was 10 μK. The solid line is a guide to the eye.

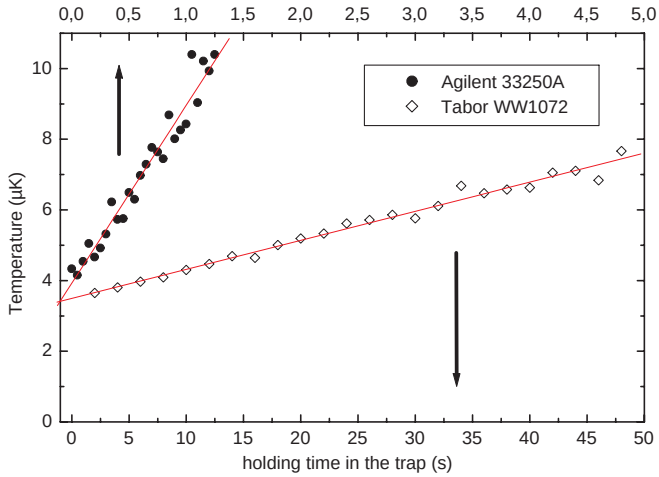

Fig. 5. (Color online) Comparison of heating of the atomic cloud in the bubble trap: Agilent 33250A synthesizer driven by NI board, full circles, or Tabor Electronics WW1072, open diamonds, is used for producing the RF ramp and the final radio-frequency ν_{RF}^{end}. Note that the horizontal scales differ by a factor 10 for the two data sets. We observe a heating rate of 5.0 μK s^{-1} in the first case and 0.082 μK s^{-1} the second one, as given by a linear fit, full lines. The lifetime reaches 32 s in this situation.

Below 5 000 points, the lack of frequency resolution in the ramp is also visible in the temperature data, Figure 4, as a clear temperature increase during the loading phase. This is explained by the excitation of the dipolar mode through sudden changes in the trap position at each frequency change, as explained in Section 2.4. For more than 5 000 frequency points, the temperature reaches the asymptotic value of 8 μK. This value is smaller than the initial temperature in the magnetic trap. This was expected as the geometric mean of the oscillation frequencies is much larger in the initial trap. The transfer within 88 ms is not fully adiabatic in this respect, the expected temperature in the RF-based trap being on the order of 2 μK for an adiabatic transfer.

3.4 Frequency noise

The heating rate in the dressed trap was measured with three different RF sources. First, we used an Agilent 33250A analog synthesizer with an RF amplitude of 500 mG for both the frequency ramp and the final holding frequency. Such RF analog synthesizers operated at fixed frequency exhibit very good relative frequency noise in most cases, typically at the -180 dB Hz^{-1} level or better. However, as mentioned by Colombe et al. [7] and confirmed by White et al. [15], the relative frequency noise increases by a few decades when a large range frequency sweep is required, as the output frequency then needs to be driven with an external analog voltage. The external voltage control was provided by a PC analog board (NI 6713), such that the modulation depth was ± 1 MHz on a central frequency of 2 MHz. We obtained both a short lifetime, typically 400 ms at $1/e$, and a strong linear heating, as shown on Figure 5 full circles. The heating rate is measured to be 5.0 μK s^{-1}. This rate, given the RF amplitude, corresponds to a relative frequency noise of $S_{\rm rel} = -100$ dB Hz^{-1} at the trap frequency of 600 Hz, see Section 2. An independent measurement of the spectral width of the RF signal produced by the Agilent synthesizer in the same conditions indeed gave the same value for the relative frequency noise $S_{\rm rel} = -100$ dB Hz^{-1}. This noise is quite high because the frequency is varied with a large modulation depth ($\Delta f/f = 1$) and the voltage noise of the NI board is directly translated into frequency noise.

We also measured the lifetime and heating rate with the setup used for phase jump characterisation, with the disadvantage however that the random phase jumps resulted in a large dispersion in the atom number data. Nevertheless, within a precision limited to 0.1 μK s^{-1} and 2 s respectively, we observed no heating and a lifetime of order 4.5 s [7]. These good results are linked to the excellent frequency stability of the second device used at fixed frequency.

Finally, the lifetime and heating measurement was repeated with the Tabor Electronics WW1072 device mentioned previously. The loading ramp was the same as described above, with 20 000 frequency points between 1 and 8 MHz, but with a total duration of 500 ms. Typical results are presented on Figure 5, open diamonds. The contrast with the Agilent data is very strong. With the Tabor device and an RF amplitude of 550 mG, the lifetime increased up to 32 s, a value comparable with the lifetime in the static magnetic trap. A small linear heating rate of 82 ± 5 nK s^{-1} is still present in the RF-based trap for this data set. No exponential parametric heating is measurable. The residual heating rate is slightly larger than the one predicted from the Tabor device specifications. At 8 MHz and for an oscillation frequency of 600 Hz, we

expect a linear heating rate of 17 $\mathrm{nK\,s^{-1}}$. This value is slightly smaller than 33 $\mathrm{nK\,s^{-1}}$, which is the lowest observed heating rate with the Tabor device.

4 Conclusion

In this paper, we set the requirements on the RF source quality for trapping in RF-induced adiabatic potentials. We present the effects of frequency noise, amplitude noise, phase jumps and finite frequency resolution. The consequence of a frequency jitter, discrete frequency steps and a random phase jump are then demonstrated experimentally.

RF source requirements may be divided into two parts, concerning the ramping stage and the holding stage. Once the atoms are loaded in the RF-based trap, heating and trap losses are avoided if the relative frequency noise and the amplitude noise are below $S_{\mathrm{rel}}(\nu_z) = -118$ $\mathrm{dB\,Hz^{-1}}$ and $S_a < -90$ $\mathrm{dB\,Hz^{-1}}$ respectively. This is relatively easy to meet, although care has to be taken on the choice of low noise RF attenuators and amplifiers. The best results were obtained with the Tabor Electronics device, with a typical heating rate of 0.082 $\mu\mathrm{K\,s^{-1}}$ and a lifetime of up to 32 s. Finally, the lifetime would be affected if the RF amplitude is below a few tens of mG, as Landau-Zener losses then occur at the avoided crossing [20].

For the initial frequency sweep, the use of DDS technology ensures phase continuity, and losses or heating are limited if the number of frequency points is large enough, say, 10 000 at least for a few MHz ramp. In the loading stage, once the number of frequency steps is sufficient, the heating will mostly be given by the non adiabatic deformation of the trapping potential when the atoms are transferred from the magnetic to the dressed trap. As the value of the lowest oscillation frequency in the dressed trap is of the order of a few Hz, this heating may be difficult to avoid. On the other hand, cooling directly in the RF-based trap is made possible by the long lifetimes and low heating rates reported here [21,22]. In any case, these good performances make the RF-based trap compatible with the confinement of Bose-Einstein condensates.

This work was supported by the Région Ile-de-France (contract number E1213) and by the European Community through the Research Training Network 'FASTNet' under contract number HPRN-CT-2002-00304 and Marie Curie Training Network 'Atom Chips' under contract number MRTN-CT-2003-505032. Laboratoire de physique des lasers is UMR 7538 of CNRS and Paris 13 University. The LPL is a member of the Institut Francilien de Recherche sur les Atomes Froids.

References

1. H.F. Hess, Phys. Rev. B **34**, 3476 (1986)
2. N. Masuhara, J.M. Doyle, J.C. Sandberg, D. Kleppner, T.J. Greytak, H.F. Hess, G.P. Kochanski, Phys. Rev. Lett. **61**, 935 (1988)
3. E.A. Cornell, C.E. Wieman, Rev. Mod. Phys. **74**, 875 (2002)
4. W. Ketterle, Rev. Mod. Phys. **74**, 1131 (2002)
5. C.A. Regal, C. Ticknor, J.L. Bohn, D.S. Jin, Nature **424**, 47 (2003)
6. O. Zobay, B.M. Garraway, Phys. Rev. Lett. **86**, 1195 (2001)
7. Y. Colombe, E. Knyazchyan, O. Morizot, B. Mercier, V. Lorent, H. Perrin, Europhys. Lett. **67**, 593 (2004)
8. T. Schumm, S. Hofferberth, L.M. Andersson, S. Wildermuth, S. Groth, I. Bar-Joseph, J. Schmiedmayer, P. Krüger, Nature Phys. **1**, 57 (2005)
9. M.H.T. Extavour, L.J. Le Blanc, T. Schumm, B. Cieslak, S. Myrskog, A. Stummer, S. Aubin, J.H. Thywissen, Atomic Physics **20**, 241 (2006)
10. G.-B. Jo, Y. Shin, T.A. Pasquini, M. Saba, W. Ketterle, D.E. Pritchard, M. Vengalattore, M. Prentiss, Phys. Rev. Lett. **98**, 030407 (2007)
11. I. Lesanovsky, T. Schumm, S. Hofferberth, L.M. Andersson, P. Krüger, J. Schmiedmayer, Phys. Rev. A **73**, 033619 (2006)
12. Ph. W. Courteille, B. Deh, J. Fortàgh, A. Günther, S. Kraft, C. Marzok, S. Slama, C. Zimmermann, J. Phys. B **39**, 1055 (2006)
13. O. Morizot, Y. Colombe, V. Lorent, H. Perrin, B.M. Garraway, Phys. Rev. A **74**, 023617 (2006)
14. I. Lesanovsky, W. von Klitzing, Phys. Rev. Lett. **99**, 083001 (2007)
15. M. White, H. Gao, M. Pasienski, B. DeMarco, Phys. Rev. A **74**, 023616 (2006)
16. M.E. Gehm, K.M. O'Hara, T.A. Savard, J.E. Thomas, Phys. Rev. A **58**, 3914 (1998)
17. W. Ketterle, D.S. Durfee, D.M. Stamper-Kurn, *Making, probing and understanding Bose-Einstein condensates*, edited by M. Inguscio, S. Stringari, C.E. Wieman (IOS Press, Amsterdam, 1999) pp. 67–176
18. The factor $B_{\mathrm{RF}}/2$ arises from the fact that only half of the power of the linearly polarized RF has an effect on the atoms.
19. B.-G. Goldberg, *Digital Techniques in Frequency Synthesis* (Mac Graw-Hill, New-York, 1996)
20. O. Zobay, B.M. Garraway, Phys. Rev. A **69**, 023605 (2004)
21. C.L. Garrido Alzar, H. Perrin, B.M. Garraway, V. Lorent, Phys. Rev. A **74**, 053413 (2006)
22. S. Hofferberth, I. Lesanovsky, B. Fischer, J. Verdu, J. Schmiedmayer, Nature Phys. **2**, 710 (2006)

Chapitre 5

Conclusion

Nous avons démarré en 1999 un nouveau projet au Laboratoire de physique des lasers, avec l'intention d'étudier les gaz dégénérés en dimension restreinte, et plus particulièrement à deux dimensions. Cependant, la recherche n'est pas linéaire ; en chemin nous avons rencontré des difficultés imprévues et nous avons exploré de nouvelles possibilités qui ont orienté différemment notre recherche. La problématique des dimensions restreintes est restée le fil conducteur de nos expériences.

Notre première réalisation est celle d'un condensat à 3 mm seulement d'une surface, ce qui en janvier 2001 était une première. Partant de notre schéma initial de piège bidimensionnel, nos expériences avec une onde évanescente nous ont permis de mieux comprendre le rôle de la rugosité de surface et de confirmer quantitativement la théorie de Carsten Henkel *et al.*, ce qui est un point important pour les expériences, de plus en plus nombreuses, menées à proximité directe d'une surface [82, 114, 115]. Nous avons également montré que la diffraction était toujours clairement observable malgré la forte diffusion, lors du rebond d'un condensat sur un miroir modulé.

Pour ce qui concerne les expériences de piégeage avec des ondes évanescentes, supportées par un prisme diélectrique [32, 71], par une fibre optique [116] ou par un guide d'onde [117], la qualité de la surface restera probablement un élément important des dispositifs futurs. On peut certainement obtenir une surface de bien meilleure qualité que celle avec laquelle nous avons travaillé [78], et une rugosité de 0,1 nm est accessible commercialement [118]. Il peut être avantageux cependant de tirer parti de la forte rugosité pour un autre type d'expérience. En effet, deux équipes viennent de mettre en évidence en présence de désordre à une dimension la localisation d'Anderson dans les gaz quantiques dégénérés [119, 120]. Le désordre est produit soit par un *speckle* optique, soit par un réseau optique à deux longueurs d'ondes très proches. Il serait très intéressant de réaliser ce type d'expérience en dimension 2 [121], la question de la dimension étant cruciale dans cette physique. Pour cette application, un prisme diélectrique supportant un piège évanescent est un système potentiellement intéressant, en raison de la très faible longueur de corrélation du désordre, donnée par la rugosité de surface et donc non limitée à une fraction de la longueur d'onde optique. L'amplitude du désordre pourrait être ajustée par la distance du piège à la surface, qui dépend simplement de

l'angle d'incidence des faisceaux à l'interface diélectrique-vide, ou avec les amplitudes respectives des champs évanescents bleu et rouge. En quelque sorte, l'observation initiale du groupe de Rudi Grimm [68] constituait un premier pas vers une expérience de diffusion d'un condensat dans un potentiel désordonné bidimensionnel.

Les expériences impliquant des champs radiofréquence ont eu un impact important dans la communauté des atomes froids, en particulier pour les expériences sur puce. Les potentiels adiabatiques sont compatibles avec les condensats, et supportent également un refroidissement par évaporation, démontré très récemment dans l'équipe. Ils offrent une grande variété de géométries accessibles à l'expérience, combinés ou non avec d'autre types de potentiels. La proposition de faire varier dans le temps le champ magnétique du piège ajoute encore aux combinaisons possibles [113]. Parmi toutes ces configurations, la réalisation d'un anneau semble particulièrement prometteuse. Un superfluide dans un anneau est l'analogue d'un supraconducteur, où la rotation et la quantification du moment angulaire jouent le rôle du champ magnétique et de la quantification du flux. Un anneau de grand diamètre [122, 123, 124, 125] est souhaitable pour mener des expériences de mesure interférométriques de rotation, la sensibilité de l'interféromètre étant proportionnelle à son aire. Un anneau de petit diamètre est plus adapté à l'observation de vortex de charge multiple [111] et facilite le maintien de la cohérence tout autour. L'idéal est de pouvoir ajuster le rayon de l'anneau [39, 113]. Cela permettrait d'explorer le domaine mésoscopique, correspondant à un nombre de quanta de moment angulaire compris entre 10 et 1000.

Pour y parvenir, nous avons proposé un piège annulaire qui satisfait à cette exigence, avec un ajustement très simple de son rayon. Une variante de ce piège vient d'être démontrée expérimentalement [108]. L'avantage de l'utilisation d'une onde stationnaire pour le confinement vertical réside dans la possibilité d'utiliser un ou plusieurs anneaux, éventuellement couplés, en jouant sur l'angle entre les faisceaux qui produisent le réseau. C'est la géométrie envisagée par Anderson *et al.* pour réaliser un SQUID à atomes froids [126]. De plus, avec quelques anneaux on bénéficie d'une détection interférométrique, qui a montré sa sensibilité dans les expériences sur les gaz 2D [29]. On revient alors à notre fil conducteur : dans de tels anneaux, on a accès naturellement à une géométrie bidimensionnelle. L'analogie la plus parlante est alors celle avec les films d'hélium superfluide [127], et l'on pourrait explorer le même type de physique avec des interactions entre particules beaucoup plus faibles que dans l'hélium.

Bibliographie

[1] M.H. Anderson, J.R. Ensher, M.R. Matthews, C.E. Wieman et E.A. Cornell, « Observation of Bose-Einstein condensation in a dilute atomic vapor ». *Science* **269**, 198–201 (1995).

[2] K.B. Davis, M.-O. Mewes, M.R. Andrews, N.J. van Druten, D.S. Durfee, D.M. Kurn et W. Ketterle, « Bose-Einstein condensation in a gas of sodium atoms ». *Phys. Rev. Lett.* **75** (22), 3969–3973 (1995).

[3] E. A. Cornell et C. E. Wieman, « Nobel Lecture : Bose-Einstein condensation in a dilute gas, the first 70 years and some recent experiments ». *Rev. Mod. Phys.* **74**, 875 (2002).

[4] W. Ketterle, « When atoms behave as waves : Bose-Einstein condensation and the atom laser ». *Rev. Mod. Phys.* **74**, 1131 (2002).

[5] M. Inguscio, S. Stringari et C. E. Wieman (éditeurs), *Bose-Einstein Condensation in Atomic Gases, Proceedings of the International School of Physics "Enrico Fermi", Course CXL*, IOS Press, Amsterdam (1999).

[6] R. Kaiser, C. Westbrook et F. David (éditeurs), *Coherent matter waves, Proceedings of the Les Houches LXXII Summer School*, Springer (2001).

[7] V. Bagnato et D. Kleppner, « Bose-Einstein condensation in low-dimensional traps ». *Phys. Rev. A* **44** (11), 7439–7441 (1991).

[8] R.E. Prange et S. Girvin (éditeurs), *The Quantum Hall Effect*, Springer (1987).

[9] T. Chakraborty et P. Pietilinen, *The Quantum Hall Effects*. Springer, deuxième édition (1995).

[10] L. Pricoupenko, H. Perrin et M. Olshanii (éditeurs), *Proceedings of the Euroschool on quantum gases in low dimensions, Les Houches 2003*, J. Phys. IV (2004).

[11] D.S. Petrov, M. Holzmann et G.V. Shlyapnikov, « Bose-Einstein condensation in quasi-2D trapped gases ». *Phys. Rev. Lett.* **84** (12), 2551–2554 (2000).

[12] D.S. Petrov, G.V. Shlyapnikov et J.T.M. Walraven, « Regimes of quantum degeneracy in trapped 1D gases ». *Phys. Rev. Lett.* **85** (18), 3745–3749 (2000).

[13] D.S. Petrov et G.V. Shlyapnikov, « Interatomic collisions in a tightly confined Bose gas ». *Phys. Rev. A* **64**, 012 706, 1–14 (2001).

[14] F. Dalfovo, S. Giorgini, L.P. Pitaevskii et S. Stringari, « Theory of Bose-Einstein condensation in trapped gases ». *Rev. Mod. Phys.* **71** (3), 463–512 (1999).

[15] A. Görlitz, J.M. Vogels, A.E. Leanhardt, C. Raman, T.L. Gustavson, J.R. Abo-Shaeer, A.P. Chikkatur, S. Gupta, S. Inouye, T. Rosenband et W. Ketterle, « Realization of Bose-Einstein condensates in lower dimensions ». *Phys. Rev. Lett.* **87** (13), 130 402, 1–4 (2001).

[16] S. Dettmer, D. Hellweg, P. Ryytty, J.J. Arlt, W. Ertmer, K. Sengstock, D.S. Petrov, G.V. Shlyapnikov, H. Kreutzmann, L. Santos et M. Lewenstein, « Observation of phase fluctuations in elongated Bose-Einstein condensates ». *Phys. Rev. Lett.* **87** (16), 160 406, 1–4 (2001).

[17] S. Richard, F. Gerbier, J.H. Thywissen, M. Hugbart, P. Bouyer et A. Aspect, « Momentum spectroscopy of 1D phase fluctuations in Bose-Einstein condensates ». *Phys. Rev. Lett.* **91** (1), 010 405, 1–4 (2003).

[18] M. Hugbart, J. A. Retter, F. Gerbier, A. F. Varón, S. Richard, J. H. Thywissen, D. Clément, P. Bouyer et A. Aspect, « Coherence length of an elongated condensate ». *Eur. Phys. J. D* **35**, 155 (2005).

[19] J. Estève, J.-B. Trebbia, T. Schumm, A. Aspect, C.I. Westbrook et I. Bouchoule, « Observations of Density Fluctuations in an Elongated Bose Gas : Ideal Gas and Quasicondensate Regimes ». *Phys. Rev. Lett.* **96**, 130 403 (2006).

[20] L. Tonks, « The complete equation of state of one, two and three-dimensional gases of hard elastic spheres ». *Phys. Rev.* **50** (10), 955–963 (1936).

[21] M. Girardeau, « Relationship between systems of impenetrable bosons and fermions in one dimension ». *J. Math. Phys.* **1**, 516–523 (1960).

[22] M. Olshanii, « Atomic scattering in the presence of an external confinement and a gas of impenetrable bosons ». *Phys. Rev. Lett.* **81** (5), 938–941 (1998).

[23] B. Paredes, A. Widera, V. Murg, O. Mandel, S. Fölling, I. Cirac, G.V. Shlyapnikov, T.W. Hänsch et I. Bloch, « Tonks-Girardeau gas of ultracold atoms in an optical lattice ». *Nature* **429**, 277 (2004).

[24] T. Kinoshita, T. R. Wenger et D. S. Weiss, « Observation of a one-dimensional Tonks-Girardeau gas ». *Science* **305**, 1125 (2004).

[25] B. Paredes, P. Fedichev, J. I. Cirac et P. Zoller, « 1/2-Anyons in small atomic Bose-Einstein condensates ». *Phys. Rev. Lett.* **87**, 010 402 (2001).

[26] V. Berezinskii, « Destruction of long-range order in one-dimensional and 2-dimensional systems having a continuous symmetry group, 1 - classical systems ». *Sov. Phys. JETP-USSR* **32**, 493 (1971).

[27] V. Berezinskii, « Destruction of long-range order in one-dimensional and 2-dimensional systems having a continuous symmetry group, 2 - quantum systems ». *Sov. Phys. JETP-USSR* **34**, 610 (1972).

[28] J.M. Kosterlitz et D.J. Thouless, « Ordering, metastability and phase transitions in two-dimensional systems ». *J. Phys. C : Solid State Phys.* **6**, 1181–1203 (1973).

[29] Z. Hadzibabic, P. Krüger, M. Cheneau, B. Battelier et J. Dalibard, « Berezinskii-Kosterlitz-Thouless crossover in a trapped atomic gas ». *Nature* **441**, 1118 (2006).

[30] J. Reichel, W. Hänsel et T.W. Hänsch, « Atomic Micromanipulation with Magnetic Surface Traps ». *Phys. Rev. Lett.* **83**, 3398 (1999).

[31] R. Folman, P. Krüger, J. Schmiedmayer, J. Denschlag et C. Henkel, « Microscopic atom optics : from wires to an atom chip ». *Adv. At. Mol. Opt. Phys.* **48**, 263 (2002).

[32] Yu.B. Ovchinnikov, S.V. Shul'ga et V.I. Balykin, « An atomic trap based on evanescent light waves ». *J. Phys. B : At. Mol. Opt. Phys.* **24**, 3173–3178 (1991).

[33] Y. Colombe, D. Kadio, M. Olshanii, B. Mercier, V. Lorent et H. Perrin, « Schemes for loading a Bose-Einstein condensate into a two-dimensional dipole trap ». *J. Opt. B : Quantum Semiclass. Opt.* **5**, S155–S163 (2003).

[34] H. Perrin, Y. Colombe, B. Mercier, V. Lorent et C. Henkel, « Diffuse reflection of a Bose-Einstein condensate from a rough evanescent wave mirror ». *J. Phys. B : At. Mol. Opt. Phys.* **39**, 4649–4658 (2006).

[35] O. Zobay et B.M. Garraway, « Two-dimensional atom trapping in field-induced adiabatic potentials ». *Phys. Rev. Lett.* **86** (7), 1195–1198 (2001).

[36] Y. Colombe, E. Knyazchyan, O. Morizot, B. Mercier, V. Lorent et H. Perrin, « Ultracold atoms confined in rf-induced two-dimensional trapping potentials ». *Europhys. Lett.* **67** (4), 593–599 (2004).

[37] O. Morizot, C.L. Garrido Alzar, P.-E. Pottie, V. Lorent et H. Perrin, « Trapping and cooling of rf-dressed atoms in a quadrupole magnetic field ». *J. Phys. B : At. Mol. Opt. Phys.* **40**, 4013–4022 (2007).

[38] T. Schumm, S. Hofferberth, L.M. Andersson, S. Wildermuth, S. Groth, I. Bar-Joseph, J. Schmiedmayer et P. Krüger, « Matter wave interferometry in a double well on an atom chip ». *Nature Phys.* **1**, 57 (2005).

[39] O. Morizot, Y. Colombe, V. Lorent, H. Perrin et B.M. Garraway, « Ring trap for ultracold atoms ». *Phys. Rev. A* **74**, 023 617 (2006).

[40] C.L. Garrido Alzar, H. Perrin, B.M. Garraway et V. Lorent, « Evaporative cooling in a radio-frequency trap ». *Phys. Rev. A* **74**, 053 413 (2006).

[41] M.H.T. Extavour, L.J. Le Blanc, T. Schumm, B. Cieslak, S. Myrskog, A. Stummer, S. Aubin and J.H. Thywissen, « Dual-species quantum degeneracy of ^{40}K and ^{87}Rb on an atom chip ». *Atomic Physics* **20**, 241 (2006).

[42] G.-B. Jo, Y. Shin, T.A. Pasquini, M. Saba, W. Ketterle and D.E. Pritchard, M. Vengalattore and M. Prentiss, « Long phase coherence time and number squeezing of two Bose-Einstein condensates on an atom chip ». *Phys. Rev. Lett.* **98**, 030 407 (2007).

[43] M. White, H. Gao, M. Pasienski et B. DeMarco, « Bose-Einstein condensates in rf-dressed adiabatic potentials ». *Phys. Rev. A* **74** (2), 023 616 (2006).

[44] Y. Colombe, *Condensat de Bose-Einstein, champs évanescents et piégeage bidimensionnel*. Thèse de doctorat, Université Paris XIII (2004).

[45] O. Morizot, *Pièges radiofréquence très anisotropes pour un condensat de Bose-Einstein*. Thèse de doctorat, Université Paris XIII (2007).

[46] P. Szriftgiser, *Cavité gravitationnelle et optique atomique temporelle*. Thèse de doctorat, Université Paris VI (1996).

[47] T. Esslinger, I. Bloch et T.W. Hänsch, « Bose-Einstein condensation in a quadrupole-Ioffe-configuration trap ». *Phys. Rev. A* **58** (4), R2664–R2667 (1998).

[48] W. Wohlleben, F. Chevy, K. Madison et J. Dalibard, « An atom faucet ». *Eur. Phys. J. D* **15**, 237–244 (2001).

[49] E. Dimova, O. Morizot, G. Stern, C.L. Garrido Alzar, A. Fioretti, V. Lorent, D. Comparat et H. Perrin, « Continuous transfer and laser guiding between two cold atom traps ». *Eur. Phys. J. D* **42**, 299 (2007).

[50] O. Morizot, *Conception et construction d'un piège magnéto-optique alimenté par un distributeur séquentiel de rubidium*. Stage de fin d'études de l'École Supérieure d'Optique (2003).

[51] Y. Levy, « Étude du champ inhomogène obtenu par la réflexion totale d'une onde plane sur un système de couches minces ». *Nouv. Rev. d'Optique appliquée* **3** (1), 25–30 (1972).

[52] R. Kaiser, Y. Lévy, N. Vansteenkiste, A. Aspect, W. Seifert, D. Leipold et J. Mlynek, « Resonant enhancement of evanescent waves with a thin dielectric waveguide ». *Opt. Commun.* **104**, 234–240 (1994).

[53] W. Seifert, R. Kaiser, A. Aspect et J. Mlynek, « Reflection of atoms from a dielectric wave guide ». *Opt. Commun.* **111**, 566–576 (1994).

[54] G. Labeyrie, A. Landragin, J. von Zanthier, R. Kaiser, N. Vansteenkiste, C. Westbrook et A. Aspect, « Detailed study of a high-finesse planar waveguide for evanescent wave atomic mirrors ». *Quantum Semiclass. Opt.* **8** (3), 603–627 (1996).

[55] O. Morizot, L. Longchambon, R. Kollengode Easwaran, R. Dubessy, E. Knyazchyan, P.-E. Pottie, V. Lorent et H. Perrin, « Influence of the Radio-Frequency source properties on RF-based atom traps ». *Eur. Phys. J. D* **47**, 209 (2008).

[56] O. Morizot, J. De Lapeyre de Bellair, F. Wiotte, O. Lopez, P.-E. Pottie et H. Perrin, « Agile low phase noise radio-frequency sine wave generator applied to experiments on ultracold atoms » (2007). Preprint arXiv:0704.1974v1, http://arxiv.org/abs/0704.1974.

[57] R.J. Cook et R.K. Hill, « An electromagnetic mirror for neutral atoms ». *Opt. Commun.* **43** (4), 258–260 (1982).

[58] V.I. Balykin, V.S. Letokhov, Yu.B. Ovchinnikov et A.I. Sidorov, « Reflection of an atomic beam from a gradient of an optical field ». *JETP Lett.* **45** (6), 353–356 (1987).

[59] M.A. Kasevich, D.S. Weiss et S. Chu, « Normal-incidence reflection of slow atoms from an optical evanescent wave ». *Opt. Lett.* **15** (11), 607–609 (1990).

[60] C.G. Aminoff, A.M. Steane, P. Bouyer, P. Desbiolles, J. Dalibard et C. Cohen-Tannoudji, « Cesium atoms bouncing in a stable gravitational cavity ». *Phys. Rev. Lett.* **71** (19), 3083–3086 (1993).

[61] A. Landragin, J.-Y. Courtois, G. Labeyrie, N. Vansteenkiste, C.I. Westbrook et A. Aspect, « Measurement of the van der Waals force in an atomic mirror ». *Phys. Rev. Lett.* **77** (8), 1464–1467 (1996).

[62] H. Perrin, A. Kuhn, I. Bouchoule et C. Salomon, « Sideband cooling of neutral atoms in a far-detuned optical lattice ». *Europhys. Lett.* **42**, 395 (1998).

[63] I. Bouchoule, H. Perrin, A. Kuhn, M. Morinaga et C. Salomon, « Neutral atoms prepared in Fock states of a one-dimensional harmonic potential ». *Phys. Rev. A* **59**, R8 (1999).

[64] Z. Hadzibabic, S. Stock, B. Battelier, V. Bretin et J. Dalibard, « Interference of an Array of Independent Bose-Einstein Condensates ». *Phys. Rev. Lett.* **93**, 180 403 (2004).

[65] J. Söding, R. Grimm et Yu.B. Ovchinnikov, « Gravitational laser trap for atoms with evanescent-wave cooling ». *Opt. Commun.* **119**, 652–662 (1995).

[66] Yu.B. Ovchinnikov, I. Manek et R. Grimm, « Surface trap for Cs atoms based on evanescent-wave cooling ». *Phys. Rev. Lett.* **79** (12), 2225–2228 (1997).

[67] P. Desbiolles, M. Arndt, P. Szriftgiser et J. Dalibard, « Elementary Sisyphus process close to a dielectric surface ». *Phys. Rev. A* **54** (5), 4292–4298 (1996).

[68] D. Rychtarik, B. Engeser, H.-C. Nägerl et R. Grimm, « Two-dimensional Bose-Einstein condensate in an optical surface trap ». *Phys. Rev. Lett.* **92** (17), 173 003, 1–4 (2004).

[69] H. Gauck, M. Hartl, D. Schneble, H. Schnitzler, T. Pfau et J. Mlynek, « Quasi-2D gas of laser cooled atoms in a planar matter waveguide ». *Phys. Rev. Lett.* **81** (24), 5298–5301 (1998).

[70] M. Hammes, D. Rychtarik, H.-C. Nägerl et R. Grimm, « Cold-atom gas at very high densities in an optical surface microtrap ». *Phys. Rev. A* **66** (5), 051 401 (2002).

[71] M. Hammes, D. Rychtarik, B. Engeser, H.-C. Nägerl et R. Grimm, « Evanescent-wave trapping and evaporative cooling of an atomic gas at the crossover to two dimensions ». *Phys. Rev. Lett.* **90** (17), 173 001, 1–4 (2003).

[72] A. Landragin, *Réflexion d'atomes sur un miroir à onde évanescente : mesure de la force de van der Waals et diffraction atomique*. Thèse de doctorat, Université Paris XI (1997).

[73] R. Grimm, M. Weidemüller et Yu.B. Ovchinnikov, « Optical dipole traps for neutral atoms ». *Adv. At. Mol. Opt. Phys.* **42**, 95–170 (2000).

[74] Y. Colombe, H. Perrin, B. Mercier et V. Lorent, « Adiabatic transportation of a Bose-Einstein condensate to a dielectric surface ». *J. Phys. IV (Proceedings)* **119**, 159 (2004).

[75] A. Messiah, *Mécanique quantique*. Dunod (2003).

[76] D. Schrader, S. Kuhr, W. Alt, M. Müller, V. Gomer et D. Meschede, « An optical conveyor belt for single neutral atoms ». *Appl. Phys. B* **73**, 819–824 (2001).

[77] W. Hänsel, J. Reichel, P. Hommelhoff et T.W. Hänsch, « Magnetic conveyor belt for transporting and merging trapped atom clouds ». *Phys. Rev. Lett.* **86** (4), 608–611 (2001).

[78] A. Landragin, G. Labeyrie, K. Henkel, R. Kaiser, N. Vansteenkiste, C.I. Westbrook et A. Aspect, « Specular versus diffuse reflection of atoms from an evanescent-wave mirror ». *Opt. Lett.* **21** (19), 1591–1593 (1996).

[79] C. Henkel, *Réflexion et diffraction d'atomes lents par un miroir à onde évanescente*. Thèse de doctorat, Université Paris XI (1996).

[80] C. Henkel, K. Mølmer, R. Kaiser, N. Vansteenkiste, C.I. Westbrook et A. Aspect, « Diffuse atomic reflection at a rough mirror ». *Phys. Rev. A* **55** (2), 1160–1178 (1997).

[81] M. Boyd, E.W. Streed, P. Medley, G.K. Campbell, J. Mun, W. Ketterle et D.E. Pritchard, « Atom trapping with a thin magnetic film ». *Preprint arXiv :* pages cond–mat/0608 370 (2006).

[82] J. Estève, C. Aussibal, T. Schumm, C. Figl, D. Mailly, I. Bouchoule, C.I. Westbrook et A. Aspect, « Role of wire imperfections in micromagnetic traps for atoms ». *Phys. Rev. A* **70** (4), 043 629 (2004).

[83] T. Schumm, J. Estève, C. Figl, J.-B. Trebbia, C. Aussibal, H. Nguyen, D. Mailly, I. Bouchoule, C.I. Westbrook et A. Aspect, « Atom chips in the real world : the effects of wire corrugation ». *Eur. Jour. Phys. D* **32** (2), 171 (2005).

[84] J. Fortágh, H. Ott, S. Kraft, A. Günther et C. Zimmermann, « Surface effects in magnetic microtraps ». *Phys. Rev. A* **66** (4), 041 604 (2002).

[85] A. E. Leanhardt, A. P. Chikkatur, D. Kielpinski, Y. Shin, T. L. Gustavson, W. Ketterle et D. E. Pritchard, « Propagation of Bose-Einstein Condensates in a Magnetic Waveguide ». *Phys. Rev. Lett.* **89** (4), 040 401 (2002).

[86] S. Kraft, A. Günther, H. Ott, D. Wharam, Zimmermann C. et J. Fortágh, « Anomalous longitudinal magnetic field near the surface of copper conductors ». *J. Phys. B : At. Mol. Opt. Phys.* **35** (21), L469 (2002).

[87] M. P. A. Jones, C. J. Vale, D. Sahagun, B. V. Hall, C. C. Eberlein, B. E. Sauer, K. Furusawa, D. Richardson et E. A. Hinds, « Cold atoms probe the magnetic field near a wire ». *J. Phys. B : At. Mol. Opt. Phys.* **37** (2), L15 (2004).

[88] M.R. Andrews, C.G. Townsend, H.-J. Miesner, D.S. Durfee, D.M. Kurn et W. Ketterle, « Observation of interference between two Bose condensates ». *Phys. Rev. Lett.* **275** (5300), 637 (1997).

[89] A. Steane, P. Szriftgiser, P. Desbiolles et J. Dalibard, « Phase modulation of atomic de Broglie waves ». *Phys. Rev. Lett.* **74** (25), 4972–4975 (1995).

[90] K. Bongs, S. Burger, G. Birkl, K. Sengstock, W. Ertmer, K. Rzazewski, A. Sanpera et M. Lewenstein, « Coherent evolution of bouncing Bose-Einstein condensates ». *Phys. Rev. Lett.* **83** (18), 3577–3580 (1999).

[91] C. Henkel, A.M. Steane, R. Kaiser et J. Dalibard, « A modulated mirror for atomic interferometry ». *J. Phys. II France* **4** (11), 1877–1896 (1994).

[92] P. Szriftgiser, D. Guéry-Odelin, M. Arndt et J. Dalibard, « Atomic wave diffraction and interference using temporal slits ». *Phys. Rev. Lett.* **77** (1), 4–7 (1996).

[93] Y. Colombe, B. Mercier, H. Perrin et V. Lorent, « Diffraction of a Bose-Einstein Condensate in the Time Domain ». *Phys. Rev. A* **72**, 061 601 (2005).

[94] Ph.W. Courteille, B. Deh, J. Fortàgh, A. Günther, S. Kraft, C. Marzok, S. Slama, C. Zimmermann, « Highly versatile atomic micro traps generated by multifrequency magnetic field modulation ». *J. Phys. B : At. Mol. Opt. Phys.* **39**, 1055 (2006).

[95] I. Lesanovsky, T. Schumm, S. Hofferberth, L. M. Andersson, P. Krüger, J. Schmiedmayer, « Adiabatic radio frequency potentials for the coherent manipulation of matter waves ». *Phys. Rev. A* **73**, 033 619 (2006).

[96] H. F. Hess, « Evaporative cooling of magnetically trapped and compressed spin-polarized hydrogen ». *Phys. Rev. B* **34**, 3476 (1986).

[97] N. Masuhara, J. M. Doyle, J. C. Sandberg, D. Kleppner, T. J. Greytak, H. F. Hess et G. P. Kochanski, « Evaporative cooling of spin-polarized atomic hydrogen ». *Phys. Rev. Lett.* **61**, 935 (1988).

[98] A.J. Moerdijk, B.J. Verhaar et T.M. Nagtegaal, « Collisions of dressed ground-state atoms ». *Phys. Rev. A* **53** (6), 4343–4351 (1996).

[99] R.J.C. Spreeuw, C. Gerz, L.S. Goldner, W.D. Phillips, S.L. Rolston, C.I. Westbrook, M.W. Reynolds et I.F. Silvera, « Demonstration of neutral atom trapping with microwaves ». *Phys. Rev. Lett.* **72** (20), 3162–3165 (1994).

[100] D.T. Pegg et G.W. Series, « Semi-classical theory of the Hanle effect with transverse static and oscillating magnetic fields ». *J. Phys. B : Atom. Mol. Phys.* **3**, L33 (1970).

[101] S. Hofferberth, I. Lesanovsky, B. Fischer, J. Verdu et J. Schmiedmayer, « Radiofrequency-dressed-state potentials for neutral atoms ». *Nature Phys.* **2**, 710 (2006).

[102] O. Zobay et B.M. Garraway, « Atom trapping and two-dimensional Bose-Einstein condensates in field-induced adiabatic potentials ». *Phys. Rev. A* **69**, 023 605, 1–15 (2004).

[103] M.E. Gehm, K.M. O'Hara, T.A. Savard et J.E. Thomas, « Dynamics of noise-induced heating in atom traps ». *Phys. Rev. A* **58** (5), 3914–3921 (1998). Erratum : Phys. Rev. A **61**, 029902 (2000).

[104] B.-G. Goldberg, *Digital Techniques in Frequency Synthesis.* New-York, Mac Graw-Hill (1996).

[105] O.J. Luiten, M.W. Reynolds et J.T.M. Walraven, « Kinetic theory of the evaporative cooling of a trapped gas ». *Phys. Rev. A* **53** (1), 381–389 (1996).

[106] G. A. Bird, *Molecular gas dynamics and the direct simulation of gas flows.* Clarendon, Oxford Univ. Press (1994).

[107] D. Guéry-Odelin, *Dynamique collisionnelle des gaz d'alcalins lourds : du refroidissement évaporatif à la condensation de Bose-Einstein.* Thèse de doctorat, Université Paris VI (1998).

[108] W. H. Heathcote, E. Nugent, B. T. Sheard et C. J. Foot, « A ring trap for ultracold atoms in an RF-dressed state ». *New Journal of Physics* **10** (4), 043 012 (2008).

[109] S. C. Whitmore et W. Zimmermann, « Observation of Stable Superfluid Circulation in Liquid-Helium II at the Level of One, Two, and Three Quantum Units ». *Phys. Rev. Lett.* **15**, 389 (1965).

[110] J. File et R. G. Mills, « Observation of Persistent Current in a Superconducting Solenoid ». *Phys. Rev. Lett.* **10**, 93 (1963).

[111] C. Ryu, M. F. Andersen, P. Cladé, V. Natarajan, K. Helmerson et W. D. Phillips, « Observation of Persistent Flow of a Bose-Einstein Condensate in a Toroidal Trap ». *Phys. Rev. Lett.* **99**, 260 401 (2007).

[112] K. W. Madison, F. Chevy, W. Wohlleben et J. Dalibard, « Vortex formation in a stirred Bose-Einstein condensate ». *Phys. Rev. Lett.* **84**, 806 (2000).

[113] I. Lesanovsky et W. von Klitzing, « Time-Averaged Adiabatic Potentials : Versatile Matter-Wave Guides and Atom Traps ». *Phys. Rev. Lett.* **99**, 083 001 (2007).

[114] M. Boyd, E. W. Streed, P. Medley, G. K. Campbell, J. Mun, W. Ketterle et D. E. Pritchard, « Atom trapping with a thin magnetic film ». *Phys. Rev. A* **76**, 043 624 (2007).

[115] P. Krüger, L. M. Andersson, S. Wildermuth, S. Hofferberth, E. Haller, S. Aigner, S. Groth, I. Bar-Joseph et J. Schmiedmayer, « Potential roughness near lithographically fabricated atom chips ». *Phys. Rev. A* **76**, 063 621 (2007).

[116] G. Sagué, E. Vetsch, W. Alt, D. Meschede et A. Rauschenbeutel, « Cold-Atom Physics Using Ultrathin Optical Fibers : Light-Induced Dipole Forces and Surface Interactions ». *Phys. Rev. Lett.* **99**, 163 602 (2007).

[117] A. H. Barnett, S. P. Smith, M. Olshanii, K. S. Johnson, A. W. Adams et M. Prentiss, « Substrate-based atom waveguide using guided two-color evanescent light fields ». *Phys. Rev. A* **61**, 023 608 (2000).

[118] B. Engeser, *A novel surface trapping apparatus for ultracold cesium atoms and the investigation of an Efimov resonance*. Thèse de doctorat, Leopold-Franzens-Universität Innsbruck (2006).

[119] J. Billy, V. Josse, Z. Zuo, A. Bernard, B. Hambrecht, P. Lugan, D. Clément, L. Sanchez-Palencia, P. Bouyer et A. Aspect, « Direct observation of Anderson localization of matter waves in a controlled disorder ». *Nature* **453**, 891 (2008).

[120] G. Roati, C. D'Errico, L. Fallani, M. Fattori, C. Fort, M. Zaccanti, G. Modugno, M. Modugno et M. Inguscio, « Anderson localization of a non-interacting Bose ?Einstein condensate ». *Nature* **453**, 895 (2008).

[121] C. Miniatura, R.C. Kuhn, D. Delande et C.A. Mueller, « Quantum Diffusion of Matter Waves in 2D Speckle Potentials » (2008). Preprint arXiv:0807.3698, http://arxiv.org/abs/0807.3698.

[122] J.A. Sauer, M.D. Barrett et M.S. Chapman, « Storage ring for neutral atoms ». *Phys. Rev. Lett.* **87** (27), 270 401, 1–4 (2001).

[123] A.S. Arnold et E. Riis, « Bose-Einstein condensates in 'giant' toroidal magnetic traps ». *J. Mod. Opt.* **49** (5/6), 959–964 (2002).

[124] A.S. Arnold, « Adaptable-radius, time-orbiting magnetic ring trap for Bose-Einstein condensates ». *J. Phys. B : At. Mol. Opt. Phys.* **37**, L29–L33 (2004).

[125] S. Gupta, K. W. Murch, K. L. Moore, T. P. Purdy et D. M. Stamper-Kurn, « Bose-Einstein Condensation in a Circular Waveguide ». *Phys. Rev. Lett.* **95**, 143 201 (2005).

[126] B. P. Anderson, K. Dholakia et E. M. Wright, « Atomic-phase interference devices based on ring-shaped Bose-Einstein condensates : Two-ring case ». *Phys. Rev. A* **67**, 033 601 (2003).

[127] M. H. W. Chan, A. W. Yanof et J. D. Reppy, « Superfluidity of Thin ^{4}He Films ». *Phys. Rev. Lett.* **32**, 1347 (1974).

Résumé

Cette habilitation porte sur une série d'expériences faites avec comme leitmotiv la condensation de Bose-Einstein à deux dimensions. Dans une première série d'expériences, nous avons utilisé le caractère très anisotrope des champs évanescents, propice au confinement d'un gaz bidimensionnel. La production d'un condensat à 3 mm seulement de la surface supportant une onde évanescente a constitué une première. Nos expériences de rebond du condensat sur une seule onde évanescente ont permis de caractériser très précisément l'interaction entre les atomes et le champ diffusé par les défauts de surface. Nous avons ainsi confirmé quantitativement la théorie de Carsten Henkel *et al.*. Nous avons également montré que la diffraction était toujours clairement observable malgré la forte diffusion, lors du rebond d'un condensat sur un miroir modulé.

Dans un second temps, sur la proposition d'Oliver Zobay et Barry Garraway, nous avons mis au point une nouvelle approche pour confiner les atomes dans des potentiels très anisotropes. La combinaison d'un champ radiofréquence (RF) et d'un champ magnétique statique résulte en un potentiel adiabatique dont la géométrie peut être largement contrôlée, y compris dynamiquement. Ces potentiels RF, que nous avons mis en œuvre pour la première fois, permettent de réaliser une « bulle » à atomes, un double puits, un anneau... Nous nous sommes intéressés principalement à produire un piège quasi bidimensionnel dans l'épaisseur de la bulle. Ces pièges sont compatibles avec les condensats de Bose-Einstein, et les atomes peuvent être refroidis par évaporation *in situ*.

Mots clés : atomes froids – rubidium – condensat de Bose-Einstein – piège dipolaire – champ radiofréquence – champ évanescent – gaz 2D – potentiels adiabatiques

Abstract

This habilitation is devoted to a series of experiments in the context of Bose-Einstein condensation (BEC) in 2D. First, evanescent light fields were used to create highly anisotropic potentials. The production of a condensate at a distance of 3 mm only from a surface was demonstrated for the first time. A precise characterization of the interaction between the atoms and the scattered light field was obtained through the experimental study of the reflection of the condensate from an evanescent field. The diffuse reflection theory of Carsten Henkel *et al.* was confirmed on a quantitative basis. Despite a strong diffusion, the diffraction in the time domain off a modulated atom mirror was observed with a good contrast.

The second part of the manuscript is devoted to the new approach of the adiabatic RF potentials, proposed by Oliver Zobay and Barry Garraway. These potentials can trap atoms dressed by a RF field, and placed in an inhomogeneous magnetic field. Their geometry is very flexible, allowing the realization of double wells or ring traps, and can be controlled dynamically. We demontrated for the first time the trapping of RF-dressed atoms in a bubble-like geometry. Moreover, these traps are compatible with the high level of requirement of Bose-Einstein condensates, and with RF-induced evaporative cooling.

Key words : cold atoms – rubidium – Bose-Einstein condensation – dipole trap – radiofrequency field – evanescent field – 2D gas – adiabatic potentials